Neutrino Geophysics
and
Observation of Geo-Neutrinos at KamLAND

Enomoto Sanshiro
Tohoku University

February 2005

Abstract

Neutrinos from radioactive isotopes in the Earth, such as ^{238}U, ^{232}Th and ^{40}K, are expected to bring unique insights in the Earth's internal composition and energy generation mechanism. An Earth model presented in this study predicts 38.5 TNU (i.e., events per 10^{32} protons per year) of geo-neutrino flux at Kamioka, Japan, with about 20% of uncertainties. 575 ton-year exposure of the Kamioka Liquid-scintillator Anti-Neutrino Detector (KamLAND), which consists of 1000 tonnes of organic liquid scintillator, observed 113 events of geo-neutrino candidates. The number of background events are estimated to be 91.6 ± 9.5(syst.)±9.6(stat.). The excess from the background is significant at 93.5%. If this excess is attributed to geo-neutrinos, the flux is estimated to be $62.8^{+44.9}_{-38.3}$ TNU. An upper limit of geo-neutrino flux is set to be 172.2 TNU at 99% CL. Combined with spectrum shape analysis under a geochemical constraint in U/Th ratio, the flux is estimated to be $51.5^{+36.8}_{-33.8}$. The observation is in good agreement with the geophysical/geochemical prediction.

Acknowledgments

The work presented here is a result from the efforts of many KamLAND collaborators. I would like to express my genuine appreciation to every KamLAND collaborator, for their vision and hard work to fulfill the experiment. I would like to give special recognition to Suzuki Atsuto, the KamLAND group leader, and to Inoue Kunio, my adviser, for giving me the opportunity of performing this research and for their support over the years.

The KamLAND experiment is supported by the COE program under grant 09CE2003 of the Japanese Ministry of Education, Culture, Sports, Science and Technology, and under the United States Department of Energy grant DEFG03-00ER41138. The reactor data are provided by courtesy of the following electric associations in Japan: Hokkaido, Tohoku, Tokyo, Hokuriku, Chubu, Kansai, Chugoku, Shikoku and Kyushu Electric Power Companies, Japan Atomic Power Co. and Japan Nuclear Cycle Development Institute. The Kamioka Mining and Smelting Company has provided service for activities in the mine. Part of my funding was provided by JSPS Research Fellowships for Young Scientists.

I am sincerely indebted to Yuri Kamyshkov and Alan Wintenberg for their kind-hearted help and patience during my first foreign stay at ORNL, and to Stuart Freedman, Bruce Berger and Brian Fujikawa for their substantial and invaluable assistance during my long stay at LBL. I am deeply grateful to Sakamoto Hiroshi and Tamura Norio for the insights they gave me in development of a new data acquisition system, and for their support by understanding my concepts.

My deepest thanks go to Nikolai Tolich, Jason Detwiler, Glenn Horton-Smith, Evgueni Yakushev and Naoko Kurahashi, with whom I worked closely over the years, for their friendship and assistance. Discussions and collaborative works with them stimulated me to come up with new ideas, new understandings and new viewpoints, and also made our works highly enjoyable. I hope to work with them again on a physics experiment in the future.

Finally, I would like to thank my family and all of my friends, especially for my parents, Enomoto Masayoshi and Chizuru, for their endless support throughout my life.

Contents

Chapter 1

Introduction

The radius of the Earth, 6371 km, is huge by human standards. Most of the things that relate directly to our activities take place in a very thin layer near the surface. The deepest that any person can get below the surface is only 4 km, and the deepest borehole ever drilled is less than 20 km. The maximum depth of rock samples taken on the surface originate from a depth of about 200km, still far from the lower constitution of the Earth.

Elaborate studies to understand the structure and chemical composition of the whole Earth have extensively been conducted. Most remarkably, seismology has revealed the physical properties of the whole Earth, showing the crust-mantle-core layer structure, their density profiles, and non-uniformity in seismic wave speed that implies global mantle convection. Cosmo-chemical approach, using the CI Carbonaceous Chondrite meteorites as a basic ingredient of the Earth, successfully modeled the bulk chemical composition of the Earth. Combining physical properties known from the seismological analysis, lithology tells us the crystal structure and chemical constitution of rocks in each layer of the Earth. However, since the deep part of the Earth is essentially unreachable, there is no direct observation about the chemical composition of the whole Earth.

Neutrinos from radioactive elements in the Earth, such as Uranium, Thorium and Potassium, have been expected to bring direct insight into the bulk Earth chemical composition, because their cross section is extremely small and travel to the surface practically without any interaction. Neutrinos are also expected to provide fruitful information about Earth's energetics, because neutrino sources are also heat sources as well, and such radiogenic heats are believed to contribute a large part of Earth's heat generation, among other heat sources such as primordial energy of planetary accretion and latent heat of core solidification. Needless to say, all Earth's activities such as earthquakes, volcanoes, terrestrial magnetism and plate tectonics are all powered by and controlled by Earth's heat generation and heat transportation processes. Hence understanding Earth's energy generation processes, as well as the present condition of Earth's energy sources, is essential to all fields of the Earth sciences.

Use of neutrinos to study Earth science was first proposed by G.Eder [3] and G.Marx [4] in 1966 and 1969 respectively, and then reviewed several times by several authors [5–12]. However, due to extremely small cross section of neutrinos, no observation has been ever made.

Kamioka Liquid-scintillator AntiNeutrino Detector (KamLAND) [1,2], which consists of 1000 tons of ultra-pure liquid scintillator surrounded by 1879 photomultiplier tubes, has discriminative sensitivity to the electron-type antineutrinos and is capable to detect few MeV neutrinos. KamLAND is designed primarily to detect antineutrinos from nuclear power reactors and demonstrate neutrino oscillations, however, it is also the first detector sensitive to terrestrial antineutrinos (geo-neutrinos).

The purpose of this study is to make the first observation of geo-neutrinos, by using the KamLAND detector. Geophysics with neutrinos, namely neutrino-geophysics, is also discussed in detail.

The dissertation consists of three parts. In the first part, Chapter 2, geophysics with neutrinos (neutrino-geophysics) is presented and discussed. Since neutrino geophysics is a new field, several new approaches are suggested here. This part also includes my attempt to reconcile disharmony between the high-energy physics methodology and the Earth science methodology; high-energy physics strictly keeps classical (frequentist) statistics, where error estimations are crucial, while geological and geochemical data rarely comes with error estimations.

Chapter 3 to Chapter 7 are dedicated to the second part, geo-neutrino observation at KamLAND. It includes the KamLAND detector design, detection method, data collection, event selection, background estimation, and data analysis. In an attempt to search new physics signals, estimation of all potential backgrounds is essential, thus detailed discussions on this issue take place in this part. In the same reason, detection efficiencies are carefully estimated as well.

The third part, Neutrino Geophysics with KamLAND observations, is discussed in Chapter 8. Future prospects of KamLAND observation, as well as prospects of some other planned geo-neutrino detectors, are also presented. Based on the results of this study, near and far future geo-neutrino experiments are proposed, with considering geophysical/geochemical interests.

The dissertation is conclude in Chapter 9.

Chapter 2

Neutrino Geophysics

2.1 Geo-Neutrinos and Radiogenic Heat Generation

The total heat released from Earth's surface was estimated by H.N.Pollack *et al.* (1993) [13] to be 44.2±1.0 TW, by compiling 24,774 bore-hole observations at 20,201 sites. On a $5^\circ \times 5^\circ$ grid, the observations cover 62% of Earth's surface. Heat flow of regions where no observatins are available is estimated with a geological map by referencing observations of the same geological units. Corrections for the effects of hydrothermal circulation in the young oceanic crust are applied (This estimation was recently revised by A.M.Hofmeister (2005) [14], with corrections in oceanic heat flux, giving a new estimation of 31±1 TW).

As will be discussed later, cosmo-chemical analyses expect significant amount of radioactive isotopes contained in the Earth, radiogenic heat generation of which totals up to about 20TW. The amount of radiogenic heat generation was much larger in the early Earth because of their decay nature, hence the role of radiogenic heat to Earth's evolution and the present energetic activities is essential.

Radioactive isotopes that are abundant in the present Earth are classified into three groups; isotopes in the ^{238}U ($\tau_{1/2} = 4.47 \times 10^9$ year) decay series, isotopes in the ^{232}Th ($\tau_{1/2} = 14.0 \times 10^9$ year) decay series, and ^{40}K ($\tau_{1/2} = 1.28 \times 10^9$ year). All other isotopes, such as isotopes in the ^{235}U ($\tau_{1/2} = 0.71 \times 10^9$ year) decay series and the ^{237}Np ($\tau_{1/2} = 0.002 \times 10^9$ year), have already decayed away due to their short half-lives. Exceptions are ^{87}Rb ($\tau_{1/2} = 49.7 \times 10^9$ year), ^{138}La ($\tau_{1/2} = 110.0 \times 10^9$ year), and ^{176}Lu ($\tau_{1/2} = 21.0 \times 10^9$ year), however their contribution to radiogenic energy generation are negligible as compared with ^{238}U, ^{232}Th and ^{40}K, and their decay Q values are also small (less than 0.5MeV).

Radiogenic heat is produced by decays of isotopes, in which processes electron-type (anti-) neutrinos are emitted.

$$^{238}\mathrm{U} \xrightarrow[100\%]{} {}^{206}\mathrm{Pb} + 8\,^{4}\mathrm{He} + 6e^{-} + 6\bar{\nu_e} + 51.7\ [\mathrm{MeV}] \tag{2.1}$$

$$^{232}\mathrm{Th} \xrightarrow[100\%]{} {}^{208}\mathrm{Pb} + 6\,^{4}\mathrm{He} + 4e^{-} + 4\bar{\nu_e} + 42.7\ [\mathrm{MeV}] \tag{2.2}$$

$$^{40}\mathrm{K} \xrightarrow[89.28\%]{} {}^{40}\mathrm{Ca} + e^{-} + \bar{\nu_e} + 1.311\ [\mathrm{MeV}] \tag{2.3}$$

$$^{40}\mathrm{K} + e^{-} \xrightarrow[10.72\%]{} {}^{40}\mathrm{Ar} + \nu_e + 1.505\ [\mathrm{MeV}] \tag{2.4}$$

Thus the amount of radiogenic heat generation and neutrino luminosity relate directly to each other.

Antineutrinos are emitted by beta decays, and the energy spectra of one beta decay with maximum electron energy $E_{\max}$ is given by a well-established formula,

$$dN(E_e) \;=\; \frac{{G_F}^2|M|^2}{2\pi^3\hbar^7c^5}F(Z,E_e)(E_{\max}-E_e)^2\sqrt{{E_e}^2-{m_e}^2c^4}E_e\;dE_e \tag{2.5}$$

$$E_{\bar{\nu_e}} \;=\; E_{\max} - E_e \tag{2.6}$$

where $E_{\max}$ is the maximum electron energy of beta decay. $F(Z,E_e)$ is the Fermi Function, corresponding to the effect of electrical field of nuclei, given by

$$\begin{aligned} F(Z,E_e) \;&=\; 2(1+\gamma)(2\sqrt{W^2-1}R)^{2(\gamma-1)}e^{\pi y}\frac{|\Gamma(\gamma+iy)|^2}{|\Gamma(2\gamma+1)|^2} \\ \gamma \;&=\; \sqrt{1-(\alpha Z)^2} \qquad W \;=\; \frac{E_e}{mc^2} \qquad y \;=\; \alpha Z\frac{W}{\sqrt{W^2-1}} \\ R \;&=\; 0.426\alpha A^{1/3} \qquad \alpha \;=\; \frac{e^2}{\hbar c} \;=\; 1/137.035989 \end{aligned} \tag{2.7}$$

Under radioactive equilibrium, anti-neutrino spectra of decay series are calculated by summing up the normalized spectra of every beta-decay of every isotope, over the decay series, with weights of production ratio of the isotopes R_{isotope} and branching ratio R_{branch} of the beta decays.

$$\frac{dN}{dE_\nu} \;=\; \sum_{\mathrm{isotope}}\sum_{\mathrm{branch}} R_{\mathrm{isotope}}R_{\mathrm{branch}}\left(\frac{1}{N}\frac{dN}{dE_\nu}\right)_{\mathrm{isotope,\ branch}} \tag{2.8}$$

R_{isotope} is given by summing up parent isotopes' production ratios and branching ratios recursively.

$$R_{\mathrm{isotope}} = \begin{cases} 1 & \text{decay series head} \\ \sum_{\mathrm{parent}}\sum_{\mathrm{branch}} R_{\mathrm{parent}}R_{\mathrm{branch}} & \text{daughter isotopes} \end{cases} \tag{2.9}$$

Figure 2.1 shows the anti-neutrino spectra from ^{40}K, ^{238}U series and ^{232}Th series. In this calculation, 82 beta decays in the U series and 70 beta decays in the Th series are included.

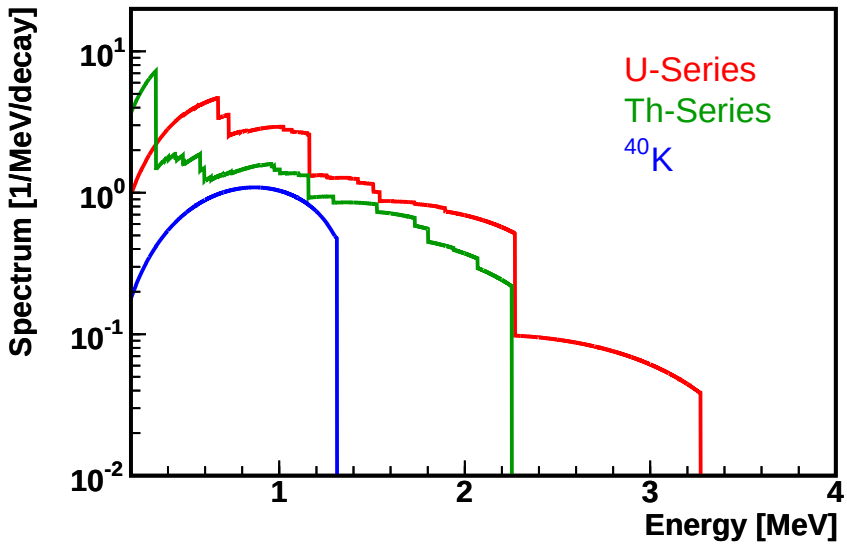

Figure 2.1: Spectra of the U-Series, Th-Series and ^{40}K Geo-Neutrinos. Antineutrinos are generated by beta decays of these radioactive isotopes. In this calculation, 82 beta decays in the U series and 70 beta decays in the Th series are included. Neutrinos from ^{40}K electron capture is not shown in this figure.

Table 2.1: Radiogenic Heat Generation per Decay

	^{238}U Series	^{232}Th Series	^{40}K	
			β^- (89.28%)	EC (10.72%)
Q [MeV/decay]	51.7	42.7	1.311	1.505
Q_ν [MeV/decay]	3.96	2.23	0.801	0.051
Q_{heat} [MeV/decay]	47.7	40.4	0.531	1.454

Radiogenic heat generation is calculated by subtracting neutrino energy from the decay Q value.

$$Q_{\text{heat}} \;=\; Q - Q_\nu \;=\; Q - \int_0^{E_{\max}} E_\nu \frac{dN}{dE_\nu}\, dE_\nu \tag{2.10}$$

where $N(E_\nu)$ is the neutrino spectrum given by (2.5). By summing all decays in the U-series, Th-series and ^{40}K, radiogenic heat generation is calculated as summarized in Table 2.1.

With atomic weights, natural abundances and halflives, neutrino luminosity $L_{\bar{\nu}_e}$ and heat generation from unit mass of U, Th and K are calculated as summarized in Table 2.2. From these calculations, the relation between neutrino luminosity and radiogenic heat generation is expressed by:

Table 2.2: Radiogenic Heat Generation and Neutrino Luminosity

Isotope

	^{238}U	^{232}Th	^{40}K
Natural Abundance [%]	99.27	100	0.01167
$N_{\rm atom}$/mass [1/kg]	2.530×10^{24}	2.596×10^{24}	1.506×10^{25}
Lifetime [sec]	2.034×10^{17}	6.397×10^{17}	5.814×10^{16}
$N_{\rm decay}$/mass [1/sec/kg]	1.244×10^{7}	4.058×10^{6}	2.590×10^{8}
$N_{\bar{\nu}_e}/N_{\rm decay}$	6	4	0.8927
$L_{\bar{\nu}_e}$/mass [1/sec/kg]	7.464×10^{7}	1.623×10^{7}	2.312×10^{8}
$Q_{\rm heat}$/mass [W/kg]	9.515×10^{-5}	2.628×10^{-5}	2.613×10^{-5}

Natural Element

	Uranium	Thorium	Potassium
$L_{\bar{\nu}_e}$/mass [1/sec/kg]	7.410×10^{7}	1.623×10^{7}	2.698×10^{4}
$Q_{\rm heat}$/mass [W/kg]	9.446×10^{-5}	2.628×10^{-5}	3.049×10^{-9}

$$\text{Uranium}: \quad \frac{L_{\bar{\nu}_e}}{[1/\text{sec}]} = 7.84 \times 10^{11} \cdot \frac{Q_{\rm heat}}{[\text{W}]} = 7.41 \times 10^{7} \cdot \frac{M}{[\text{kg}]} \tag{2.11}$$

$$\text{Thorium}: \quad \frac{L_{\bar{\nu}_e}}{[1/\text{sec}]} = 6.16 \times 10^{10} \cdot \frac{Q_{\rm heat}}{[\text{W}]} = 1.62 \times 10^{7} \cdot \frac{M}{[\text{kg}]} \tag{2.12}$$

$$\text{Potassium}: \quad \frac{L_{\bar{\nu}_e}}{[1/\text{sec}]} = 8.85 \times 10^{12} \cdot \frac{Q_{\rm heat}}{[\text{W}]} = 2.70 \times 10^{4} \cdot \frac{M}{[\text{kg}]} \tag{2.13}$$

2.2 A Reference Earth Model

To estimate geo-neutrino flux at surface, we need to know the distribution of neutrino sources. However, this is the region of our interest, to which we can bring some knowledge from our geo-neutrino observation.

In this section, a reference Earth model is constructed for neutrino flux estimation. It should be emphasized that the purpose of the model construction is to provide a stating point to discuss geophysical topics using geo-neutrino observations, not to build up a complete Earth model. Hence the model is constructed with keeping it in mind that it should clearly outline the relation between geophysical features and our observation. Well-established geophysical/geochemical knowledge is positively included, with providing a way to incorporate ones own insight into the model for their discussion.

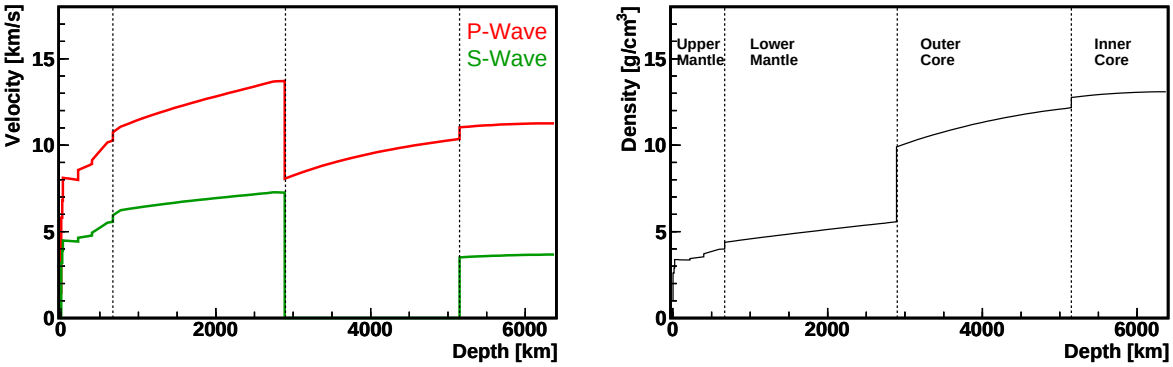

Figure 2.2: Preliminary Reference Earth Model given by A.M.Dziewonski *et al.* (1981). Seismic wave velocities (Vp and Vs) and density as a function of depth are shown. In this profile, the Earth's layer structure, the crust, upper mantle, lower mantle, outer core, and inner core is clearly seen.

2.2.1 Structural Model

Seismology has revealed the detailed geophysical feature of the whole Earth. In 1981, A.M.Dziewonski and D.L.Anderson [15] presented the Preliminary Earth Reference Model (PREM), describing the seismic wave speeds (Vp, Vs), elastic properties (Q_μ, Q_K), and other parameters such as density and pressure, as a function of radius. The model was constructed by an inversion method with more than 1000 measurements of eigenfrequencies of the Earth, 500 summary observations of body wave travel time, 100 normal mode Q values, mass and orbital moment of the Earth. Although the model is described with parameters as a function of radius, transverse isotropy was introduced in the calculation to the outer 220km of the mantle, in order to explain the discrepancy between short-period Love wave and Rayleigh wave data. Figure 2.2 shows the seismic wave speeds and density profiles given in the PREM model. As shown in the figure, Earth's global layer structure, crust, several layers of mantle, liquid outer core and solid inner core, is clearly demonstrated, with understanding of their physical properties.

Seismological analysis is also useful to determine the local crustal structure. C.Bassin *et al.* (2000) [16] compiled seismic wave measurements and made a $2° \times 2°$ grid crustal thickness map (distributed as CRUST 2.0 data set), describing the thickness and density of soft sediment, hard sediment, upper crust, middle crust, and lower crust. The CRUST 2.0 is an updated version of the former crustal structure data set, CRUST 5.0, which gives crustal structure estimation at $5° \times 5°$ resolution. The CRUST 5.0 is constructed based on 560 seismic refraction measurements published between 1948 and 1995. Compressional wave velocity of each layer is based on measurements, and shear wave velocity and density are estimated using empirical V_p-V_s and V_p-density relationships. For areas where no measurements are available, seismic wave velocities and density are estimated from statistical average of regions with a similar crustal age and tectonic setting. Figure 2.3 and Figure 2.4 shows the map of crustal thickness given by the CRUST 2.0 dataset.

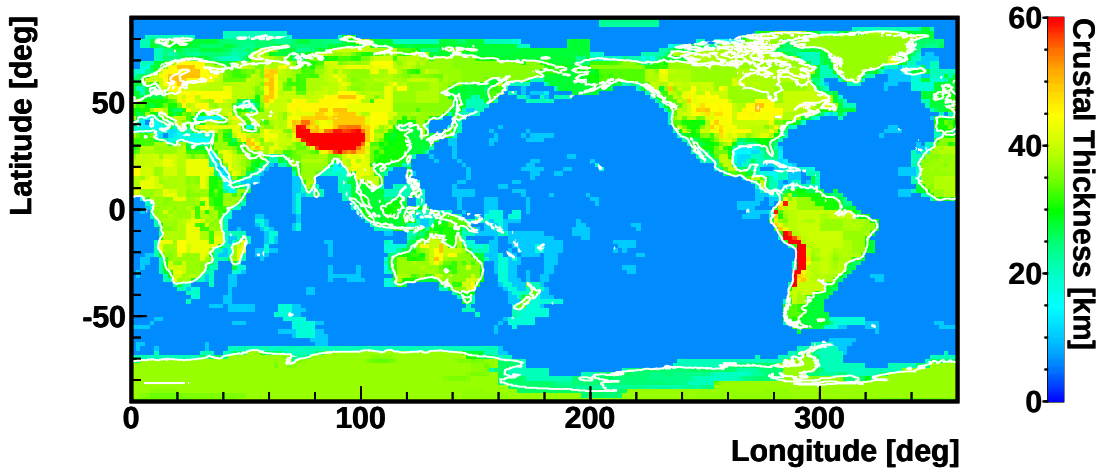

Figure 2.3: Crustal Thickness Map given by C.Bassin *et al.* (CRUST 2.0). This shows crustal thickness in a grid of $2° \times 2°$. The map is constructed based on accumulated seismic refraction measurements published since 1948. Further details are presented in Appendix A.

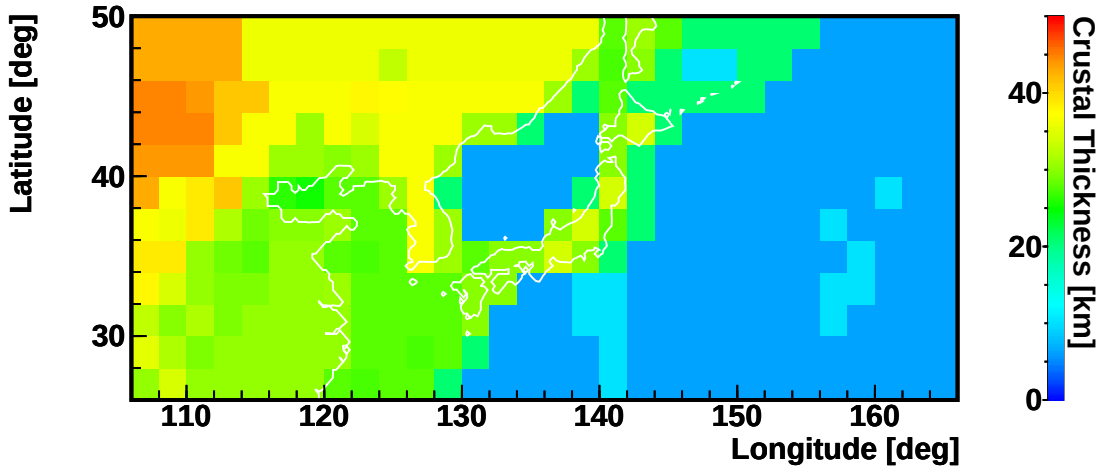

Figure 2.4: Crustal Thickness Map given by C.Bassin *et al.* (CRUST 2.0). The same dataset as Figure 2.3, but with focus on Japan Islands.

A sediment thickness map with even better resolution ($1° \times 1°$) is provided by G.Laske (1997) *et al.* [17]. Details of those data sets are presented in Appendix A.

D.Zhao *et al.* (1992) [18] analyzed more than 13,000 arrival times of 562 shallow earthquakes around the Japan Islands. The earthquake arrival times are collected at 208 stations covering the whole Japan Islands, and the data is compiled as University Network Earthquake Catalog, distributed by the Earthquake Prediction Data Center (EPDC). By applying an inversion method, D.Zhao *et al.* obtained a precise map of the Conrad and

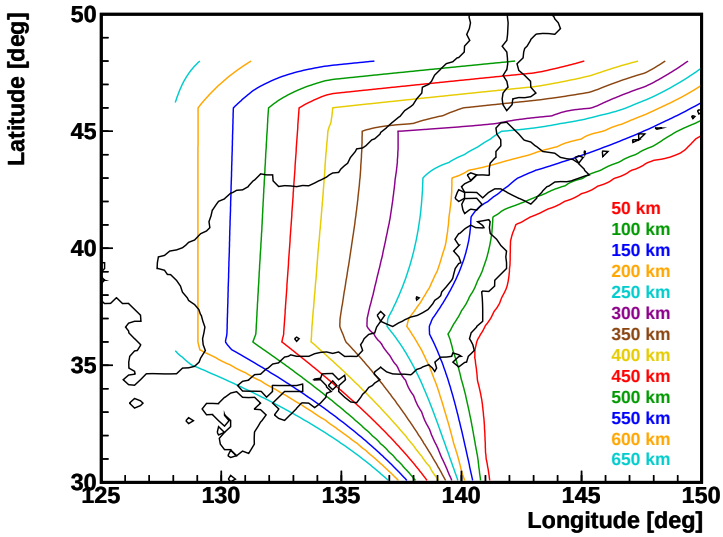

Figure 2.5: Subducting Slab Depth beneath Japan given by Zhao *et al.*. The map is constructed based on more than 13,000 arrival times of 562 shallow earthquakes. Further details of the data set provided by Zhao *et al.* (1992) are presented in Appendix A.

Moho discontinuity depth beneath the Japan Islands. The map provided by D.Zhao *et al.* is shown in Appendix A. They also determined the depth of the subducting plate beneath Japan. The map provided by the authors is shown in Figure 2.5.

Recent seismological analysis observed non-uniform seismic wave speed in the mantle. The small anomalies in seismic wave speed from the PREM model, are thought to be representing temperature variation; the fast parts are dense therefore are cold, and the slow parts are sparse thus are hot. Figure A.5 in Appendix A shows seismic speed anomaly analyzed by C.Mégnin *et al.* (2000) [19]. Figure 2.6 shows the same data, but displayed on a cross section of the Earth. It is believed that the temperature variation pattern corresponds the mantle convection pattern; there are two large *super plumes* (up-going hot plume) beneath South Pacific and Africa, there is one large down-going cold plume beneath Asia. It also shows chunk of slab accumulated at the boundary of the upper mantle and lower mantle, and at the boundary of the lower mantle and the core, beneath plate subducting zones such as Japan.

Given these precise and comprehensive structural data, Earth's physical structure is now well understood. Figure 2.7 is a picture of Earth structure revealed by seismological analysis.

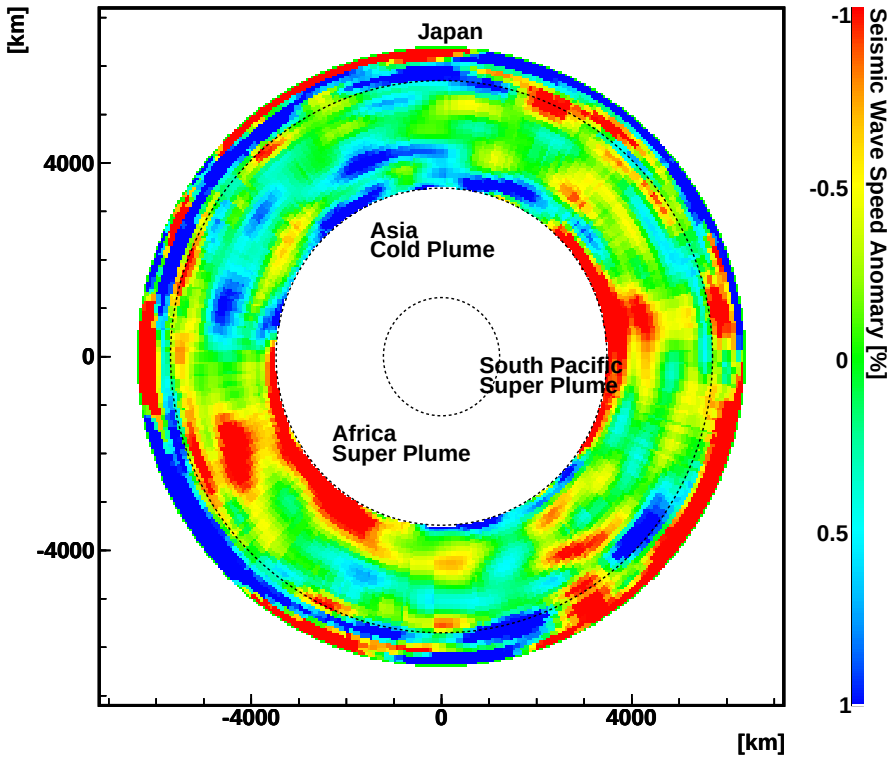

Figure 2.6: Mantle Tomography by Seismic Wave Analysis. The color indicates the seismic speed anomaly, and the data is shown along a cross section of the Earth that contains the KamLAND site and the center. Seismic wave is slower at the blue regions, and is faster at the red regions. It is believed that regions with faster seismic wave are dense therefore are cold, and regions with slower seismic wave are sparse thus are hot. Two hot plumes beneath South Pacific and beneath Africa, one cold plume beneath Asia are clearly seen. Accumulation of slab on the 670km discontinuity and on core-mantle boundary (CMB) are also seen. Further details of the dataset is presented in Appendix A.

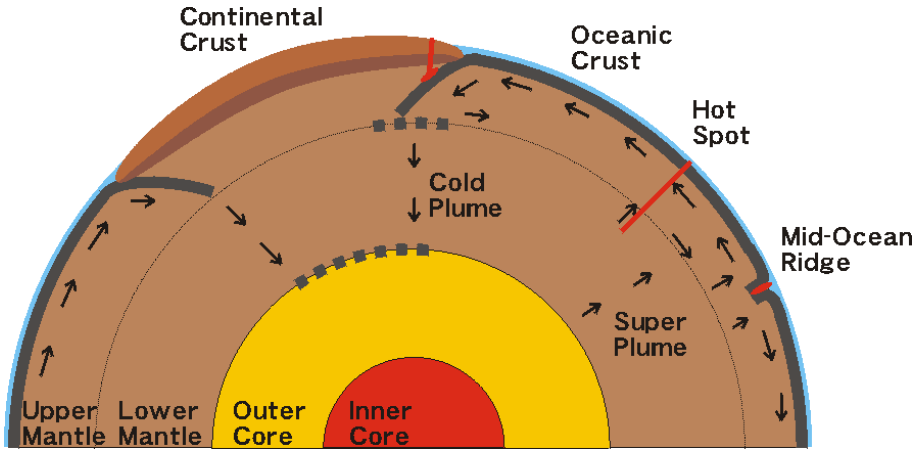

Figure 2.7: Earth Structural Model revealed by Seismological Analysis. The solid part of the Earth consists of several layers; from outer to inner, crust, mantle, outer liquid core, and inner solid core. The crust forming ocean floors (the oceanic crust) is quite different from the crust forming continents (the continental crust); the continental crust usually consists of two layers (upper and lower) separated by the Conrad discontinuity. The upper continental crust is typically composed of Granite while the lower continental crust is typically basaltic in composition. The oceanic crust is formed at Mid-Ocean Ridges and subducts at ocean trenches. The oceanic crust is basaltic in composition, and the typical timescale of formation and subduction is about 1 Ga. The mantle is sub-divided into two layers, the upper mantle and the lower mantle. Seismological properties are clearly different from each other, however, it is not clear whether corresponding differences in chemical composition exists or not. Recent seismological analyses show seismic speed non-uniformity in the upper mantle and the lower mantle. The pattern of the non-uniformity suggests the global mantle convection. Two up-going streams (the Super Plumes) beneath South Pacific Ocean and Africa, and one down-going stream (the Cold Plume) beneath Asia are clearly seen. The pattern of non-uniformity also shows accumulated slab on the 670km discontinuity (the boundary of the upper and lower mantle) and on the core-mantle boundary (CMB) beneath plate subduction zone. The cores are commonly believed to be very high density Fe-Ni alloy, with some inclusion of other elements.

2.2.2 Geochemical Model

Compared with the physical properties of the Earth, chemical properties of the Earth are rather less understood. Geo-neutrinos are expected to bring information about chemical composition of the bulk Earth, thus this is one of the regions of our interest in geo-neutrino studies.

The Bulk Composition of the Earth The bulk chemical composition of the Earth is studied based on analyses of CI carbonaceous chondrite meteorite composition, which is thought to be close to Earth's ingredients because of its inclusion of volatile elements and compositional similarities to the solar photosphere. The bulk composition of the silicate Earth (i.e. mantle + crust) is derived from it by considering escape of volatile elements and separation of the core. With taking account of lithological and geological measurements on the surface, W.F.McDonough *et al.* (1995) [20] constructed a model of bulk silicate Earth composition, known as the Bulk Silicate Earth (BSE) model.

The BSE model gives chemical composition of an imaginary rock, Pyrolite, or primitive mantle (PM), that corresponds to early mantle existed prior to crustal separation. According to the BSE model, Uranium and Thorium amount in the primitive mantle is said to be 20.3 ppb and 79.5 ppb, with 15% and 20% *subjective judgement of uncertainties* by the authors, respectiely. The BSE model is one of the fundamental bases of geochemistry, and it provides a starting point to construct a geochemical model of the Earth.

Core Earth's core is studied with seismic waves, terrestrial magnetism and Earth's orbital behavior. Analysis of meteorites, especially CI carbonaceous chondrite and iron meteorites, helps understand the chemical composition of Earth's core.

Although the chemical composition of Earth's core is obtained by basically subtracting the silicate Earth composition from the CI carbonaceous chondrite composition, refractory lithophile elements such as Uranium and Thorium are commonly believed to be absent from the core, regardless of those compositional models; the core is mainly Fe-Ni alloy with density of $10 \sim 12\mathrm{g/cm}^3$, and laboratory compression experiments show that only low-atomic-weight elements such as H, C, N, O, Mg, Si, and S can be contained in such high density alloy [20, 21].

Mantle The continental crust is formed by partial melting of the mantle. This process extract incompatible elements such as Uranium and Thorium from the mantle into the crust. Although the partial melting occurs at relatively shallow depth (30-70km), global mantle convection mixes the deep interior mantle and the surface mantle, resulting in a general depletion in incompatible elements throughout the whole mantle.

Little is known about the chemical composition of the lower part of the mantle, since we cannot essentially reach that part. Studies are based on seismology and cosmo-chemistry, as frequently mentioned, and laboratory experiments of ultra-high pressure and ultra-high temperature lithology.

Things are slightly better in understanding the upper portion of the mantle, because some mantle samples are available on the surface as ultramafic massifs which are believed to be exposure of the mantle, ultramafic xenoliths which are direct samples of mantle rocks transported to the surface in ascending magmas, and ultramafic magmas which are product of partial melting of the shallow mantle. Additionally, conditions of pressure and temperature are easier to reproduce at laboratories. However, it is not clear whether those mantle samples represent the unbiased mantle composition, because special tectonic settings are responsible to bring the samples to the surface.

Continental Crust The continental crust constitutes only 0.4% of the total Earth mass, but about half of Uranium and Thorium are believed to be contained in the continental crust; Large Ion Lithophile (LIL) elements such as Uranium and Thorium are highly imcompatible with the mantle and the core, and are concentrated in the crust by the processes of planetary differentiation.

The chemical composition of the continental crust is estimated by three different approaches, which usually lead to different results. The first approach, Tectonic Models, relies on plate tectonic process models and assign a common or average lithology for each tectonic environment. The second approach, Geologic Models, uses geological map and chemical analyses of representative rock samples collected at the surface. The third approach, Seismic Models, is based on observed seismic profiles and laboratory lithology studies. The surface heat-flow measurements are also effectively used to constrain the amount of heat-generating elements such as Uranium, Thorium and Potassium.

Estimations based on the tectonic models naturally depend on the models of crustal formation. A commonly referenced estimation was made by S.R.Taylor and S.M.McLennan (1995) [23], which infers andesite crustal composition. A recent model proposes more contribution of oceanic island accretion, resulting in more basaltic composition. Estimations based on the geologic model are biased by exposed rock sampling, and usually lead to the most felsic composition, as extreme as dacite. The seismic models are the most commonly employed technique, however, difficulties arise due to possible non-uniqueness of lithological interpretations of seismic velocity profiles.

A recent estimation of crustal composition based on the tectonic model is made by S.M.McLennan and S.R.Taylor (1999) [22], and S.R.Taylor and S.M.McLennan (1995) [23]. K.H.Wedepohl (1995) [24] made an estimation of crustal composition by utilizing the seismic model. R.L.Rudnick and D.M.Fountain (1995) [25] also employed the seismic model to estimate the chemical composition of the lower portion of the crust, with using the upper crustal composition estimated by S.R.Taylor and S.M.McLennan (1995) [23]. K.C.Condie (1993) [26] estimated the composition of the upper crust with the geologic model, with and without corrections of crust lost by erosion.

Table 2.3 summarizes Uranium and Thorium concentrations reported in those estimations.

Oceanic Crust and Oceanic Sediment The oceanic crust covers approximately the half of the Earth surface. Most of the oceanic crust is formed at mid-ocean ridges, some of them are formed at intra-plate volcanoes, back-arc basins such as the Sea of Japan,

Table 2.3: Uranium and Thorium Concentrations in Continental Crust

	Uranium Concentration [ppm]		
	Upper Crust	Middle Crust	Lower Crust
McLennan & Taylor (1999)	2.8	0.28	
	0.91		
Wedepohl (1995)	2.5	0.93	
	1.7		
Rudnick & Fountain (1995)	(2.8)	1.6	0.2
	1.42		
Condie (1993)	2.4 / 2.2	-	-

	Thorium Concentration [ppm]		
	Upper Crust	Middle Crust	Lower Crust
McLennan & Taylor (1999)	10.7	1.06	
	3.5		
Wedepohl (1995)	10.3	6.6	
	8.5		
Rudnick & Fountain (1995)	(10.7)	6.1	1.2
	5.6		
Condie (1993)	9.1 / 8.6	-	-

and oceanic plateaus. The oceanic crusts, especially ones formed at mid-ocean ridges, are relatively homogeneous in thickness ($\sim$7km) and in chemical composition, as compared with the continental crust. The time scale of oceanic plate formation and subduction is 1-1.3 Ga.

The oceanic crust is basaltic in composition, whose Uranium and Thorium concentrations (~ 0.10 ppm and ~ 0.22 ppm, respectively [27]) are higher than those of the mantle (~ 0.01 ppm and ~ 0.05 ppm), but lower than those of the continental crust (~ 1 ppm and ~ 4 ppm). This is believed to be a result of the upper mantle's depletion in incompatible elements; Hofmann (1988) [30] demonstrated that the composition of Mid-Ocean-Ridge Basalt (MORB) is successfully reproduced by a two stage model, with melt extraction of the primary mantle as the first step and extraction from the depleted mantle as the second step.

The oceanic crust, especially old oceanic crust, is covered with thick sediment that originates detrital sources (volcanic and continental) and biological products. Sediment on the oceanic crust is systematically surveyed by Deep Sea Drilling Project (DSDP) and Ocean Drilling Program (ODP), and composition of sediment on subducting plates is compiled by T.Plank *et al.* (1988) [28] as GLOSS (Global Subducting Sediment), giving estimated Uranium and Thorium concentration to be 1.68 ppm and 6.91 ppm respectively.

Table 2.4: A Reference Earth Model

		U [ppm]	Th [ppm]	Reference
Sediment	Continental	2.8	10.7	-
	Oceanic	1.68	6.91	Plank *et al.* (1998) [28]
Continental Crust	Upper	2.8	10.7	Rudnick *et al.* (1995) [25]
	Middle	1.6	6.1	Rudnick *et al.* (1995) [25]
	Lower	0.2	1.2	Rudnick *et al.* (1995) [25]
Oceanic Crust		0.10	0.22	Taylor *et al.* (1985) [27]
Mantle	Upper	0.012	0.048	-
	Lower	0.012	0.048	-
Core	Outer	0	0	McDonough (1999) [21]
	Inner	0	0	McDonough (1999) [21]
Bulk Silicate (BSE Model)		0.02	0.08	McDonough (1995) [20]

2.2.3 A Reference Earth Model

Based on these structural and geochemical Earth models, a reference Earth model for geo-neutrino flux estimation is constructed. Here I rely on the structural features of the Earth revealed by the seismological analyses, and construct the model in order that geochemical features are directly related to our geo-neutrino observations, because geochemical knowledge, in particular of the deep interior portion of the Earth, is much more uncertain than structural picture of the Earth. Errors are not assigned intentionally; all uncertainties, including local variation of geology, and incorrectness of the model, are all discussed later. The purpose of the reference model is to provide a starting point to discuss these issues with geo-neutrino observations.

Based on the structural model, the solid Earth is divided into ten parts: continental sediment (CS), oceanic sediment (OS), upper continental crust (UCC), middle continental crust (MCC), lower continental crust (LCC), oceanic crust (OC), upper mantle (UM), lower mantle (LM), outer core, and inner core. Although the oceanic crust usually consists of three layers, they are united into one component because contribution of the oceanic crust to the bulk Earth as a U/Th reservoir, radiogenic heat source, and geo-neutrino source is negligible and such treatment reduces unnecessary complication. Following the geochemical argument that Uranium and Thorium are absent from the core, the core is omitted from the discussion below.

As a first step, each part is assumed to be uniform in chemical composition. Uranium and Thorium concentrations of each part are assigned as shown in Table 2.4.

For the composition of the continental crust, I adopt the values estimated by R.L.Rudnick and D.M.Fountain (1995) [25], just because their estimation gives compositions of three layers of continental crust. It should be noted that Rudnick *et al.* refer for their upper crustal composition to S.M.McLennan and S.R.Taylor (1999) [22].

For the composition of the continental sediment, I simply adopted the same value as

that of the upper continental crust, because the origin of the continental sediment is the continental crust and usually its composition is very close to that of well-homogenized continental crust.

Since no reliable estimation of the mantle composition is available, I adjusted it in order that the total silicate composition equals to the composition of the bulk silicate Earth estimated by W.F.McDonough *et al.* [20] (BSE Model), under the assumption that the mantle is completely homogeneous throughout the upper mantle to the lower mantle. All these assumptions are tested later.

2.3 Neutrino Propagation through the Earth

As demonstrated by recent studies of neutrinos [2], neutrinos change their flavor (eigenstate of weak interaction) into another kind. The phenomenon, neutrino oscillation, is a consequence of finite neutrino masses and mixing angles.

Although there are at least three generations of neutrinos, here we use two-flavor case oscillation, because parameters of three generation oscillation are not yet precisely determined, and more essentially, two generation oscillation is a very good approximation.

The time development of neutrino wave function in their mass eigenstates $\bar{\nu_1}$ and $\bar{\nu_2}$ are given by the Schrödinger equation.

$$\frac{d}{dt}\begin{pmatrix} \bar{\nu_1}(t) \\ \bar{\nu_2}(t) \end{pmatrix} = \frac{1}{i\hbar}\begin{pmatrix} E_1 & 0 \\ 0 & E_2 \end{pmatrix}\begin{pmatrix} \bar{\nu_1}(t) \\ \bar{\nu_2}(t) \end{pmatrix} \tag{2.14}$$

The flavor eigenstates are generally expressed by unitary conversion of mass eigenstates.

$$\begin{pmatrix} \bar{\nu_e}(t) \\ \bar{\nu_\mu}(t) \end{pmatrix} = \begin{pmatrix} \cos\theta & \sin\theta \\ -\sin\theta & \cos\theta \end{pmatrix}\begin{pmatrix} \bar{\nu_1}(t) \\ \bar{\nu_2}(t) \end{pmatrix} \tag{2.15}$$

From these equations, we have the time development equation of neutrinos in flavor eigenstates.

$$\frac{d}{dt}\begin{pmatrix} \bar{\nu_e}(t) \\ \bar{\nu_\mu}(t) \end{pmatrix} = \frac{1}{i\hbar}\begin{pmatrix} -\frac{\Delta m^2}{4E}\cos 2\theta & \frac{\Delta m^2}{4E}\sin 2\theta \\ \frac{\Delta m^2}{4E}\sin 2\theta & \frac{\Delta m^2}{4E}\cos 2\theta \end{pmatrix}\begin{pmatrix} \bar{\nu_e}(t) \\ \bar{\nu_\mu}(t) \end{pmatrix} \tag{2.16}$$

where Δm^2 is the difference of squared masses between the two neutrinos, $\Delta m^2 = {m_2}^2 - {m_1}^2$. The survival probability, that is the probability of electron neutrinos to be detected as electron neutrinos after traveling certain distance L, is then calculated by

$$\begin{aligned} P(\bar{\nu_e}(0) \to \bar{\nu_e}(L)) &= |\langle \bar{\nu_e}|\bar{\nu_e}(t)\rangle|^2 \\ &= 1 - \sin^2 2\theta \sin^2(\frac{\Delta m^2}{4E}\frac{t}{\hbar}) \\ &= 1 - \sin^2 2\theta \sin^2(\frac{1}{c\hbar}\frac{\Delta m^2 L}{4E}) \end{aligned} \tag{2.17}$$

The neutrino oscillation parameters, Δm^2 and $\sin^2 2\theta$, are well determined by recent neutrino studies. A global analysis of KamLAND reactor neutrino observation and solar

neutrino observation [2] reported the oscillation parameters to be $\Delta m^2 = 7.9^{+0.6}_{-0.5}\times 10^{-5}\mathrm{eV}^2$ and $\tan^2\theta = 0.40^{+0.10}_{-0.07}$ ($\sin^2 2\theta = 0.82^{+0.07}_{-0.07}$).

If neutrino sources spread over vast region compared to its oscillation length that is characterized by $L \sim \pi c\hbar\frac{4E}{\Delta m^2}$, the effect of neutrino oscillation to the total neutrino flux is well averaged, giving average survival probability:

$$P(\bar{\nu_e} \to \bar{\nu_e}) \;\sim\; 1 - \frac{1}{2}\sin^2 2\theta \tag{2.18}$$

When neutrinos propagate in matter, neutrinos feel potential of electrons and nucleons. The Neutral weak current by electrons and nucleons works equally to all generations of neutrinos, while the charged weak current by electrons affects only to electron-type neutrinos.

By the effective charged current interaction between neutrinos and electrons

$$H_{\mathrm{eff}} = \frac{G_F}{\sqrt{2}}\,\bar{\nu_e}\gamma_\mu(1-\gamma_5)\nu_e\;\bar{e}\gamma_\mu(1-\gamma_5)e \tag{2.19}$$

electron type anti-neutrinos receive extra energy of $-\sqrt{2}G_F n_e$, where n_e is the electron number density. Thus the time development of neutrino wave function is given by

$$\frac{d}{dt}\begin{pmatrix}\bar{\nu_e}(t)\\ \bar{\nu_\mu}(t)\end{pmatrix} = \frac{1}{i\hbar}\begin{pmatrix}-\frac{\Delta m^2}{4E}\cos 2\theta - \sqrt{2}G_F n_e & \frac{\Delta m^2}{4E}\sin 2\theta\\ \frac{\Delta m^2}{4E}\sin 2\theta & \frac{\Delta m^2}{4E}\cos 2\theta\end{pmatrix}\begin{pmatrix}\bar{\nu_e}(t)\\ \bar{\nu_\mu}(t)\end{pmatrix} \tag{2.20}$$

The energy matrix is diagonalized by new mass eigenstates $\bar{\nu_1}'$ and $\bar{\nu_2}'$ with new mixing matrix,

$$\begin{pmatrix}\bar{\nu_e}(t)\\ \bar{\nu_\mu}(t)\end{pmatrix} = \begin{pmatrix}\cos\theta' & \sin\theta'\\ -\sin\theta' & \cos\theta'\end{pmatrix}\begin{pmatrix}\bar{\nu_1}'(t)\\ \bar{\nu_2}'(t)\end{pmatrix} \tag{2.21}$$

where

$$\cos 2\theta' = \frac{-A/\Delta m^2 + \cos 2\theta}{\sqrt{(A/\Delta m^2 - \cos 2\theta)^2 + \sin^2 2\theta}} \tag{2.22}$$

$$\sin 2\theta' = \frac{\sin 2\theta}{\sqrt{(A/\Delta m^2 - \cos 2\theta)^2 + \sin^2 2\theta}} \tag{2.23}$$

with

$$A = -2\sqrt{2}G_F n_e E \tag{2.24}$$

The mass difference in matter is given by

$$\Delta m'^2 = \sqrt{(A - \Delta m^2 - \cos 2\theta)^2 + (\Delta m^2)^2\sin^2 2\theta} \tag{2.25}$$

If the electron density is constant, the survival probability in matter is calculated in the same way as the vacuum oscillation case.

$$P(\bar{\nu_e}(0) \to \bar{\nu_e}(L)) \;=\; 1 - \sin^2 2\theta' \sin^2(\frac{1}{4c\hbar}\frac{\Delta m'^2 L}{E}) \tag{2.26}$$

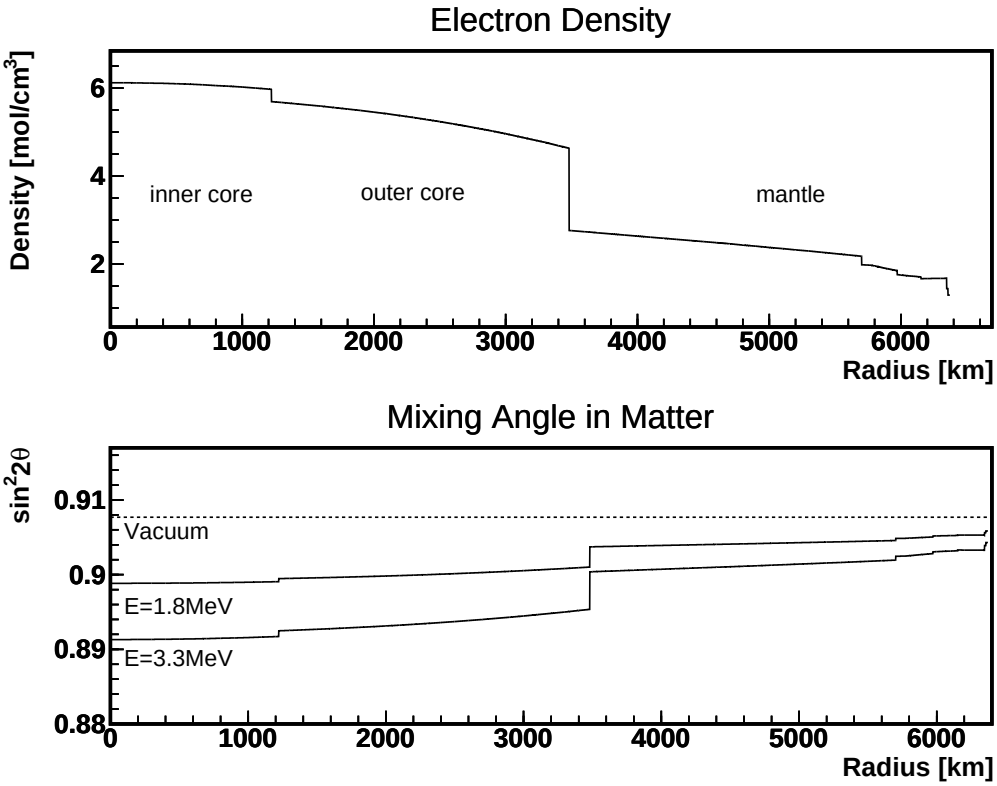

Figure 2.8: Neutrino Mixing Angle in Matter

The average survival probability is then,

$$P(\bar{\nu_e} \to \bar{\nu_e}) \ \sim \ 1 - \frac{1}{2}\sin^2 2\theta' \tag{2.27}$$

Figure 2.8 shows the mixing angle and oscillation length in the Earth. Although the electron density in the Earth is not constant, the calculation result gives us some ideas how electrons in the Earth affect neutrino oscillation.

If neutrinos propagate in matter where electron density is not constant, the behavior of survival probability is not trivial. When neutrinos pass though boundaries where electron density changes steeply, changes in wave function depend on the state of the wave function (i.e. the phase of the wave function when and where the wave function experiences the density change) and speed of the variation (i.e. adiabatic or non-adiabatic). Such characteristics makes it difficult to predict the survival probability of neutrinos after traveling through the Earth, even to predict the average survival probability, because adiabatic passages change not only the mixing angle (which recovers at opposite direction passage, i.e. passage from the core to the mantle after passage from the mantle to the core) but also the amplitude of $|\nu_e\rangle$ and $|\nu_\mu\rangle$ superposition (which does not recover at opposite direction passage).

To study this effect, numerical tracing of the time development equation (2.20) is performed. Figure 2.9 shows the oscillation pattern of neutrinos that are generated at

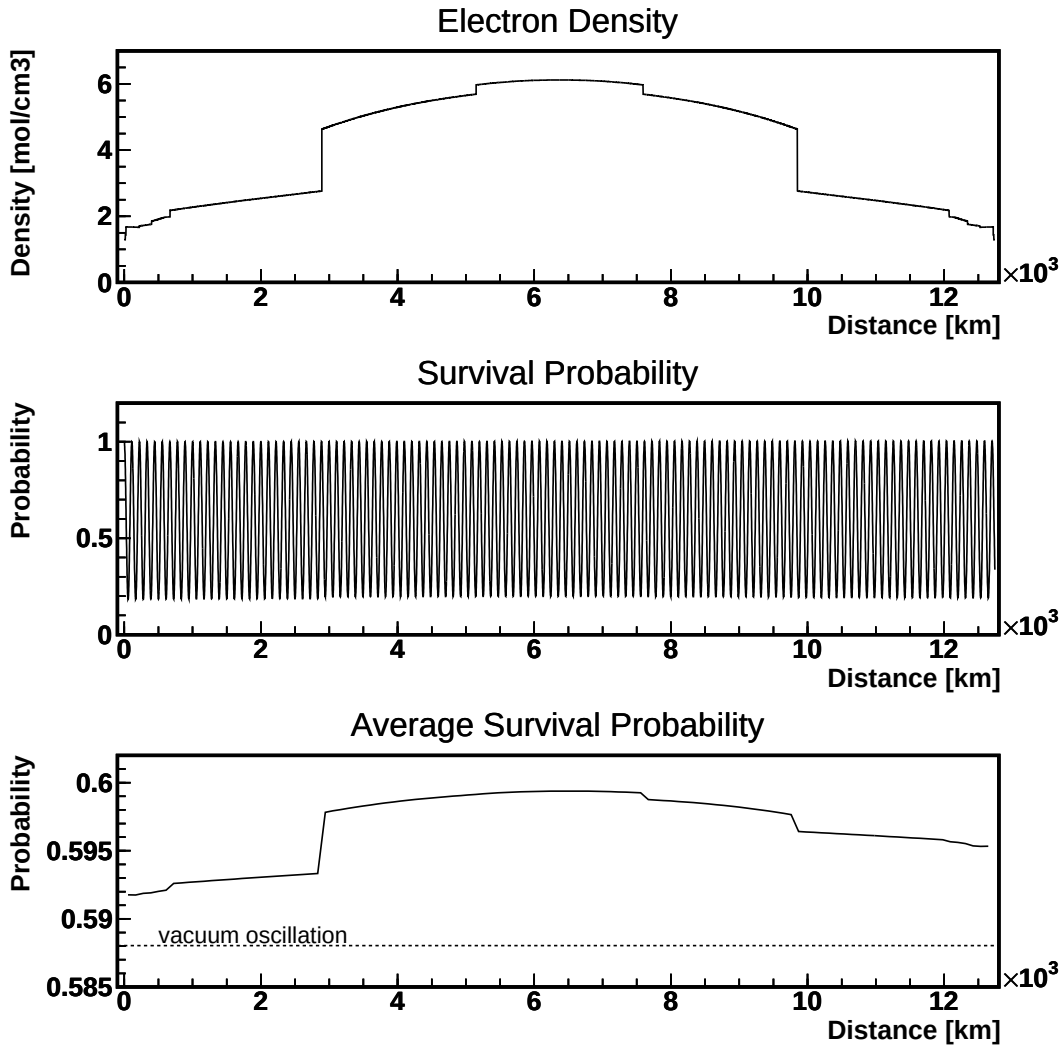

Figure 2.9: Neutrino Oscillation through the Earth. Mono-energetic neutrinos are generated at the opposite side of the Earth, and the survival probability is calculated along the trajectory with numerical calculation. The upper panel shows the electron density profile along the neutrino trajectory, and the middle panel shows the survival probability. The lower panel shows average survival probability which is defined as the mean of one oscillation cycle.

the opposite point of the detector. The average survival probability at each point on the trajectory is also shown in the figure. The same calculations are repeated but slightly different generation points, to change relative position of boundaries to the wave function. Figure 2.10 shows the average survival probability of neutrinos generated in this way. As shown in Figure 2.10, variation of the average survival probability respect to different generation points is less than 1%, and the effect of matter in oscillation to the average survival probability is about 2%.

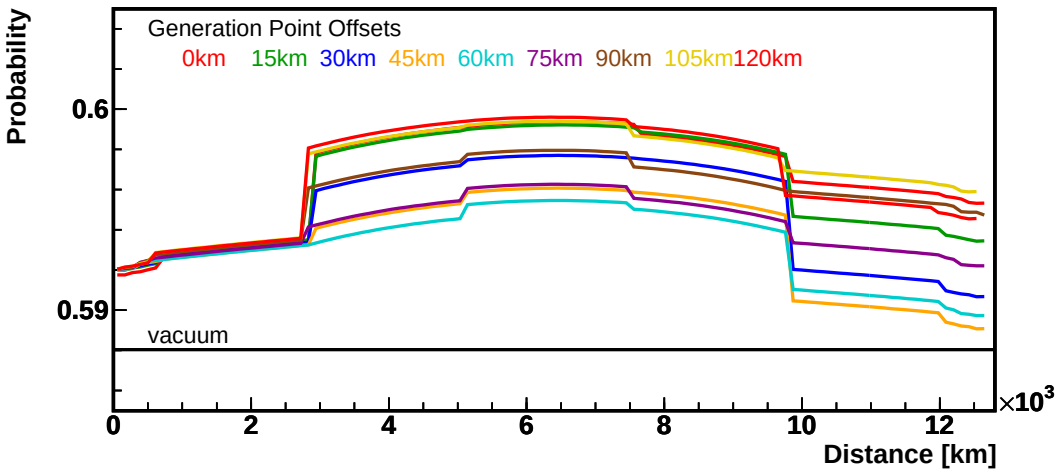

Figure 2.10: Average Survival Probability Variation. Neutrinos are generated around the opposite side of the Earth, with small variations in position. Sensitivity of wavefunction on adiabatic passages is seen.

2.4 Neutrino Flux Integration

The differential neutrino flux $\frac{d\Phi_x}{dE_\nu}$, the flux between energy E_ν and $E_\nu + dE_\nu$ from source labeled X, at the surface $\vec{r}_{\text{detector}}$ is given by the following integration.

$$\frac{d\Phi_x}{dE_\nu} = A_x \cdot \frac{dN_x}{dE_\nu} \cdot \int_{\text{Earth}} \frac{a_x(\vec{r})\rho(\vec{r})}{4\pi|\vec{r} - \vec{r}_{\text{detector}}|^2} P(\bar{\nu}_e(\vec{r}) \to \bar{\nu}_e(\vec{r}_{\text{detector}}); E_\nu)\, dV \tag{2.28}$$

where A_x is the activity of the source X per unit mass, $\frac{dN_x}{dE_\nu}$ is the neutrino spectrum of the source X given by (2.1), $a_x(\vec{r})$ is the source concentration at position $\vec{r}$, $\rho(\vec{r})$ is the density at position $\vec{r}$, and $P(\bar{\nu}_e(\vec{r}) \to \bar{\nu}_e(\vec{r}_{\text{detector}}); E_\nu)$ is the survival probability of electron-type anti-neutrinos with energy E_ν. The integration is taken over the entire volume of the Earth.

The total flux is given by integrating the differential flux over energy;

$$\Phi_x = \int_{E_\nu=0}^{E_{\max}} \frac{d\Phi_x}{dE_\nu} dE_\nu \tag{2.29}$$

These integrations are not easily performed because the survival probability depends on the source distribution and neutrino energy, requiring huge amount of calculation. However, since the spacial integration is taken over the scale much larger than the oscillation length, the effect of neutrino oscillation is well averaged. Similar averaging appears on the energy axis as well, because the survival probability becomes a quickly varying function of the energy if the neutrino travels long distance, where finite energy resolution of detectors smears out such variations.

Under the assumption that the survival probability is well averaged by the integration over space and energy, and that the shape of neutrino spectra is not modified by neutrino oscillation, the total flux is calculated by

$$\Phi_x = A_x \cdot N_x \cdot \int_{\text{Earth}} \frac{a_x(\vec{r})\rho(\vec{r})}{4\pi|\vec{r} - \vec{r}_{\text{detector}}|^2} P(\bar{\nu_e}(\vec{r}) \to \bar{\nu_e}(\vec{r}_{\text{detector}}))\, dV. \tag{2.30}$$

Figure 2.11 shows the relative importance of each region of the Earth to the total geo-neutrino flux observed at the KamLAND site (36.42°N, 137.31°E), estimated with a simple Monte-Carlo (MC) method. As seen in the figure, contribution of near-by region is dominant, but contribution of thin continental crust on the rear hemisphere is not negligible as well.

Given this characteristics of the source distribution, the division scheme of numerical flux integration is designed as shown in Figure 2.12. In this method, namely Flux-Weighted Symmetrical Division Method, small block sizes are assigned to the near-by region, and the block sizes are increased as the distance increases reflecting decrease of relative importance, but keeping the radial block size small for the surface region to correctly handle the continental crust on the rear hemisphere. Radial symmetries are preserved in order that integration of symmetrical region such as the mantle and the core can be performed efficiently.

Although this method effectively reduces the amount of calculation without losing precision, some systematic biases are introduced by large blocks on structural boundaries such as the boundary of the mantle and the core. To avoid this problem, another dividing scheme is incorporated, as shown in Figure 2.13. In this scheme, namely Edge-Adaptive Recursive Division Method, structural boundaries are automatically detected by comparing the structural properties at the apices of the blocks, and the blocks are sub-divided on the boundaries. This procedure is repeated recursively several times until integration converges.

With these integration methods and the reference geochemical model shown in Table 2.4, the geo-neutrino flux at KamLAND (36.42°N, 137.31°E) is calculated. The result is summarized in Table 2.5.

In the table, the flux is expressed with two units, [1/cm^2/sec] and [TNU]. The unit TNU stands for Terrestrial Neutrino Unit, and is defined as number of events per 10^{32} targets per year; thus the value depends on both of spectrum shapes and types of targets. For proton target, 1 [TNU] of the U series geo-neutrino flux corresponds to 7.674×10^4 [1/cm^2/sec], and 1 [TNU] of the Th series geo-neutrino flux corresponds to 2.477×10^5 [1/cm^2/sec]. Geo-neutrinos from ^{40}K are below the $\bar{\nu_e}p$ reaction threshold.

Figure 2.14 shows the differential geo-neutrino flux as a function of distance, defined as

$$\frac{d\Phi}{dR} = A_x \cdot N_x \cdot \int_{\text{Earth}} \frac{a_x(\vec{r})\rho(\vec{r})}{4\pi|\vec{r} - \vec{r}_{\text{detector}}|^2} P(\bar{\nu_e} \to \bar{\nu_e})\, \delta(|\vec{r} - \vec{r}_{\text{detector}}| - R)\, dV \tag{2.31}$$

this expresses the relative importance of regions as a function of distance.

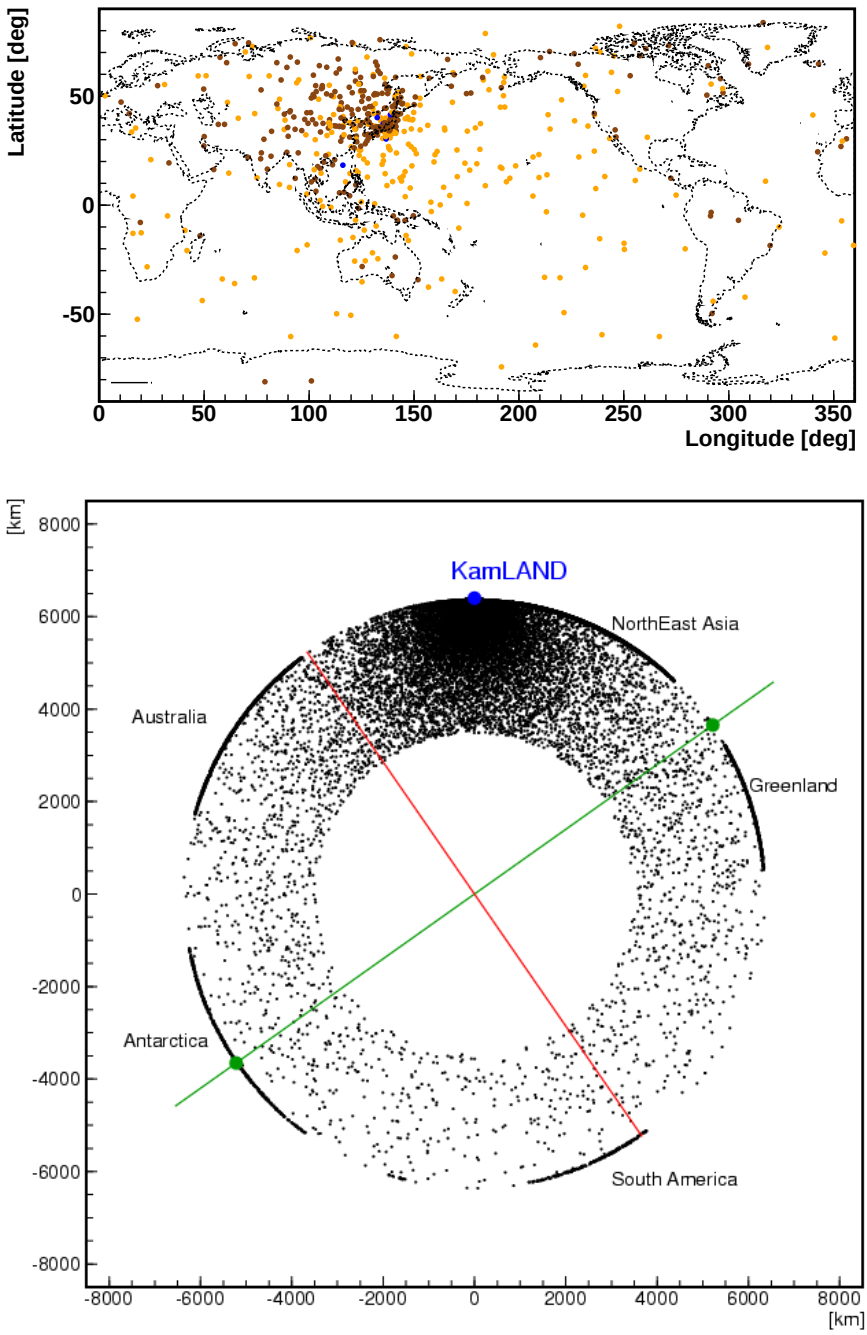

Figure 2.11: Geo-Neutrino Generation Points

Figure 2.15 shows the cumulative geo-neutrino flux as a function of distance, defined as

$$\Phi_x(R) = \int_0^R \frac{d\Phi_x}{dR} dR \tag{2.32}$$

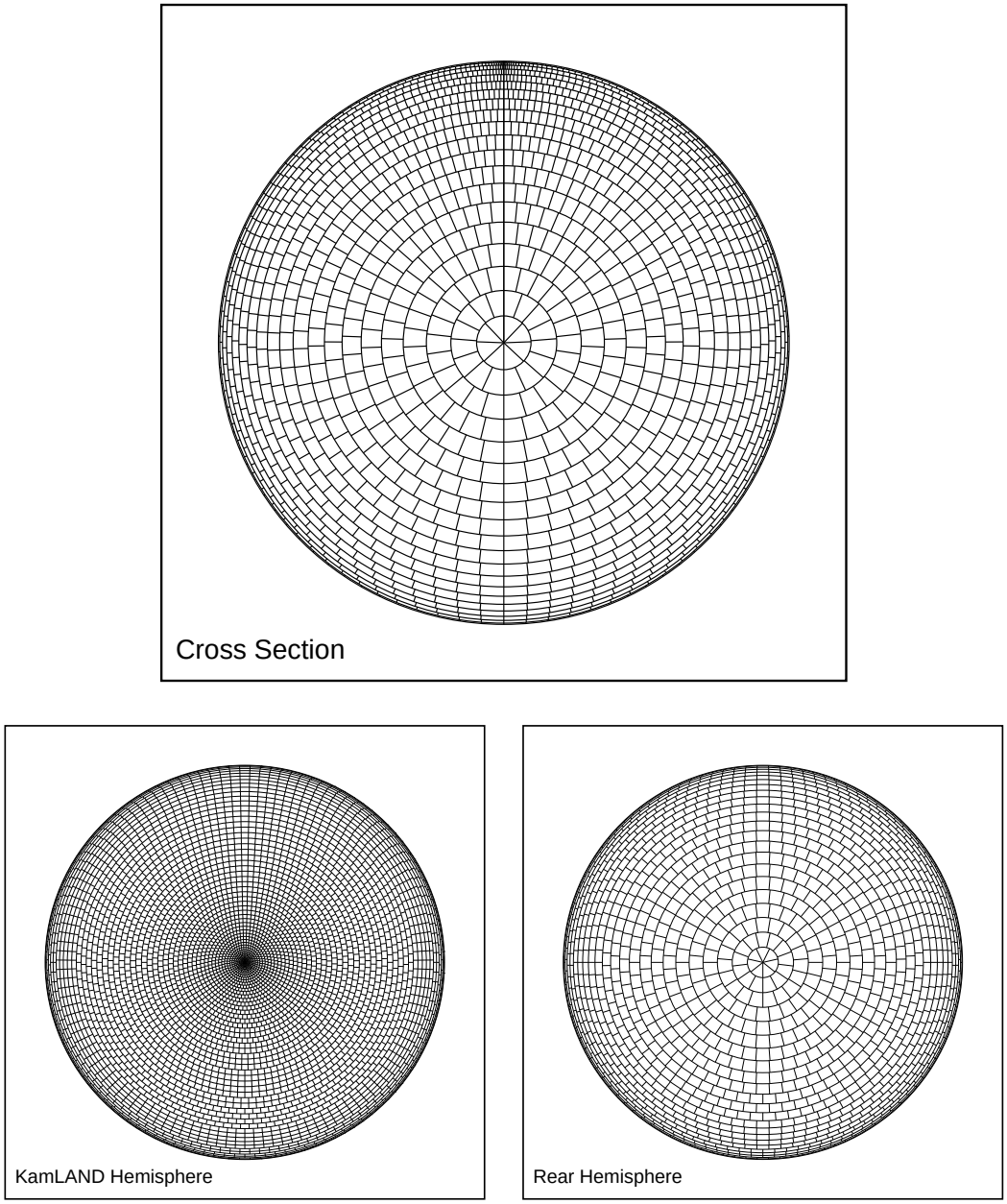

Figure 2.12: Flux-Weighted Symmetrical Division Method

Naturally $\Phi_x(R = R_{\rm Earth})$ agrees with the total flux Φ_x. This gives some ideas how each component of the Earth (crust, mantle, etc) contribute to the total geo-neutrino flux.

Assumption of survival probability averaging is examined with a simplified Earth model, which consists of two hemispheres; the continental hemisphere with 35km thickness homogeneous continental crust and the oceanic hemisphere with 6.5 km thickness homogeneous oceanic crust. Although the total geo-neutrino flux is not correct with this

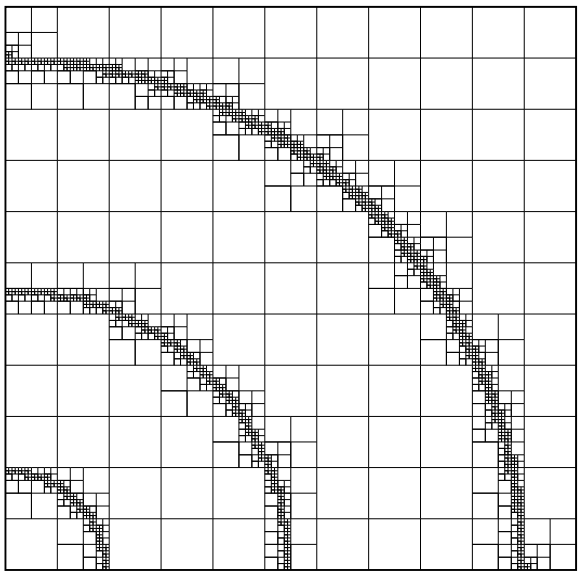

Figure 2.13: Edge-Adaptive Recursive Division Method

Table 2.5: Geo-Neutrino Flux

		U Series Geo-Neutrino		Th Series Geo-Neutrino	
		[1/cm^2/sec]	[TNU]	[1/cm^2/sec]	[TNU]
Sediment	Continental	6.11×10^4	0.80	5.07×10^4	0.20
	Oceanic	1.35×10^4	0.18	1.20×10^4	0.05
Continental Crust	Upper	1.15×10^6	15.01	9.57×10^5	3.86
	Middle	4.31×10^5	5.61	3.57×10^5	1.44
	Lower	5.25×10^4	0.68	6.85×10^4	0.28
Oceanic Crust		9.04×10^3	0.12	4.33×10^3	0.02
Mantle	Upper	2.20×10^5	2.87	1.91×10^5	0.77
	Lower	4.03×10^5	5.25	3.51×10^5	1.42
Core	Outer	0	0	0	0
	Inner	0	0	0	0
Total		2.34×10^6	30.52	1.99×10^6	8.04

simple model, its similar scale of source dispersion results in similar oscillation averaging. This simplification of the Earth model accelerates the numerical integration considerably, enabling us to study various effects in the flux integration.

Figure 2.16 shows the geo-neutrino flux at KamLAND calculated with the simplified Earth model. The flux is calculated at several *representative neutrino energies*, which is the energy used to calculate the survival probability in (2.30). The variation in the flux over the energy expresses the extent of spectrum distortion induced by the neutrino

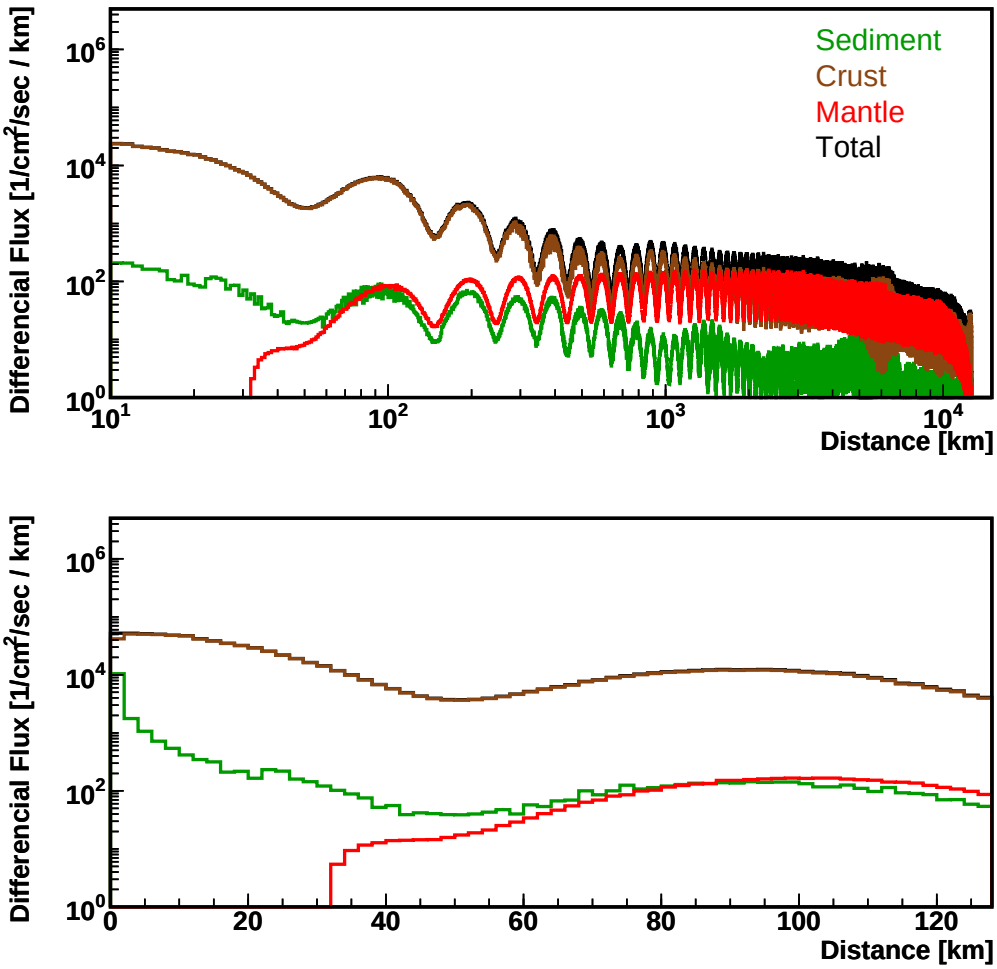

Figure 2.14: Differential Geo-Neutrino Flux

oscillation phenomenon. From this result, the spectrum distortion is found to be around $\pm 1\%$.

To see how the averaging of survival probability in the flux integration behaves, averaged survival probability $\tilde{P}$, which is defined by the ratio of the oscillated flux and the null-oscillated flux, is calculated as a function of integration radius. In this calculation, the energy dependence of survival probability is correctly handled; i.e.,

$$\tilde{P}(R) = \frac{\Phi^{\text{oscillated}}(R)}{\Phi^{\text{null-oscillated}}(R)} \tag{2.33}$$

with

$$\Phi^{\text{oscillated}}(R) = A_x \cdot \int_{E_\nu} \frac{dN_x}{dE_\nu} \cdot \int_{r=0}^{R} \frac{a_x(\vec{r})\rho(\vec{r})}{4\pi r^2} \, P(\bar{\nu_e} \to \bar{\nu_e}; E_\nu) \, dV \, dE_\nu \tag{2.34}$$

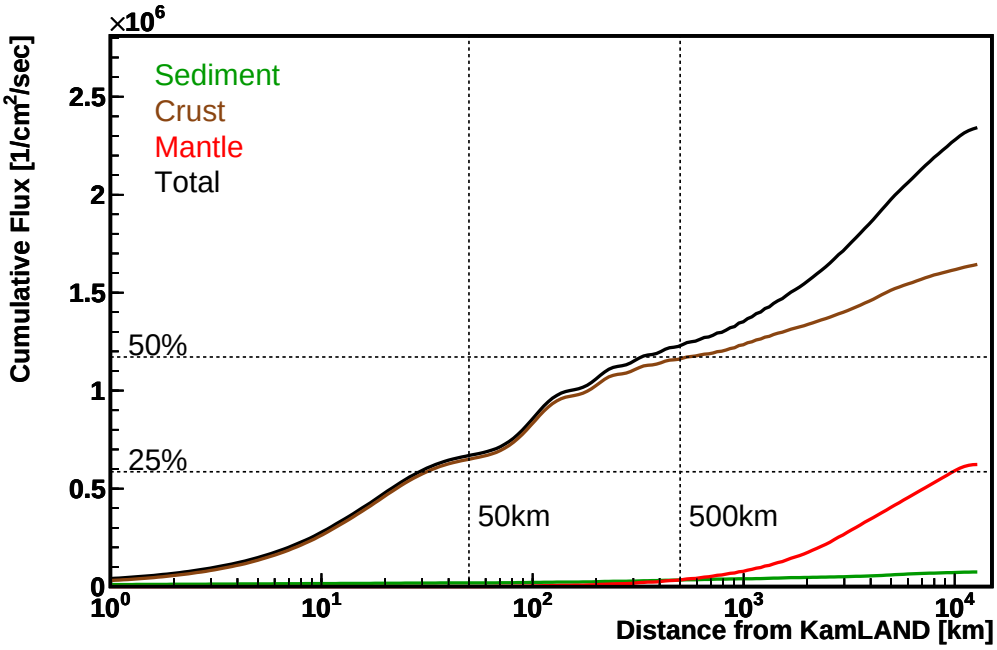

Figure 2.15: Cumulative Geo-Neutrino Flux

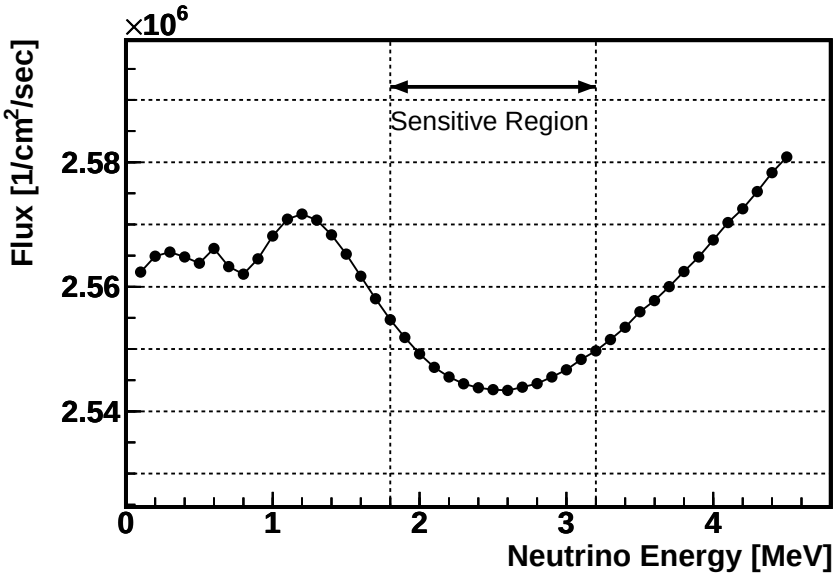

Figure 2.16: Spectrum Distortion by Neutrino Oscillation

and

$$\Phi^{\text{null-oscillated}}(R) = A_x \cdot \int_{E_\nu} \frac{dN_x}{dE_\nu} \cdot \int_{r=0}^{R} \frac{a_x(\vec{r})\rho(\vec{r})}{4\pi r^2}\, dV\, dE_\nu \tag{2.35}$$

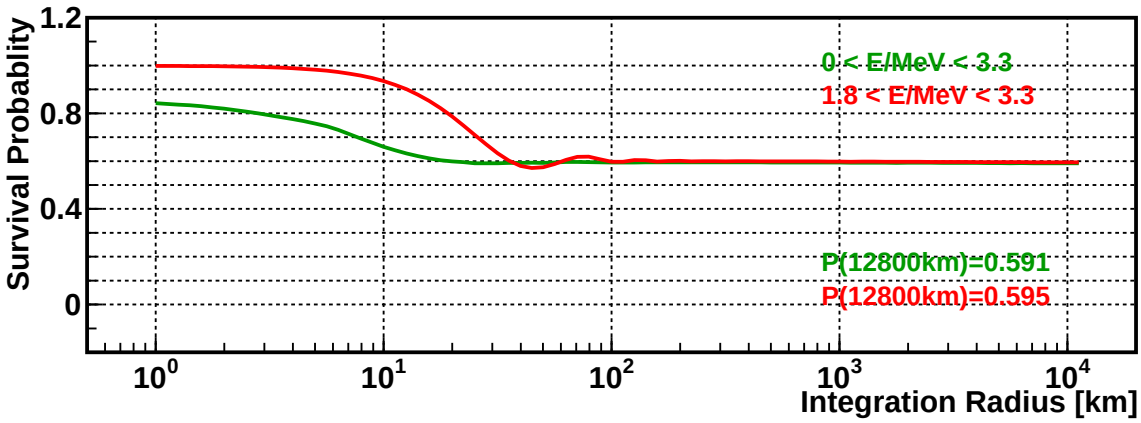

Figure 2.17: Survival Probability Averaging

Figure 2.17 shows the calculation result. It can be seen from the figure that the flux is well averaged if the integration radius is greater than ∼100 km. The averaged survival probability in the whole Earth integration is 0.595 with energy range from 1.8 MeV to 3.2 MeV, which is close to $1 - \frac{1}{2}\sin^2 2\theta$, 0.59, within 1% difference.

The uncertainty of the total geo-neutrino flux estimation induced by the uncertainty of the neutrino oscillation parameters can be easily estimated if the neutrino oscillation only scales the geo-neutrino flux by $1 - \frac{1}{2}\sin^2 2\theta$ without significantly modifying the spectrum shape; the flux error is simply converted with the same formula, as $\delta = \frac{d}{d\theta}(1 - \frac{1}{2}\sin^2 2\theta)\delta\theta$. The current most precise estimation of the oscillation parameter is $\sin^2 2\theta = 0.82^{+0.07}_{-0.07}$ [2], where 8.5% error of $\sin^2 2\theta$ is converted into 5.9% of flux estimation error.

2.5 Neutrino Geophysics

2.5.1 Flux Response Coefficient and Flux Response Chart

To separate geochemical uncertainties from the flux estimation, we define response coefficient as follows;

$$R = \Phi_x / M_x \tag{2.36}$$

where Φ_x is the geo-neutrino flux at KamLAND from source X, and M_x is the amount of the source. The response coefficients are calculated for each region of the Earth, i.e., the continental sediment (CS), oceanic sediment (OC), upper continental crust (UCC), middle continental crust (MCC), lower continental crust (LCC), oceanic crust (OC), upper mantle (UM), and lower mantle (LM). The response coefficients are also interpretable for any combination of the regions, such as the mantle as a combination of the upper mantle and the lower mantle, or the whole Earth as a combination of all regions. The coefficients are determined only with the structural model and relative position of the detector, thus are independent from any geochemical models. Table 2.6 shows the response coefficients of each region. The mass of each region is also shown in the table.

Table 2.6: Response Coefficients

		Mass [kg]	Response Coefficient [1/cm^2/sec / kg]	
			U Series	Th Series
Sediment	Continental	9.238×10^{20}	2.360×10^{-11}	5.133×10^{-12}
	Oceanic	4.114×10^{20}	1.949×10^{-11}	4.237×10^{-12}
Continental Crust	Upper	6.613×10^{21}	6.222×10^{-11}	1.353×10^{-11}
	Middle	7.325×10^{21}	3.677×10^{-11}	7.995×10^{-12}
	Lower	7.084×10^{21}	3.707×10^{-11}	8.060×10^{-12}
Oceanic Crust		4.229×10^{21}	1.679×10^{-11}	3.651×10^{-12}
Mantle	Upper	1.068×10^{24}	1.719×10^{-11}	3.738×10^{-12}
	Lower	2.937×10^{24}	1.144×10^{-11}	2.488×10^{-12}
Core	Outer	1.840×10^{24}	9.268×10^{-12}	2.016×10^{-12}
	Inner	9.841×10^{22}	8.727×10^{-12}	1.899×10^{-12}

We plot the relation of geo-neutrino flux and source mass on a 2-dimensional plane (namely, flux response chart), as shown in Figure 2.18. Each point represents the source mass and the corresponding geo-neutrino flux at KamLAND, for each structural region. The response coefficients are expressed by straight lines that cross the origin. Combination of regions is expressed by vector sum of points: $R_{A+B} = \Phi_{A+B}/M_{A+B} = (\Phi_A+\Phi_B)/(M_A+M_B)$. The points are geo-chemical model dependent, but the response lines are not; altering geochemical models moves the corresponding points along the response lines.

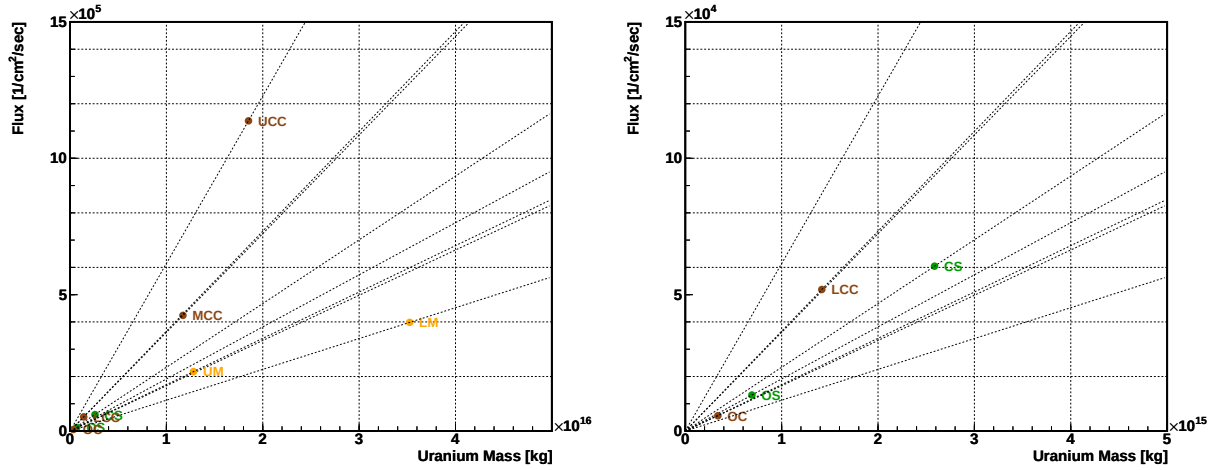

Figure 2.18: Flux Response Chart. This chart illustrates the relation between geochemical models and geo-neutrino flux. The horizontal axis is uranium mass given by a geochemical model, and the vertical axis is the corresponding geo-neutrino flux observed at KamLAND. Since the geo-neutrino flux is proportional to the source mass, altering geochemical models moves the (mass,flux) points along the straights line cross the origin (response line).

2.5.2 Crustal Models

As discussed in Section 2.2.2, the composition of the continental crust is estimated with different approaches, leading to different results. Our reference Earth model adopts an estimation made by Rudnick *et al.*, just because of my preference; altering the crustal model naturally changes the integrated geo-neutrino flux. The relation between the crustal models and the geo-neutrino flux can be clearly demonstrated with the response chart.

Figure 2.19 is a response chart of the U-series geo-neutrinos, where the three layers of the continental crust are combined into one region, the continental crust, and the two layers of the mantle are combined into one region, the mantle. The response line of the continental crust is expressed by the brown line OP, and the response line of the mantle is expressed by the orange line OQ, where O is the origin (0, 0).

Three estimations of crustal composition made by McLennan & Taylor (1999), Wedepohl (1995), and Rudnick & Fountain (1995) are plotted on the response line of the continental crust. In the reference Earth model, we rely on the BSE model and we estimate the mantle composition by subtracting the crustal composition from the BSE composition. The BSE constraint gives the total amount of Uranium and Thorium in the Bulk Silicate Earth, which is expressed by the vertical line PQ in the figure. Under this constraint, the total flux (i.e., continental crust + mantle) is indicated by an intersection point of the line PQ and the line that starts from the continental crust point and is parallel to OQ (the mantle response line). Three points on the line PQ show the total geo-neutrino fluxes of the three continental crust models. The intersection point of the line OQ and the line that starts from the total flux point and is parallel to OP (the continental crust response) shows the corresponding mantle composition.

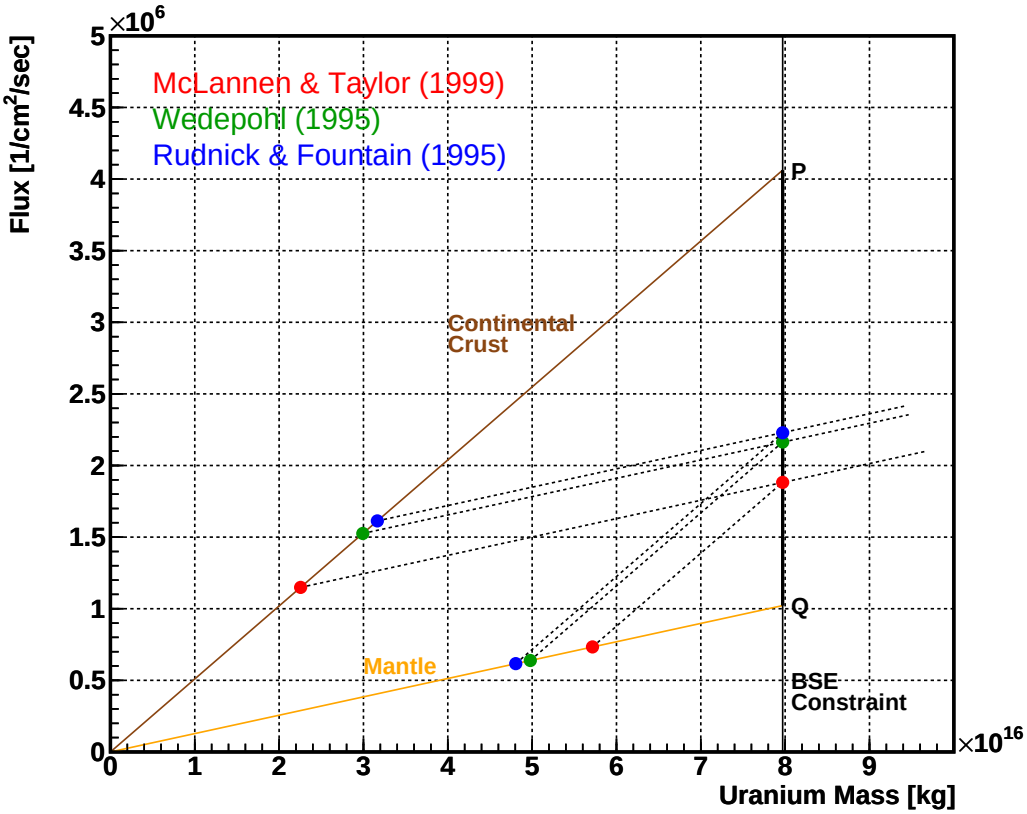

Figure 2.19: Crustal Models and Flux Response

Altering the BSE model (the total amount of Uranium and Thorium in the Silicate Earth) shifts the line PQ horizontally. From the response chart, one can directly see that the variation of the total geo-neutrino flux caused by ∼20% uncertainty of the BSE composition is about comparable to the variation among these three continental crust models.

2.5.3 Mantle Models

As frequently mentioned, formation of the crust extracts incompatible elements such as Uranium and Thorium from the mantle, resulting in depletion of incompatible elements in the mantle. Although such extracting processes occur relatively shallow depth (30-70km), global mantle convection mixes the shallow depleted mantle and the deep interior mantle, bringing about general depletion in the mantle.

Seismic analyses see huge mantle plumes (hot and cold), some of which reach to the bottom of the lower mantle (i.e. the core-mantle boundary (CMB)). Some of them cross the 670km discontinuity (the boundary of the upper mantle and lower mantle), suggesting material transportation from the lower mantle to the upper mantle, and vice versa.

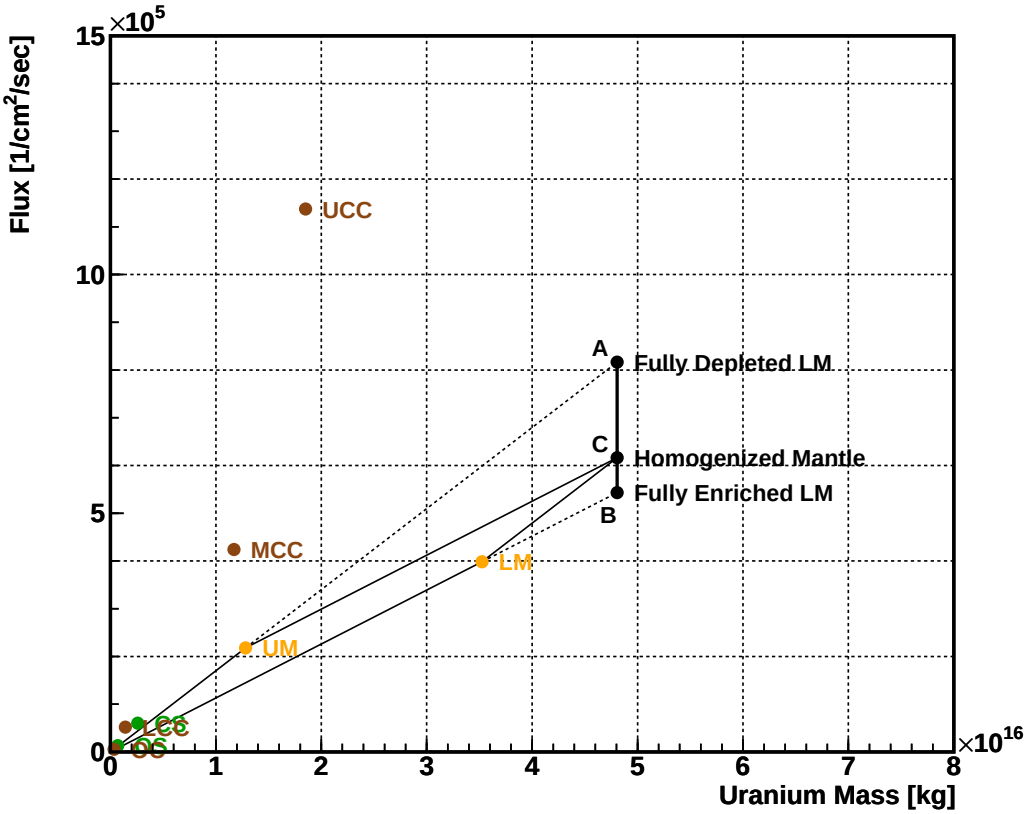

Figure 2.20: Mantle Structure and Flux Response

However, such one-layer mantle convection model is disfavored by lithological study. Christensen (1995) [29] showed that phase transition of materials at the 670km discontinuity (*endothermic transition of γ-phase to perovskite and magnesiowüstite*) acts as a barrier for the transportation, hence two-layered convection of the upper and lower mantle layers is favored.

These two mantle models, homogeneity or heterogeneity, have been a controversy in geochemistry. Geo-neutrino flux at surface is sensitive to the mantle structure, and the relation between the mantle models and the geo-neutrino flux is clearly illustrated by the response chart.

Figure 2.20 shows a response chart of the Uranium series geo-neutrinos, with focus on the mantle models. Since our reference Earth model assumes that the mantle is uniform, linear combination of the lower mantle point and upper mantle point gives the response of the bulk homogeneous mantle, as labelled by C. If sources (Uranium and Thorium) are moved from the upper mantle to the lower mantle, the point of UM moves left and LM moves right along the corresponding response lines, with keeping the total amount unchanged (which means we fix the BSE model and the crustal composition model). Including an extreme case, where all sources are contained in the lower mantle,

the response of the bulk mantle moves between the point C and point B, showing the possible variation of the total geo-neutrino flux. The figure also shows the opposite extreme case, point A, where all sources are contained in the upper mantle (although the model has no geophysical/geochemical bases).

2.5.4 Make Your Own Earth Models

As demonstrated in previous sections, the response chart outlines the relation between Earth models and geo-neutrino fluxes intuitively, with providing a way to incorporate one's prior geophysical/geochemical knowledge.

Figure 2.21 and Figure 2.22 again show the response charts for the Uranium and Thorium geo-neutrinos, respectively. The response of the bulk (silicate) Earth is also shown in the figures, as well as their BSE predictions and uncertainties. In the figures, the vertical value of "Total" indicates the flux that is expected to be observed at KamLAND, and the band of the BSE prediction shows how the uncertainties of the bulk Earth composition affect to the total geo-neutrino flux. The diagonal bundle of response lines hints us how the distribution models change the total geo-neutrino flux, including some extreme case models. On the upper horizontal axis, heat production corresponding to the source mass is also shown, providing constraints to geo-neutrino flux estimation by the heat flow observation, or inversely, providing insights into heat generation processes based on geo-neutrino observation.

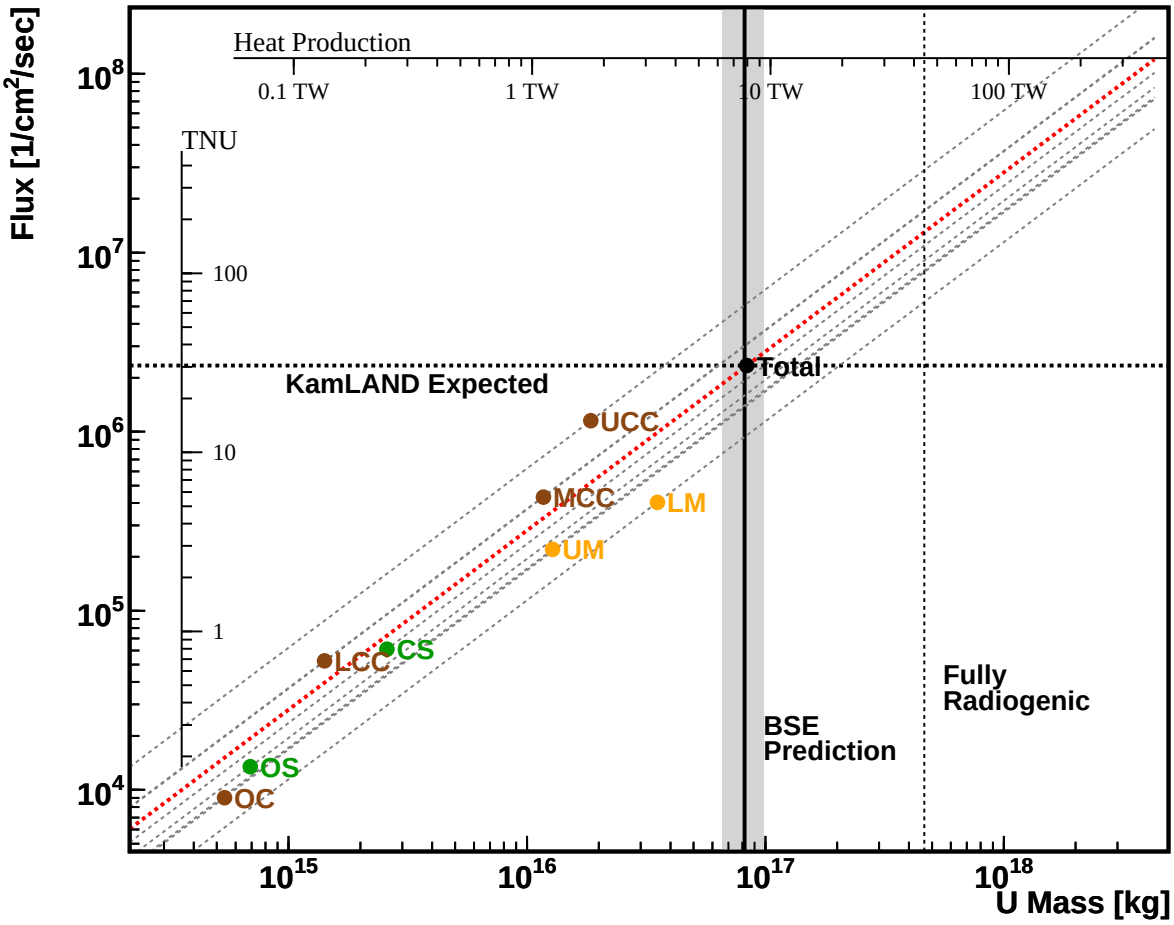

Figure 2.21: Response Chart of U Series Geo-Neutrinos

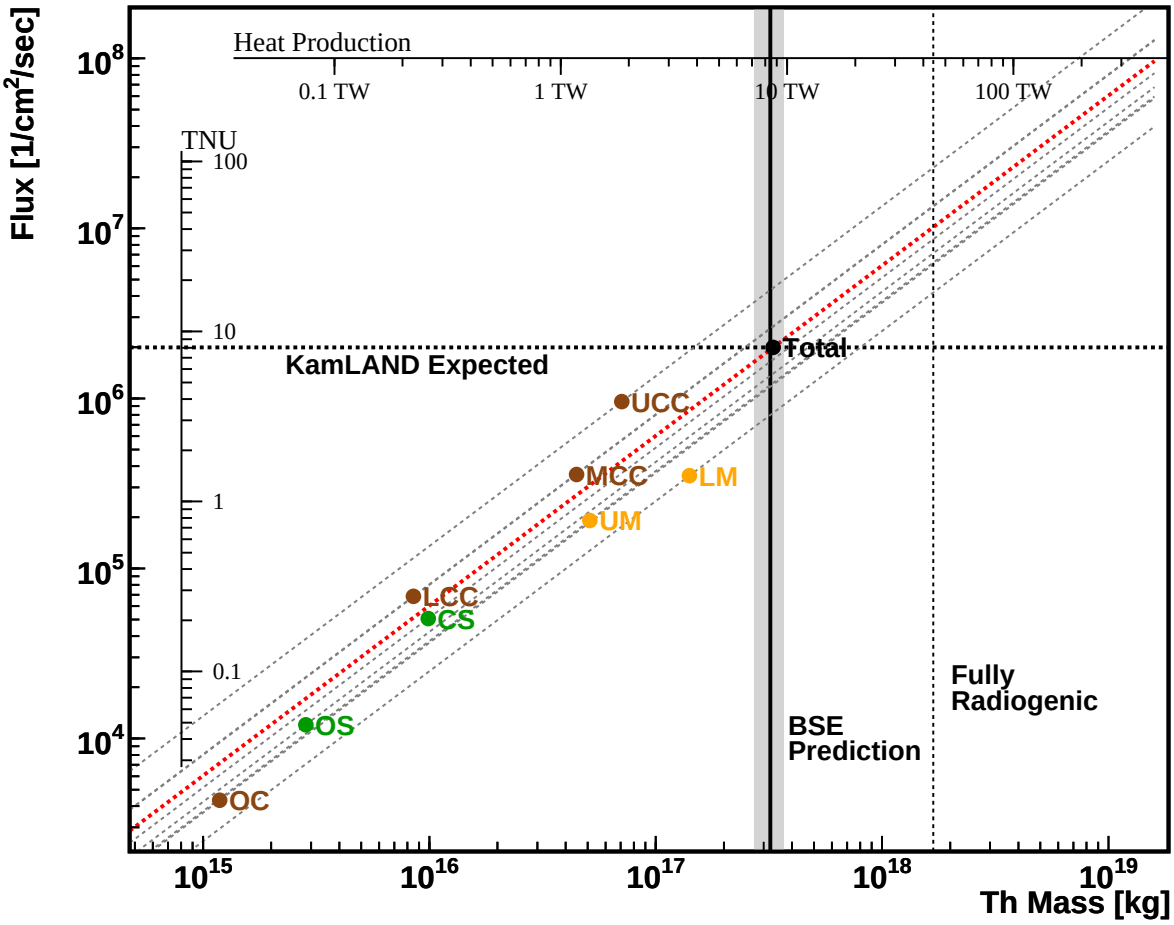

Figure 2.22: Response Chart of Th Series Geo-Neutrinos

2.6 Model Non-Realities and Uncertainties

Besides global geochemical uncertainties discussed in a previous section, the reference model is constructed on several assumptions: all regions are considered to be uniform, local geological effects are averaged, and other structures such as subducting oceanic plates are ignored.

Although these small or local variations do not affect the global geophysics significantly, the geo-neutrino flux at KamLAND is influenced considerably, because near-by region contribute a large fraction of geo-neutrino flux as shown in Section 2.4.

It should be emphasized that some topics discussed in this section might be new interests in the future; since the KamLAND detector is the first detector sensitive to geo-neutrinos, the current analysis cannot distinguish these effects from the global modeling. However, once the global models are established, geo-neutrinos are expected to provide even more insights in these fields.

2.6.1 Continental Crust Non-Uniformity

The continental crust has been being formed since the first plate tectonics took place, at around 4 Ga. Growth of the continental crust is especially rapid during the latest Archean (2.8-2.6 Ga); 50-60% of the continental crust was formed in this period. The continental crust formed in this time are thought to be different in composition from more recently formed crust, bacause relatively higher temperature of the Earth causes meling of subducting slab itself that contributes to the formation of new crust, in addition to melting of mantle induced by fluid release from the slab. In general, Archean crust is somewhat less enriched in incompatible elements than Proterozoic and Phanerozoic crust.

After Archean the continental crust is formed in a different way; the post-Archean crust is mainly formed by mantle melting induced by fluid released from subducting slabs, but also with recycled material of the continental crust that is carried on the slab as subducting sediment. Accretion of sediment on subducting plates contributes to formation of the crust as well. The amount of recycled sediment might change over time, and depends on tectonic settings of the subducting zones. C.Hawkesworth *et al.* (1997) [31] reports variation of magma compositions among several island arcs.

The effect of crust non-uniformity is studied by sub-dividing the continental crust into 17 crustal types. The CRUST 2.0 data set (C.Bassin *et al.* (2000) [16]) provides a map of crustal types in $2^\circ \times 2^\circ$ grid, as shown in Figure 2.23. Geo-neutrino fluxes from each of these crustal types are calculated and summarized in Table 2.7 and Figure 2.24.

Under the assumption of uniform upper continental crust, the island arc crust contributes $\sim$60% of geo-neutrino flux coming from the whole upper continental crust at KamLAND. The forearc crust contributes another $\sim$15%, totaling in $\sim$75% contribution. All other types of crust contribute in similar magunitude. From this result, we infer that $\sim$75% of upper continental crust geo-neutrinos come from the Japan Island Arc, the rest accounts for the bulk upper continental crust.

S.Togashi *et al.* (2000) [34] conducted a systematical survey on Japan Island Arc geochemistry, reporting the Uranium and Thorium concentration of the Japanese upper crust

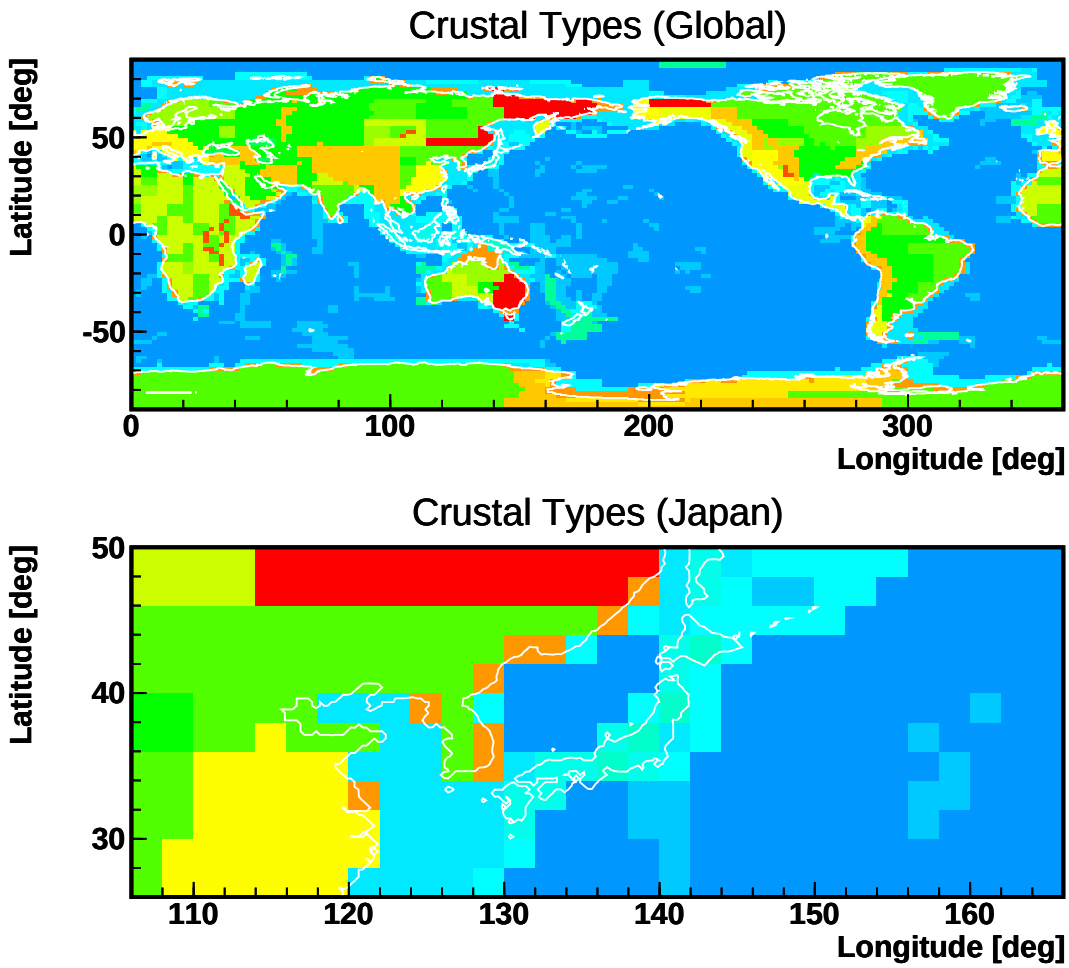

Figure 2.23: Crustal Type Map (CRUST 2.0)

Table 2.7: Geo-Neutrino Flux from Each Type of Continental Crust (U-Series)

Crustal Type	Mass [kg]	Flux at KamLAND [1/cm2/sec]	Share in Flux [%]
Continental Shelf	4.84×10^{20}	4.76×10^{4}	4.13
Continental Transition	4.62×10^{20}	3.92×10^{4}	3.40
Island Arc	1.04×10^{20}	6.98×10^{5}	60.55
Forearc	5.86×10^{19}	1.75×10^{5}	15.15
Continental Plateau	6.77×10^{19}	1.03×10^{3}	0.09
Thinned Continental	1.39×10^{19}	2.32×10^{2}	0.02
Platform	1.16×10^{21}	2.86×10^{4}	2.48
Archean	1.37×10^{21}	5.87×10^{4}	5.10
Early-Mid Proterozoic	2.79×10^{20}	6.47×10^{3}	0.56
Late Proterozoic	7.91×10^{20}	1.46×10^{4}	1.26
Continental Arc	1.17×10^{20}	2.66×10^{3}	0.23
Extended Crust	2.02×10^{20}	1.17×10^{4}	1.02
Highly Extended Crust	4.08×10^{19}	3.09×10^{2}	0.03
Orogen	9.15×10^{20}	3.07×10^{4}	2.66
Margin Shield Transition	3.35×10^{20}	1.82×10^{4}	1.58
Rifts	4.46×10^{19}	7.65×10^{2}	0.07
Phanerozoic	1.68×10^{20}	1.93×10^{4}	1.68
UCC Total	6.61×10^{21}	1.15×10^{6}	100.00

to be 2.32 ppm and 8.3 ppm, respectively. Their survey shows characteristic depletion in incompatible elements as compared with the average continental crust, and, according to the authors, this is a result from the long-term mantle evolution.

Considering that Japan Island Arc contributes ∼75% of the upper continental crust flux that contributes ∼50% of the total flux, the depletion in Uranium and Thorium reduces the total geoneutrino flux by ∼6.4% and ∼8.4%, respetively.

2.6.2 Accumulated Slab beneath Japan and Mantle Non-Uniformity

Seismological analysis shows existence of huge chunk of slab accumulated beneath Japan, at around the 670km discontinuity (the boundary of the upper mantle and the lower mantle), as shown in Figure 2.25. Since the slab originates the subducting oceanic plate, its concentrations of Uranium and Thorium might be higher than those of the average mantle reflecting higher concentration in the oceanic crust.

Using the mantle tomography data shown in Figure 2.6, geo-neutrino fluxes from the normal, hot and cold mantles are calculated, under the assumption of the uniform mantle model. The hot and cold mantles are defined such that the seismic wave speed anomaly is more than 1% and less than -1%, respectively, otherwise the mantle is identified as normal. Table 2.8 shows the geo-neutrino fluxes from the each mantle region.

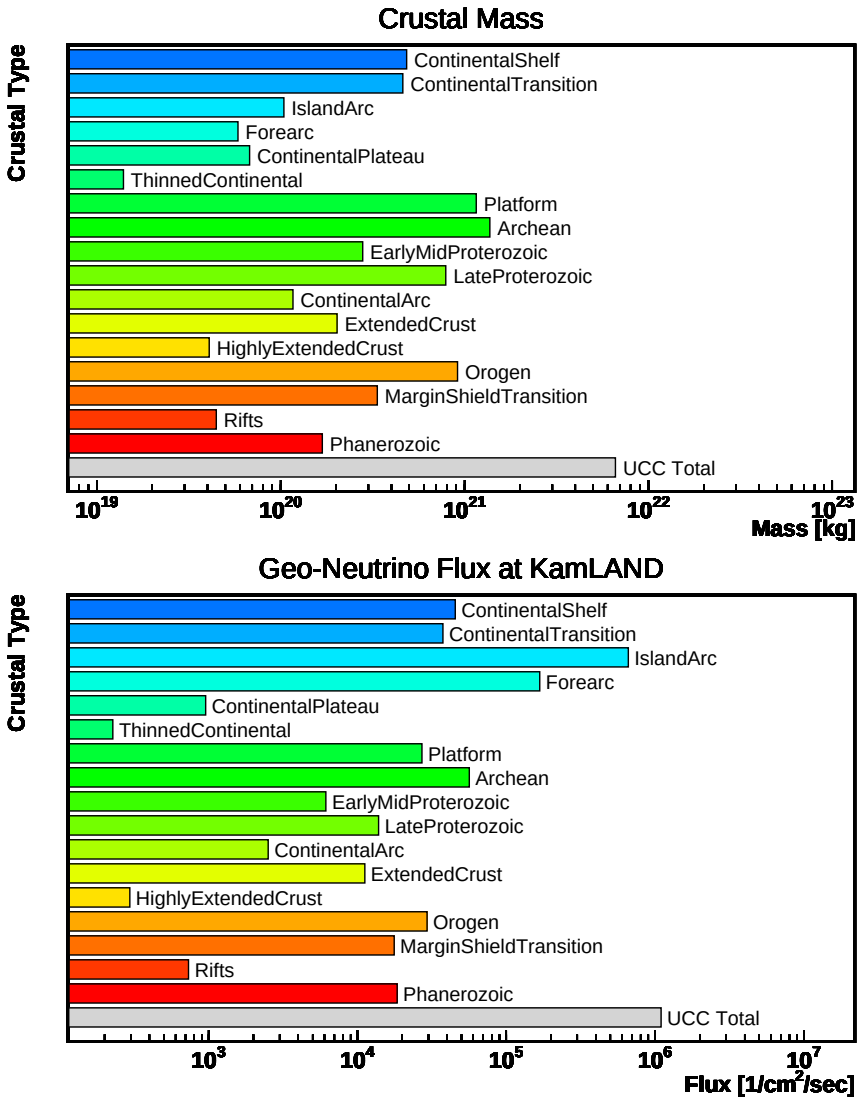

Figure 2.24: Geo-Neutrino Flux from Each Type of Continental Crust

Table 2.8: Geo-Neutrino Flux from Each Type of Mantle

Mantle Type	Mass [kg]	Flux at KamLAND [$1/\mathrm{cm}^2/\mathrm{sec}$]	Share in Flux [%]
Normal	3.34×10^{24}	4.88×10^5	77.6
Hot	3.46×10^{23}	7.25×10^4	11.5
Cold	3.16×10^{23}	6.84×10^4	10.9
Mantle Total	4.00×10^{24}	6.29×10^5	100.0

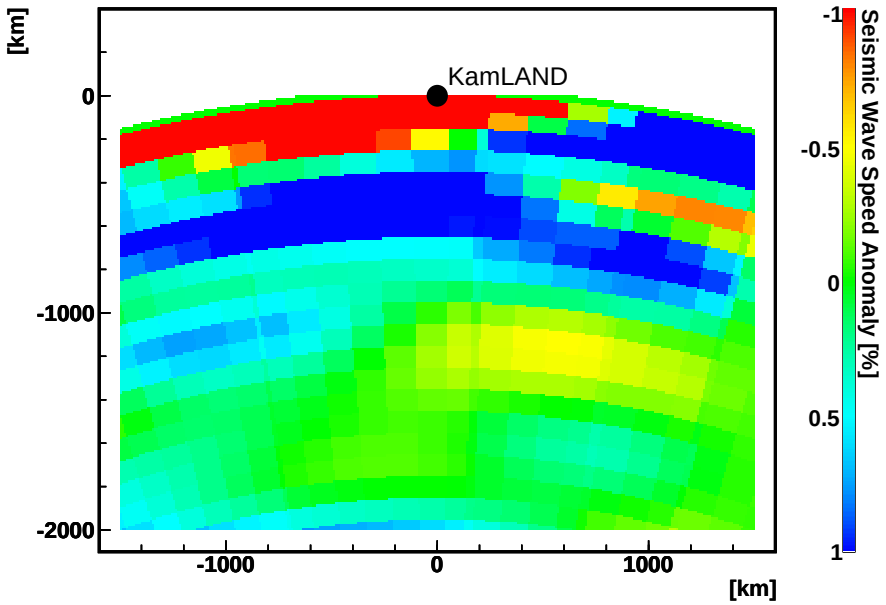

Figure 2.25: Mantle Tomography beneath Japan. This shows the same dataset as shown in Figure 2.6, but focus on the region beneath Japan. The blue regions, where seismic wave speed shows faster anomaly, are believed to be cold part of the mantle. A chunk of cold mantle, which is believed to be accumulated slab originating in plate subduction, is seen beneath Japan.

The typical thickness of the oceanic crust is about 6km, and that of subducting plate is about 50 km. Assuming that 10% of the subducting plate has the ocenic crust composition and the rest has the mantle composition, the bulk slab composition is calculated to be 0.021 ppm and 0.065 ppm, respectively for Uranium and Thorium. Assigning these concentrations to the cold mantle composition, the fluxes from the cold mantle increases by 75% and 35%, resulting in the increase of the total flux by 2.1% and 1.0%.

Although this topic is now discussed in the uncertainties section, this small difference in flux might provide important insight into the mantle structure in the future; provided the global mantle tomography seen by seismological analysis, it is discussed that there might be difference in chemical composition among the normal, hot and cold mantles. Precise observation of geo-neutrinos might bring a clue in this issue.

2.6.3 Sea of Japan

Although the crust beneath the Sea of Japan is categorized in oceanic crust, it differs from the typical oceanic crust that is formed at mid-ocean ridges and lies under vast ocean; the crust beneath the Sea of Japan contains fragments of continental crust and stretched continental crust, and sediment on the crust is much thicker than that of typical oceanic crust (such as that of Pacific Ocean, $\sim$ 1km). The composition of the sediment might be different from that of vast ocean, due to difference in geomorphological settings.

The effect of this uncertainties is estimated by assigning the composition of continental crust and sediment to those beneath the Sea of Japan, as an extreme case. The oceanic crust within 1200 km radius from KamLAND contributes about 46% of the total geo-neutrino flux from the whole oceanic crust. Assuming that half of this is from the Sea of Japan crust, and assuming that the whole Sea of Japan crust is continental in composition, the total geo-neutrino flux at KamLAND is increased by 2%.

Similar discussion applies to the oceanic sediment except for assuming that all oceanic sediment (not limited to that of Sea of Japan) has the continental sediment composition; because not only sediment beneath the Sea of Japan is different from subducting sediment in composition, but also thick sediment beneath the East China Sea and Sea of Okhotsk might have the same characteristics. Moreover, a large fraction of oceanic sediment is contained in thick layers of sediment around continents, origin of which might be continental sediment, as shown in Figure A.3 in Appendix A.

The geo-neutrino flux from the oceanic sediment contribute 0.6% of the total geo-neutrino flux at KamLAND. Assignment of the continental sediment composition increases the total flux by 0.36%.

2.6.4 Subducting Plate beneath Japan

The subducting plate beneath Japan is ignored in the global reference model. The geo-neutrino flux from the subducting plate region is calculated with crustal model given by D.Zhao *et al.* (1992) [18] shown in Figure 2.5. Thickness of the plate is conservatively set to be 10km, while the typical thickness of the oceanic crust is about 6 km.

With the normal mantle composition, geo-neutrino flux from the subducting plate is calculated to be 5.70×10^2 and 4.96×10^2 for the Uranium and Thorium series respectively, corresponding 0.025% of the total geo-neutrino flux at KamLAND. Assignment of oceanic crust composition to this region increases the total flux by 0.21% and 0.11% for the Uranium and Thorium series respectively.

2.6.5 Local Geology

The effect of local geology is studied with a geological map and large scale geochemical study over Japan. A Geological map of Japan is published from Geological Survey of Japan (GSJ) [33]. The GSJ group classifies the Japan Arc into 165 geological groups, and provides a map at 1:1,000,000 scale. Some examples of the geological map is shown in Appendix B, with some simplifications to display.

S.Togashi *et al.* (2000) [34] conducted a systematical survey of geochemistry over the Japan Arc, based on the GSJ geological map. They re-arrange the 165 geological groups defined in the GSJ geological map into 37 geological groups, and collected 166 rock samples in order that samples cover the rock varieties and abundances in each of the 37 groups. The GSJ geological map is made mainly based on steep V-shaped valley river cutting outcrops, where effects of preferential erosion is small. Therefore samples taken based on the GSJ geological map are considered to be representing the upper part weighted Japan Arc upper crust. Table 2.9 summarizes the Uranium and Thorium concentrations given

Table 2.9: Geochemical Data (S.Togashi *et al.*)

	Rock Age	Rock Type	Exposure Area [%]	Number of Samples	Group Average Th [ppm]	Group Average U [ppm]
1	Quaternary	Sedimentary	21.363	9	7.3	2.15
2	Neogene	Sedimentary	12.468	15	6.4	3.44
3	Paleogene	Sedimentary	1.897	4	8.5	1.94
4	Cretaceous	Sedimentary	2.718	7	6.8	1.55
5	Jurassic-Triassic	Sedimentary	0.505	3	8.3	2.72
6	Paleozoic	Sedimentary	0.951	5	7.5	2.11
7	Paleozoic	Accretionary (Sedimentary)	0.572	2	11.6	2.59
8	Paleozoic	Accretionary (Volcanic)	0.296	3	0.3	0.09
9	Paleozoic	Accretionary (Limestone)	0.085	3	0.3	0.51
10	Jurassic	Accretionary (Sedimentary)	6.548	11	13.2	2.53
11	Jurassic	Accretionary (Volcanic)	0.823	2	1.7	0.41
12	Jurassic	Accretionary (Limestone)	0.087	2	1.0	0.72
13	Jurassic	Accretionary (Chert)	0.344	3	1.1	0.55
14	Cretaceous	Accretionary (Sedimentary)	5.973	7	10.4	1.98
15	Paleogene	Accretionary (Sedimentary)	2.189	2	9.2	1.25
16	Unknown	Ultramafic	0.500	4	0.1	0.01
17	-	Metamorphic (HighTemperature)	1.120	11	6.0	1.31
18	-	Metamorphic (HighPressure)	2.734	9	2.8	0.64
19	Quaternary	Volcanic (Felsic-Nonalkali)	6.207	6	10.6	3.15
20	Quaternary	Volcanic (Mafic-Nonalkali)	4.755	11	2.7	0.82
21	Neogene	Plutonic (Felsic-Nonalkali)	0.909	2	9.2	2.94
22	Neogene	Plutonic (Mafic-Nonalkali)	0.142	2	0.32	0.11
23	Neogene	Volcanic (Felsic-Nonalkali)	4.200	6	10.3	2.77
24	Neogene	Volcanic (Felsic-Nonalkali)	7.404	5	4.2	1.67
25	Quaternary	Volcanic (Mafic-Alkali)	0.361	1	9.2	1.60
26	Neogene	Volcanic (Felsic-Alkali)	0.058	1	30.2	5.55
27	Paleogene	Plutonic (Felsic)	1.192	3	9.1	2.24
28	Paleogene	Plutonic (Mafic)	0.133	1	0.14	0.04
29	Paleogene	Volcanic (Felsic-Nonalkali)	0.369	1	7.0	1.73
30	Paleogene	Volcanic (Felsic-Nonalkali)	0.766	2	0.3	0.11
31	Cretaceous (Late)	Plutonic	0.619	6	19.4	5.40
32	Cretaceous (Middle)	Plutonic	5.017	3	10.6	1.90
33	Cretaceous (Early)	Plutonic	1.952	6	4.6	1.33
34	Cretaceous	Volcanic (Felsic-Nonalkali)	3.383	3	14.7	2.26
35	Cretaceous	Volcanic (Mafic-Nonalkali)	0.636	1	11.1	2.67
36	Jurassic	Plutonic (Felsic)	0.288	2	14.8	2.18
37	Jurassic-Carboniferous	Igneous	0.007	2	1.25	0.30

in the paper, and Figure B.3 and Figure B.4 in Appendix B visualize the values listed in the table. Figure 2.26 shows frequency of Uranium and Thorium concentration listed in Table 2.9 with weight of surface exposure area. The surface exposure weighted average concentration is calculated to be 2.32 ppm and 8.3 ppm, respectively for Uranium and Thorium.

Figure 2.27 shows the relative importance of each geological group in the geo-neutrino

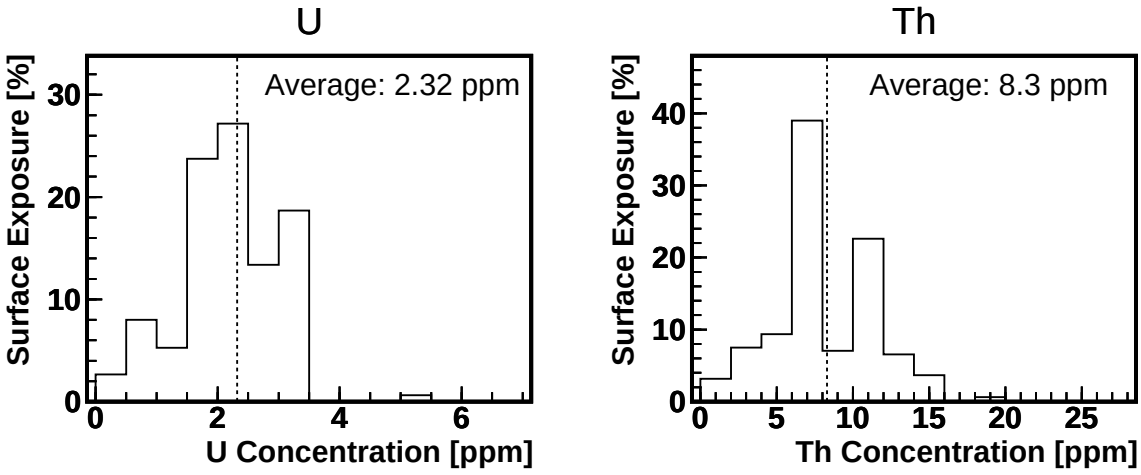

Figure 2.26: Surface Exposure Weighted U/Th Concentration

flux at KamLAND, without taking account of Uranium/Thorium concentration variation; i.e., the relative importance is defined as the ratio of geo-neutrino flux from each of the geological group calculated with an uniform crustal model. It can be seen from the figure that the total flux from the Japan upper crust is dominated by a few numbers of geological groups that surround the KamLAND site within ∼50km distance, such as High-temperature Metamorphic (Hida Metamorphic Rocks consisting the Mt. Ikenoyama etc), Cretaceous Sedimentary (Tetori Group around the lake Arimine etc), and Jurassic Plutonic (Funatsu Granite commonly seen around the Kamioka town). Geological groups that commonly appear throughout the Japan Arc, such as Quaternary Sedimentary and Neogene Sedimentary also make significant contribution.

By combining the geochemical data and the geological map, we obtain a map of Uranium and Thorium distribution. Here our purpose of doing this is not only to make the best estimation of geo-neutrino flux, but also to understand how local geological variations affect to the total geo-neutrino flux. Hence three different Uranium and Thorium distribution maps are constructed based on three different methods, then the results are compared to each other.

The first method, Homogeneous Japan Arc Model, assigns a constant Uranium or Thorium concentration over the Japan Arc. The concentration is calculated by averaging the composition of each geological group with weight of its exposure area given by the GSJ geological map. The composition of each geological group is calculated by simply taking average of all samples that belong to the geological group.

The second method, Heterogeneous Japan Arc Model, combines the geochemical data and the geological map by simply assigning corresponding geological groups; for each geological group in the GSJ geological map, the composition of corresponding group given in the geochemical data table is assigned. The composition of each geological group is calculated by simply taking average of all samples that belong to the geological

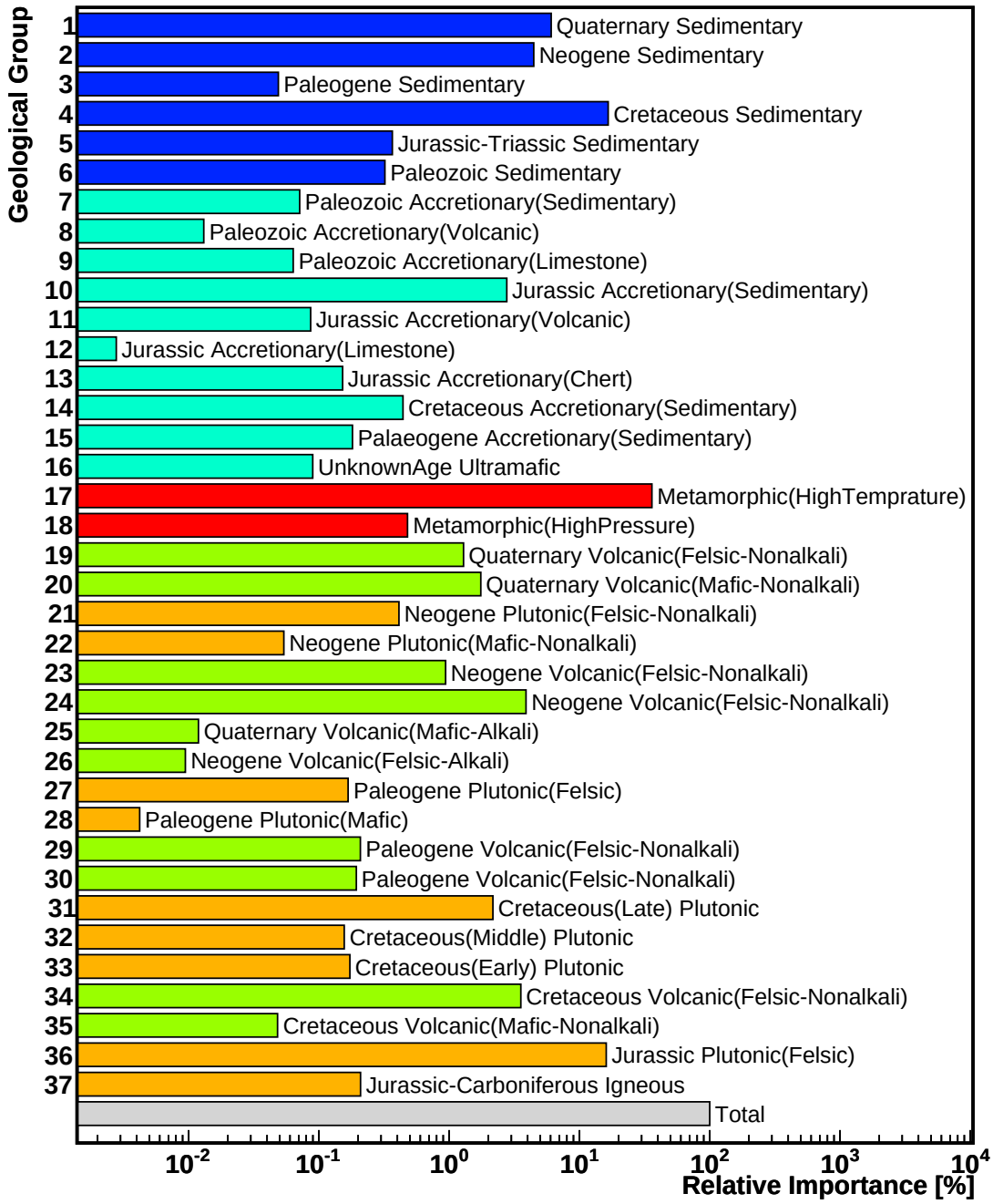

Figure 2.27: Relative Importance of Local Geological Groups

group. Figure 2.28 and Figure 2.29 show the Uranium and Thorium distribution map, respectively, constructed with this method.

The third method, Kamioka-Area Represented Heterogeneous Japan Arc Model, is

Table 2.10: Composition of Representative Rocks Collected around the KamLAND Site

	Geological Group	Average		Adapted		Geological Unit where adapted samples are collected
		Th	U	Th	U	
2	Neogene Sedimentary	6.4	3.44	2.8	4.68	Otogawa Formation
4	Cretaceous Sedimentary	6.8	1.55	4.5	1.18	Tetori Group
10	Jurassic Accretionary (Sedimentary)	13.2	2.53	16.3	2.90	Mino Belt
13	Jurassic Accretionary (Chert)	1.1	0.55	0.9	0.08	Mino Belt
17	Metamorphic (HighTemperature)	6.0	1.31	3.17	1.82	Hida,Unazuki Metamorphic Rocks
31	Cretaceous (Late) Plutonic	19.4	5.40	16.8	13.8	Naegi,Busetsu,Kadoshima Granite
34	Cretaceous Volcanic (Felsic-Nonalkali)	14.7	2.26	19.5	2.64	Nohi Rhyolite
36	Jurassic Plutonic (Felsic)	14.8	2.18	14.8	2.18	Funatsu Granite

constructed basically in the same manner as the second method, except for compositions of several geological groups that surround the KamLAND site are calculated by taking average of only samples collected around the KamLAND site. Table 2.10 shows adapted values for these geological groups. Some details of the geological groups are presented in Figure B.2 and comments of the figure.

These three methods differ from each other in the point that how local geological effects are averaged and/or weighted; the first model and the third model present two extreme cases. As far as the rock samples represent the geological groups well, the true case should lie among these models, except for some extremely anomalous cases.

In these three methods, representativeness of rock samples and homogeneity of each geological group are the key issue, because a constant Uranium/Thorium concentration is assigned to each of geological group that disperses throughout the Japan Arc. The geological groups are classified only by rock age and rock type, without considering the tectonic settings of the region.

A hint to examine this issue might be brought by comparing the Uranium/Thorium distribution maps with those made with a completely different approach. The Geological Survey of Japan (GSJ) recently published a map, called geochemical map, which shows the elemental distribution of the surface [35]. The map is constructed based on numerous sampling of river sediment, which is considered to be representing the surface elemental composition of the upper stream region. This map is quite different from the map constructed above at the point that it does not consider any geological constitution; the river sediment samples are believed to be well homogenized by the processes of erosion, transportation and sedimentation, hence they show average composition of upper stream region surface, with some weights induced by mobility. This characteristics is in contrast to the features of rock samples analyzed by Togashi *et al.* (2000), which are collected based on a geological map that shows the basement rock types.

Figure B.5 and Figure B.6 in Appendix B are the geochemical maps of Uranium and Thorium. Although the geochemical maps essentially shows the Uranium/Thorium concentration on surface, it is interesting to compare them with the Uranium/Thorium distribution maps constructed above (Figure 2.28 and Figure 2.29). Except for few regions

such as the Abukuma area and the Kitakami area, both of the maps show overall similar tendency. Taking account of the fact that the geochemical maps are constructed only with region-representing samples without considering any geological constitution, it can be concluded that the similarity between these two maps supports our assumption that each geological group is homogeneous enough and the samples are representing the group well. Systematical low Uranium/Thorium concentration in the surface geochemical maps might be a result of the erosion, transportation and sedimentation processes.

With assuming that this surface exposed geology extends to 5km in depth, geo-neutrino flux from this area is calculated, as shown in Table 2.11. Among these models, the variations of fluxes from the region are 20% and 16%, respectively for the Uranium and Thorium series geo-neutrinos. This variation corresponds 3.2% and 2.6% difference in the total flux. Although these numbers are not exactly considered to be errors in a common definition, they give some ideas how local geologies affect the geo-neutrino flux.

Table 2.11: Geo-Neutrino Flux from Surface of Japan Island Arc

Geological Group Number	Homogeneous Japan-Arc		Heterogeneous Japan-Arc		Kamioka-Area Represented	
	U-Series [1/cm^2/sec]	Th-Series [1/cm^2/sec]	U-Series [1/cm^2/sec]	Th-Series [1/cm^2/sec]	U-Series [1/cm^2/sec]	Th-Series [1/cm^2/sec]
1	22327.8	17370.2	20691.7	15277.4	20691.7	15277.4
2	16400.1	12758.7	24317.4	9838.0	33083.0	4304.1
3	180.0	140.0	150.5	143.4	150.5	143.4
4	61038.8	47485.9	40780.2	38904.1	31045.6	25745.3
5	1348.1	1048.8	1580.6	1048.8	1580.6	1048.8
6	1180.0	918.0	1073.2	829.5	1073.2	829.5
7	262.0	203.8	292.5	284.9	292.5	284.9
8	48.1	37.4	1.9	1.4	1.9	1.4
9	233.7	181.8	51.4	6.6	51.4	6.6
10	10176.5	7916.9	11097.6	12590.7	12720.6	15547.7
11	317.7	247.1	56.1	50.6	56.1	50.6
12	10.2	8.0	3.2	1.0	3.2	1.0
13	559.7	435.4	132.7	57.7	19.3	47.2
14	1625.3	1264.4	1387.1	1584.4	1387.1	1584.4
15	665.5	517.7	358.5	573.8	358.5	573.8
16	329.6	256.4	1.4	3.1	1.4	3.1
17	132483.6	103067.2	74807.6	74506.4	103931.1	39364.2
18	1762.6	1371.2	486.2	462.6	486.2	462.6
19	4738.1	3686.1	6433.2	4707.5	6433.2	4707.5
20	6430.9	5003.0	2273.0	1627.5	2273.0	1627.5
21	1516.6	1179.9	1921.9	1307.8	1921.9	1307.8
22	198.0	154.0	9.4	5.9	9.4	5.9
23	3452.4	2685.8	4122.0	3333.0	4122.0	3333.0
24	14315.3	11136.8	10304.6	5635.5	10304.6	5635.5
25	43.8	34.1	30.2	37.8	30.2	37.8
26	34.7	27.0	83.1	98.4	83.1	98.4
27	617.3	480.2	596.0	526.5	596.0	526.5
28	15.5	12.0	0.3	0.2	0.3	0.2
29	766.2	596.1	571.4	502.7	571.4	502.7
30	712.8	554.6	33.8	20.0	33.8	20.0
31	7961.3	6193.6	18530.5	14476.5	47355.7	12536.4
32	576.6	448.5	472.2	572.8	472.2	572.8
33	636.4	495.1	364.8	274.4	364.8	274.4
34	13045.8	10149.1	12708.4	17974.9	14845.2	23844.3
35	177.4	138.0	204.2	184.6	204.2	184.6
36	59122.3	45994.9	55554.6	82015.0	55554.6	82015.0
37	768.4	597.8	99.4	90.0	99.4	90.0
Total	367551.3	285940.9	293054.7	290700.6	353680.9	243741.4

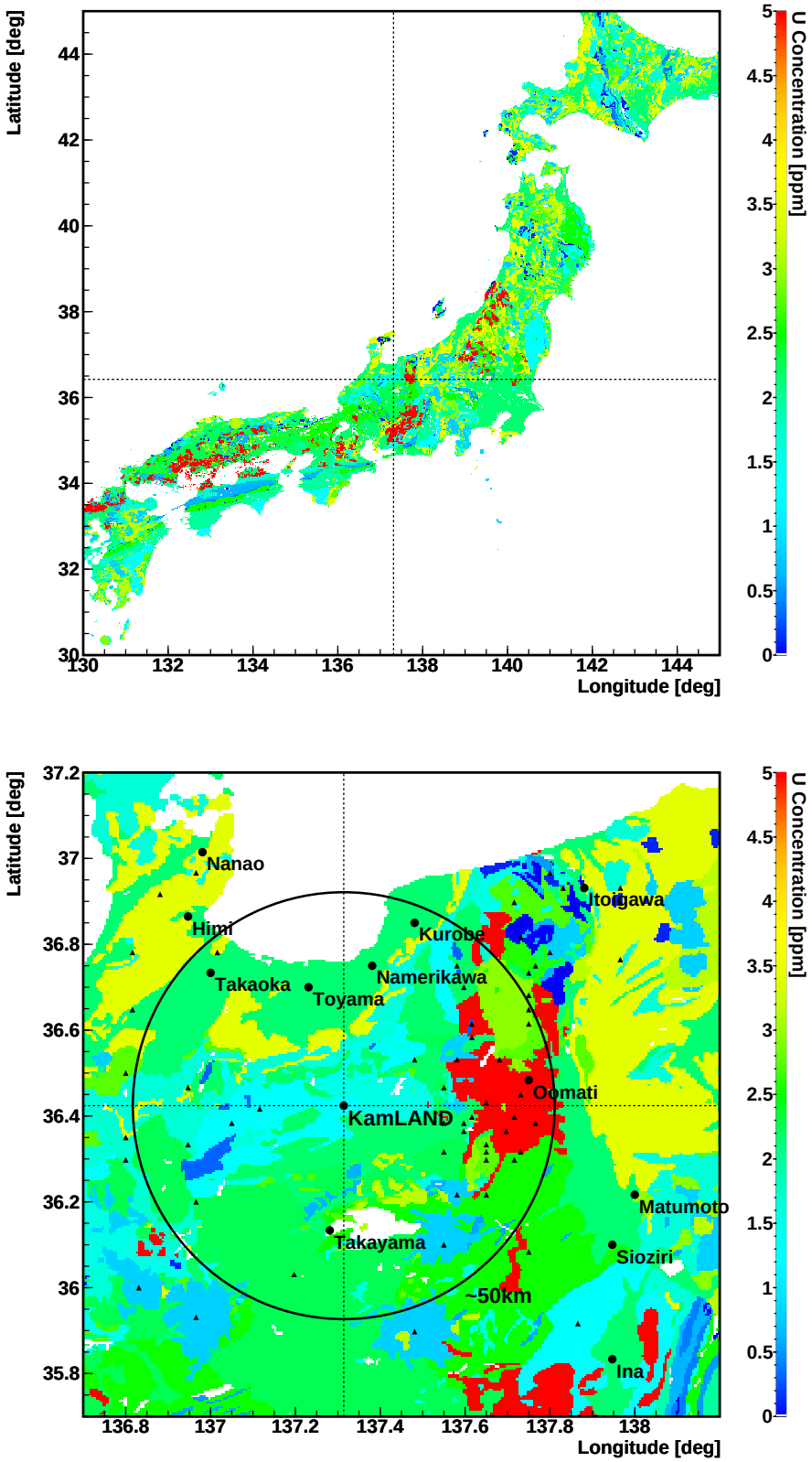

Figure 2.28: Japan and Kamioka Area Uranium Distribution Map

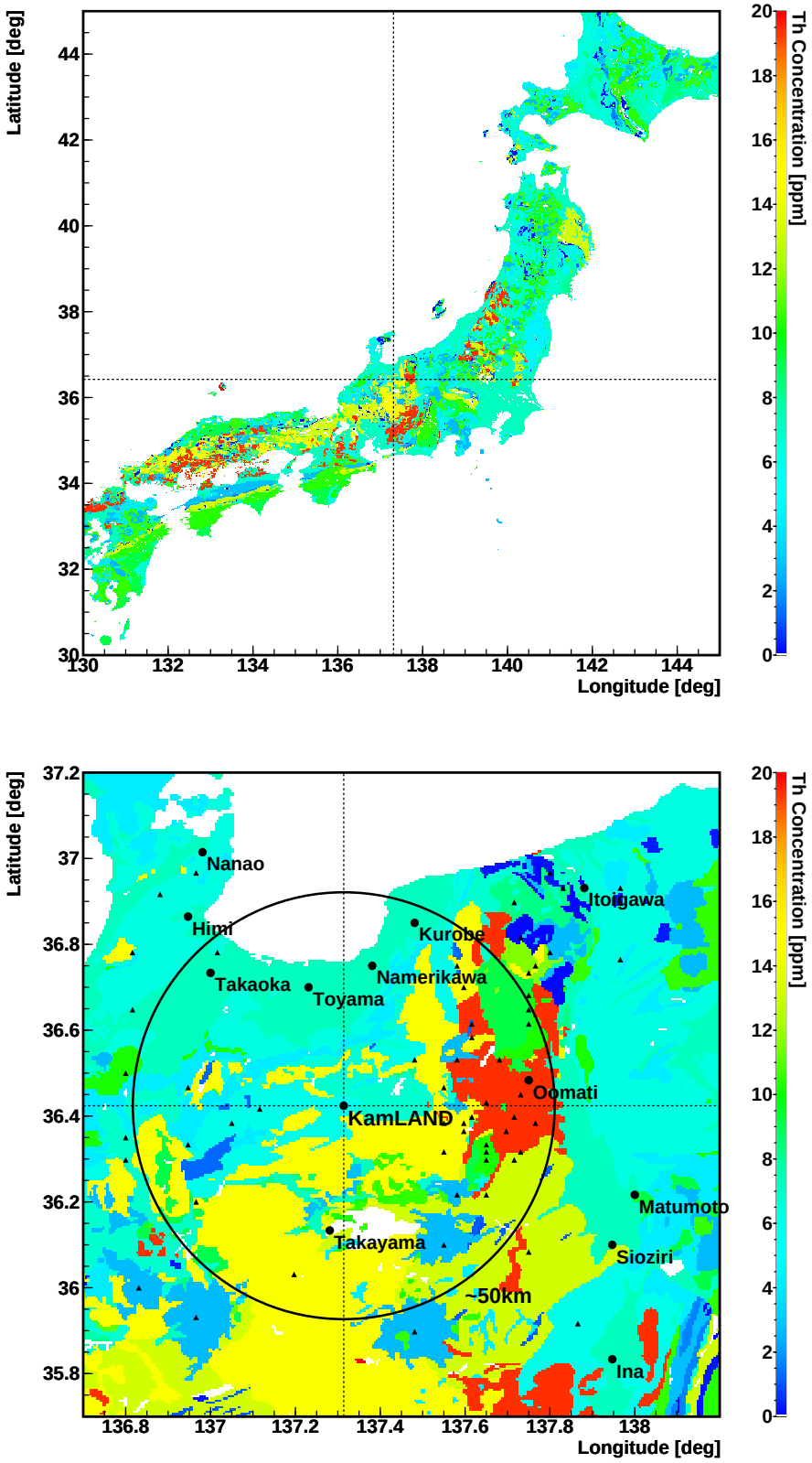

Figure 2.29: Japan and Kamioka Area Thorium Distribution Map

2.6.6 Kamioka Mine Geology

Although the contribution of geo-neutrinos from the Kamioka Mine to the total flux is estimated to be about 1%, there is potential possibility that small scale concentration of Uranium or Thorium, such as ore deposits, affects the total geo-neutrino flux significantly. Mines are formed under special tectonic settings, hence 'averaged' or 'uniform' geological models might break down.

Fortunately, geology of the mine has been intensively studied by the Kamioka Mining Company [37–39] and by the Japanese government [40]. Detail geological maps at several layers of the mine are provided by the mining company [41], some of them are shown in Figure 2.30. We collected rock samples from the mine based on the geological maps, and analyzed their Uranium and Thorium concentration. Table 2.12 summarized the result.

For the Kamiokande experiment, M.Yamamoto *et al.* (1989) [42] collected several rock samples around the former Kamiokande site, where KamLAND is now located, and analyzed their compositions. Table 2.13 summarizes the Uranium and Thorium concentrations reported in the paper.

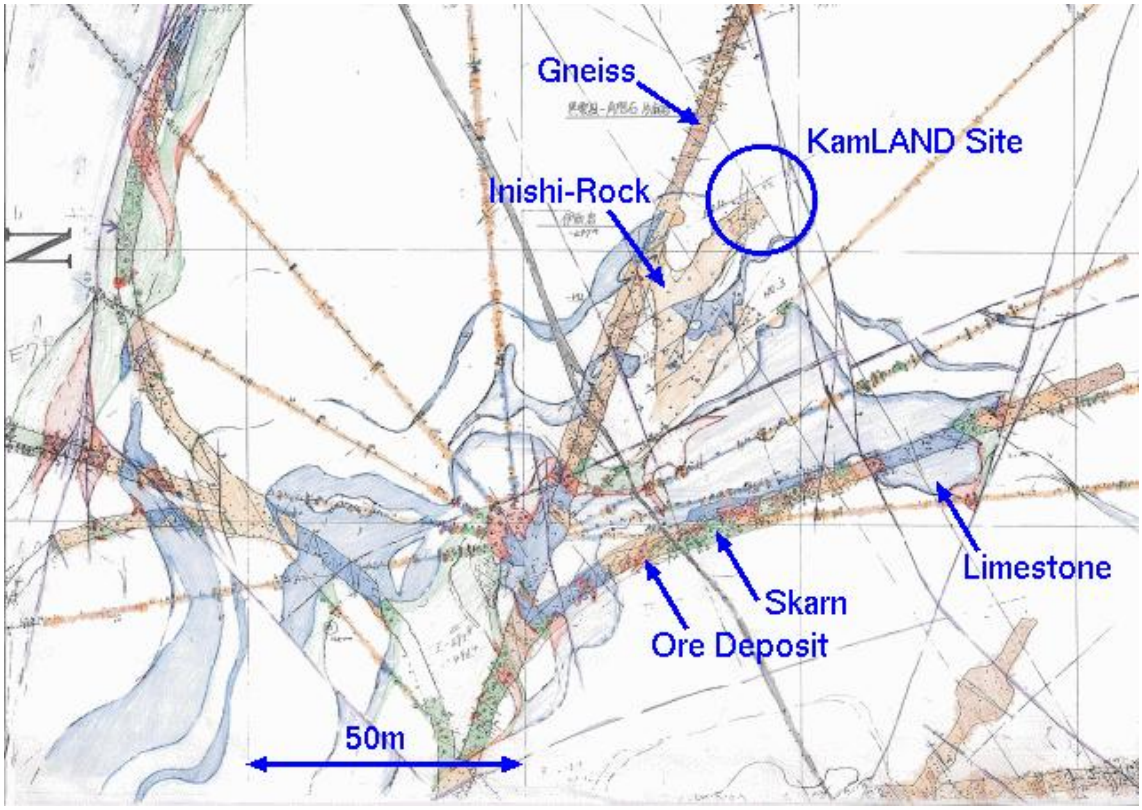

Figure 2.30: Kamioka/Mozumi Mine Geological Map

Compared with the Japanese average, or adaptive values for this region (Section 2.6.5), the mine rock samples show overall trend of depletion in Uranium and Thorium, and no unusual excess in the Uranium and/or Thorium concentration is seen.

Table 2.12: U/Th Concentrations of Kamioka Mine Rock Samples

Rock Name		U Concentration [ppm]	Th Concentration [ppm]
1	Ore	0.17 ± 0.01	0.03 ± 0.01
2	Skarn	1.4 ± 0.05	0.23 ± 0.02
3	Skarn	1.0 ± 0.03	0.47 ± 0.03
4	Inishi Rock	0.23 ± 0.03	0.44 ± 0.04
5	Inishi Rock	2.3 ± 0.06	6.0 ± 0.20
6	Inishi Rock	0.52 ± 0.01	1.5 ± 0.02
7	Gneiss	0.39 ± 0.02	0.82 ± 0.17
8	Gneiss	0.70 ± 0.02	1.3 ± 0.03
9	Limestone	0.54 ± 0.03	0.61 ± 0.16
10	Limestone	2.6 ± 0.24	0.08 ± 0.00

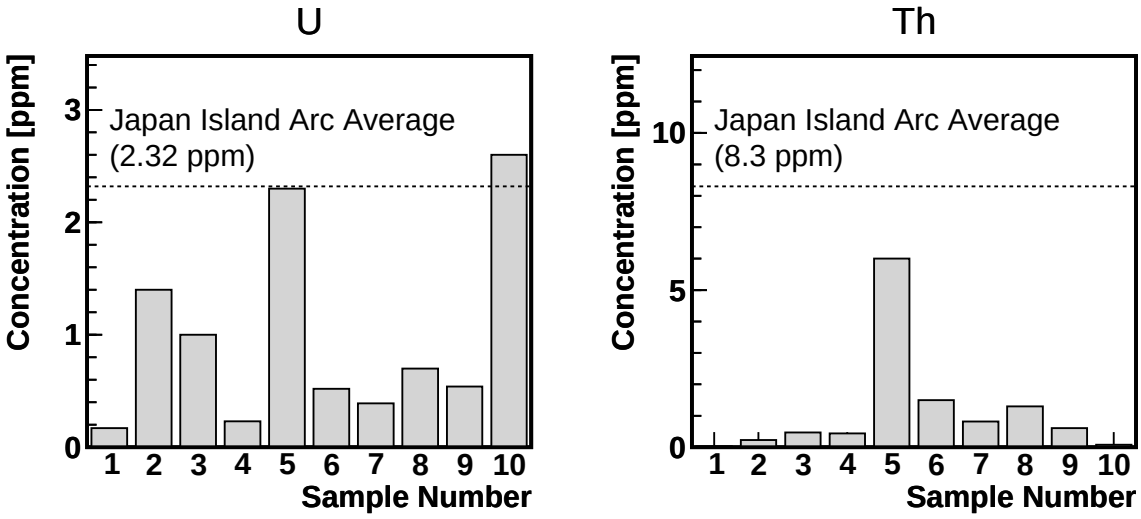

Figure 2.31: U/Th concentration of the mine rock samples

Table 2.13: U/Th Concentrations of Kamioka Mine Rock Samples (M.Yamamoto *et al.*)

Rock Name	U Concentration [ppm]	Th Concentration [ppm]
1 Chliritized Gneiss	1.89 ± 0.09	4.18 ± 0.10
2 Felsic Gneiss	0.13 ± 0.01	0.80 ± 0.08
3 Inishi Rock	0.95 ± 0.07	4.41 ± 0.18
4 Skarn	0.68 ± 0.05	0.42 ± 0.04
5 Inishi Rock	2.23 ± 0.09	7.73 ± 0.22
6 Inishi Rock	0.32 ± 0.02	1.31 ± 0.05
7 Inishi Rock	0.63 ± 0.04	3.24 ± 0.15

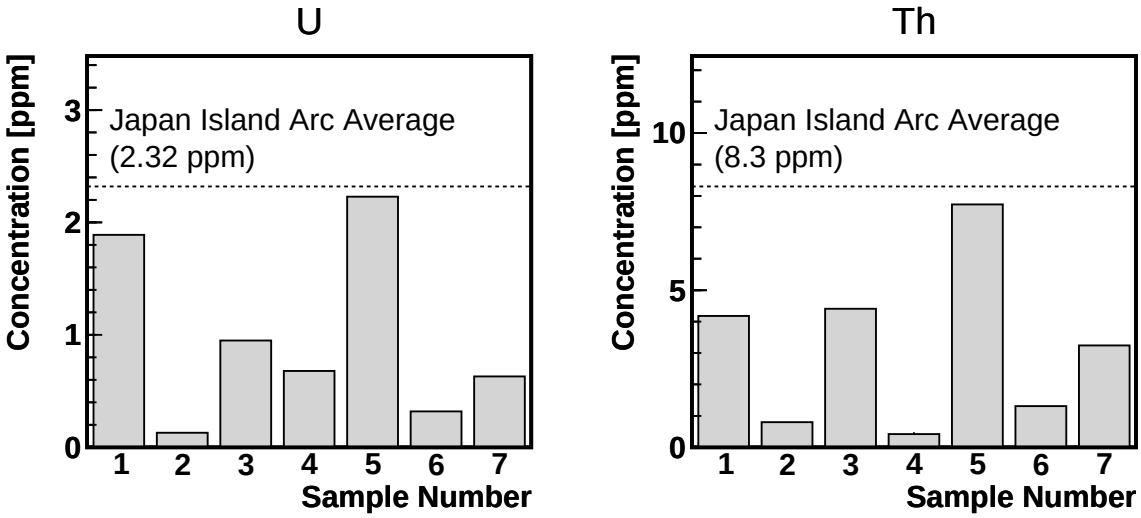

Figure 2.32: U/Th Concentrations of Kamioka Mine Rock Samples (M.Yamamoto *et al.*)

2.6.7 Uranium Mines and Deposits

Known Uranium Deposits

Explorations of Uranium mines over the Japan Islands was conducted by the Geological Survey of Japan (GSJ) and the Power Reactor and Nuclear Fuel Development Corporation from 1954 to 1988 [43], by means of geological approaches, geochemical measurements of rocks, soil and groundwater, radioactive explorations such as car-borne and man-borne surveys, and appraisal drillings. A small number of tiny Uranium deposits were discovered by the series of surveys, as listed in Table 2.14. Figure 2.33 shows the distribution of the discovered Uranium deposits.

Table 2.14: Known Japanese Uranium Deposits

	Name	Longitude [deg]	Latitude [deg]	Ore Grade [U_3O_8%]	Uranium Mass [ton U_3O_8]
1	Okushiri	139.5	42.2	0.063	34
2	Oguni	139.7	38.0	0.030	88
3	Ogawa	140.1	36.4	0.017	8.1
4	Noto	131.0	37.1	0.034	-
5	Tounou	137.1	35.4	0.057	4727
6	Murou	136.0	34.5	0.077	2
7	Okutango	135.2	35.7	0.043	62
8	Tougou	133.9	35.5	0.043	525
9	NingyouTouge	133.9	35.3	0.052	1945
10	MiyoshiMine	133.8	34.6	0.02	-
11	Mitoya	132.9	35.3	0.039	24
12	Miyoshi	132.9	34.8	0.017	79.3
13	Hagi	131.4	34.4	0.039	46
14	Toyota	131.1	34.2	0.059	275
15	Tarumizu	130.7	31.5	0.047	110
	Total			0.054	7925

Neutrino flux from M [kg] of Uranium at L [km] away from the detector is calculated with using the neutrino luminosity of Uranium, 7.41 neutrinos/sec/kg (shown in Table 2.2), by

$$F = 5.89 \times 10^{-1} \frac{M/[\text{ton}]}{(L/[\text{km}])^2} \quad [1/\text{cm}^2/\text{sec}] \tag{2.37}$$

$$= 7.68 \times 10^{-6} \frac{M/[\text{ton}]}{(L/[\text{km}])^2} \quad [\text{TNU}] \tag{2.38}$$

where neutrino oscillation is ignored.

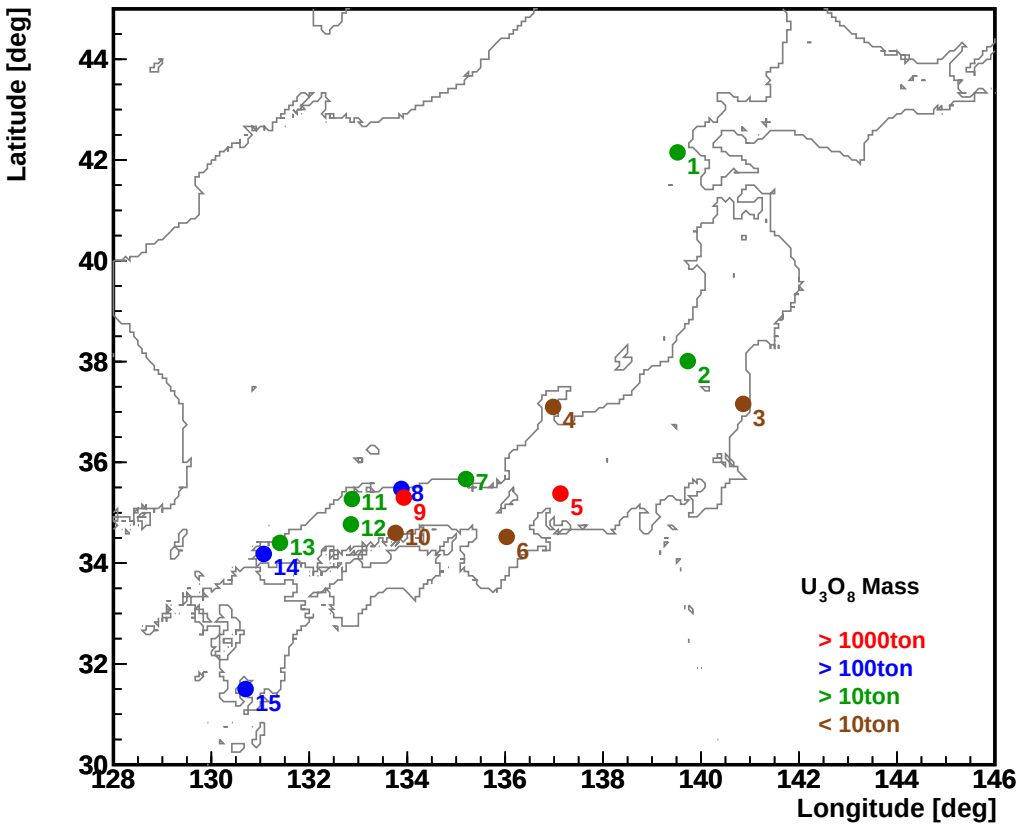

Figure 2.33: Distribution of Known Uranium Deposits in Japan

Table 2.15 shows the estimated neutrino flux at KamLAND from the known Japanese Uranium deposits. The flux is as tiny as 2.8×10^{-6} TNU, making negligible contribution to the total geo-neutrino flux.

Undiscovered Uranium Deposits

Although the exploration was performed with utilizing all available methods, not all Uranium deposits can be found in principle, especially if no part of the deposit is exposed to the surface. The exploration did not find any significant Uranium deposits around the Kamioka area (small scale Uranium concentrations were found though), however, we cannot exclude the possibility of large scale Uranium deposit beneath the Kamioka area.

One of the world largest Uranium mines is the Olympic Dam Mine in Australia, which contains about 200 ktonnes of Uranium. Canada produces the largest amount of Uranium of all countries, with total 300 ktonnes of estimated Uranium deposit, most of which are distributed in a ∼500 km wide region in the Athabasca basin, Saskatchewan. Considering the total known Uranium deposit in Japan, 8 kton, few hundred kton is a reasonable upper limit for a possible Uranium deposit beneath the Kamioka area.

Table 2.15: Geo-Neutrino Flux from Known Japanese Uranium Deposits

	Name	Distance [km]	Uranium Mass [ton U_3O_8]	Flux at KamLAND [TNU]
1	Okushiri	662	34	6.0×10^{-10}
2	Oguni	276	88	8.9×10^{-9}
3	Ogawa	325	8.1	5.9×10^{-10}
4	Noto	81	-	-
5	Tounou	117	4727	2.6×10^{-6}
6	Murou	242	2	2.6×10^{-10}
7	Okutango	209	62	1.1×10^{-8}
8	Tougou	329	525	3.7×10^{-8}
9	NingyouTouge	332	1945	1.4×10^{-7}
10	MiyoshiMine	383	-	-
11	Mitoya	423	24	1.0×10^{-9}
12	Miyoshi	447	79.3	3.0×10^{-9}
13	Hagi	587	46	1.0×10^{-9}
14	Toyota	626	275	5.4×10^{-9}
15	Tarumizu	832	110	1.2×10^{-9}
	Total			2.8×10^{-6}

From (2.38), one can see that neutrino flux from a 100 kton scale Uranium deposit located 1 km away from the detector is less than 1 TNU. Although we cannot scientifically exclude the possibility, it is extremely unlikely that undiscovered huge Uranium deposits make significant difference in the geo-neutrino flux at KamLAND.

2.6.8 Summary of Model Uncertainties

Table 2.16: Summary of Model Uncertainties

	Flux Correction [%]	Contribution to Total Flux [%]	Correction to Total Flux [%]
Continental Crust Non-Uniformity	-13(U) / -17(Th)	49	-6.4 / -8.4
Accumulated Slab beneath Japan	$+75$(U) / $+35$(Th)	2.81	$+2.1$ / $+1.0$
Subducting Plate beneath Japan	$+733$(U) / $+358$(Th)	0.025	$+0.18$ / $+0.09$
Sediments in Sea of Japan	$< +60$	< 0.6	$< +0.36$
CC Fragments in Sea of Japan	$\ll +2800$	$\ll 0.06$	$\ll +2.0$
Local Geology ($\sim$ 50 km Scale)	± 20	16	± 3.2
Mine Geology ($\sim$ 1 km Scale)	$-100 \sim +20$	1	$-1 \sim +0.2$
Uranium Deposits	~ 100000	negligible	negligible

Chapter 3

Detector

3.1 Overview

Neutrinos are detected at KamLAND by the inverse beta-decay reaction,

$$\bar{\nu_e} + p \longrightarrow e^+ + n \tag{3.1}$$

with large amount of organic liquid scintillator. The liquid scintillator essentially consists of hydrocarbon (CH_2), hydrogen nuclei of which also act as the target protons. Energy threshold of the reaction is 1.8 MeV, which is low enough to detect a part of the U-series and Th-series geo-neutrinos.

The reaction makes two correlated signals. The first signal, prompt signal, is made by the positron and two 0.51 MeV gamma particles generated by annihilation of the positron. The second signal, delayed signal, is made by a 2.2 MeV gamma particle, which is emitted in subsequence of thermal neutron capture on proton. This thermalization and capture process take about 200 μsec, and positions of neutron capture are typically 30$\sim$50 cm apart from the neutrino reaction vertices.

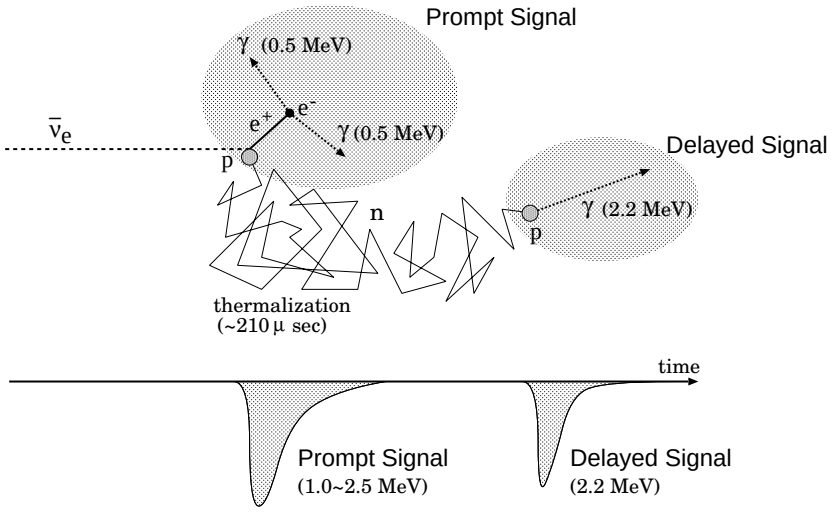

The time and space correlations of two signals are distinguishing characteristics of electron-type antineutrino events. A method of tagging these two correlated signals, the delayed coincidence method, provides an effective way to select antineutrino events with excellent separation of background events.

The KamLAND detector basically consists of 1000 tons of ultra-pure liquid scintillator (LS) contained in a 6.5 m radius spherical balloon and surrounding 1879 photomultiplier tubes (PMT) that cover 34 % of the sphere. The detector is located 1000 m underground in the Kamioka mine, just beneath the Mt. Ikenoyama summit, Gifu, Japan (36.42°N, 137.31°E). The 2700 m water equivalent thickness of rock covering the detector sufficiently reduces cosmic muon flux, resulting in 0.34Hz of muon event rate.

Figure 3.1 illustrates the KamLAND detector. The LS, balloon and PMT's are contained in a 9 m radius spherical stainless steel vessel. 1325 of 17-inch PMT and 554 of 20-inch PMT's are mounted inside the stainless steel vessel viewing the center of the LS sphere. The 6.5 m radius LS containing balloon are positioned at the center of the stainless steel vessel, being supported and constrained by a network of Kevlar ropes. Non-scintillating mineral oil (MO) is filled between the stainless steel vessel and the LS containing balloon, providing gravity/buoyancy balance to the LS sphere, and also acting as a buffer layer against radiations into the LS from the stainless steel vessel, PMT, and everything surrounding the vessel. The MO layer is further divided into two spherical shells by 8.25 m radius transparent acrylic wall, to isolate the balloon contacting MO from the PMT/vessel exposed MO and reduce radioactive contamination around the LS. The inner part of the 9 m radius stainless vessel is called the inner detector (ID).

Outside of the 9 m radius vessel is called the outer detector (OD). The space between the vessel and the cave wall is filled with 3200 tons of pure water, and viewed by 225 of 20 inch PMT's. Cosmic muons passing through the OD are tagged by the OD PMT's, by detecting cherenkov lights. The OD is partitioned into 4 segments, top, upper, lower, bottom, and each segment is laminated with light-reflective Tyvek sheets, to increase light collection efficiency and to utilize muon tracking.

On the top of the 9 m radius stainless steel vessel, a tightly shielded hole, namely chimney, is furnished. It provides access into the LS sphere, for use of detector calibration. Several devices to monitor the detector condition are also equipped in the chimney, such as LS/MO level sensors, balloon supporting rope load monitors, thermometers, pressure sensors, etc. Pipes of LS, MO, Nitrogen are mounted to the chimney as well, and PMT cables are fed into the detector through the chimney.

The ID and OD are tightly shielded to protect the detector from radioactive contamination. The cave above the ID and OD, called the dome, which is used to access the detector, is managed as clean area. Use of clean-wear, which is made of special fabric, is ruled. Filtered clean air is always supplied into the dome area.

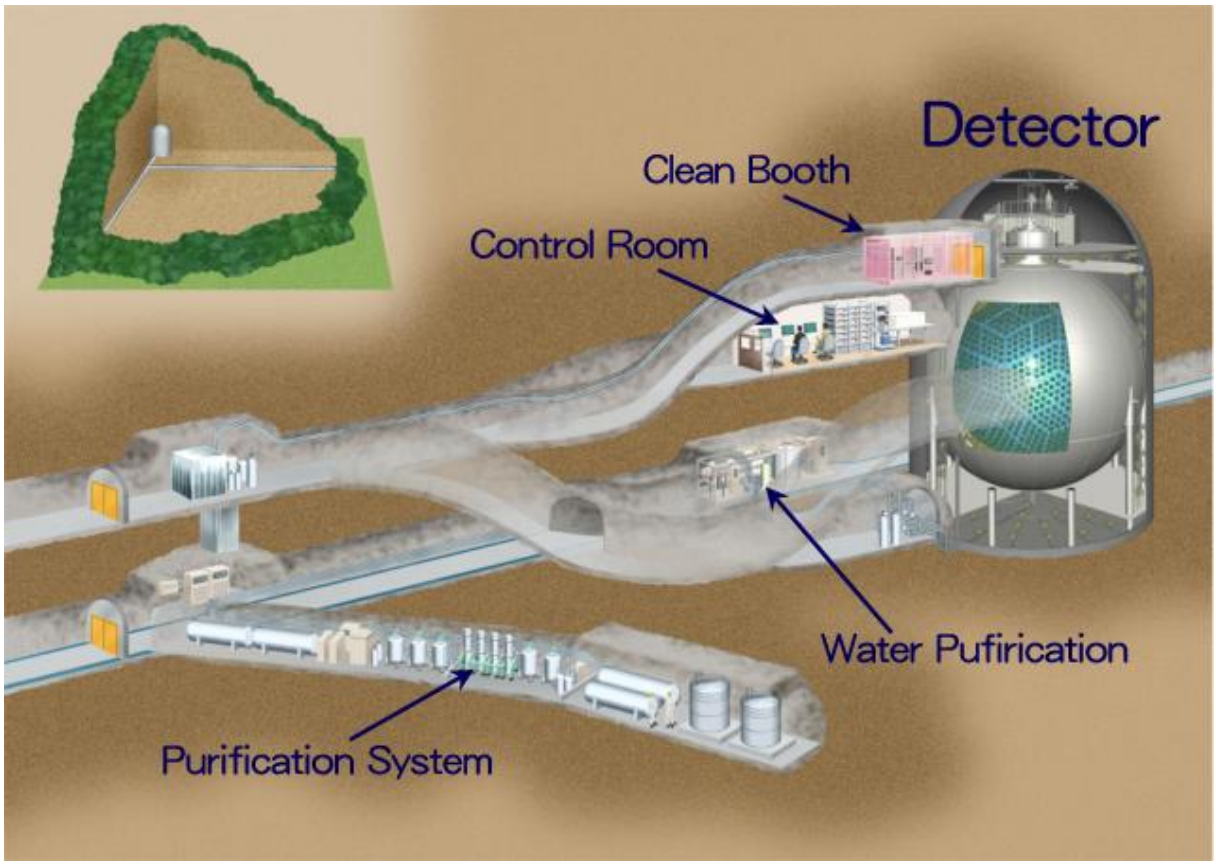

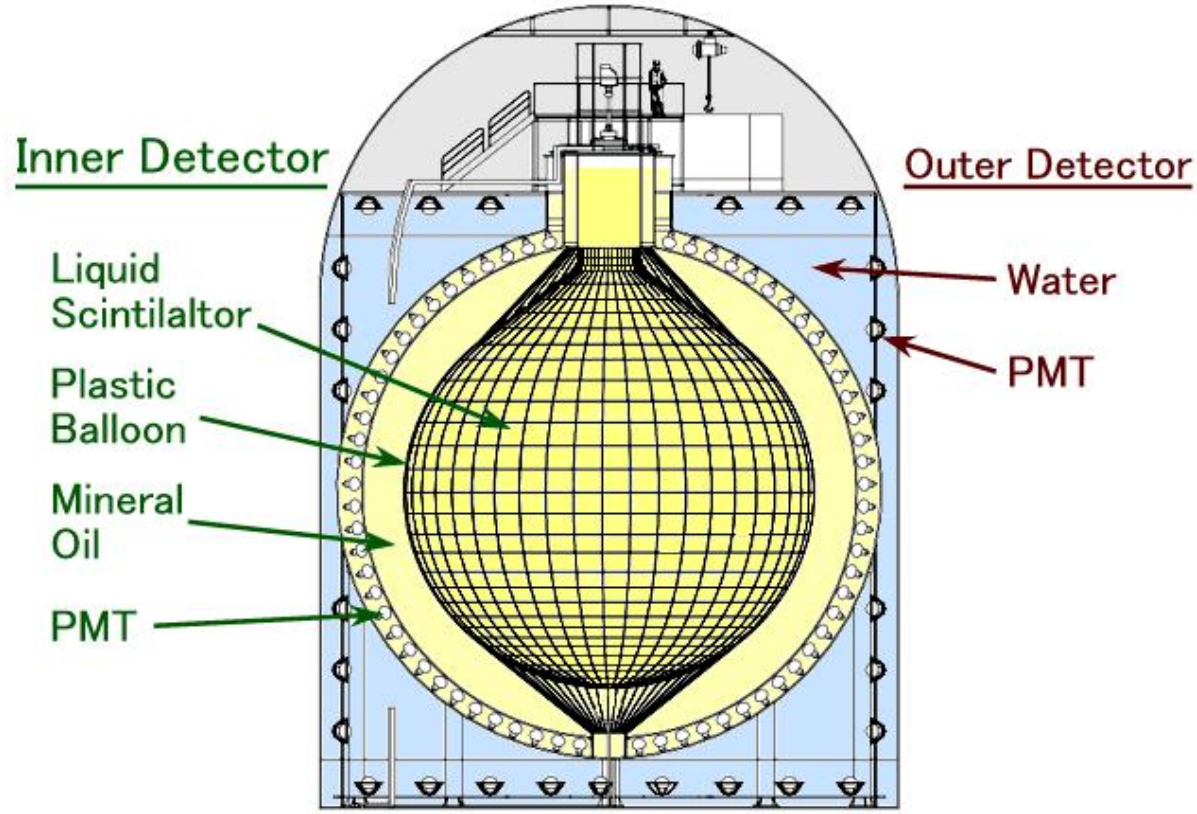

Figure 3.1: KamLAND Detector Schematic View

3.2 Detector Components

3.2.1 Liquid Scintillator

The KamLAND Liquid Scintillator (LS) is composed of 80.2% of dodecane ($C_{12}H_{26}$), 19.8% of pseudocumene (1,2,4-trimethylbenzene, C_9H_{12}), and 1.52 g/litter of PPO (2,5-diphenyloxazole, $C_{15}H_{11}NO$), where PPO is scintillating molecule, pseudocumene is energy transferor, and dodecane is diluter. This composition was determined with examining light output, optical transparency, radioactive contamination, particle identification performance, α-particle quenching factor, Hydrogen/Carbon ratio, chemical stability, factory supply capacity, and cost. Safety regulations (Fire Service Low etc.) require that the flash point of the LS be not lower than 70°C, providing a strict constraint on amount of some materials, such as pseudocumene (flash point of which is 54°C).

Among several candidates, paraffin oil such as dodecane was found to be the best diluter for the KamLAND LS. Since paraffin is an unsaturated compound, which contains neither unsaturated bond nor ring structure, it has good light transparency, high Hydrogen/Carbon ratio, and chemical stability. In fact, paraffin oil showed the best light transparency among several candidate organic diluter. Additionally, large variety in molecular structure of paraffin, such as the number of carbons and the structure of branches, enables us to make suitable property of diluter in density and/or flash point.

For the LS, we chose dodecane as the diluter, with considering the flash point and liquidity at the room temperature. For the buffer oil, which is required to have the same density as that of the LS within 0.3% difference to protect the balloon, mixture of dodecane and isoparaffin with density adjustment was used.

PPO is one of the most commonly used scintillation light emitter. The amount, 1.52 g/l, was determined by seeking balance of the light output and the cost. Addition of pseudocumene was found to improve the light output and particle identification performance, but decrease the light transparency. The fraction of pseudocumene, 20%, was decided after considering the light output, light transparency, particle identification performance, chemical stability, flash point, and cost.

Use of wavelength shifter, such as POPOP and bis-MSB, was considered, but we finally decided not to use it because the wavelength of the LS light, about 370 nm, is already in the same range as the sensitive range of PMT (see Section 3.2.3), and addition of wavelength shifter worsens the optical transparency.

The developed LS has as large light output as 57%Anthracene, and as long optical transparency as about 10 m at 400 nm. The α-quenching factor is as large as about 13 at 7.7 MeV, which reduces β-α cascade decay backgrounds sufficiently. These characteristics satisfy all the requirements of the KamLAND LS.

3.2.2 Balloon and Balloon Supporting Structure

The mineral oil (MO) layer surrounding the LS sphere shields gamma rays and neutrons from surrounding materials such as the PMT's, stainless steel tank, and rocks. It also protects the PMT's and cables from active chemical materials in the LS, such as pseu-

documene.

The LS and the MO are separated by light-transparent plastic film, called the balloon. The balloon is a 7.5 m radius sphere, containing 1000 tons of LS. 1% density difference between the inner LS and the outer MO makes 10 tons of load to the balloon, and this load is supported by a network of 44 longitudinal and 30 transversal Kevlar ropes.

In addition to being optically transparent, the balloon film is required to be mechanically strong, chemically tolerant, thin, and clean in terms of radioactivity. Since the outer MO is contaminated by radon from various materials contacting the MO layer, the balloon is also required to be radon-tight.

Among numerous candidate materials, it was found that stretched Nylon film (ON) has enough mechanical strength, and stretched EVOH film (XL) has the highest gas tightness and good chemical tolerance. Hence we adopted multi-layer film consisting of three layers of 25 μm thickness ON and two layers of 14 μm thickness XL for the KamLAND balloon (XL/ON/ON/ON/XL), where the number of the ON layers were decided by finding the best balance of mechanical strength and thickness.

The mechanical strength of the film was measured to be about 8 kg/cm, which is greater than estimated KamLAND balloon load, 2.1 kg/cm (1% MO-LS density difference). The balloon supporting ropes will reduce the balloon load, providing further safety.

Long-term chemical tolerance was examined by comparing mechanical strength before and after placing the film in 60°C LS for 2 months, and no significant difference was seen. 65 cm radius test balloons were also used to check the long-term chemical/mechanical stability, by leaving them for 9 months with LS inside and MO outside, and no serious damages were found.

Optical transparency of the film was measured to be 93% at λ=400nm. Radon tightness was measured such that the film can maintain 1.8×10^{-6} of Radon density ratio between the two sides. ICP-MS analysis showed that Uranium and Thorium contamination of the film is 0.018 ppb and 0.014 ppb respectively, and flame atomic absorption measurement resulted in 0.27 ppb of ^{40}K contamination. All these properties meets all the requirements.

3.2.3 Photomultiplier Tubes (PMT)

At KamLAND, geo-neutrinos make only a few MeV signals, where one MeV visible energy corresponds to about 200 photo-electrons (including PMT's quantum efficiency). This means that most of PMT's have only one photo-electron hit per event, requiring the PMT to have good energy response downto one photo-electron level. Due to nature of a scintillation detector (in contrast to a cherenkov detector), time is practically the only information that can be used to separate multiple signals, hence good time resolution is a key issue as well, in particular to detect short-interval cascade decays such as proton decays. Good time resolution directly connects to good vertex reconstruction resolution, leading to reducing systematic errors at various aspects.

A new PMT has been developed for the KamLAND experiment based on the former 20-inch PMT (R3600) developed for the Super Kamiokande experiment, with aiming substantial improvement in energy and time response. The first decision in new PMT

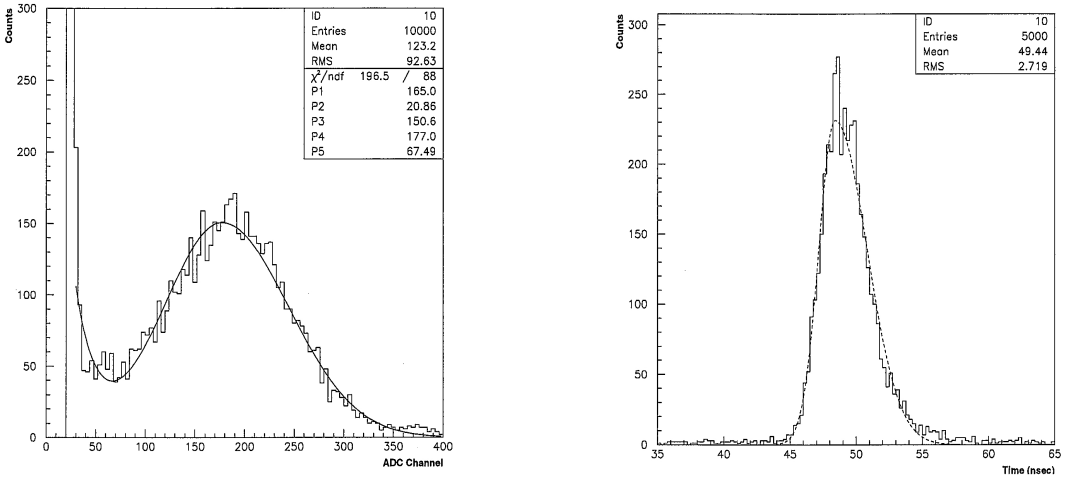

Figure 3.2: KamLAND PMT Characteristics. Left panel shows the pulse height distribution for 1 p.e. level light, and the right panel shows the transit time distribution.

design is not to use the edge region of photo-cathodes, where energy and time response is significantly worse than the central region. The sensitive region is decided to be 17-inch diameter (hence the new PMT, R7250, is called the '17-inch PMT'), and outside of the central region is masked with black plastic plates. This decision enabled us to replace the dinode from the venetian blind type which is suitable for large diameter photo-cathodes to the linear focusing type which has good time and energy response.

Figure 3.2 shows the distribution of transit time (time from photon hit to electrical pulse output), and distribution of charge output to 1 photo-electron (p.e.) level laser light. The FWHM of transit time, called transit time spread (TTS), was found to be 3.6 nsec. This is in great improvement from that of the former PMT (R3600), 6 nsec. The height of 1 p.e. peak in ratio to the height of left valley, called peak-to-valley ratio, was found to be 3.9, also showing excellent improvement from that of the former PMT, 1.5.

Figure 3.3 shows distribution of several characteristic parameters of the newly developed 17-inch PMT (R7250), such as luminous sensitivity, which is output current to 1 lumen of blue light, supply voltage to obtain 10^7 gain (measured with DC tungsten light), dark current, dark pulse rate, TTS, and peak-to-valley ratio, in comparison with the former 20-inch PMT (R3600). Substantial improvements in energy and time response are clearly seen.

3.2.4 Purification System

The KamLAND LS are essentially composed of paraffin and pseudocumene, which are made from crude oil with multiple refining processes. Consequently, such oil contains very small amount of impurities. On top of that, non-ionicity of mineral oil naturally leads to low contamination of ionic materials, such as Uranium, Thorium and Potassium. ICP-MS analysis showed that the primitive KamLAND LS (i.e., before any purification) contains 10^{-13}g/g of Uranium, $< 10^{-12}$g/g of Thorium and 7×10^{-11}g/g of Potassium, which is already in as low radioactivity as ultra-pure water used for the Super-Kamiokande

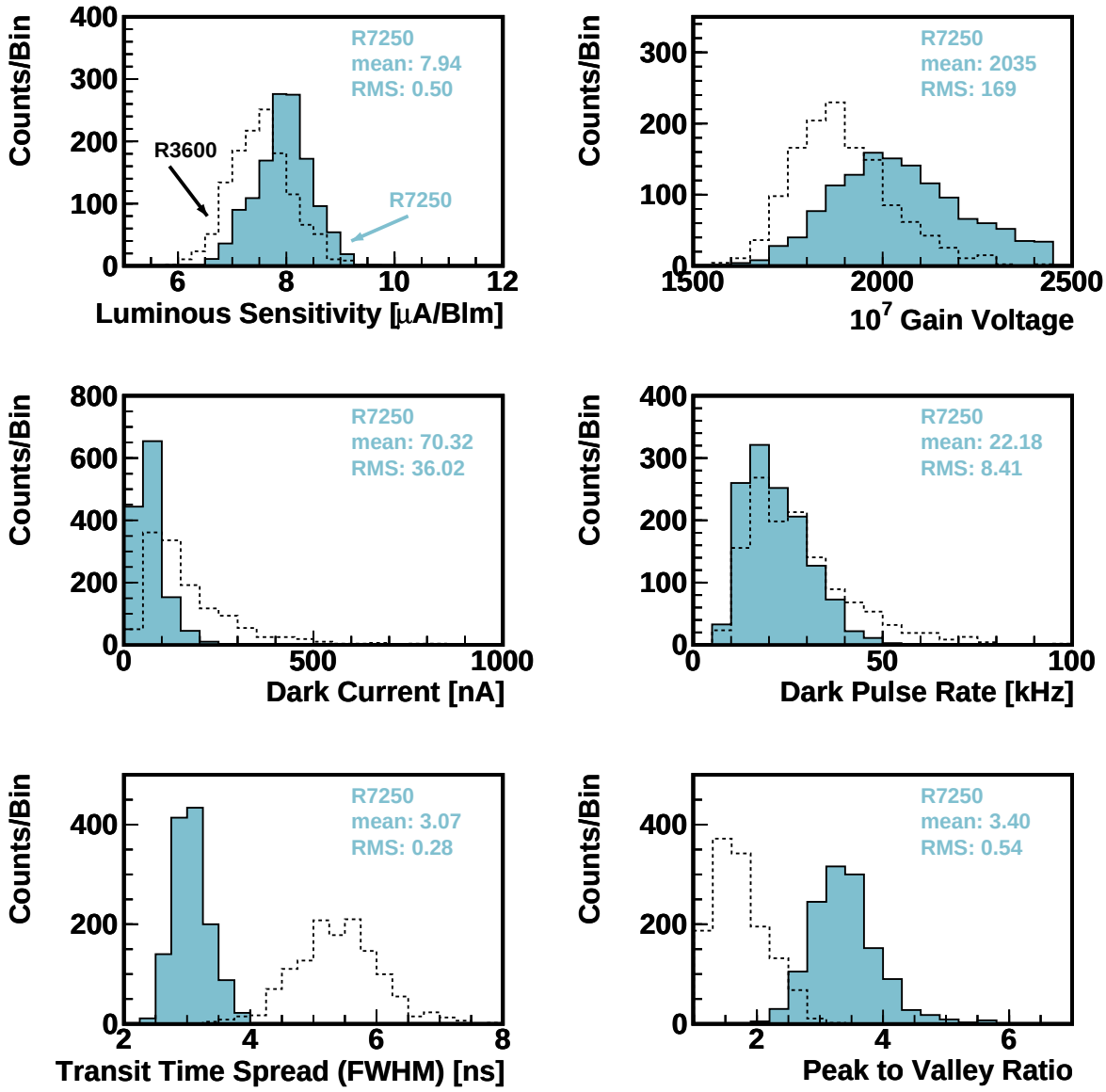

Figure 3.3: KamLAND PMT Improvements. Some characteristic parameters are shown in comparison with the former 20-inch PMT (R3600). Substantial improvements in energy and time responses are clearly seen.

experiment.

However, detection of few MeV neutrinos requires further reduction of radioactive contamination. The neutrino event rate at KamLAND is expected to be around 1 events/day, and to reduce the rate of accidental coincidence events to a tolerable level (<0.1 events/day), Uranium, Thorium and Potassium need to be removed to $< 10^{-14}$g/g, $< 10^{-14}$g/g and $< 10^{-15}$g/g, respectively.

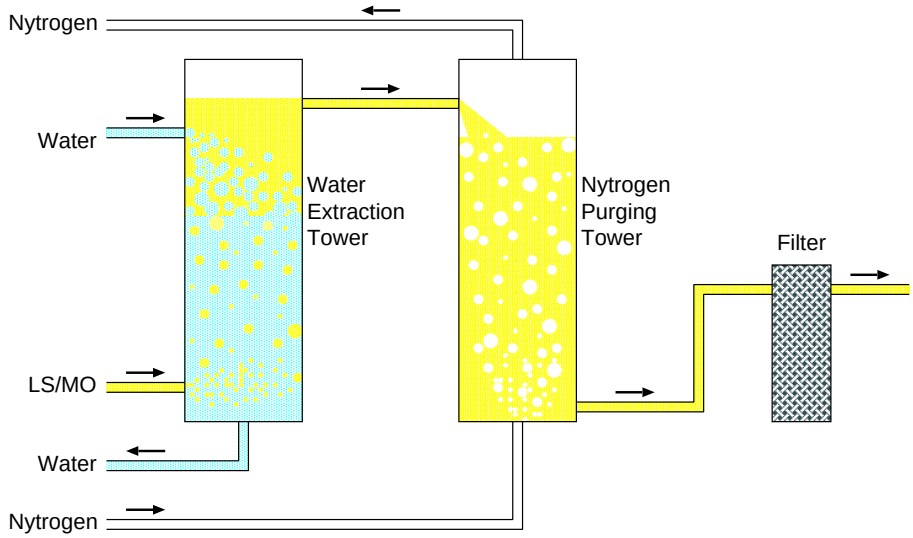

Figure 3.4: Purification System Overview

The LS and MO is purified by means of water extraction, Nitrogen purging, and filtering. Figure 3.4 shows outline of the LS/MO purification system.

The water extraction method utilizes solubility difference of impurities between LS/MO and water. Uranium, Thorium and Potassium are ionic elements and consequently tend to be concentrated in water rather than non-ionic organic solvent such as LS and MO (the solubility differ at several orders of magnitude). In mixture of LS/MO and water, these elements move to water and thus the LS/MO is sufficiently purified. At KamLAND, we mix LS/MO and pure water for a few seconds by streaming them at opposite directions at the 'Water-Extraction Tower'.

The LS/MO is then fed to the 'Nitrogen Purging Tower' and bubbled with Nitrogen gas. Nitrogen bubbling is a process that is commonly employed to maintain liquid scintillator quality, and it purges Oxygen, water, and Radon contained in the LS. Oxygen in LS causes 'Oxygen Quenching', which reduces light output of the LS and also affects light emission timing. Radon is generated by decays of radioactive materials contained in the stainless steel tank, pipe, and everything contacting the LS and MO, and is a major source of radioactive backgrounds.

Finally the LS and MO are filtered with 0.1μm mesh, which removes dust and large molecular impurities.

After these purification processes, Uranium, Thorium and Potassium are reduced to be lower than the ICP-MS detection limit ($\sim 10^{-13}$g/g). Radioactive contamination of the LS was measured with the KamLAND detector itself after data taking operation was started, and the amount of Uranium, Thorium and Potassium were found to be 3.5×10^{-18}g/g, 5.2×10^{-17}g/g and $< 2.7 \times 10^{16}$g/g respectively. Details of radioactive contamination of the LS is discussed in Chapter 6.

3.2.5 Front-End Electronics (FEE)

The primary purpose of the KamLAND experiment is to detect few MeV neutrinos. Since most of PMT's have just one photo-electron hit at this energy region, the front-end electronics (FEE) is required to record one photo-electron signal precisely. With 10^7 PMT gain, the one photo-electron makes 1.6 pC charge output, pulse height of which is around few milli Volts.

On the other hand, the KamLAND detector is exposed to very high-energy cosmic muons, which make more than 1000 photo-electron hits to every PMT. Taking account of one photo-electron signal threshold, the FEE needs to manage over 10,000 magnitude of dynamic range.

The event rate at 1 MeV threshold is expected to be few tens Hz. Unlike accelerator experiments, event timing is not aligned (to beam bunches etc), and timing of events cannot be predicted (by beam cycle etc). The FEE is required to collect every signal without a beforehand notice, including cases that the signal comes just after another signal.

The physics interest of KamLAND is not limited to neutrinos from nuclear power rectors, the Sun and the Earth. With the huge liquid scintillator target, KamLAND is also playing an unique role in observation of supernova neutrinos and nucleon decays. A typical supernova at the center of the Milky Way Galaxy could make 1 kHz of high-energy neutrino events for a few seconds, and a proton decay event makes multiple signals of cascade decay such as $p \to K^+\bar{\nu_\mu}$; $K^+(\tau = 12\text{ns}) \to \pi^+\pi^0$; $\pi^0 \to \gamma\gamma$; $\pi^+(\tau = 26\text{ns}) \to \mu^+\nu_\mu$; $\mu^+(\tau = 2.2\mu\text{s}) \to e^+\nu_e\bar{\nu_\mu}$. The FEE is required to collect these signals properly.

The KamLAND FEE records waveform of every PMT hit signal to handle short-interval multiple signals such as proton decay events. Waveforms are captured on local (i.e., each PMT) discriminator hits and then digitized on global trigger decisions. While this period (between capture and digitize), waveforms are held on an analog memory device, providing the trigger circuitry to collect all PMT hit information and make decisions. This scheme makes it possible to record events that are not predicted. Every PMT channel has duplicated waveform digitizer channels to avoid deadtime induced by signal processing time (A/D conversion etc). Three amplifiers with different gains are connected to every PMT channel in order to realize a wide dynamic range. Each FEE card equips large buffer memory on it to store digitized event data for a certain time, to utilize for efficient readout and also to hold data in case that readout cannot keep up with data digitizing, such as a case of supernova.

Figure 3.5 is a diagram of the KamLAND FEE card. A key technology of the FEE is the Analog Transient Waveform Digitizer (ATWD) chip, which holds analog signal waveform on arrays of capacitors, and digitizes the waveform on request. Each ATWD chip equips 4 independent analog input channels, and each waveform data consists of 128 of 10-bit samples, with sampling interval about 1.5 nsec (configurable).

While the ATWD chip is under operation, the input signals are cyclically recorded in the capacitor array in the chip. When the 'capture' signal arises, the sampling is stopped and the waveform existing on the capacitor array at this moment is held. If the 'digitize' signal comes, the held waveform is digitized, otherwise the waveform is disposed. After

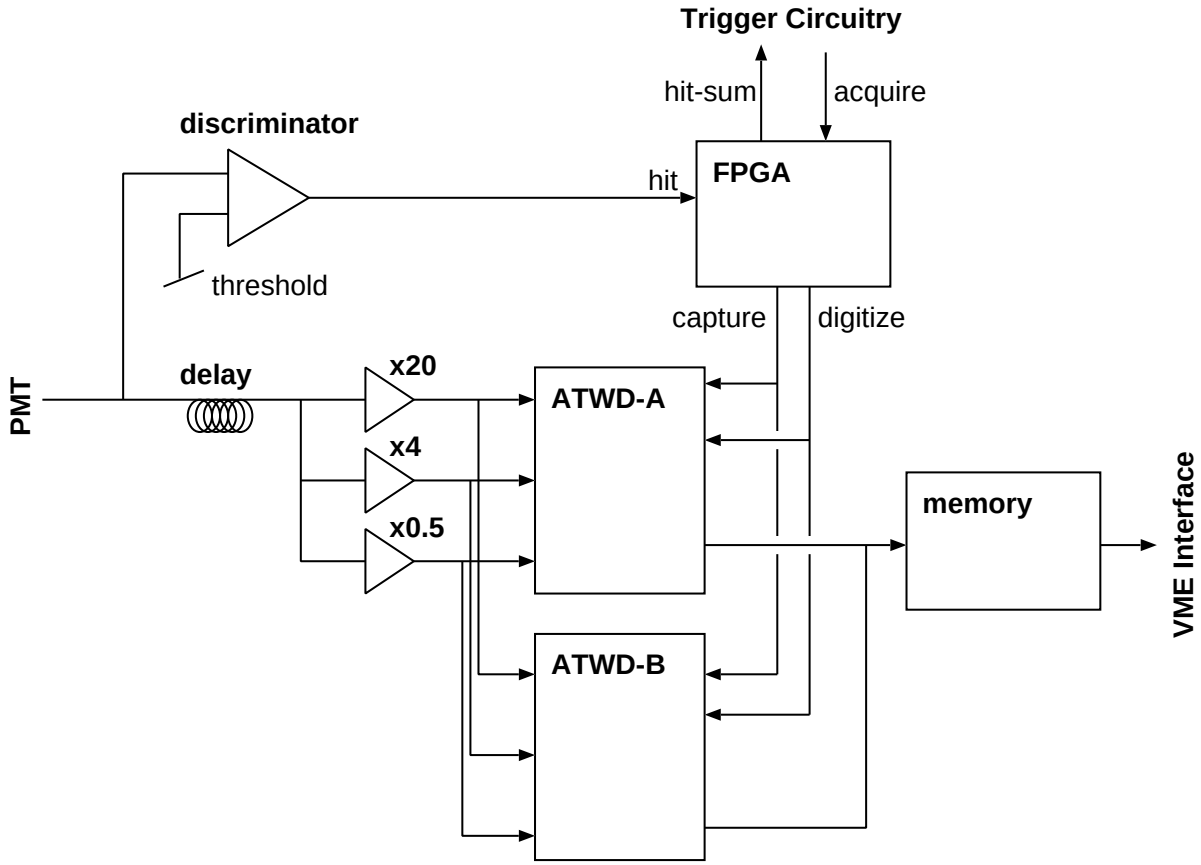

Figure 3.5: KamLAND Front-End Electronics (FEE) Diagram

the digitization or the clearance is completed, the ATWD chip starts waveform sampling.

Capture signals are issued based on hits of the local discriminators. The hit information is compiled on a controller circuitry implemented on a Field Programmable Gate Array (FPGA) chip, and sent out to the trigger circuitry as the 'hit-sum' signal, which encodes the number of PMT hits per FEE card. If the trigger circuitry decides to collect the event, it sends out the 'acquire' signal to the FEE cards, and the controller circuitry on the FPGA issue the 'digitize' signal to the ATWD chips. After digitization, the data is transfered to a buffer memory equipped on every FEE cards. The data in the buffer memory is then readout by data acquisition software running on the front-end PC's via the VME bus interface.

As mentioned before, the signal processing line is duplicated to eliminate deadtime induced by signal processing time. Two ATWD chips are connected to one PMT channel (ATWD-A and ATWD-B), and they are launched alternately by control of the FPGA chip. Three amplifiers with different gains, $\times 20$ (high-gain), $\times 4$ (middle-gain) and $\times 0.5$ (low-gain), are connected to one PMT channel, providing wide dynamic range. One remaining ATWD input channel is connected to a 40 MHz clock line, for use of sampling interval calibration.

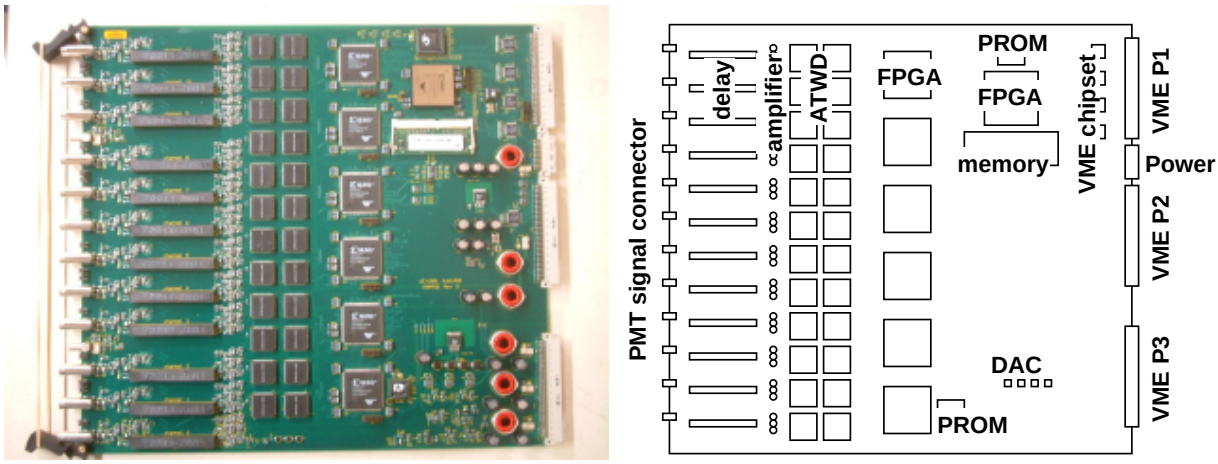

Figure 3.6: KamLAND Front-End Electronics (FEE)

The FEE card is highly configurable. The ATWD sampling intervals, the ATWD pedestal levels, and the discriminator thresholds are programmed at run-time by the online software. Operation of the ATWD chips, such as waveform capture timing, usage of the dual ATWD's, and data transfer to the buffer memory are all controlled by the FPGA chips, logic of which is configured by programs stored in the EPROM's at power-on cycle.

The FEE card also equips a number of self calibration functions. To calibrate the waveform sampling interval, 40 MHz clock signal is connected to an analog input of every ATWD chip. To calibrate the gain of the amplifiers and the gain of the A/D converters in the ATWD chip, signal from a built-in test pulser can be fed to the point of PMT signal input. These calibration data are acquired by control of the online software via the VME interface or by commands from the trigger circuitry.

Figure 3.6 shows a picture of a KamLAND FEE card and its layout. The FEE is implemented as a 9U size VME card, with extension of a special power supply connector. Upto 12 PMT's are connected to one FEE card. The communication lines to the trigger circuitry are connected to the user pins of the VME P2 connector. The FEE card is configured by the online software through the VME bus, and data are transfered to PC by control of the online software through the VME bus. The buffer memories on the FEE cards enable the online software to transfer data blocks with direct memory access (DMA) mode, which is about 10 times as fast as normal programmed access mode.

3.2.6 Trigger and Trigger Circuitry

Trigger decisions are made based on the number of hit PMT's within a certain time window. Each FEE card outputs the 4-bit 'hit-sum' signal, which encodes the number of fired discriminators on the FEE card (thus the hit-sum ranges from 0 to 12). Since there are 200 FEE cards in total, 200 of 4-bit hit-sum signals are fed to the trigger circuitry. Each PMT hit signal is stretched to a 125 nsec long gate, and digital sum of the gates is computed at the trigger circuitry. If the digital sum of PMT hits, NSum, excesses a

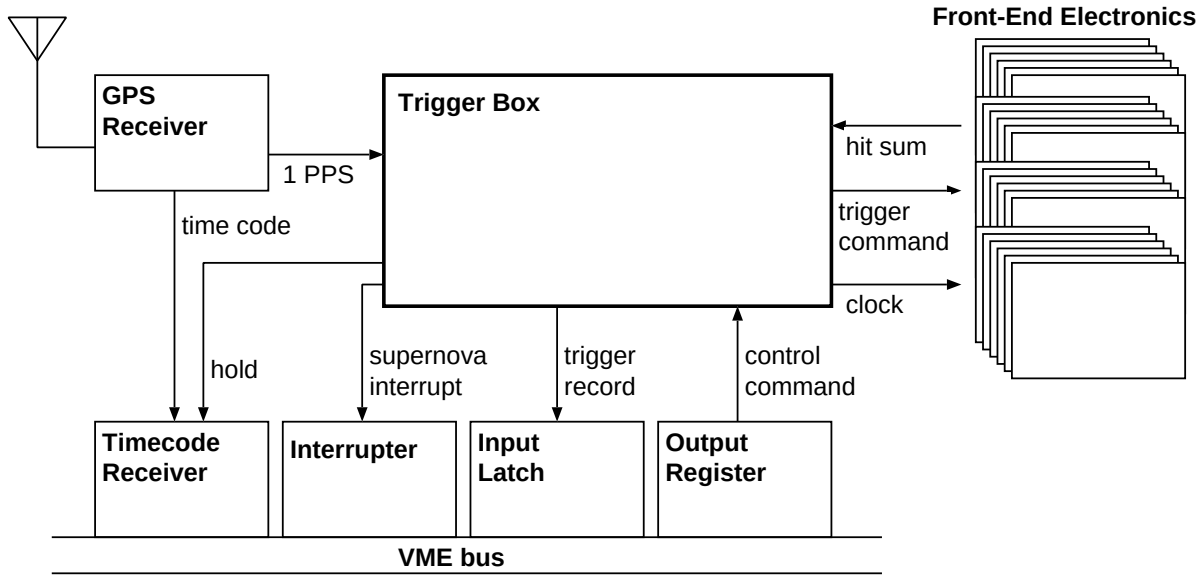

Figure 3.7: KamLAND Trigger Circuitry

preset threshold, the 'acquire' command is sent to the FEE cards.

Figure 3.7 shows a schematic diagram of the trigger subsystem. The trigger circuitry receives PMT hit signals from every FEE card, and sends various commands (trigger commands) to the FEE. The trigger commands include the acquire commands that command to acquire waveforms, the calibration commands that command to perform self-calibration (with the built-in test pulser and 40 MHz clock signal etc.), and some other control commands such as initialization. There are two types of acquire commands; i.e., the global acquisition which commands to acquire waveforms of hit channels, and the forced-acquisition which commands to acquire waveforms of all channels regardless of discriminator hits.

A Global Positioning System (GPS) receiver is connected to the trigger circuitry and all time information used in the system is synchronized to the GPS time. The trigger circuitry also provides the 40 MHz system clock to the FEE cards. The 40 MHz clock is synchronized to the GPS time at the trigger circuitry, and is used to generate event timestamps at the FEE cards. Every waveform data comes with a timestamp, which is later used by the event-builder software to re-arrange the waveform data fragments into *events*.

The trigger circuitry has its own data stream (trigger data stream) connected to the online software. The trigger data is transfered to a font-end PC via an input latch module on the VME bus. The trigger records contain various information of every issued trigger, such as trigger type, timestamp, and NSum. Some trigger types do not involve acquire signals to the FEE (i.e., do not acquire waveforms), but the NSum and timestamp are recorded by the trigger circuitry; the tiny event data size of this kind of triggers allows us to lower the trigger threshold significantly, where the NSum data is quite useful because of small occupancy of PMT hits. When the trigger circuitry detects a supernova candidate,

it notifies the online system through an interrupter module.

An output register on the VME bus is used to send commands from the online software to the trigger. Almost all parameters used on trigger decisions, such as trigger thresholds, prescaling rate, enabling/disabling specific trigger types, and supernova criteria, are set by the online software in prior to data taking. All trigger logic is implemented on three FPGA's on the trigger board, and can be easily re-configured by replacing EPROM's.

The most important trigger in normal physics run is the *prompt* trigger, that is issued when the NSum excesses 200, which roughly corresponds to more than 200 ID PMT hits. Following every prompt trigger, the *delayed* trigger is enabled for 1 msec, which is issued when the NSum excesses 120. The delayed trigger was introduced to improve detection efficiency of timely correlated multiple signals, such as cascade decays. Another important trigger for physics run is the OD-to-ID trigger, which is issued when any of OD segment detects certain number of photons. Some other triggers, such as triggers issued every 1 sec (1PPS trigger) and triggers issued at a lower threshold without a capture command (history trigger) are also implemented.

Following is a list of triggers currently implemented.

ID NSum Triggers

ID Singles This trigger is issued when the ID NSum excesses a preset ID-Singles-Trigger threshold. It sends a global acquisition command to the ID FEE cards.

ID Prompt This trigger is issued when the ID NSum excesses a preset ID-Prompt-Trigger threshold. It sends a global acquisition command to the ID FEE cards.

ID Delayed This trigger is issued when the ID NSum excesses a preset ID-Delayed-Trigger threshold within 1 msec window following a prompt trigger. It sends a global acquisition command to the ID FEE cards.

ID Prescale This trigger is issued when the ID NSum excesses a preset ID-Prescale-Trigger threshold, with prescaling of a preset fraction of time. It sends a global acquisition command to the ID FEE cards.

ID 5-inch This trigger is issued when the NSum of chimney 5-inch PMT's excesses a preset ID-5inch-Trigger threshold. It sends a global acquisition command to the ID FEE cards.

OD-to-ID This trigger is issued when any of OD NSum triggers (described below) is issued. It sends a global acquisition command to the ID FEE cards.

OD NSum Triggers

OD Top Singles This trigger is issued when the NSum of the OD top section excesses a preset OD-Top-Singles-Trigger threshold. It sends a global acquisition command to the OD FEE cards.

OD Upper Singles This trigger is issued when the NSum of the OD upper side section excesses a preset OD-Upper-Singles-Trigger threshold. It sends a global acquisition command to the OD FEE cards.

OD Lower Singles This trigger is issued when the NSum of the OD lower side section excesses a preset OD-Lower-Singles-Trigger threshold. It sends a global acquisition command to the OD FEE cards.

OD Bottom Singles This trigger is issued when the NSum of the OD bottom section excesses a preset OD-Bottom-Singles-Trigger threshold. It sends a global acquisition command to the OD FEE cards.

ID-to-OD This trigger is issued when any of ID NSum triggers is issued. It sends a global acquisition command to the OD FEE cards.

History Triggers

ID History This trigger is issued during the ID NSum excesses a preset ID-History-Trigger threshold. It does not send any acquisition command to the FEE cards (does not acquire waveforms). The trigger record is generated every 25 nsec while the NSum is above the threshold, up to 200 nsec maximum.

OD Top History This trigger is issued during the NSum of the OD top section excesses a preset OD-Top-History-Trigger threshold. The behavior of the trigger circuitry is same as that of the ID History trigger.

OD Upper History This trigger is issued during the NSum of the OD upper side section excesses a preset OD-Upper-History-Trigger threshold. The behavior of the trigger circuitry is same as that of the ID History trigger.

OD Lower History This trigger is issued during the NSum of the OD lower side section excesses a preset OD-Lower-History-Trigger threshold. The behavior of the trigger circuitry is same as that of the ID History trigger.

OD Bottom History This trigger is issued during the NSum of the OD bottom section excesses a preset OD-Bottom-History-Trigger threshold. The behavior of the trigger circuitry is same as that of the ID History trigger.

GPS Triggers

1 PPS Trigger This trigger is issued every second in synchronization with the GPS time. It had been configured not to send any acquisition command to the FEE cards until February 15 2004, then changed to send the acquisition command to the all FEE cards.

GPS Trigger This trigger is issued at the start of the run and every 32 seconds thereafter. It sends a global acquisition command to the OD FEE cards, and issues an interrupt to the GPS interface module on the VME to record the GPS time.

Calibration Triggers

ID Calibration Forced This trigger is issued on external input to the trigger board. The input can be made by calibration devices such as laser and LED. It sends a forced acquisition command to the ID FEE cards.

ID Calibration Global This trigger is issued on external input to the trigger board. It sends a global acquisition command to the ID FEE cards.

OD Calibration Forced This trigger is issued on external input to the trigger board. It sends a forced acquisition command to the OD FEE cards.

OD Calibration Global This trigger is issued on external input to the trigger board. It sends a global acquisition command to the OD FEE cards.

Acquire Trigger This trigger is to command the FEE cards to acquire self-calibration data, such as pedestal, 40 MHz clock waveform, and built-in test pulser waveform. The Acquisition Triggers are usually issued under control of the online software.

Other Triggers

Supernova Trigger This trigger is issued when the trigger logic detected a supernova candidate. It does not send any commands to the FEE cards. An interrupt is sent to the online software via the VME interrupt module to notify the state, and the trigger conditions are changed to a predefined values (supernova mode). The supernova trigger mode lasts for 1 minute, and any operation to the data acquisition system is prohibited during this period to preserve the data.

Disable Trigger The trigger is *disabled* when the trigger data buffer becomes almost full. The Disable-Trigger trigger is issued on the trigger-disable condition. It does not send any commands to the FEE cards.

Enable Trigger When the buffer-almost-full condition is recovered, the trigger is *enabled*. The Enable-Trigger trigger is issued on the trigger-enable condition. It does not send any commands to the FEE cards.

The following table lists the current trigger parameters for normal physics runs.

ID Single Threshold	200
ID Prompt Threshold	200
ID Delayed Threshold	120
Delayed Trigger Window Length	1 msec
ID Prescaling Fraction	no prescaling
ID Prescale Threshold	-
ID 5-inch Threshold	7
OD Top Single Threshold	6
OD Upper Single Threshold	5
OD Lower Single Threshold	6
OD Bottom Single Threshold	7
ID History Threshold	120
OD Top History Threshold	6
OD Upper History Threshold	5
OD Lower History Threshold	6
OD Bottom History Threshold	7

3.2.7 Data Acquisition Software

The primary task of data acquisition (DAQ) software is to read data from electronics devices and store the data onto storage devices. At KamLAND, total 15 VME crates are used, each of which is connected to one front-end PC exclusively. Therefore data transportation from 15 front-end PC's to back-end PC's is also a primary task of the DAQ system. Data buffering, data stream conjunction, and data flow control are naturally involved in the data transportation process.

In addition to data readout, transportation and recording, data monitoring is also an important task of a DAQ system. Since a DAQ system is the only software that works with data in realtime and also the only software that has direct connections to electronics devices, it is responsible to monitor the data, display conditions to operators, and control the devices appropriately. Consequently, quick online analysis becomes a part of DAQ system.

The DAQ system is also an interface of the devices to operators. Electronics devices are configured by the DAQ software based on operators' control and/or automated control, and the DAQ system itself is controlled by operators' command. DAQ system is required to detect and notify any system failures, and to reject improper operator commands. Logging and managing of operator control history, run conditions and all relevant information is closely related to this aspect of the DAQ system.

Since a number of PC's are involved in the DAQ system, control of remote processes is an essential function of the DAQ system. The system needs to provide a framework on which processes distributed over a network work efficiently in cooperation. The framework includes remote process control, command/message exchanging, and parameter sharing.

The KamLAND DAQ system, namely KiNOKO, which stands for "Kinoko Is Network-distributed Object-oriented Kamland Online-system", was designed to comprehensively handle these requirements by making practical use of recently developed computer technologies such as distributed object systems and component architectures. The distributed object system has realized a seamlessly integrated parallel processing environment over networked computers, which leads to true scalability covering from a single process system to a multiple computer system. The component architecture has enabled users to construct a DAQ system by a simple procedure of combining single-function *components* at runtime, resulting in high flexibility and reusability. Reuse of well-tested system components has naturally increased the system stability and reliability. Newly developed script parsing method is utilized to describe the experiment-specific configurations, data format and online analysis procedures, bringing about notable improvements in flexibility, maintainability and user-friendliness, without sacrificing performance. Owning to these innovative features, even non-experts of the DAQ system actually have modified the DAQ system by themselves in order to make it fit for their own needs. The DAQ system, KiNOKO, has been opened to the public and has widely been applied to a number of other experiments, from a single channel CAMAC system to a high-rate signal sampling application with multiple computers. Feedbacks from these applications have been contributing toward further improvements of the system usability and stability, and by the time of KamLAND operation, the system had become stable enough.

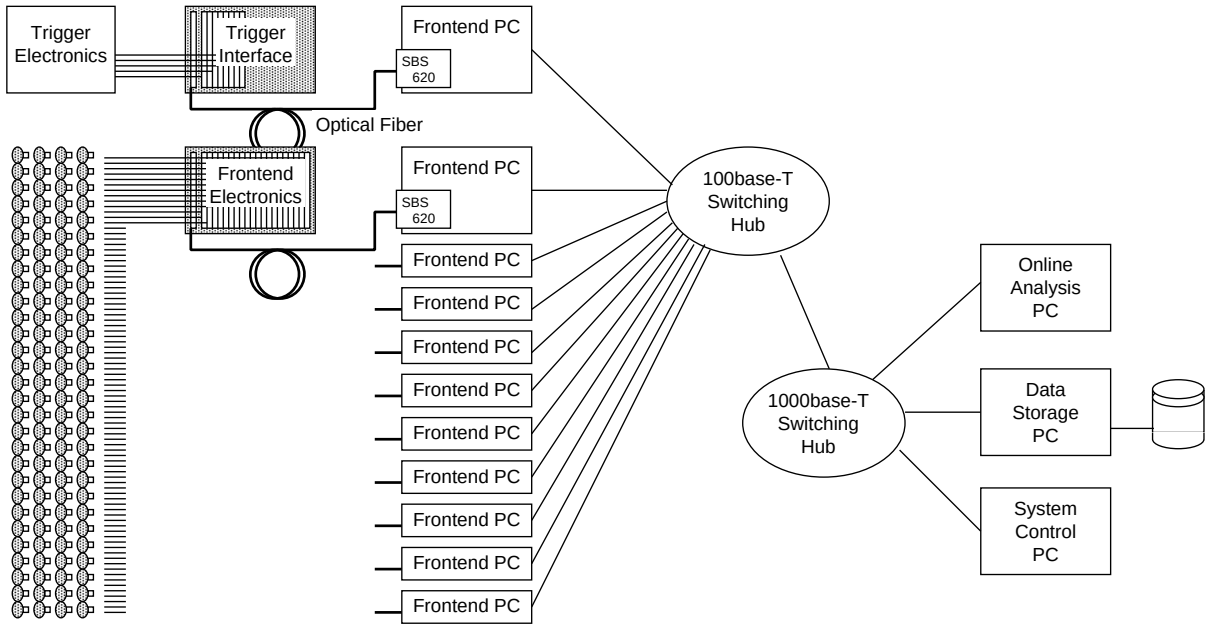

Figure 3.8: DAQ Computers and Networks

At KamLAND, total 15 VME crates are used, 10 for the FEE cards, 1 for the trigger circuitry, and 4 for the so-called MACRO electronics which was prepared as a backup of the main FEE electronics. Each VME crate is connected to one front-end PC through a pair of VME-PCI bus bridge cards and an 200m of optical fiber cable. The frond-end PC's are connected to back-end PC's with 100Base-T and 1000Base-T ethernet and network switches. Figure 3.8 shows the structure of the VME crates, computers and network. There are three back-end PC's, one for data processing, one for data recording, and one for system control.

Figure 3.9 shows the structure of data stream and component deployment over the DAQ PC's. Data on electronics devices are read by the Collector components which are configured with readout scripts. The data is then transported to a hub PC by the Transporter components, merged into one data stream by the Buffer component. From the buffer, the main data stream goes to the Recorder component through the Data Compressor component. The Data Compressor component compresses the waveform data by discarding redundant parts and by utilizing the Huffman encoding. The Data Compressor typically compresses the data blocks to 60$\sim$70% as small as the original size.

The data stream is branched at the buffer, for quick online analysis and realtime data monitoring. The trigger data records are analyzed by the Trigger Data Analyzer and the FEE data blocks are analyzed by the Online Data Analyzer. Since the analyzed trigger data is useful for on-site quick diagnosis, the analyzed data stream is branched at another buffer (Buffer 2), one goes to online data viewers and the other goes to Data Recorder after data filtering by the Trigger Data Filter component. Among these components, only the Trigger Data Analyzer, Online Data Processor and Data Compressor components were

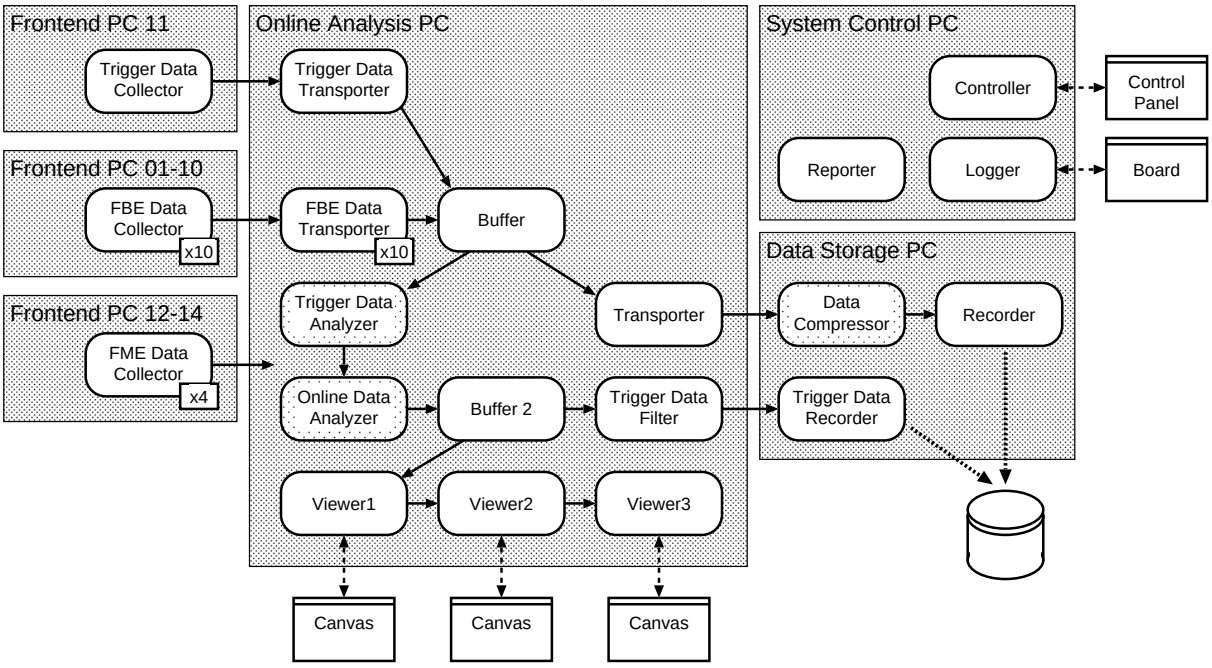

Figure 3.9: DAQ Software Structure (Component Deployment)

developed for KamLAND-specific purpose, and all other components are reusable generic components.

The front-end part of the DAQ system is able to transfer data blocks from the FEE electronics at about 10 MB/sec per VME crate. The overall system performance was measured to be around 30 MB/sec to 40 MB/sec, which is by far above the actual operation rate, about 3 MB/sec to 5 MB/sec. The current bottle neck is the network speed; the system performance can be further improved, by re-arranging the network topology and/or parallelizing data recording.

Figure 3.10 and Figure 3.11 are examples of collected events. The former one is a non-muon event and the latter one is a muon event. The figures show the distribution of hit time and hit charge of each PMT, obtained after event building and waveform analysis (details of which are described in Chapter 4).

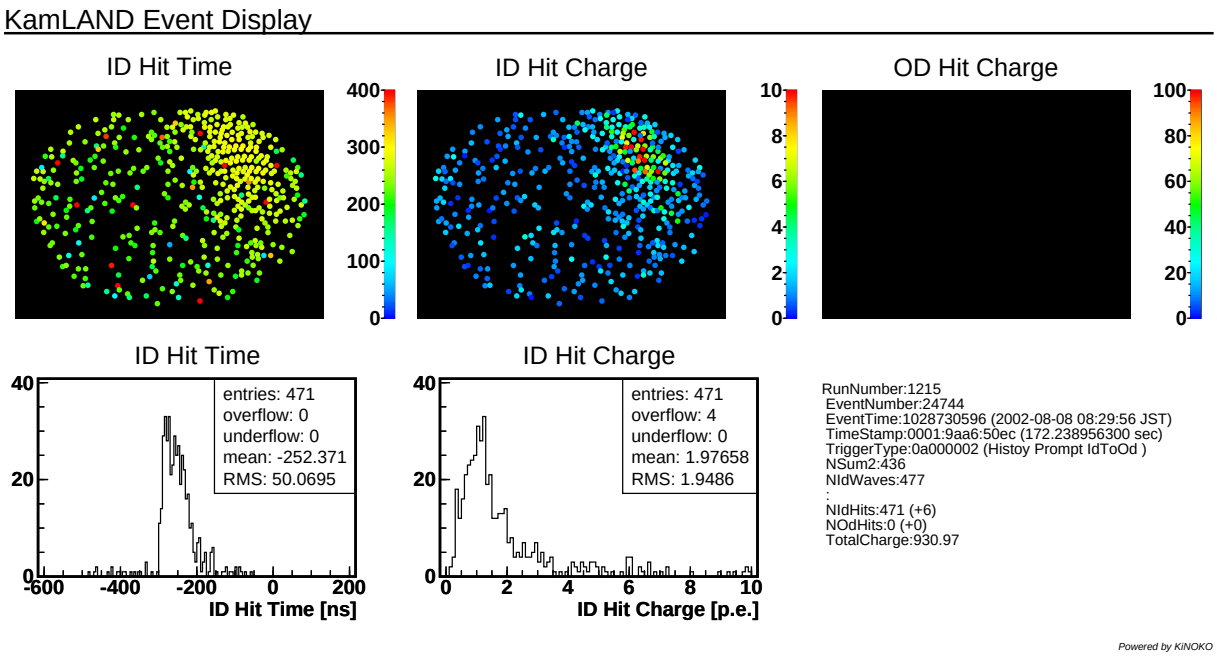

Figure 3.10: A Typical Non-Muon Event

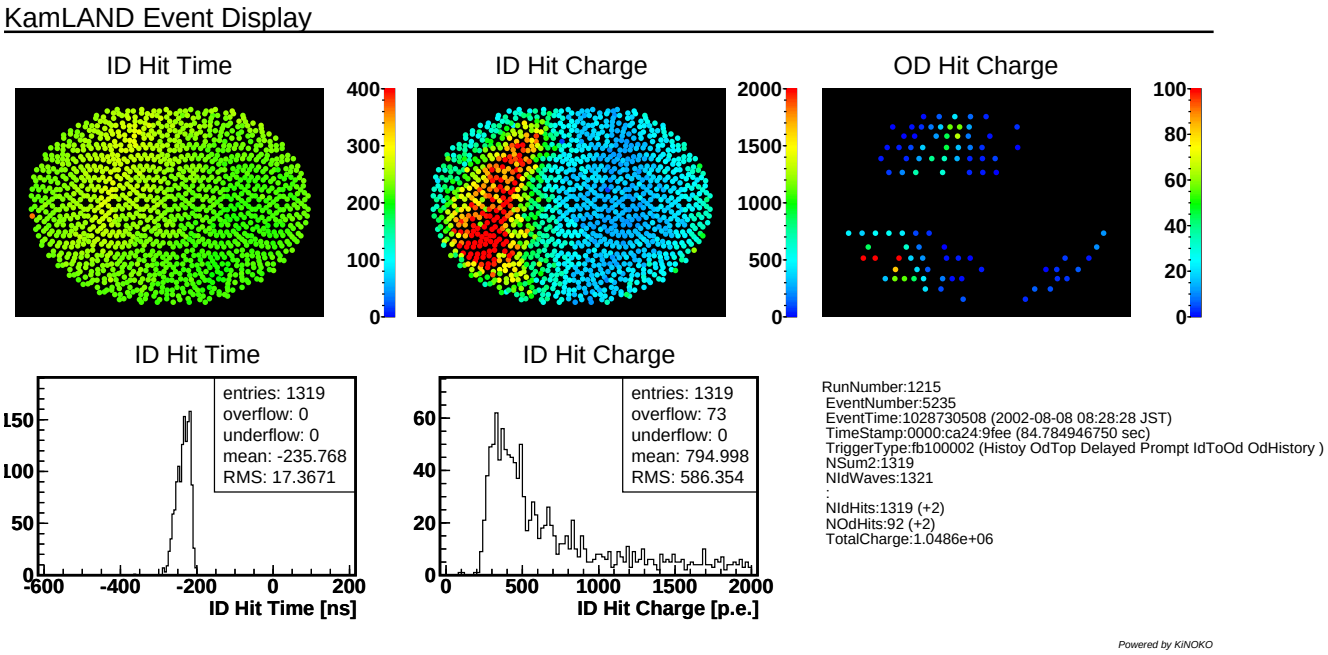

Figure 3.11: A Typical Muon Event

3.3 Calibration Equipment

For detector calibration, various devices are furnished in the ID and OD. The most important calibration device is the 'Z-axis deployment system', which places a variety of calibration signal sources, such as radioactive isotopes, LASER light diffuser and LED, along the vertical center axis of the detector (Z-Axis). Along the acrylic wall supporting frames, several LED's (Peripheral LED) are mounted. A full volume '4π' calibration system, which deploys calibration signal sources off-axis the detector, is under construction. As already discussed, the Front-End electronics equips a built-in pulser and 40MHz clock wave sources to calibrate every analog circuitry and digitizer channel.

The Z-axis deployment system places calibration signal sources through the chimney. The chimney is tightly shielded by a gate valve and a glove box that furnishes a transfer box for Nitrogen gas purging. The glove box is encompassed by a clean booth with pressurized clean air.

With the Z-axis deployment system, a LASER light source located at the center of the detector is used to calibrate PMT hit timing. Radioactive sources located at various positions along the Z axis provide essential data sets for vertex reconstruction and energy estimation. Table 3.1 lists the radioactive sources that are currently used at KamLAND. Level and decay structure diagrams of these isotopes are shown in Appendix D.

Table 3.1: Calibration Sources

Source Name	Decay Type	Visible Particle
^{60}Co	β	1.173 MeV γ + 1.133 MeV γ
^{65}Zn	EC	1.115 MeV γ
^{203}Hg	β	0.279 MeV γ
^{68}Ge	β^+	0.511 MeV γ $\times$2
^{241}Am/^{9}Be	^{9}Be$(\alpha, n)^{12}$C	neutron (+ 4.429 MeV γ)

Chapter 4

Event Reconstruction and Calibration

4.1 Event Building

The digitized PMT hit data (waveform data) is first stored in memories on the front-end electronics (FEE) cards, and then transfered to a buffer allocated on each front-end PC. The data blocks on each front-end PC are gathered into a data hub PC and then recorded on a storage device with trigger data blocks which come from another data stream. Consequently, data fragments consisting one event are dispersed throughout vast range of data stream. The event builder software sorts the data fragments and arranges data blocks in unit of event.

Each FEE card equips 32 MB of memory, and 200 FEE cards are used in total. Therefore waveform data fragments consisting one event can be apart from each other at distance of 6400 MB at most. To reduce loads of event building, the current DAQ software is configured not to transfer more than 8 MB from one FEE card at one readout cycle, however, the maximum distance is still 1600 MB. The independent data stream from the trigger circuitry and the buffers on the front-end PC's might result in further separation of trigger data records from corresponding waveform data blocks.

The event builder software manages this difficulty with a straightforward way; recent developments in the PC technology have barely enabled the event builder to place few GB of data blocks on silicon memory devices, hence the event builder simply searches and gathers data fragments by taking timestamp matches of the on-memory data blocks. Further development of the PC technologies will enable us to handle even larger data blocks, leading to better performance in data readout.

4.2 Waveform Analysis

The waveform analysis software extracts PMT hit information from recorded waveform data. The ultimate goal of the waveform analysis is to obtain lists of every photon hit time, and a number of attempts have been actually made to do this. However, difficulties

arise from the fact that the waveforms differ at each PMT and also differ with each hit within the same PMT. Non-linear responses of the PMT and electronics circuitry further increase the difficulty, and the finite waveform sampling interval introduces another kind of difficulties as well.

The current waveform analyzer extracts only the first photon arrival time and the total hit charge, where multi-hit information is inclusively handled within the total hit charge.

At the beginning of every run, 50 of pedestal waveforms, 50 of test-pulser waveforms, and 50 of 40 MHz clock waveforms are taken for every ATWD channel. The waveform analyzer first subtracts the pedestal waveform, and then search the first peak, by calculating the first and second derivatives of the waveform data. The first photon arrival time is then computed by fitting the leading edge of the first peak. The vertical scale of the waveform, which corresponds to voltage, is calibrated with the test-pulser waveforms, and the horizontal scale of the waveform, which corresponds to time, is calibrated with the 40MHz clock waveforms.

4.3 PMT Hit Corrections

The waveform analyzer extracts hit charge in terms of PMT output charge and hit time in terms of pulse arrival time at the FEE discriminator respect to the trigger time. The sampled charges are not exactly equal to the number of photo-electrons, due to fluctuations of the PMT gain, FEE amplifier gain, and signal attenuation in the cables and the FEE instruments. Similarly, the pulse rising times in waveforms are not exactly equal to the photon arrival time at PMT, due to fluctuations of the PMT response (transit time) and non-identicalness of channels, such as cable length.

PMT hit charge is calibrated at every PMT and at every ATWD chip on every run, by collecting single photo-electron hits, where single photo-electron hit signals are collected from low occupancy events (less than 180 hits out of 1325 17-inch PMT's), after applying essential event quality cuts and post-muon vetoes. Figure 4.1 shows an example of charge (waveform integration) distribution of low-occupancy events, focusing on one typical PMT channel. By fitting the single photo-electron charge peak, charge scale of the PMT/ATWD channel in the run is determined. After the gain correction, the hit charge is expressed in the unit of photo-electron (p.e.).

PMT hit time is calibrated with a LASER light source. Light from a 500 nm dye LASER flasher is led to a diffuser ball positioned at the detector center through a 230 m optical fiber cable. Light intensity is controlled with Neutral Density (ND) filters mounted between the LASER flasher and the optical fiber. In addition to the fiber to the diffuser ball, another optical fiber with the same length is connected to the LASER flasher, the other end of the fiber is connected to a monitor PMT, the output of which is led to a reference FEE channel. Triggers of FEE global acquisition are issued by the trigger circuitry on external timing signals from the LASER flasher.

Figure 4.2 shows an example of the measured timing offset as a function of hit charge. Due to slewing effects, extracted hit timings are biased by pulse heights. The relation is

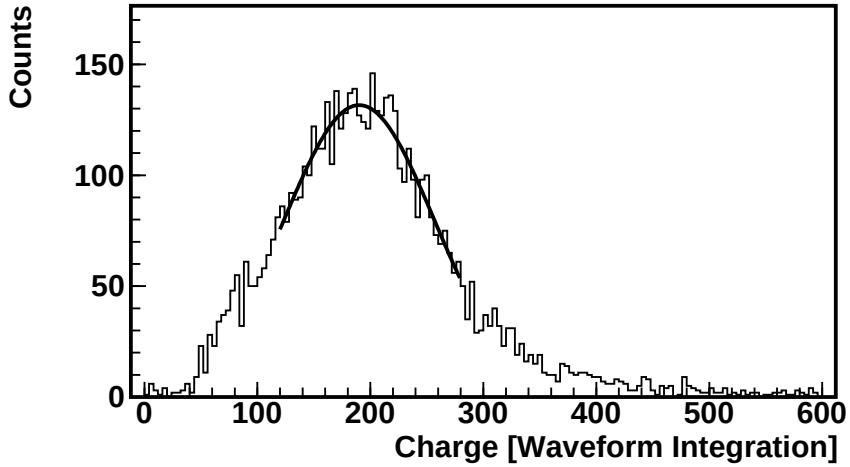

Figure 4.1: PMT Hit Gain Calibration (Single Photo-Electron Charge)

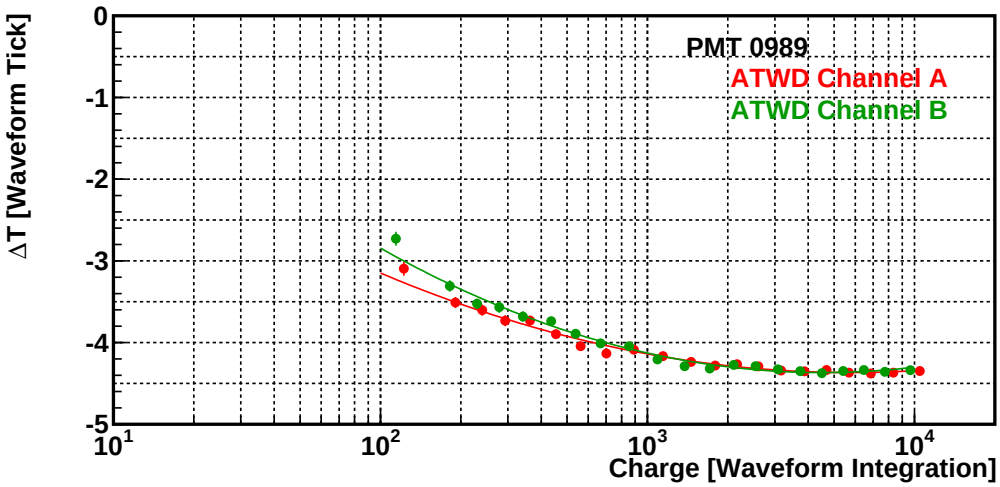

Figure 4.2: T-Q Correlation

fitted with a polynomial function of $\log_{10} Q$, defined as

$$\Delta T(Q) = P_0 + P_1 \cdot \log_{10} Q + P_2 \cdot (\log_{10} Q)^2 \tag{4.1}$$

where P_0, P_1 and P_2 are free parameters. P_0 represents the absolute timing offset induced by the PMT response, cable length etc., and P_1 and P_2 represent the slewing effect. The fit is made for each PMT and ATWD channel individually.

Figure 4.3 shows the distribution of hit time respect to the reference channel hit time, before and after the timing correction. The timing resolution is improved by the correction from 6.7 nsec to 2.0 nsec.

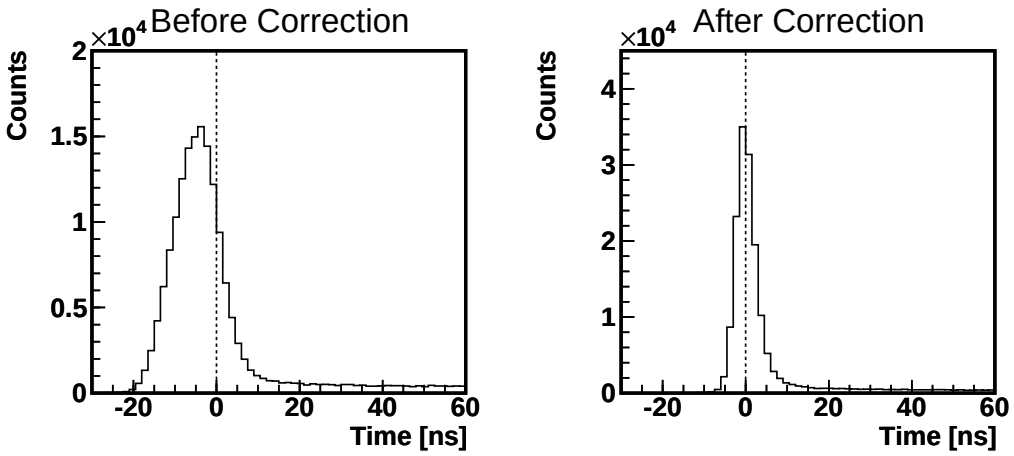

Figure 4.3: Hit Timing Correction

4.4 Muon Tracking

Events by cosmic muons are easily identified by their enormous light output in the inner detector (ID) by the scintillation and/or cherenkov light yield processes, and/or outer detector (OD) hits by the cherenkov light yield process. Figure 4.4 shows the distribution of the sum of ID hit charge and the sum of the number of OD hits. In the figure, three clusters are clearly seen; two clusters with large ID charge and large number of OD hits are those of muon events, the one with higher ID charge is muons passing through the liquid scintillator (LS), and the other one with lower ID charge is muons passing through only the mineral oil (MO) layer which surrounds the LS contained in the balloon. Muons passing through the LS yield both of scintillation light and cherenkov light, while muons passing through the MO emit only cherenkov light.

If the total ID charge is greater than 10000 p.e., we identify the event as a muon event. If the total ID charge is greater than 500 p.e. and the number of OD hits is greater than 5, we also identify it as a muon event. This criterion is shown in the Figure 4.4, indicated by a red dot line.

Tracks of muons passing through the ID are reconstructed based on PMT hit timings. In the LS, muons emit both of the scintillation photons and the Cherenkov photons. The direction of the Cherenkov photons respect to the muon track is fixed by physics processes to the Cherenkov angle $\cos\theta_c = 1/n$, which is determined only by the refractive index of the LS (n). On the other hand, the scintillation photons are emitted isotropically from each point of the muon track. However, the earliest scintillation photon trajectory, which is defined as the trajectory of photons that arrive at a PMT earliest, coincides with the trajectory of the cherenkov photons, as shown in Figure 4.5. This fact simplifies the muon tracking algorithm.

Based on the simple geometrical relations, muon tracks are reconstructed by finding a track that best reproduces the observed PMT hit time profile. The reflective index of the LS and MO are measured to be around 1.4 to 1.6 at all relevant wavelength, and position

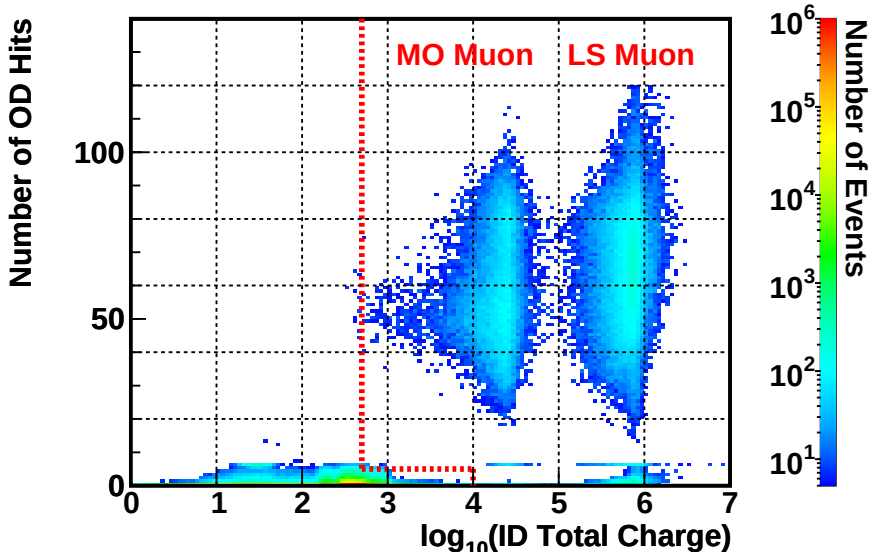

Figure 4.4: ID Charge and OD Hit Distribution

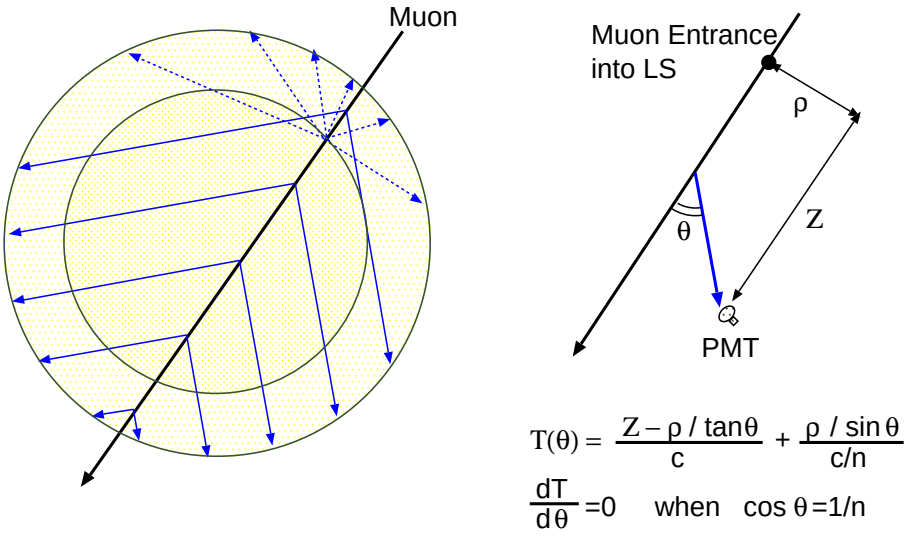

Figure 4.5: Muon Tracking; the Earliest Photon Trajectory

dependent speed of light parameterization is introduced to account for the difference in the reflective index between the LS and MO.

Muon tracks are poorly reconstructed in cases such that charge deposit of the muon is too small, the muon stops in the middle of detector, and/or multiple muons pass through the detector at the same time. Such muons are classified into 'mis-reconstructed muons', designating that the reconstructed tracks are not reliable. The ratio of mis-reconstructed

muons in all muons passing through the LS is about 0.2%.

Figure 4.6 shows the relation between the total ID PMT hit charge and the muon track impact parameter (distance to a muon track from the detector center) of well-reconstructed muons. Muons with ID charge greater than 10^5 p.e., which are considered to be LS muons, are mostly reconstructed with the impact parameter smaller than 650 cm, which corresponds to the LS sphere radius, and muons with ID charge less than 10^5 p.e. are reconstructed with the impact parameter greater than 650 cm. This fact indicates that the total charges and the reconstructed tracks are consistent with each other.

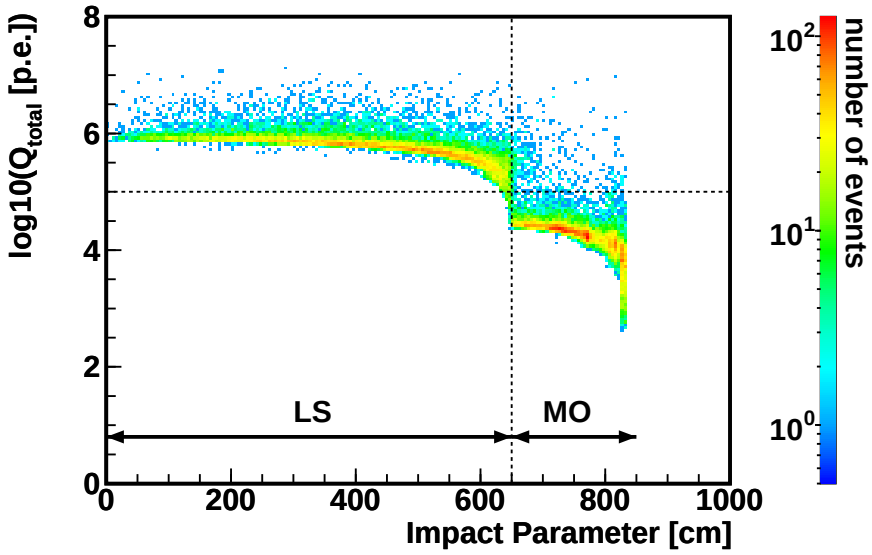

Figure 4.6: Relation between Muon ID Charge and Muon Track Impact Parameter

Figure 4.7 shows the relation between the reconstructed track length and the ID charge. The linear relation between the track length and the total ID charge seen in both of the MO muons and LS muons also demonstrates the validity of muon tracking. With the MO muons, which emit only cherenkov photons, the cherenkov charge per unit length $(dQ/dL)_{\mathrm{cherenkov}}$ is estimated to be 31.45 p.e./cm, by fitting the peak of the $Q_{\mathrm{total}}/L_{\mathrm{MO}}$ histogram. With the LS muons, which emit both of cherenkov photons and scintillation photons, the scintillation charge per unit length $(dQ/dL)_{\mathrm{scintillation}}$ is estimated to be 629.4 p.e./cm, by fitting the peak of the $(Q_{\mathrm{total}} - Q_{\mathrm{cherenkov}})/L_{\mathrm{LS}}$ histogram, where $Q_{\mathrm{cherenkov}}$ is obtained from the $(dQ/dL)_{\mathrm{cherenkov}}$ value estimated with the MO muons. These dQ/dL values are used to discriminate showering muons, which make larger charge deposit by electromagnetic cascade showers.

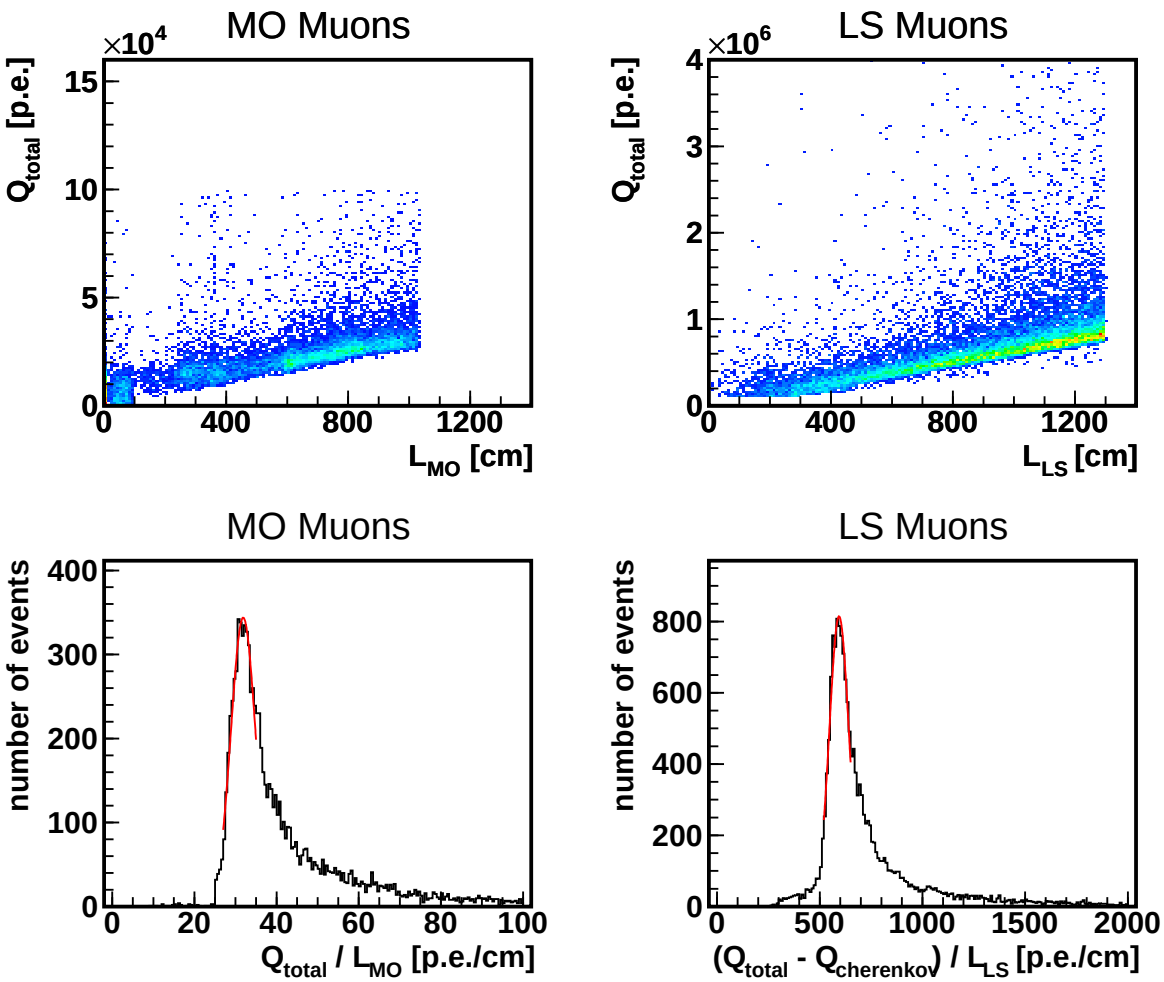

Figure 4.7: Muon Charge Deposits

4.5 Vertex Finding

Vertices of point-like events are reconstructed based on timing information of PMT hits. For an event occurring at position (x, y, z), the time of hit to a PMT labelled by i, T_i^{hit}, is related to the photon emission time t_i with the time-of-flight $T_i^{\text{flight}}(x, y, z)$ as

$$t_i = T_i^{\text{hit}} - T_i^{\text{flight}}(x, y, z) \tag{4.2}$$

For vertex finding, $\{T_i^{\text{hit}}\}$ is the set of observed data, (x, y, z) is the parameters to be determined. For a given vertex position (x, y, z), photon emission time t_i is calculated from corresponding PMT hit time T_i^{hit}. We use the set of t_i and their derivatives as test statistics to reconstruct the vertex.

Without the absorption/re-emission and reflection processes, the time of flight is di-

rectly calculated from the vertex position and the PMT position (x_i, y_i, z_i) as

$$T_i^{\text{flight}}(x,y,z) = \frac{\sqrt{(x-x_i)^2+(y-y_i)^2+(z-z_i)^2}}{c/n_{\text{eff}}} \tag{4.3}$$

where c is the speed of light in vacuum and n_{eff} is the effective refractive-index which inclusively represents all processes that affect to the average photon propagation speed. From (4.3), derivatives of t_i respect to the vertex position is obtained as

$$\begin{aligned} \frac{dt_i}{dx} &= -\frac{dT_i^{\text{flight}}(x,y,z)}{dx} \\ &= \frac{x_i - x}{c/n_{\text{eff}}\sqrt{(x-x_i)^2+(y-y_i)^2+(z-z_i)^2}} \end{aligned} \tag{4.4}$$

$$\tag{4.5}$$

The first step of finding vertices is to locate the position (x, y, z) that produces the smallest deviation of the set $\{t_i\}$ in each event, by iterating test vertex positions. However, the set of photon emission time $\{t_i\}$ does not converge into a narrow time window because of spread photon emission time spectrum of the LS (time constants of which range from ∼10 nsec to ∼100 nsec) and absorption/re-emission processes occurring around the vertices (which introduces ∼50 nsec of equivalent time constant).

Regardless of these processes, the distribution of t_i is independent from the distribution of dt_i/dx. This fact leads to another robust algorithm to locate vertices. For a given test vertex (x, y, z), the covariance of t_i and dt_i/dx that consist one event is calculated by

$$\begin{aligned} S_{t_i,\frac{dt_i}{dx}} &= \frac{1}{\sum_i w_i}\sum_i w_i \cdot (t - \langle t_i\rangle)\cdot\left(\frac{dt_i}{dx} - \left\langle\frac{dt_i}{dx}\right\rangle\right) \\ &= \frac{1}{\sum_i w_i}\sum_i w_i \cdot \left(t_i\frac{dt_i}{dx}\right) - \langle t_i\rangle\left\langle\frac{dt_i}{dx}\right\rangle \end{aligned} \tag{4.6}$$

where w_i is a weighting factor that is a function of photon traveling distance. The independence of $\{t_i\}$ and $\{dt_i/dx\}$ requires that $S_{t_i,\frac{dt_i}{dx}}$ be zero, and test vertices are iterated to find the position where this condition is satisfied.

Figure 4.8 shows the distribution of reconstructed vertices of ^{60}Co source located at various positions along the Z-axis. The vertex reconstruction resolution is found to be around 20 cm, and few centi meters of biases are seen. The vertex reconstruction biases were measured with various calibration sources located at various points of the Z-axis, as summarized in Figure 4.9. For sources located in the range from Z = −5.5m to +5.5m, the vertex bias is less than 5 cm at energies from ∼1 MeV (^{68}Ge, ^{65}Zn) to ∼8MeV (Am/Be).

4.6 Energy Estimation

Energies of events are estimated based on total charge of PMT hits, after applying a number of corrections. The quantity is called the 'visible energy', which is defined such

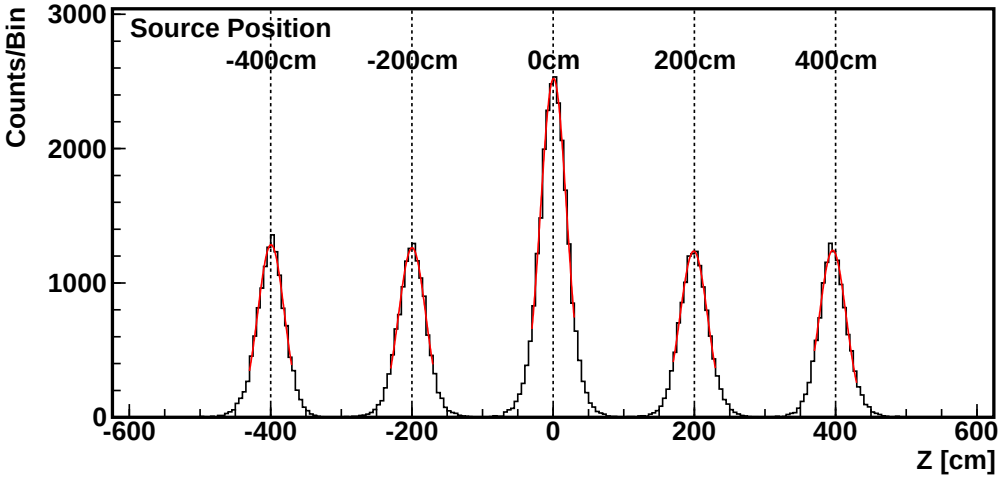

Figure 4.8: Reconstructed Vertex Positions of ^{60}Co Located along the Z-axis

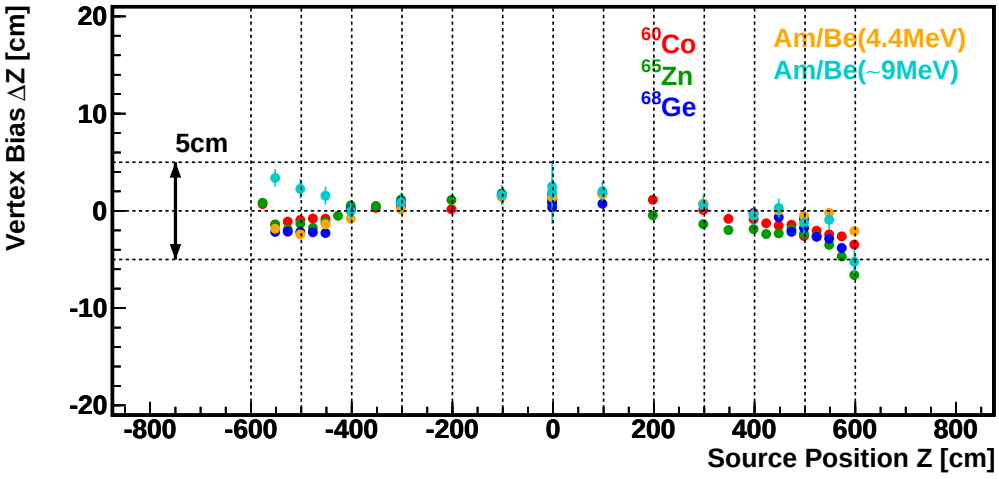

Figure 4.9: Vertex Reconstruction Bias

that visible energy of a 2.22 MeV gamma particle (emitted by neutron capture on proton) is 2.22 MeV and is proportional to photon yields in the LS. The visible energy is not exactly equal to the energy deposited into the LS, due to the non-linear quenching effects and contributions of cherenkov photons.

Visible energies are estimated by comparing sum of 'expected hit charge' Q_i^{expected} of PMT labelled as i with sum of actually observed hit charge Q_i^{observed} of PMT i, as

$$E_{\text{vis}} = E_0 \times \frac{\sum_i Q_i^{\text{observed}} - Q^{\text{dark-hits}}}{\sum_i Q_i^{\text{expected}}} \tag{4.7}$$

where $Q^{\text{dark-hits}}$ is the contribution from PMT dark hits, calculated from single hit rates. The constant factor E_0 is determined such that the 2.22 MeV gamma ray energy be 2.2 MeV of visible energy.

The expected charge is calculated from the vertex position with corrections of photon propagation processes.

$$Q_i^{\text{expected}} = \frac{e^{-L_i/\lambda}}{4\pi {L_i}^2}\ \eta_i\ \xi_i\ \cos\theta_i \tag{4.8}$$

where L_i is the distance from the vertex to the PMT i, λ is the light attenuation length, η_i is the light loss by shadowing of the balloon and balloon supporting ropes, ξ_i is the threshold effect of the FEE channel discriminators, and θ_i is the light incidence angle on the PMT.

The shadowing of the balloon and balloon supporting ropes are first modeled with the geometrical information and then calibrated with ^{60}Co source calibration data. Since the balloon supporting ropes are denser at the top and the bottom region than the equator region, this correction in particular betters Z-dependent deviations. Shadowing of the balloon and some other component of the detector have slight time dependence. This time dependence is traced with weekly conducted ^{60}Co calibration data.

The light attenuation length λ is measured with ^{65}Zn calibration data, with varying the source position along the Z axis from -5.5 m to $+5.5$ m. After applying the corrections of the shadowing effect, threshold effect and incident angle to PMT, the charge distribution as a function of distance L is fitted with an exponential curve, resulting in the estimated attenuation length to be 22 m.

Even after applying all these corrections, small time-dependent variation of energy estimation remains (note that the PMT gains and PMT dark hit rates are calibrated on every run). This variation is traced and corrected by looking at the ^{40}K peak (1.46 MeV gamma) which is seen in the single energy spectrum. After this correction, the time variation of visible spectrum, which is measured with the 2.2 MeV gamma rays emitted by neutron capture on proton, is less than 1.3% throughout the dataset.

Figure 4.10 shows the reconstructed visible energy spectrum of various calibration sources. Table 4.1 summarizes the estimated visible energy and its resolution for each calibration sources, as well as visible energy of other mono-energetic gamma ray sources by neutron capture reactions. The energy resolution is estimated from this result to be $7.25\%/\sqrt{E_{\text{vis}}/[\text{MeV}]}$. Figure 4.11 shows the estimated visible energies of sources located at various positions along the Z-axis. The position dependence of the estimated visible energy is less than 0.8% over Z=$-$600cm to 600cm, except for ^{208}Hg.

4.7 Energy Scale

The visible energy, which is proportional to photon yield of the LS, is not exactly equal to the energy deposited in the LS, due to non-linear quenching effects of the LS and contribution of cherenkov photons.

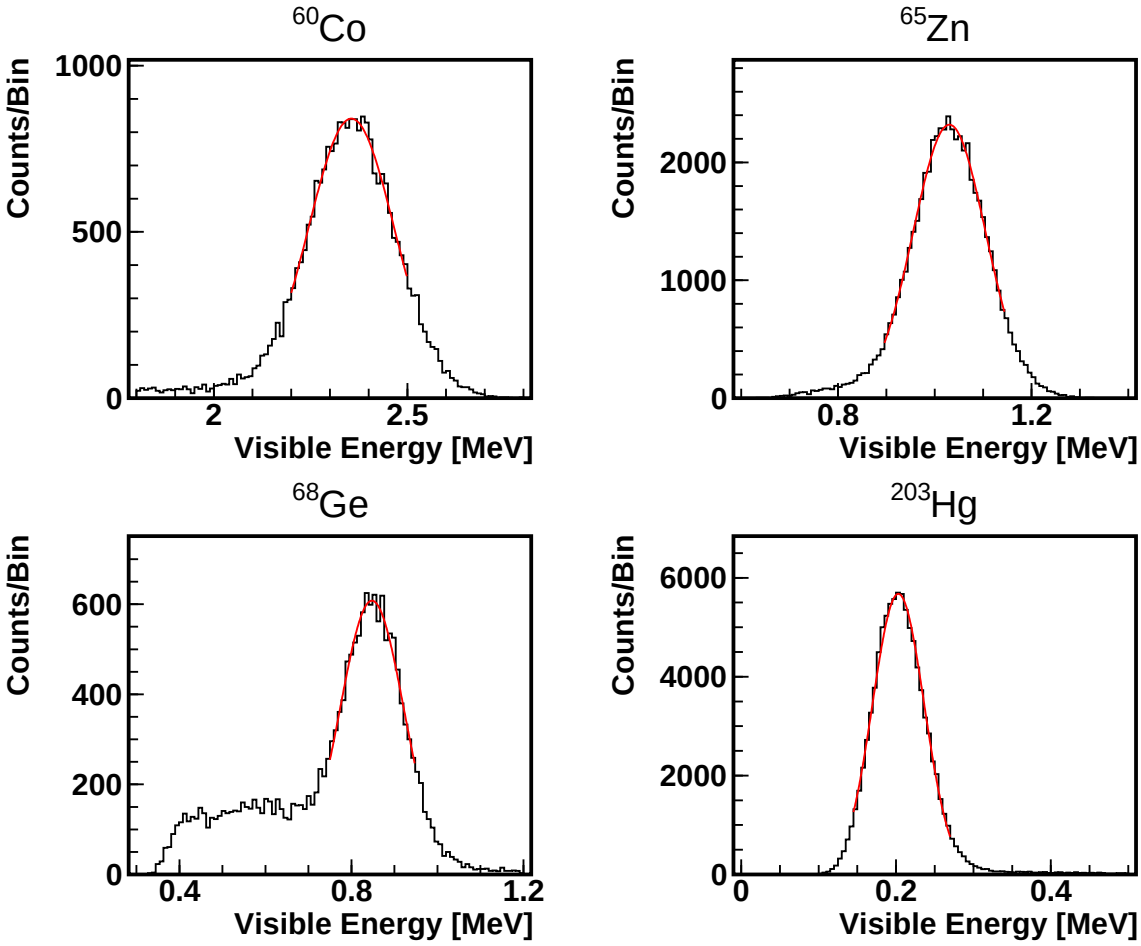

Figure 4.10: Visible Energy Spectrum of Calibration Sources

Table 4.1: Estimated Visible Energies of Calibration Sources

Source	Gamma Energy [MeV]	Visible Energy [MeV]	Resolution [MeV]
^{60}Co	1.173 + 1.333	2.346	0.112
^{65}Zn	1.116	1.021	0.073
^{68}Ge	0.511 × 2	0.846	0.072
^{203}Hg	0.279	0.197	0.036
$np \rightarrow D\gamma$	2.225	2.211	-
$n^{12}\mathrm{C} \rightarrow^{13}\mathrm{C}\gamma$	4.947	5.061	-

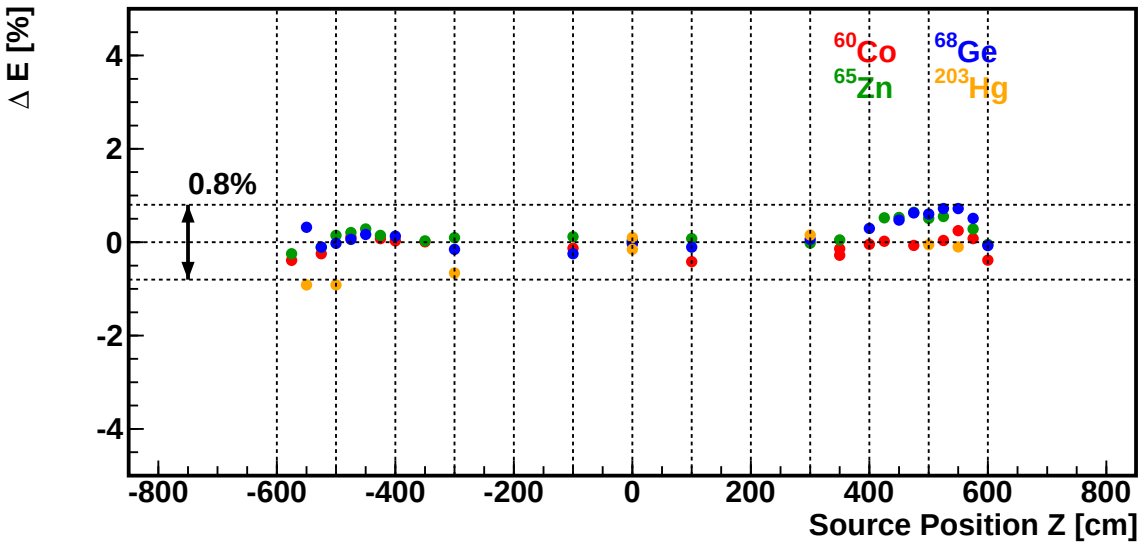

Figure 4.11: Position Dependence of Visible Energy Estimation

Quenching is an effect caused by saturation of energy passing to the LS on ionization processes, and results in reduced photon yield. The relation is expressed as a function of energy deposition dE/dx by the Birk's formula, as

$$\Delta E_{\text{vis}} = \frac{A}{1 + k_b \frac{1}{\rho}\frac{dE}{dx} + C\left(\frac{1}{\rho}\frac{dE}{dx}\right)^2 + \ldots} \Delta E \tag{4.9}$$

or as a simplified formula,

$$\Delta E_{\text{vis}} = \frac{A}{1 + k_b \frac{dE}{dx}} \Delta E \tag{4.10}$$

where k_b (and C) are the Birk's constants determined by characteristics of LS, ρ is the density of the LS, A is a factor to convert photon yield to estimated energy. As a natural consequence of saturation, the quenching effect increases as energy deposition density increases (which is related to large mass and/or charge). The quenching factor of ~ 5 MeV alpha particles reaches $\sim 1/10$, while that of 5 MeV electron is only a few percents.

In the energy ranges related to the geo-neutrino analysis, cherenkov photons are emitted only by electrons and positrons. Due to low optical transparency of the LS at the wavelength of cherenkov photons, most of cherenkov photons are absorbed in the LS. However, photons re-emitted from the LS following cherenkov photon absorption make significant contribution to the total charge. Since the absorption/re-emission processes are involved, the estimation of cherenkov photon contribution is not obvious.

The total photon yield (i.e., the visible energy) is expressed by sum of scintillation

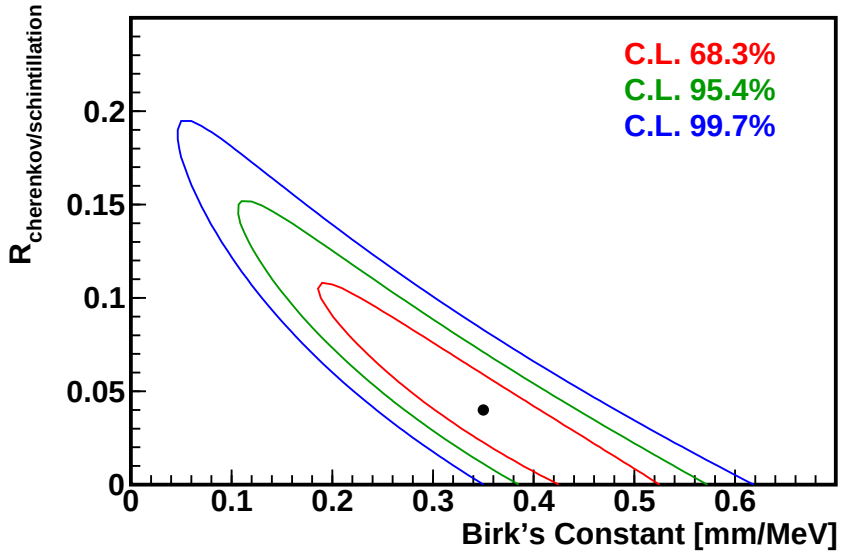

Figure 4.12: Energy Scale Parameter Determination

photon contribution and cherenkov photon contribution,

$$\begin{aligned} \Delta E_{\rm vis} &= \left(A_{\rm sci} \cdot \frac{dN_{\rm sci}}{dE} + A_{\rm ch} \cdot \frac{dN_{\rm ch}}{dE} \right) \Delta E \\ &= A \left\{ \frac{1}{1+R} \cdot \frac{1}{1+k_b \frac{dE}{dx}} + \frac{R}{1+R} \cdot \frac{dN_{\rm ch}}{dE} \right\} \Delta E \end{aligned} \tag{4.11}$$

where $N_{\rm sci}$ and $N_{\rm ch}$ are the numbers of scintillation and cherenkov photons, $A_{\rm sci}$ and $A_{\rm ch}$ are normalization parameters to be determined. Effects of cherenkov photon absorption/re-emission is parameterized within $A_{\rm ch}$.

Except for the absolute scaling parameter A, which is adjusted in a way that the visible energy of 2.2 MeV gamma rays be 2.2 MeV, there are two parameters to be determined; the ratio of scintillation photons and cherenkov photons R, and the Birk's constant k_b. The source calibration data listed in Table 4.1 are used to fix these parameters.

Calculation of energy deposition (dE/dx) in the LS is not trivial because gamma rays themselves do not directly ionize the LS; the correct energy deposition is obtained only by tracing all the gamma particle scattering on electron, electron-positron pair creation, and photo-electron effects. This calculation is done with a Monte-Calro (MC) simulation program, constructed on the GEANT4 simulation package distributed from CERN. The MC program is used only to simulate the interactions of gamma rays and the processes of electron/positron energy loss. Photon yield is calculated from the simulation results with (4.11).

By fitting the observed visible energies of the calibration sources to the photon yield formula (4.11) and the energy deposit simulation, the Birk's constant k_b and the scintillation/cherenkov photon ratio parameter R are determined as shown in Figure 4.12. The

best fit of these parameters are found to be 0.35 mm/MeV and 0.04, respectively. Figure 4.13 shows the ratios of visible energy (photon yield) and real energy (energy deposition) as a function of real energy, for gamma, electron and positron respectively, which are calculated from the determined parameters. In the figure, the bundle of green lines shows the 1-σ error region, and the black lines at the center of the green line bundle indicate the best-fit $E_{\mathrm{visible}}/E_{\mathrm{real}}$ relation. Figure 4.14 shows the error of energy estimations of several gamma ray sources, after applying the gamma ray energy scale. The dot lines in the figure shows the error range, calculated from the errors of visible energy estimation (time and position dependence) and the errors of energy scale parameters (cherenkov/scintillation ratio and Birk's constant). The error is about 2% at the all relavant energy range.

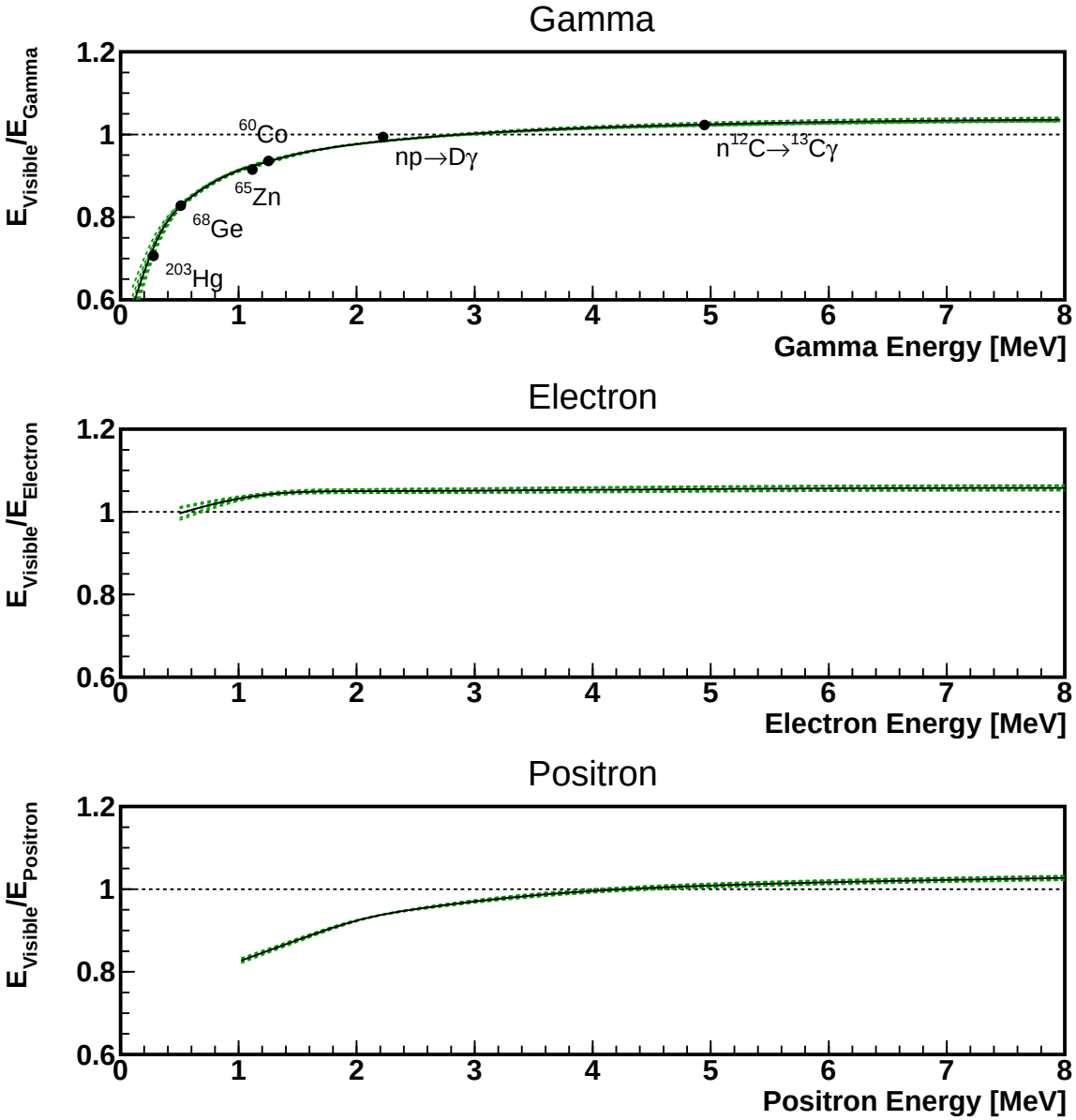

Figure 4.13: Energy Scale. Conversion factors from *real* energy to visible energy are shown for the gamma particle, electron and positron respectively. The conversion factors are calculated from the determined energy scale parameters (cherenkov/scintillation photon yield ratio and the Birk's constant). The green lines show the best fit point and the bundles of black dot lines show the 1-σ error range. The positron energy includes energy of two 0.51 MeV gamma particles emitted after electron-positron annihilation.

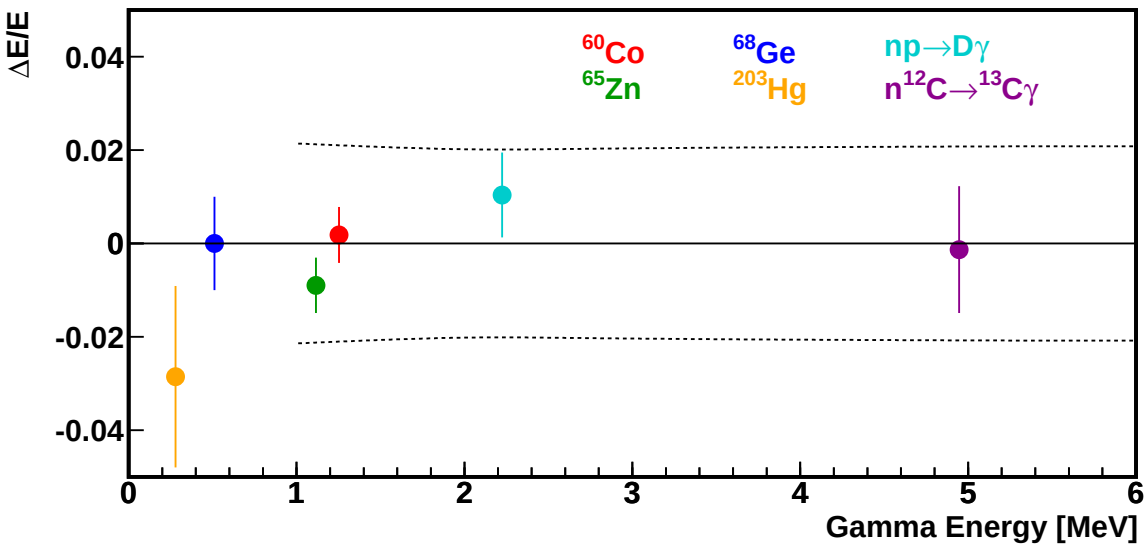

Figure 4.14: Energy Estimation Error

Chapter 5

Event Selection

5.1 Event Selection Outline

As discussed in Chapter 2, the energy range of geo-neutrinos extends from 0 MeV to 3.3 MeV. As discussed in Chapter 3, we detect geo-neutrinos by the reaction of $\bar{\nu_e}p \rightarrow e^+n$, energy threshold of which is 1.8 MeV. The reaction makes two correlated signals. The first signal, prompt signal, is made by the positron and two 0.51 MeV gamma particles generated by annihilation of the positron. The second signal, delayed signal, is made by a 2.2 MeV gamma particle, which is emitted in subsequence of thermal neutron capture on proton. This thermalization and capture process take about 200 μsec, and positions of neutron capture are typically 30$\sim$50 cm apart from the neutrino reaction vertices.

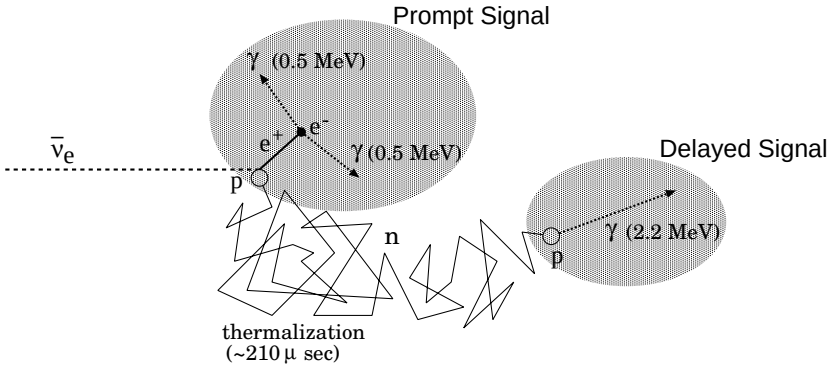

These correlated signals are tagged by the means of delayed coincidence method. We search pairs of signals that occur within short interval (order of neutron thermalization and capture time) and within short distance (order of thermal neutron disperse). We also confine events to those with 2.2 MeV delayed signals.

Cosmic muons are a major source of backgrounds. Not only generate unstable isotopes, but also they disturb the detector for a certain span. The detector is vetoed for a period after muons. Details of muon induced backgrounds, as well as all other backgrounds, are discussed in Chapter 6.

5.2 Dataset Summary

In this analysis, data collected at KamLAND between March 12 2002 and January 12 2004 is used. The total length of physics runs after basic run quality cuts is 574 days, which corresponds to 85.5% of the calender time, 671 days.

5.3 Good Run Selection

Not all of collected physics data are appropriate for physical data analysis; fails of readout electronics circuit might affect recorded signals, mis-operations could result in improper detector configuration, and external troubles such as power fail may seriously affect the detector condition. If such troubles are noticed by operators, as usually the case, the condition is recorded in a database and such runs are not used for physics analysis.

Some of those troubles are not recognized by operators. To reject those runs, quality of collected data is examined in prior to physics analysis, and if any anomaly is found in the data, the run or the part of the run is discarded.

The quality of data is examined in several aspects. First of all, runs shorter than 6 minutes are discarded, unless a good reason of taking such short run is provided; it is empirically known that operators frequently do not leave any comments for short test runs.

One of the most essential parameters to monitor the detector condition is the trigger rate. For both of the inner detector (ID) and the outer detector (OD), trigger rate is monitored throughout the run, and if any unusual condition is found, the run or that part of the run is discarded. The trigger circuitry is *disabled* for few milli seconds if the buffers in the trigger data stream become full. The trigger disable is not abnormal itself, and occurs few times a day. However, too frequent trigger disable could be a sign of abnormal detector condition, thus we also monitor the rate and length of trigger disables and use it as a run selection criterion. Trigger rate monitoring is in particular effective to find a flusher PMT and/or electronics malfunction.

We also monitor the condition of every PMT channel, in a way described later. If the number of channels judged to be wrong is low, as usually the case, we just disable the channels; otherwise we discard the whole run. Increase of faulty channels often forms a cluster, such as all channels connected to one readout card, all PMT channels connected to one HV supply, etc. Hence monitoring faulty channels is especially useful to detect fails of the readout cards and/or HV supply devices.

Condition of PMT channels is examined by basically looking at hit rates. For each ID PMT channels, we calculate the frequency of channel hits in non-muon events, muon events, and all events. The ratio of the ATWD-A channel hits and the ATWD-B channel hits is also examined for each PMT channel. Channels with too high charge output are scanned by comparing hit charge of muon events with that of neighbor channels. Frequency of zero-charge hits is also used to test the channel. For the OD channels, we use frequency of hits in all (muon) events.

In addition to the criteria described above, we test quality of run by looking at event

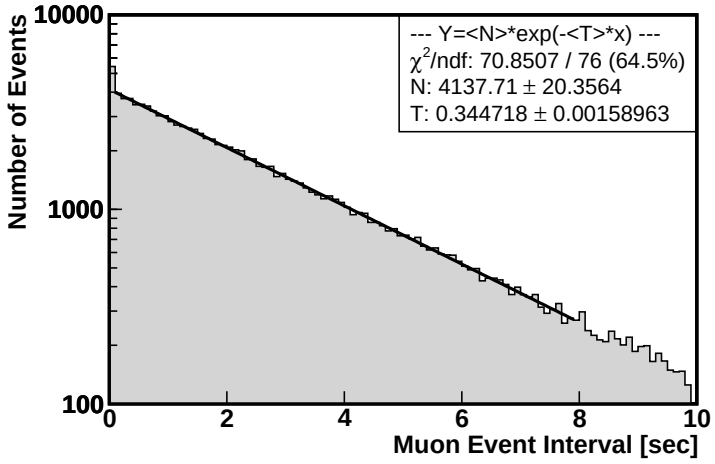

Figure 5.1: Muon Event Interval

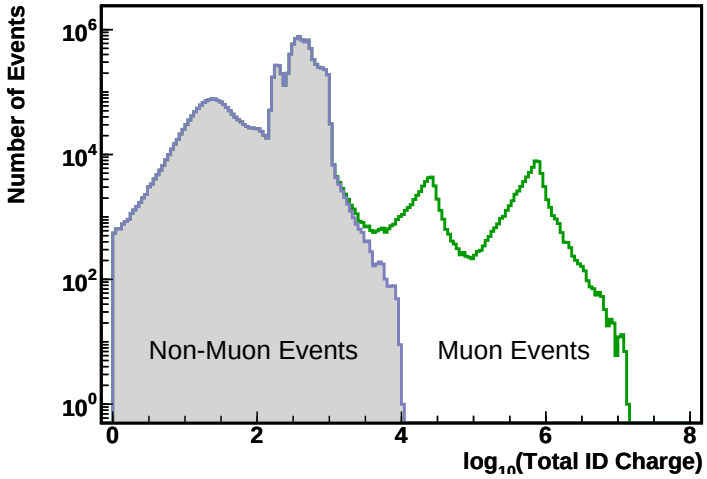

Figure 5.2: ID Charge Distribution before/after the Muon Cut

rate with energy 1.5 MeV to 10 MeV, and muon event rate.

5.4 Cosmic Muon Event Cut

As discussed in Section 4.4, cosmic muon events are easily identified by their enormous light output and/or OD hits. With the same muon selection criteria as presented in Section 4.4, muon events are identified and rejected from the neutrino event candidates.

Figure 5.1 shows the distribution of intervals between two muons. The rate of muons that pass through the detector is estimated from the interval distribution to be 0.34 Hz. Figure 5.2 shows the distribution of ID charge, before and after the muon event cut.

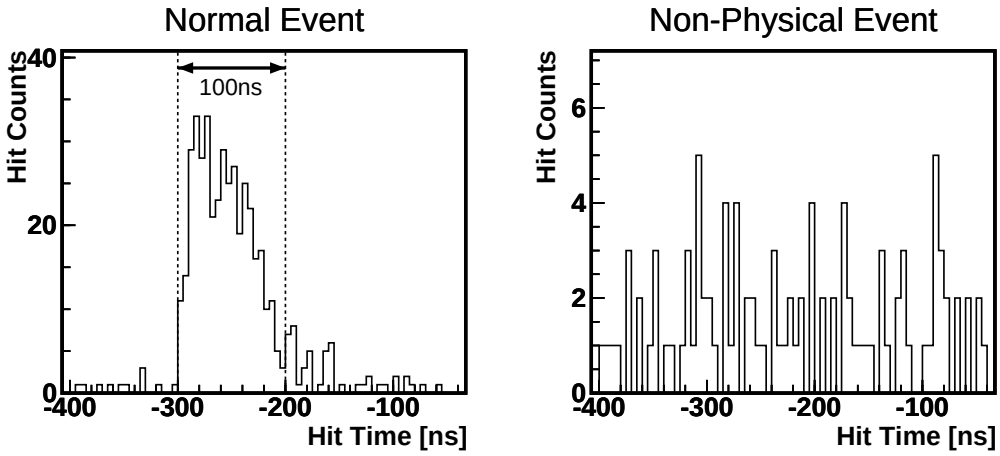

Figure 5.3: PMT Hit Time Profile of a Normal Event and a Non-Physical Event

5.5 Good Event Selection

In prior to event reconstruction, we apply a basic cut to reject non-physical events. Non-physical events are characterized by their abnormal PMT hit time distribution, as shown in Figure 5.3. A point-like vertex single physics event should have PMT hits distributed within about 100 nsec time window, which roughly corresponds to photon travel time throughout the detector, including the effect of photon absorption and re-emission. As shown in the figure, events identified as non-physical are lacking in this feature.

Behavior of the readout electronics after muon is suspected as a cause of such non-physical events. A huge pulse of muon might impact the readout circuit too severely, and/or large overshoots and undershoots following a muon hit might influence its functionality. In actual fact, such non-physical events are concentrated within short periods after muon hits (Figure 5.7).

To select such non-physical events, we introduce a parameter Nhit_{100} that represents the number of hits within 100 nsec time window. The 100 nsec time window is adjusted for each event in order that that maximum number of hits are contained within the window. Figure 5.5 shows the distribution of the number of hits within the 100 nsec window (Nhit_{100}) v.s. the total number of hits (Nhit). Non-physical events are clearly separated on the plane. We reject such events by requiring $\mathrm{Nhit}_{100} > \frac{1}{2}(\mathrm{Nhit} + 50)$, which is shown with a solid line in the figure.

As described below, we apply 2 msec veto after every muon, which effectively suppress those non-physical events. Also as described later, we use only events with Nhit greater than or equal to 200. After those cuts, the ratio of non-physical events is 0.0002%. Thus inefficiency incuded by the non-physical event cut is 0.0002% at most. Figure 5.5 shows the distribution of ID charge before and after the non-physical event cut.

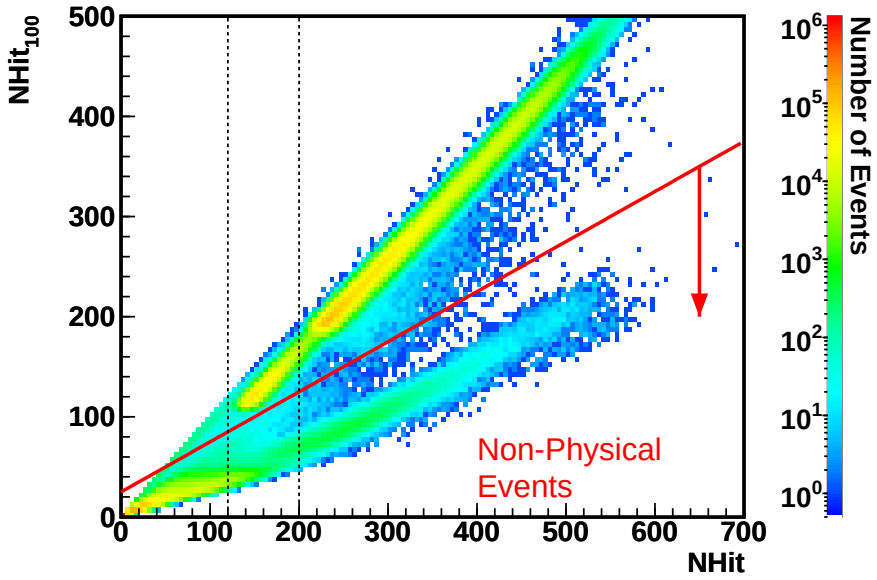

Figure 5.4: Hit Time Distribution: Nhit_{100} v.s. Nhit

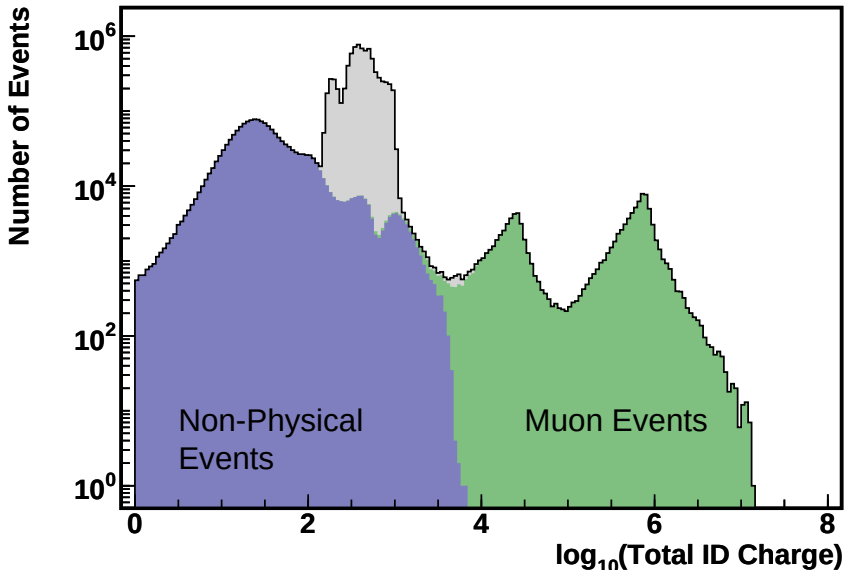

Figure 5.5: ID Charge Distribution before/after the Non-Physical Event Cut

5.6 Muon Spallation Cut

5.6.1 Muon Veto

Interactions between cosmic muons and nuclei in the LS generate neutrons, which are then captured on a proton and make 2.2 MeV gamma ray signal. If more than two neutrons

generated by one muon are detected, they could be mis-identified as a neutrino event, because of spatial and timing correlation of these signals.

After a muon event, significant number of readout electronics channels are occupied by multiple signals within a short period following a muon, despite of the dual waveform digitizer composition. A/D conversion and data transportation of one waveform takes about 25 μsec. If amplitude of a signal is such large that all three gain channels are triggered, the signal processing takes about 75 μ sec at most. Hence multiple signals following muons could occupy readout channels upto several hundred micro seconds. Signals arrive at the FEE during this period are not acquired, and become "missing waveform", resulting in possible bias to event reconstruction. Figure 5.7 shows the time distribution of such missing waveform events, identified by comparing the number of digitized waveforms and the number of PMT hits recorded by the trigger circuit.

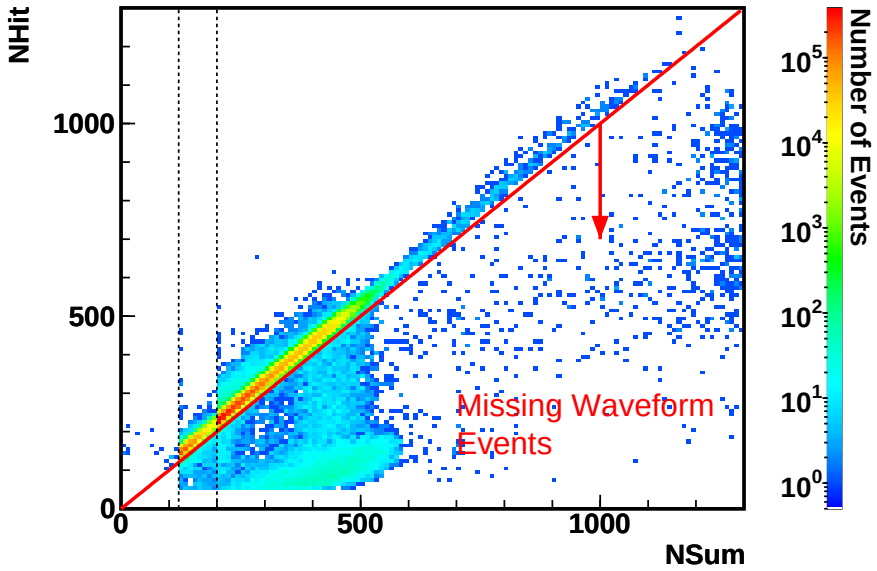

Figure 5.6: Missing Waveform Events after Muon

To avoid these problems, we veto the whole detector for 2 msec. As discussed in Chapter 6, neutron capture time in the KamLAND LS is about 200 μ sec, hence the 2 msec veto sufficiently reduce the muon induced neutrons. Figure 5.8 shows energy spectra before and after the 2 msec veto. A peak at 2.2 MeV seen in the "before veto" spectrum vanishes in the "after veto" spectrum. The dead time introduced by this veto is 0.07%, as directly calculated from the measured muon rate 0.34 Hz.

5.6.2 Spallation Veto

Interactions between cosmic muons and nuclei in the LS produce not only neutrons but also a variety of unstable isotopes. Most of them have as short halflife as few milli seconds,

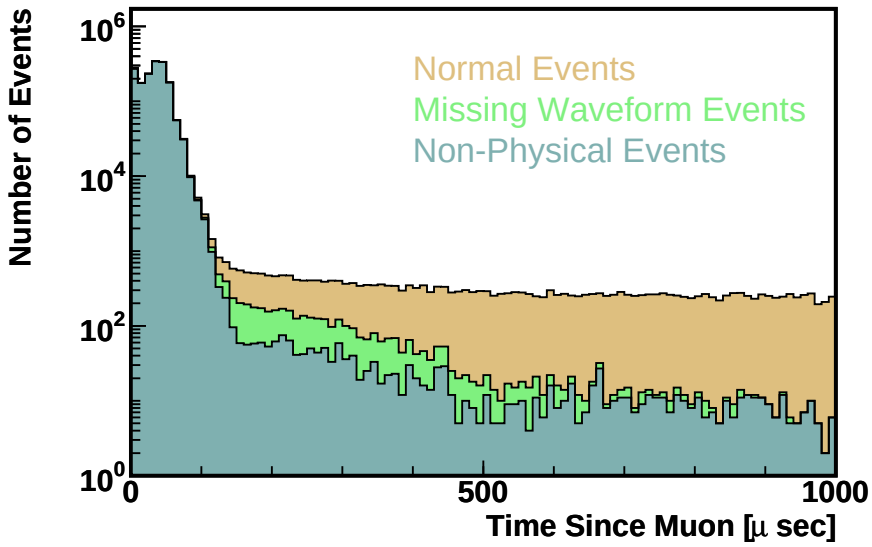

Figure 5.7: Missing Waveform Events after Muon

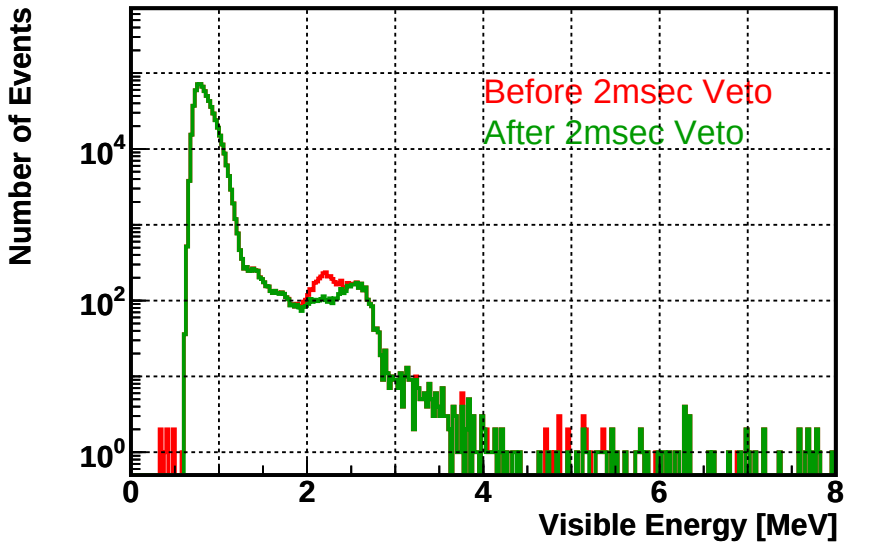

Figure 5.8: Energy Spectra before/after Muon 2msec Veto

and some of them have rather long lives, such as ^{11}Be ($\tau_{1/2}$=13.8 sec), ^{11}C ($\tau_{1/2}$=10.4 min), ^{10}C ($\tau_{1/2}$=19.3 sec), and ^{7}Be ($\tau_{1/2}$=53.3 day).

Among those muon spallation products, the most serious background source is ^{9}Li ($\tau_{1/2}$=0.18 sec) and ^{8}He ($\tau_{1/2}$=0.12 sec), which emit neutrons in their decay process. Decays of ^{9}Li and ^{5}He with neutron emission almost perfectly mimic neutrino events,

with prompt signals by beta decays of ^{9}Li/^{8}He itself, and delayed signals by capture of emitted neutron on proton. We apply vetoes to reduce these backgrounds to a tolerable level.

Some of muons passing through the detector make cascade showers, initiated by high-energy gamma rays. As will be quantitatively discussed in Chapter 6, such showering muons produce considerably more ^{9}Li and/or ^{8}He than non-showering muons do. Therefore we apply two different vetoes, one to showering muons and the other to non-showering muons separately; we veto the whole detector for 2 sec after showering muons, and we partially veto the detector along muon tracks for 2 sec after non-showering muons. The partial volume veto is applied only to delayed events with vertices within 3 m distance from muon tracks. If muon tracks are poorly reconstructed, we apply the whole volume veto. If muon tracks are outside the LS, which is judged by total charge to be less than 4.0×10^4 p.e. (see Chapter 4), we do not apply the spallation veto.

Discrimination of showering muons is performed based on residual charge $Q_{\rm res}$, which is defined as excess of charge deposit from the sum of minimum ionization charge deposit and equivalent charge of cherenkov light emission;

$$Q_{\rm res} = Q - \left\{ L_{\rm LS} \cdot \left(\frac{dQ}{dL}\right)_{\rm ionization} + (L_{\rm LS} + L_{\rm MO}) \cdot \left(\frac{dQ}{dL}\right)_{\rm cherenkov} \right\} \tag{5.1}$$

where $L_{\rm LS}$ and $L_{\rm MO}$ is length of a muon track in the LS and MO respectively, $\left(\frac{dQ}{dL}\right)_{\rm ionization}$ is the photon yield per unit length by the ionization process in the LS, and $\left(\frac{dQ}{dL}\right)_{\rm cherenkov}$ is the photon yield per unit length by the cherenkov process. $\left(\frac{dQ}{dL}\right)_{\rm ionization}$ and $\left(\frac{dQ}{dL}\right)_{\rm cherenkov}$ are estimated to be 629.4 p.e./cm and 31.45 p.e./cm, respectively (Section 4.4).

Figure 5.9 shows the distribution of the residual charge. We define showering muons as muons with residual charge more than 10^6. The rate of showering muons is estimated from the data to be 0.02 Hz, which introduces 4% of dead time.

We also apply the 2 sec whole volume veto after every *trigger disable* period, as well as start of run and any similar circumstances, since we do not know the physical context of the period.

5.7 Fiducial Volume Selection

As demonstrated in Chapter 4, events within 5.5 m radius from the balloon center are reconstructed within 2% energy estimation error and 5cm vertex finding error. However, the region near the ballon suffers from gamma rays from external sources, such as ^{40}K on the balloon and/or balloon supporing ropes, ^{210}Tl in the stainless tank, PMT, and/or surronding rocks. As discussed in Chapter 6, the rate of accidental coincidence in this region is considerably high, enough to hide the tiny geo-neutrino signals.

Figure 5.10 shows single event energy spectra for several radii of fiducial volumes. Figure 5.11 shows radial distribution of single events. As shown these figures, event rate is rapidly reduced as the radius of fiducial volume decreases.

As discussed in Chapter 6, the accidental coincidence rate in the 5.5 m radius fiducial volume is estimated to be 10.1 events/livetime, and that in the 5.0 m radius fiducial

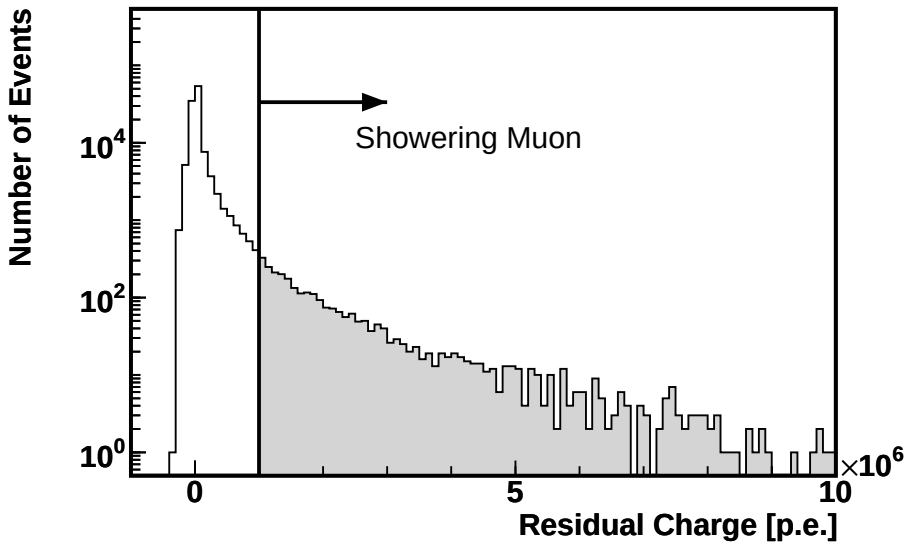

Figure 5.9: Muon Residual Charge Distribution

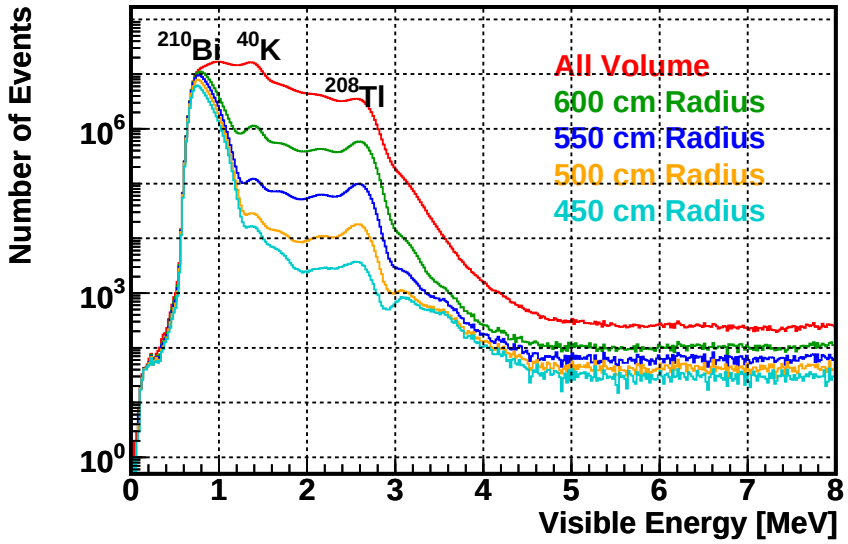

Figure 5.10: Single Event Spectra for Several Radii of Fiducial Volume

volume is 1.62 events/livetime. Comparing with the expected geo-neutrino signal, about 10 events/livetime, we decide on the fiducial volume to set 5 m radius.

As shown in the Figure 6.18 in Chapter 6, accidental coincidence events are also concentrated along the center Z axis. Until 19 April 2004, three thermometers have been placed along the Z axis, and these events are caused by radioactive material in the ther-

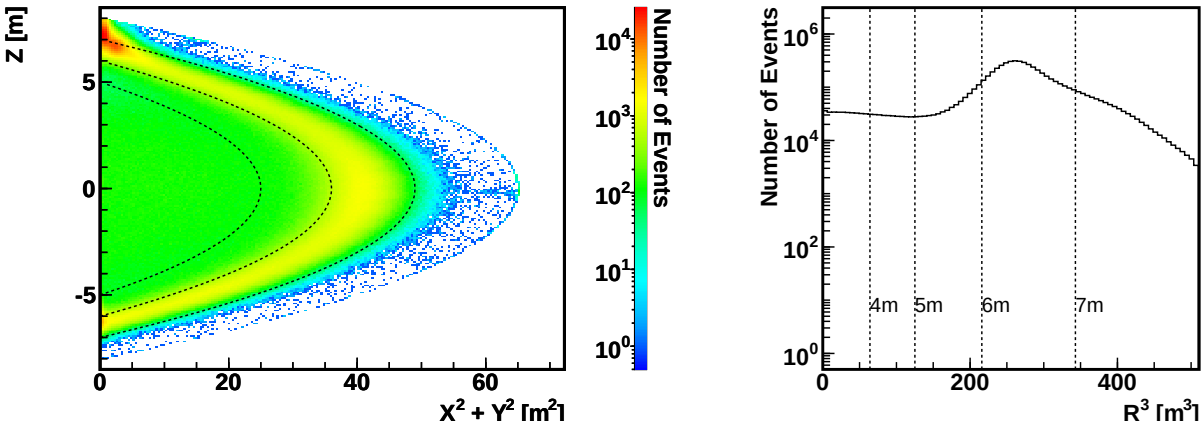

Figure 5.11: Radial Distribution of Single Events

mometer and/or thermometer supporting wire. The thermometers and the supporting wires are composed of heavy material, such as stainless, and making complete understanding of the isotopic composition of them is unrealistic. Interactions of these unidentified heavy isotopes with cosmic muons or α, γ rays are practically unknown. Since we are seeking few events of new signal out of several trillions of events, we conservatively remove the region from our fiducial volume.

The radial fiducial volume cut is applied to both of the prompt signals and delayed signals; i.e., we require that vertices of prompt signals be within 5 m radius and vertices of delayed signals be within 5 m radius. Applying the fiducial volume cut to only one of prompt or delayed signal results in involvement of outer vertex signals where events are not reconstructed confidently.

For the removal of the cylindrical region along the Z axis, we apply cut only to the delayed signals. Judging from the distribution of accidental coincidence event vertices (shown in Chapter 6), we require that the delayed event vertices be outside of the 1.2 m radius cylinder along the Z axis.

5.8 Coincidence Event Selection

Now that we obtained the basic set of single events, we select neutrino candidate events from it by seeking pairs of delayed coincidence signals. Neutrino delayed coincidence events are characterized by spatially correlated, timely correlated two signals, follower of which have 2.2 MeV visible energy. Consequently, we apply cuts to distance of signal pairs, interval of signal pairs, and energy of follower (delayed) signal of the signal pairs.

The distance and interval of prompt and delayed signals are essentially determined by the neutron thermalization and capture process. The distances are also affected by finite resolution of vertex reconstruction. Those processes are studied by a Monte-Carlo (MC) simulation, which is constructed based on the GEANT package distributed from CERN,

with definitions of the KamLAND LS composition and physical properties. Details of the simulation is discussed in Chapter 7. Figure 5.12 shows the simulated distribution of distance and interval of the prompt and delayed signals.

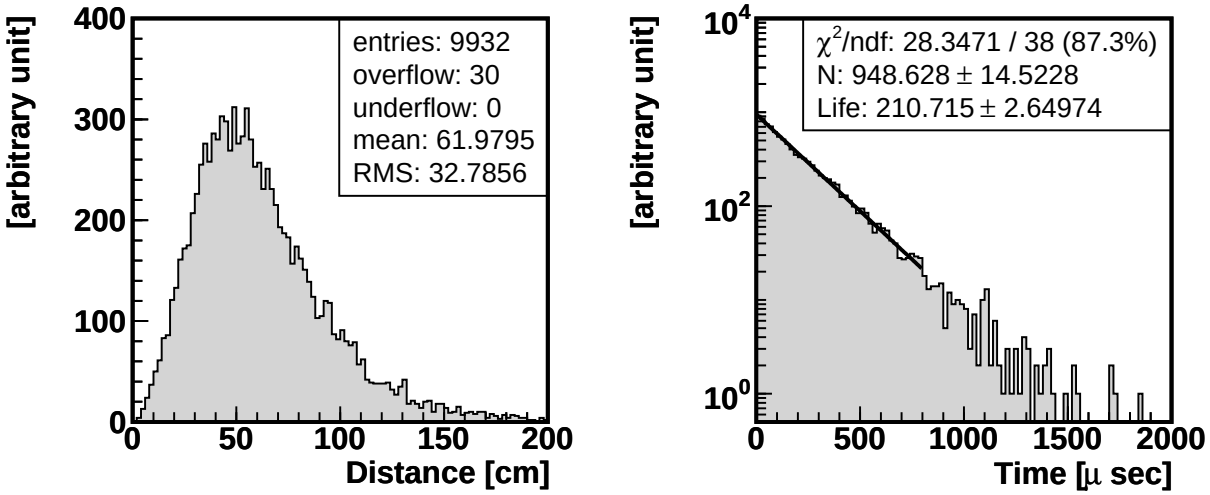

Figure 5.12: Spatial and Timing Correlation of Neutrino Coincidence Signals (MC)

From the simulation, the mean distance is estimated to be 62 cm, and the mean interval is estimated to be 210 μsec. The cut values are decided with taking account of selection efficiency and accidental coincidence background rate. The accidental coincidence occurs randomly in space and time, by definition, and increases linearly as interval cut is loosened, increases cubically as distance cut is loosened. Considering the nature of new signal search study, we set the cut values rather tightly, requiring that the distance be less than 100 cm and interval be less than 1 msec. The accidental background rate with these cuts is discussed in Chapter 6, and the selection efficiency of these cuts is discussed in Chapter 7.

For the energy of the delayed signals, we require that the reconstructed visible energy be between 1.8 MeV and 2.6 MeV. This range is decided based on the energy resolution, $7.25\%/\sqrt{E_{\rm vis}/[\rm MeV]}$, which corresponds to 0.11 MeV at 2.2 MeV. The energy window from 1.8 MeV to 2.6 MeV contains 99.97% of the delayed signal of neutrino events.

Finally, we define the analysis energy window for the prompt signals. The geo-neutrino energy ranges from 0 MeV to 3.3 MeV. The energy threshold of the $\bar{\nu}_e p \rightarrow e^+ n$ reaction is 1.8 MeV. The 1.8 MeV neutrinos make delayed coincidence events with 0 MeV positron, visible energy of which is 1.0 MeV with including annihilation gamma rays. Thus the visible energy of the geo-neutrino event prompt signals ranges from 1.0 MeV to 2.5 MeV. Considering the energy resolution, $7.25\%/\sqrt{E_{\rm vis}/[\rm MeV]}$, we define the analysis window to be from 0.9 MeV to 2.7 MeV.

5.9 Selected Candidate Events Summary

After all cuts discussed above, 113 geo-neutrino candidate events are selected. The candidate event set includes backgrounds of neutrinos from nuclear power reactors, cosmic muon induced isotopes, and events caused by radioactivity in the LS. These backgrounds are discussed in detail in Chapter 6.

Figure 5.13 shows the distribution of the prompt signal energy, delayed signal energy, distance between prompt and delayed signals, and interval between the prompt and delayed signals. The plots show the distribution after all cuts except for a cut to the displayed value (i.e., so called 'N-1 plots').

Figure 5.14 shows the two dimensional scatter plots of two characteristic parameters ('N-2' plots). The red squares indicate the geo-neutrino event selection criteria, and the green squares indicate the reactor neutrino event selection criteria for neutrino oscillation analysis. Events with prompt signal energy greater than 2.7 MeV are mainly reactor neutrino events, and the reactor neutrino events distributes into the geo-neutrino analysis region. The reactor neutrino events are not clearly separated from the geo-neutrino events by the event selection criteria, however, accidental coincidence events disperse differently from neutrino events and rejected by the coincidence event selection efficiently. Few events with delayed energy about 5 MeV are events with neutron capture on ^{12}C, which makes 4.95 MeV gamma rays.

Figure 5.15 shows the distribution of candidate event vertices. Vertices are distributed uniformly, and no significant clusters are seen.

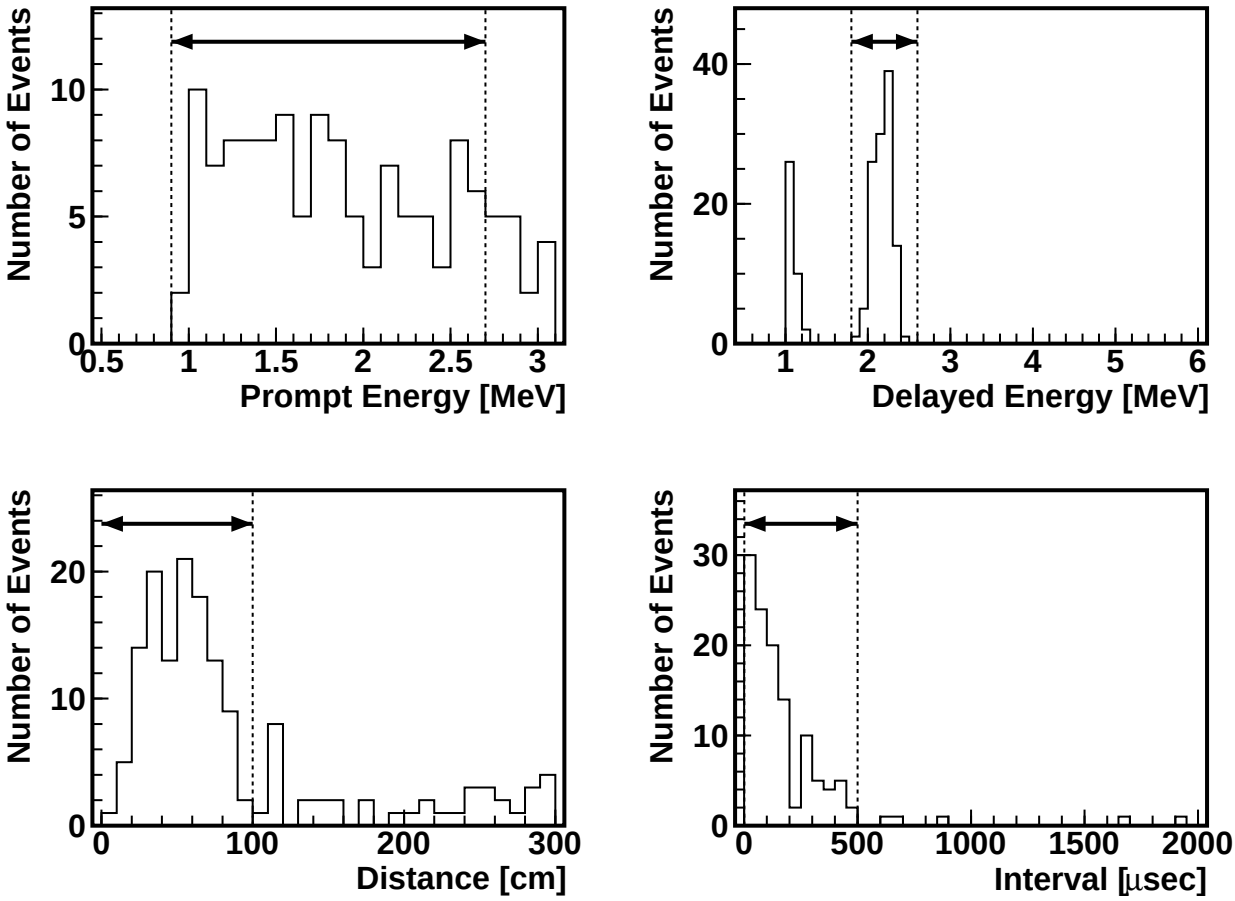

Figure 5.13: Selected Geo-neutrino Event Candidates

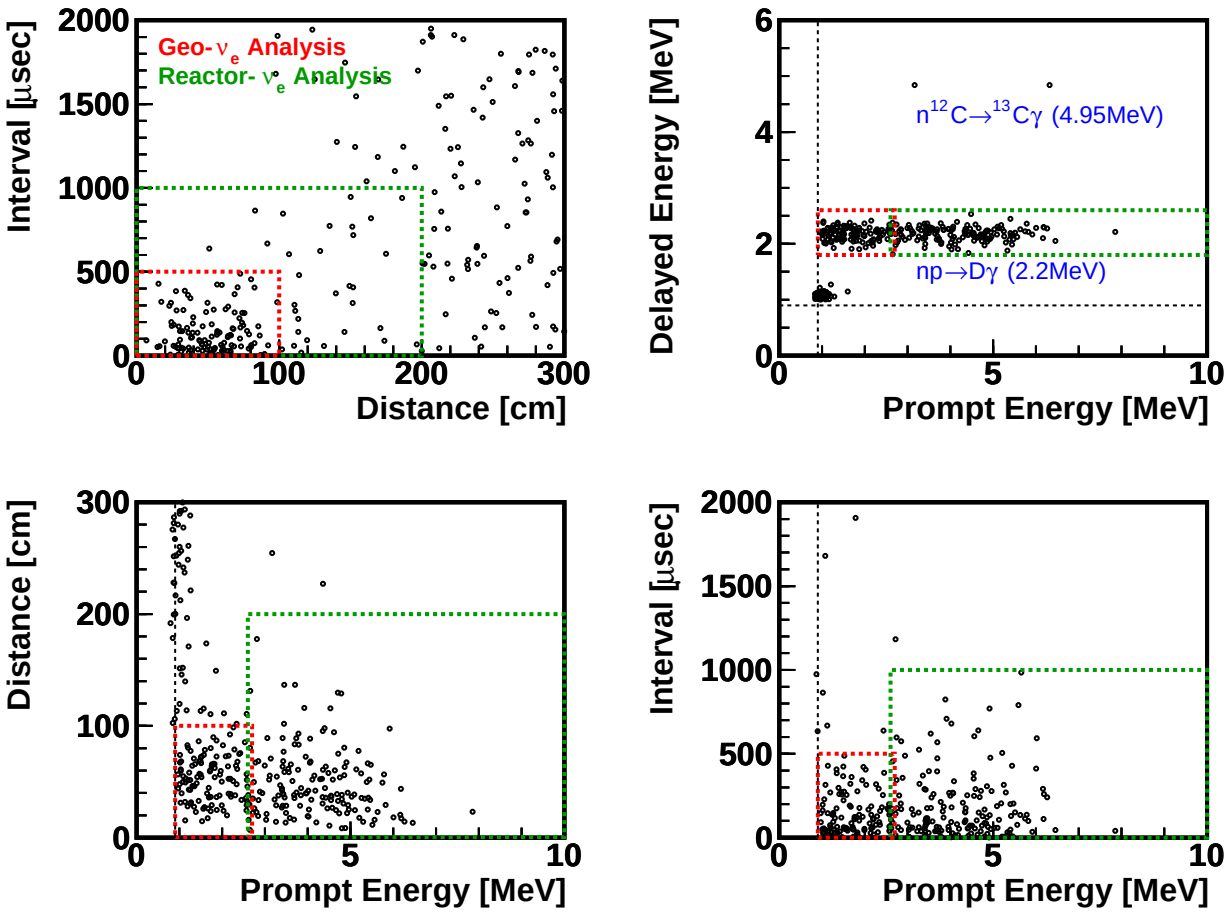

Figure 5.14: Selected Geo-neutrino Event Candidates

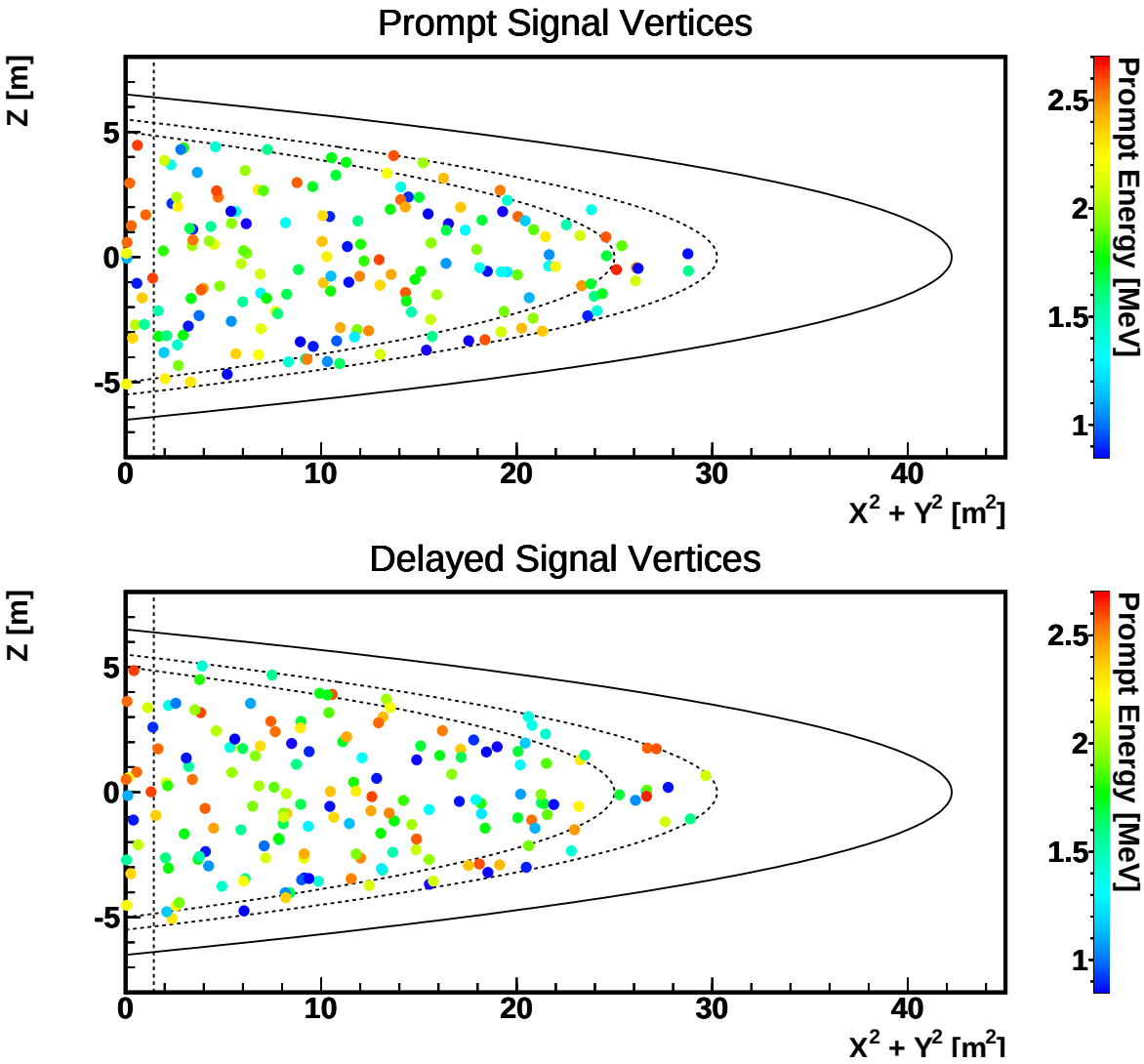

Figure 5.15: Vertex Distribution of Selected Candidate Events

Chapter 6

Backgrounds

6.1 Reactor Neutrino Backgrounds

The primary purpose of the KamLAND experiment is to detect anti-neutrinos from nuclear power reactors surrounding the KamLAND site and demonstrate neutrino oscillation phenomena. Thus the site is chosen in order that enough number of reactor neutrinos are detected. On the other hand, such neutrinos are one of the most serious backgrounds for geo-neutrino observation.

Reactor neutrinos are generated by beta decays of unstable isotopes produced by reactor fuel fissions. Such isotopes are generally very short-lived and neutrinos are emitted instantly following fuel fissions. Neutrino flux from short-lived isotopes is thus directly calculated from operation conditions of each reactor.

On the other hand, fissions of reactor fuel produce small amount of long-lived isotopes, such as ^{106}Ru($\tau_{1/2}$=374day), ^{144}Ce($\tau_{1/2}$=285day), and ^{90}Sr($\tau_{1/2}$=28year). Such isotopes are accumulated in fuel blocks gradually during operation of nuclear reactors, and decays slowly thereafter, even after the fuel blocks are removed from reactor cores. The amount of these long-lived isotopes depends on history of each reactor operation.

6.1.1 Neutrinos from Short-Lived Isotopes in Reactors

Figure 6.1 shows location of commercial reactors in Japan. Table 6.1 summarizes their thermal power P [GW], distance to KamLAND d [km], power flux $P/(4\pi d^2)$ [GW/cm^2], and contribution to KamLAND in power flux. Reactors in Korea are also listed in the table.

When reactors are under operation, the output power is almost 100% of their capacity. Reactors are stopped for some periods for maintenance, resulting in average operation efficiency about 80%. This brings about ~ 1.9GW/cm^2 average power flux at KamLAND. As discussed later, reactor fuels generate energy of about 200MeV per fission, with emitting about 6 electron-type anti-neutrinos. Therefore we expect approximately 3.6×10^6 1/cm^2/sec of reactor-origin neutrino flux at KamLAND. This amount of neutrino flux is comparable to the geo-neutrino flux at KamLAND.

Reactor fuels are mainly composed of ^{235}U, ^{238}U, ^{239}Pu, and ^{241}Pu. A typical reactor

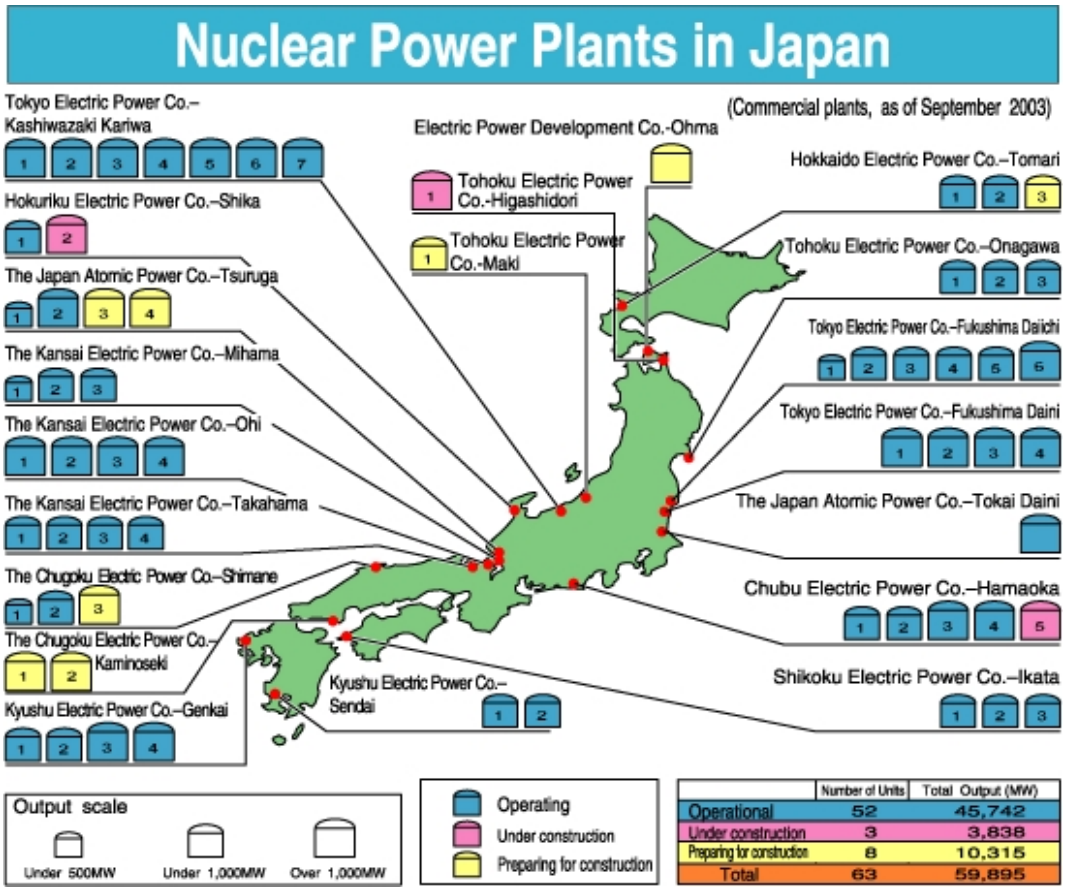

Figure 6.1: Japanese Power Reactor Location

core contains these fuels at the ratio of 0.6 : 0.08 : 0.3 : 0.05. Energy released by fission of these nuclei is given by Y.Declais *et al.* (1994) [44] as shown in the Table 6.2.

Composition of reactor core fuel changes during the processes of energy generation in a reactor; neutron capture on ^{238}U produces ^{239}Pu via two beta decays, and ^{239}Pu becomes ^{241}Pu by capturing two neutrons. This process, called fuel burn-up, progresses as an alternative of energy generation by fission.

Understanding the reactor core is a key issue for nuclear power reactor operation, thus detailed studies and analyses have been performed. Under an special agreement between Tohoku University and the Japanese nuclear power reactor operators, detailed reactor operation data is provided, including data of estimated fuel composition and fission rates of each reactor core at each time. Figure 6.2 shows an example of reactor operation data. The errors of reactor power and fuel composition are estimated to be 2.1% and 1.0%, respectively.

Antineutrino spectrum of ^{235}U fission was studied by K.Schreckenbach *et al.* (1985) [45], by measuring electron spectrum from ^{235}U fission products with a magnetic beta spectrometer. With the High Flux Reactor of the Institut Laue-Langevin (ILL), 93% enriched $^{235}UO_2$ was exposed to thermal neutron flux for total 15 hours. Antineutrino

Table 6.1: List of Japanese and Korean Reactors

Reactor Name	Thermal Power [GW]	Number of Cores	Distance [km]	Power Flux [GW/cm^2]	Contribution [%]
Kashiwazaki	24.5	7	160	7.62×10^{-15}	30.9
Ohi	13.7	4	179	3.40×10^{-15}	13.8
Takahama	10.2	4	191	2.22×10^{-15}	9.0
Shika	1.9	1	88	1.95×10^{-15}	7.9
Tsuruga	4.5	2	138	1.88×10^{-15}	7.6
Hamaoka	10.6	4	214	1.84×10^{-15}	7.5
Mihara	4.9	3	146	1.83×10^{-15}	7.4
Fukushima 1	14.2	6	349	0.93×10^{-15}	3.8
Fukushima 2	13.2	4	351	0.85×10^{-15}	3.5
Tokai 2	3.3	1	295	0.30×10^{-15}	1.2
Shimane	3.8	2	401	0.19×10^{-15}	0.8
Onagawa	4.1	3	431	0.18×10^{-15}	0.7
Ikata	6.0	3	561	0.15×10^{-15}	0.6
Genkai	6.7	4	754	0.094×10^{-15}	0.4
Sendai	5.3	2	830	0.061×10^{-15}	0.2
Tomari	3.3	2	783	0.043×10^{-15}	0.2
Fugen	0.5	1	138	0.21×10^{-15}	0.9
Monju	0.8	1	141	0.32×10^{-15}	1.3
Kori	9.5	4	735	0.14×10^{-15}	0.6
Wolsong	8.4	4	709	0.13×10^{-15}	0.5
Yonggwang	14.9	5	986	0.12×10^{-15}	0.5
Ulchin	11.8	4	712	0.19×10^{-15}	0.8
Total	176.1	71	-	2.4×10^{-14}	100

Table 6.2: Energy Release by Fission

Isotope	Energy Release [MeV]
^{235}U	201.8 ± 0.5
^{238}U	205.0 ± 0.7
^{239}Pu	210.3 ± 0.6
^{241}Pu	212.6 ± 0.7

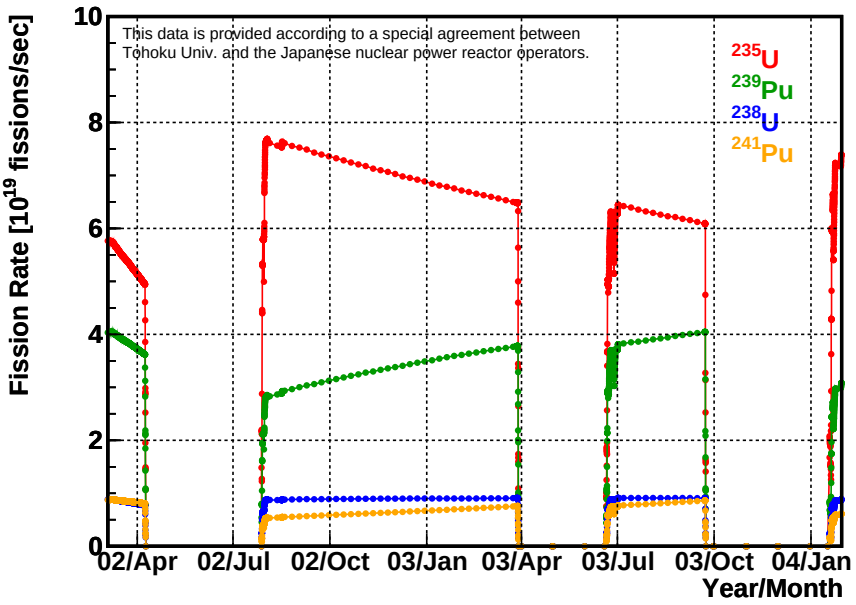

Figure 6.2: Example of Reactor Operation Data (a typical 1.3GW class BWR)

spectrum was then obtained by fitting the measured beta spectrum with a set of 30 hypothetical beta branches.

In a similar way, antineutrino spectra of ^{239}Pu and ^{241}Pu fissions were obtained by F.Feilitzsch *et al.* (1982) [46] and A.A.Hahn *et al.* (1989) [47]. The same beta spectrometer and reactor was used in those studies. For ^{239}Pu spectrum, ^{239}Pu evaporated as the oxide on a thin Ni foil was exposed to thermal neutron flux for 6 hours, 23 hours and 38 hours, and the spectrum was fitted with 25 hypothetical beta branches. Above 1.5 MeV, the difference in the beta spectra between 23 hour irradiation and 38 hour irradiation was less than 1.2%. The set of hypothetical beta branches reproduced the original beta spectrum at better than 1% accuracy. For ^{241}Pu spectrum, 83% enriched $^{241}PuO_2$ was exposed to thermal neutron flux for 45 hours, and the electron spectrum was fitted with a set of 30 hypothetical beta branches, which reproduces the original beta spectrum at better than 1% accuracy.

For ^{238}U, no measurement has been made, because ^{238}U fission is induced only by high-energy neutrons. P.Vogel *et al.* (1981) [48, 49] conducted a theoretical calculation of antineutrino spectrum of several reactor fuel fissions, based on the data set in the ENDF/B-V Fission Product Library of the Evaluated Nuclear Data File, Version V, which is distributed from the National Nuclear Data Center at the Brookhaven National Laboratory. Antineutrino spectra were obtained by solving differential equations that describe processes of fission, subsequent beta decay, and possible neutron capture by fission fragments. In the calculation, dependences on initial neutron energy, neutron flux in the reactor, and exposure time are considered.

Figure 6.3 shows the antineutrino spectra of fuel fission, ^{238}U from K.Schreckenbach *et*

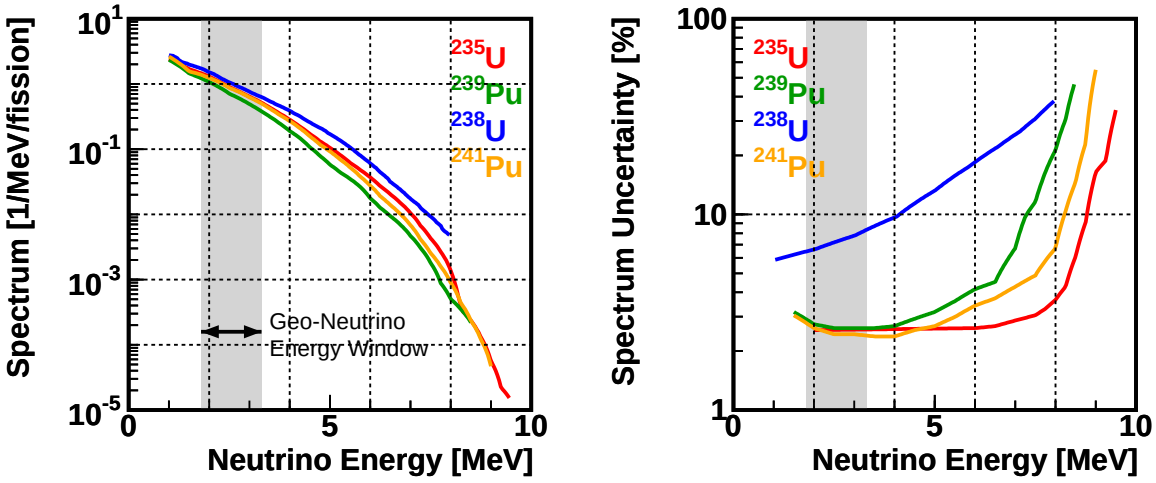

Figure 6.3: Reactor Fuel Fission Spectra

al. (1985) [45], ^{239}Pu and ^{241}Pu from A.A.Hahn *et al.* (1989) [47], and ^{238}U from P.Vogel *et al.* (1981) [48].

The neutrino spectrum from these nuclear reactors at KamLAND is calculated by summing up fluxes from all reactor cores with taking account of solid angles and the neutrino oscillation phenomenon;

$$\frac{d\Phi(t)}{dE} = \sum_{\text{reactor core}} \left\{ R_{\text{core}}(t) \cdot \frac{1}{4\pi {d_{\text{core}}}^2} \cdot P(\bar{\nu_e} \to \bar{\nu_e}) \sum_{\text{fuel}} (r_{\text{fuel}}(t))_{\text{core}} \left(\frac{dN}{dE}\right)_{\text{fuel}} \right\} \quad (6.1)$$

where R_{core} denotes the fission rate of each core, d_{core} is the distance to the core, $P(\bar{\nu_e} \to \bar{\nu_e})$ is the neutrino survival probability, $(r_{\text{fuel}})_{\text{core}}$ is ratio of each fission fuel in the core, and $\left(\frac{dN}{dE}\right)_{\text{fuel}}$ is the fission spectrum of the fission fuel. Note that the fission rates R_{core} and the fuel compositions $(r_{\text{fuel}})_{\text{core}}$ vary depending on reactor operation.

As discussed in Section 2.3, the neutrino survival probability is given by

$$P(\bar{\nu_e}(0) \to \bar{\nu_e}(L)) = 1 - \sin^2 2\theta \sin^2\left(\frac{1}{c\hbar}\frac{\Delta m^2 L}{4E}\right) \quad (6.2)$$

where L is the distance from generation point, Δm^2 is the difference of squared mass of two generation neutrinos $({m_2}^2 - {m_1}^2)$, and θ is the mixing angle of the two generations. The neutrino oscillation phenomenon, as well as the values of Δm^2 and θ, is well established by global analysis of solar neutrino experiments and a recent KamLAND reactor neutrino data. The latest estimation is given by [2], presenting $\Delta m^2 = 7.9^{+0.6}_{-0.5} \times 10^{-5}\text{eV}^2$ and $\tan^2\theta = 0.40^{+0.10}_{-0.07}$.

The reactor neutrino spectrum at KamLAND is then calculated by integrating the flux over time and multiplying the $\bar{\nu_e}p$ cross section;

$$\frac{dN}{dE_{\bar{\nu_e}}} = N_{\text{proton}} \cdot \varepsilon(E_{\bar{\nu_e}}) \cdot \sigma(E_{\bar{\nu_e}}) \int_t \frac{d\Phi(t)}{dE_{\bar{\nu_e}}} dt \quad (6.3)$$

where N_{proton} is the number of target protons in the fiducial volume, ε is the detection efficiency, and σ is the cross section discussed in Section 7.4. Visible energy spectrum is then obtained by applying the neutrino energy to positron energy conversion formula presented in Section 7.4. Figure 6.4 shows the reactor neutrino background spectrum, with $7.25\%/\sqrt{E/[\text{MeV}]}$ energy resolution. The expected geo-neutrino signal spectra, calculated based on my best model discussed in Chapter 2, are also shown in the figure.

With including all systematic uncertainties discussed in Section 7.6, the number of reactor neutrino events is estimated to be 58.0±5.3 events/livetime.

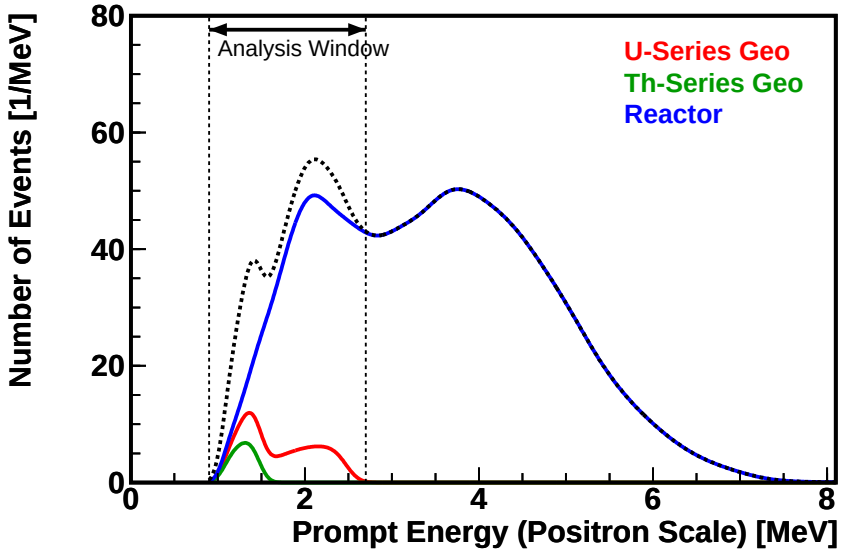

Figure 6.4: Reactor Neutrino Background Spectrum

6.1.2 Neutrinos from Long-Lived Isotopes in Reactor Fuels

Compared to the short-lived fission products, estimation of neutrino flux from the long-lived fission products is rather difficult, because the flux depends not only the current reactor operation condition, but also history of past reactor operations and current location of spent fuels.

As discussed in a previous section, the neutrino spectra of short-lived fission products are obtained based on measurement of beta spectra from fuels exposed to thermal neutron flux for a few tens of hours (except for ^{238}U). It means that neutrinos from isotopes whose lifetime is shorter than few hours are all included in the short-lived isotope spectra. V.I.Kopeikin (2001) *et al.* [50] listed six long-lived fission products with maximum neutrino energy greater than 1.8 MeV. Table 6.3 shows the yields of those fission products given by V.I.Kopeikin *et al.* (2001).

Three of those isotopes, ^{97}Zr, ^{132}I and ^{93}Y, attain equilibrium within ten days, thus neutrino flux from these isotopes is not seriously affected by past reactor operation and/or

Table 6.3: Long-lived Fission Products (V.I.Kopeikin *et al.* (2001))

Fission Fragment	Halflife	E_{max} MeV	Yield [%] ^{235}U	^{239}Pu	^{241}Pu	^{238}U
^{97}Zr	16.91 h	1.92	5.95	5.30	4.89	5.50
^{132}I	2.295 h	2.14	4.30	5.40	4.14	5.16
^{93}Y	10.18 h	2.87	6.40	3.89	3.15	4.97
^{106}Ru	373 day	3.54	0.40	4.31	6.18	2.55
^{144}Ce	285 day	3.00	5.48	3.74	4.39	4.50
^{90}Sr	28.8 year	2.28	5.82	2.10	1.57	3.12

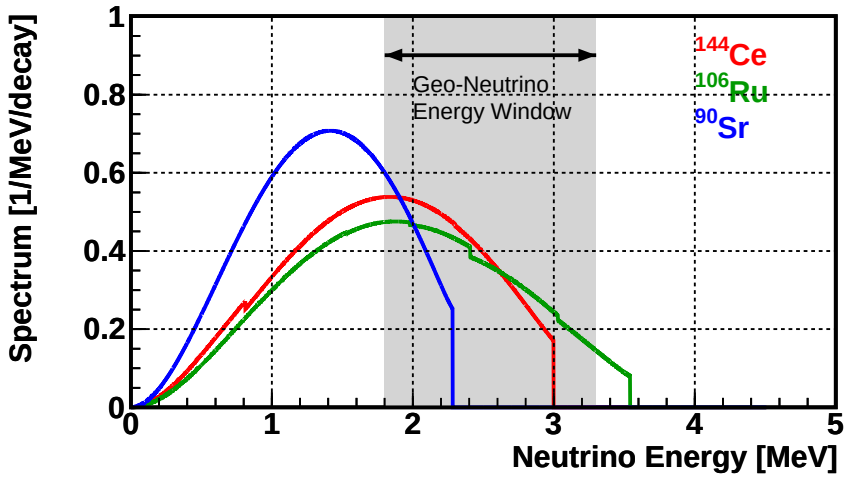

Figure 6.5: Long-lived Fission Product Spectrum

spent fuel storage. Neutrino flux from the other three isotopes, ^{106}Ru, ^{144}Ce and ^{90}Sr, changes gradually according to their slow activity variation. The following list shows some details of decays of these isotopes. Figure 6.5 shows calculated neutrino spectrum of these isotopes.

$$^{106}\mathrm{Ru}\ (374\mathrm{day}) \xrightarrow{Q_\beta=0.039\mathrm{MeV}} {}^{106}\mathrm{Rh}\ (29.8\mathrm{sec}) \xrightarrow{Q_\beta=3.541\mathrm{MeV}} {}^{106}\mathrm{Pd}\ (\mathrm{stable})$$

$$^{144}\mathrm{Ce}\ (285\mathrm{day}) \xrightarrow{Q_\beta=0.320\mathrm{MeV}} {}^{144}\mathrm{Pr}\ (17.2\mathrm{min}) \xrightarrow{Q_\beta=2.998\mathrm{MeV}} {}^{144}\mathrm{Nd}\ (2.29\times10^{15}\mathrm{y})$$

$$^{90}\mathrm{Sr}\ (28.8\mathrm{y}) \xrightarrow{Q_\beta=0.546\mathrm{MeV}} {}^{90}\mathrm{Y}\ (64.1\mathrm{sec}) \xrightarrow{Q_\beta=2.282\mathrm{MeV}} {}^{90}\mathrm{Zr}\ (\mathrm{stable})$$

The reactor operation data provided by the electric power companies is available only

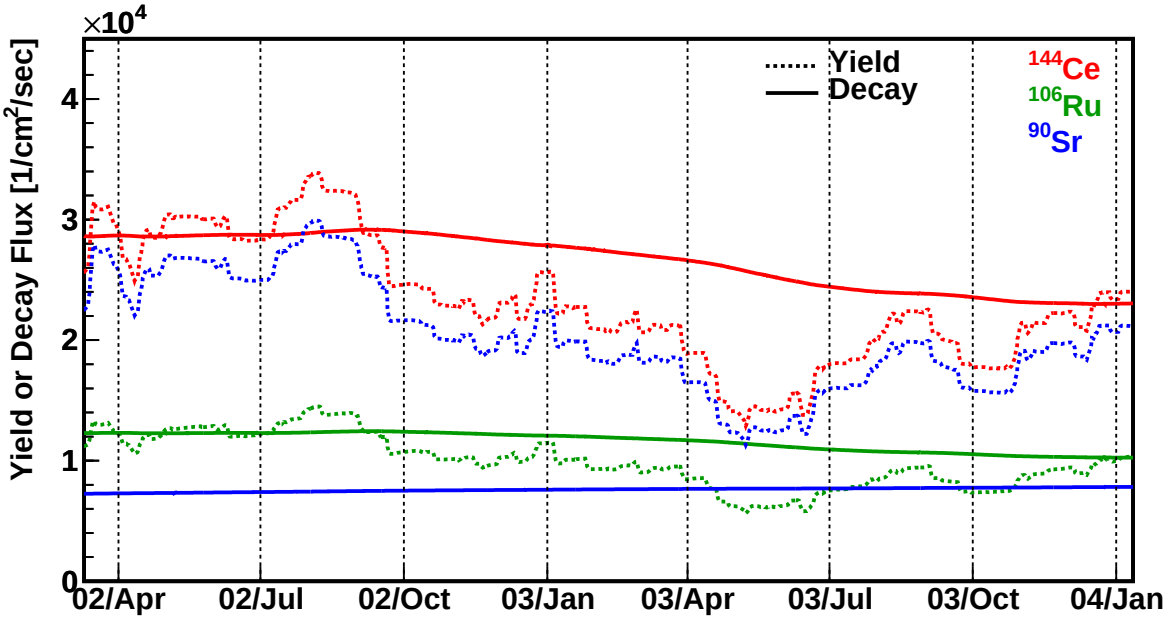

Figure 6.6: Yield Rate and Decay Rate of Long-lived Fission Products

that of after March 2002. Yield of long-lived fission products is estimated with published reactor operation data [51], which provides annual or monthly electrical power output from each reactor, with assuming a typical fuel composition and relation of electrical power output and thermal power output of a typical Boiling-Water Reactor (BWR). This process involves 10% error in the estimated fission rate.

Also assuming that all spent fuels are stored just beside the reactors, *decay flux*, which is defined as sum of decay rate from all fuel storages with weight of solid angle (i.e., $\sum_{\text{storage-}i} \frac{1}{4\pi {L_i}^2} R_i^{\text{decay}}$), is calculated as shown in Figure 6.6. With considering neutrino oscillation, the numbers of events from these isotopes are calculated to be 0.815 events/livetime (^{144}Ce), 0.525 events/livetime (^{106}Ru), and 0.0334 events/livetime (^{90}Sr).

After fuel is removed from a reactor core, the spent fuel is stored in a storage next to a reactor for a while, typically for ten years. The fuel is then transfered somewhere for permanent storage or fuel reprocessing. Most of neutrino flux from spent fuel come from the fuel stored at the Kashiwazaki Power Plant and power plants around the Wakasa Bay, both of which are only ∼170km away from KamLAND. On the other hand, all nuclear-related facilities in Japan and overseas are located much farther than these power plants. Therefore, it is reasonable to assume that fuel transportation moves the spent fuel farther than before.

The half-lives of ^{144}Ce and ^{106}Ru are much shorter than the period of fuel storage next to the reactor core. Thus the neutrino flux estimation is not seriously affected by fuel transportation. In fact, relation of yield and decay is clearly seen in Figure 6.6. On the other hand, the halflife of ^{90}Sr is much longer than the temporary storage period. Here

we conservatively assign 100% error to the neutrino flux from ^{90}Sr, which contributes only 2.4% of the all long-lived isotope events at KamLAND.

With including all other systematic uncertainties discussed in Section 7.6, the number of events by long-lived fission product is estimated to be 1.37±0.17 events/livetime.

6.2 Muon Induced Backgrounds

Cosmic muons passing through the detector and/or around the detector react with isotopes consisting the Liquid Scintillator (LS) and/or other materials, producing various types of unstable isotopes and/or neutrons. These unstable isotopes and neutrons make correlated signals in time and space, thus are possible background sources of the neutrino events.

6.2.1 Muon Induced Neutrons

For every muon we veto the whole detector volume for 2 msec. Using neutron capture time 210 μsec, the probability that a neutron survives longer than the veto period is calculated to be 7.3×10^{-5}. The average neutron productivity of non-showering muon is measured to be around 0.2 neutrons/muon, thus the probability that more than one neutrons are left after the veto is $\sim 10^{-10}$, making negligible contribution to the neutrino event candidates. For showering muons, which lead to 2 sec whole volume veto, the number of produced neutron is about 100 at most. The probability of a neutron surviving longer than 2 sec is $< 10^{-4000}$ as calculated from the lifetime. Contribution of this is negligible as well.

6.2.2 Muon Induced Fast Neutrons

Neutrons are also generated by muons that do not pass through the detector; 100 MeV to 1 GeV neutrons generated outside the detector can reach to the LS, with penetrating few meters of the surrounding rocks, the outer detector (OD), the stainless tank, and the buffer mineral oil layer. Some neutrons generated by muons passing through only the OD also might have no associated muon event due to inefficiency of the OD. These high energy neutrons (fast neutrons) could mimic a neutrino event, because protons scattered by fast neutrons also have high energy, enough to excess the threshold even after large quenching. Since associated muons are not detected, no veto is applied for these fast neutron events.

Fast Neutrons induced by OD Muons

The rate of fast neutrons generated by muons passing through the OD (OD Muon) is estimated by finding delayed coincidence events that have associated OD hits. Figure 6.7 shows the distribution of prompt-delayed event interval and delayed event energy. The interval is consistent with the neutron capture time (210 μsec), and the delayed signal energy peaks at 2.2 MeV, which is the gamma ray energy emitted after neutron capture on proton.

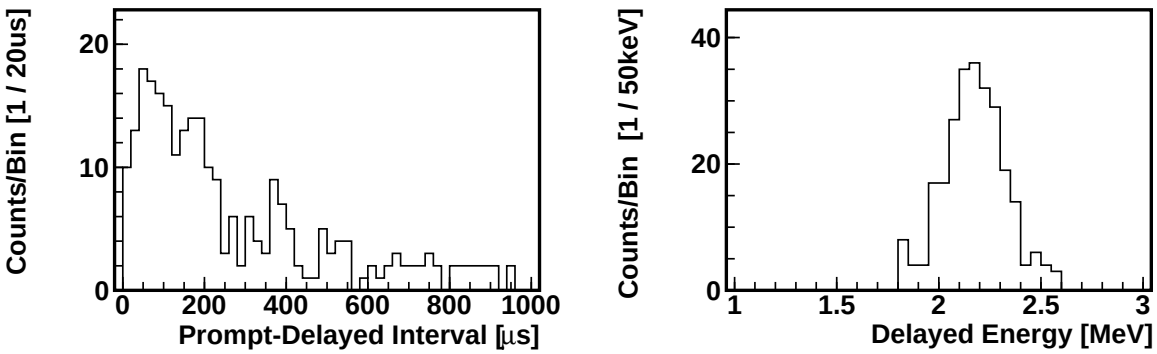

Figure 6.7: Fast Neutron Samples

Figure 6.8 shows the distribution of prompt signal energy. Most of fast neutron events have much higher energy than neutrino events, and at the low energy region, the spectrum shape does not have distinctive feature. Figure 6.9 shows the radial distribution of prompt signal vertex. Since fast neutrons penetrate into the LS from the outside, the number decreases as approaching to the center. From the radial distribution, the number of fast neutrons penetrate into the 5 m radius fiducial volume is estimated to be 3.83 ± 1.10. Taking account of the OD efficiency, 92%, the number of fast neutron background events in the 5 m radius fiducial volume induced by untagged OD muons is estimated to be 0.33 ± 0.10, in the energy region of 0.9MeV $< E_{\rm promt} <$ 13.5MeV. Assuming uniform energy distribution, the number of events within the geo-neutrino window is 0.047 ± 0.014.

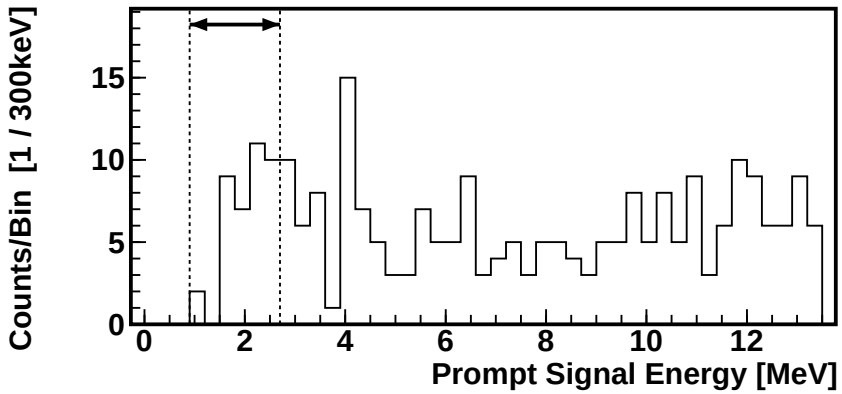

Figure 6.8: Fast Neutron Prompt Energy Spectrum

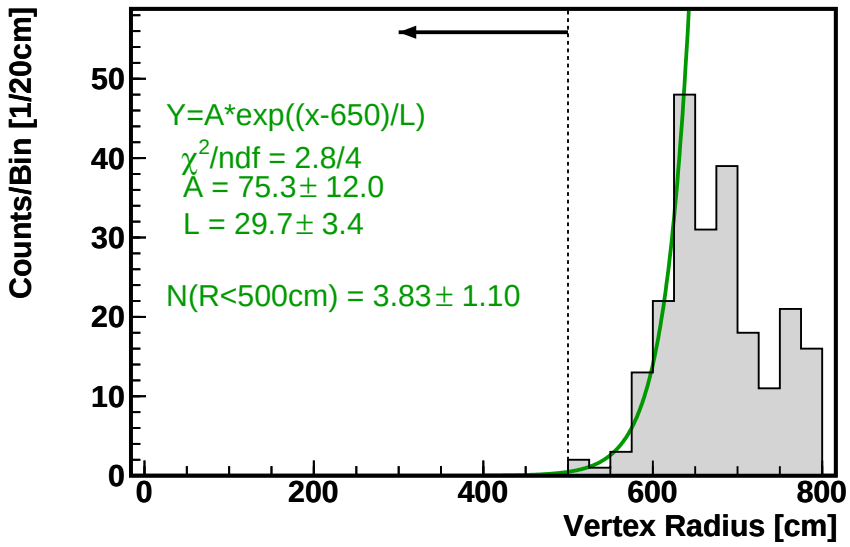

Figure 6.9: Fast Neutron Vertex Distribution

Fast Neutrons induced by Rock Muons

The rate of fast neutrons generated by muons that does not pass through the detector (Rock Muon) is estimated by the Monte Carlo (MC) method. Interactions between muons and surrounding rocks are simulated with the FLUKA-2002 simulation package, and interactions of neutrons with material along the neutron tracks are simulated with GEANT4. Muon energy spectrum and angular distribution are taken from KamLAND measurement.

Figure 6.10 shows the simulated prompt signal spectrum of fast neutrons induced by OD muons and rock muons. From the simulation, fraction of rock muon induced fast neutrons in all fast neutron events at 0 MeV to 10 MeV region is estimated to be 5.4%. Combined with the number of the OD muon induced fast neutron events estimated above, the number of rock muon induced fast neutron event background is estimated to be 0.031±0.009.

6.2.3 Muon Induced Unstable Isotopes

Muons going through the detector disintegrate isotopes around the tracks. Such disintegration processes by high-energy muons, or muon spallation processes, generally produce unstable isotopes, halflives of which typically range from tens of milli seconds to hundreds of milli seconds.

T.Hagner *et al.* (2000) [52] studied the muon spallation reaction in organic liquid scintillator with using the SPS muon beam at CERN. Production cross sections of these isotopes are measured at two different muon energies, 100GeV and 190GeV. Table 6.4 lists isotopes that might be produced by muon spallation reactions, as well as the cross

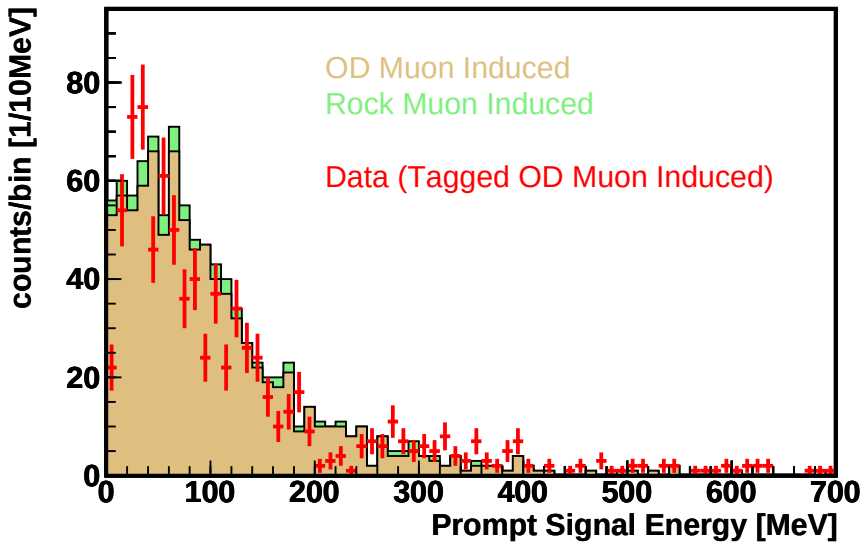

Figure 6.10: Fast Neutron Event Simulation

Table 6.4: Muon Spallation Products

Isotope	Halflife	Decay Mode	Q Value [MeV]	Production Rate [1/day/(100ton CH_2)]
^{6}He	806.7 msec	β^-	3.51	0.26±0.03
^{7}Be	53.24 day	EC	0.86	0.34±0.04
^{8}Li	838 msec	β^-	16.00	0.070±0.017
^{8}B	170 msec	β^-	17.98	0.11±0.02
^{9}C	126.5 msec	β^+	16.49	0.077±0.025
^{10}C	19.255 sec	β^+	3.65	1.95±0.21
^{11}Be	13.81 sec	β^-	11.51	<0.034
^{11}C	20.39 min	β^+	1.98	14.55±1.49
^{9}Li/^{8}He	178.3/119.0 msec	β^-+n	13.61/10.65	0.034±0.007
^{12}B	20.2 msec	β^-	13.37	0.9

section measured by T.Hagner *et al.*

To remove these isotopes, we apply muon spallation vetoes as described in Section 5.6, 2 sec whole volume veto or 2 sec partial volume veto, depending on deposited charge. With these 2 sec vetoes, spallation products are suppressed firmly enough, and probability of making correlated coincidence events by more than two survived isotopes is negligible. However, isotopes that emit neutrons, such as ^{9}Li and ^{8}He, need to be estimated carefully because their decays with neutron emission mimic delayed coincidence events. One remaining ^{9}Li or ^{8}He nucleus makes one fake coincidence event.

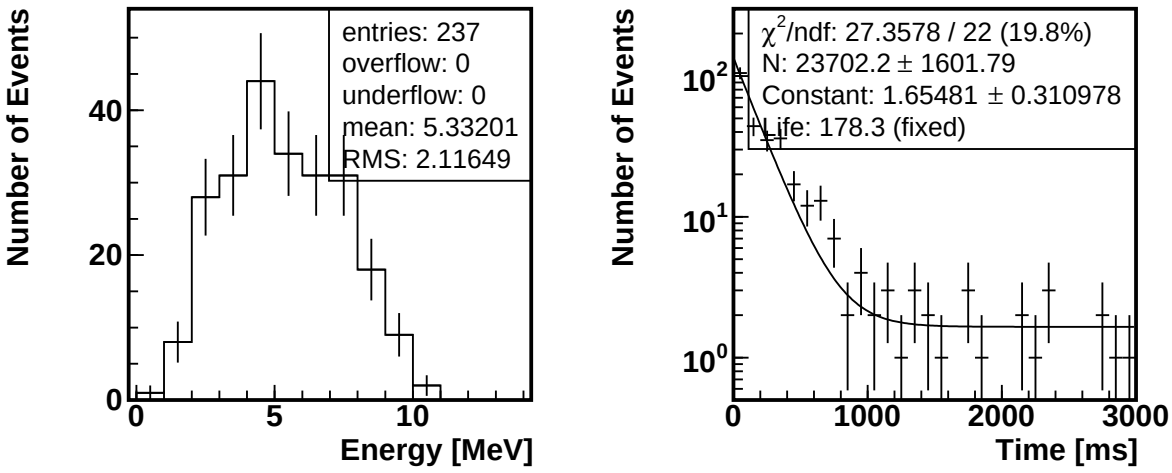

Figure 6.11: Energy and Time Distribution of Showering Muon Spallation Events

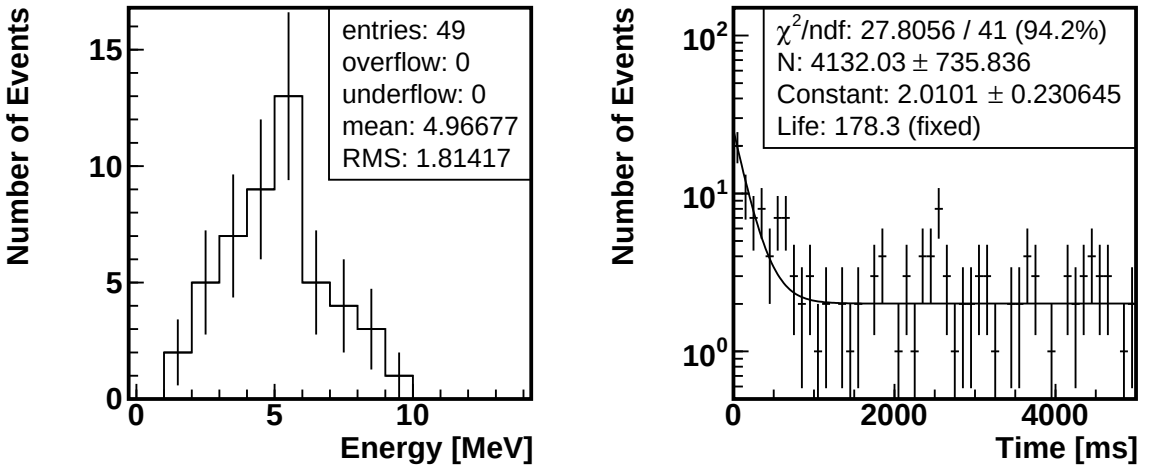

Figure 6.12: Energy and Time Distribution of Non-Showering Muon Spallation Events

Candidates of ^{9}Li and ^{8}He are selected by applying the same delayed coincidence selection criteria as neutrino event selection but coincidences with associated muon events.

Figure 6.11 shows the distribution of prompt signal energy and prompt signal time since associated muons, for delayed coincidence events associated with a showering muon. Figure 6.12 shows the distribution of the same values, but associated with non-showering muons and delayed vertices are within 3m from the muon track. To obtain the energy spectra, events that happens less than 500 msec since associated muon events are selected and off-time event spectra are subtracted.

With the time distribution of spallation events following showering muons, the ratio

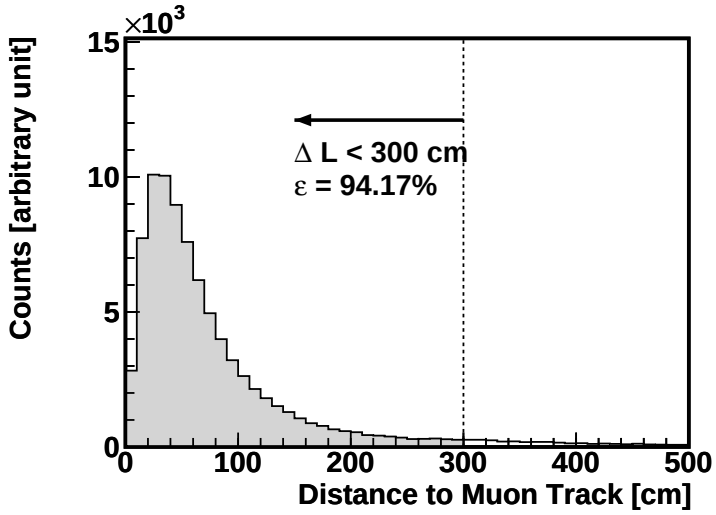

Figure 6.13: Distance of Neutron Vertices from Associated Muon Tracks

of ^{9}Li and ^{8}He in the sample is studied. Un-binned likelihood is constructed with parameterizing the ratio. From the likelihood analysis, the ratio of ^{8}He events is estimated to be less than 15% at 90% C.L.

By fitting the time distributions with the lifetime of ^{9}Li and constant backgrounds, the number of spallation events are estimated to be 474.04±32.04 for showering muons and 82.64±14.71 for non-showering muons. Then the number of events that are left after the spallation 2 sec veto are calculated to be 0.0064±0.00043 and 0.00116±0.00020, respectively.

To estimate the reduction efficiency of the 3 m radius cylindrical cut applied to non-showering muons, vertex distribution of non-showering muon induced neutrons is studied. Figure 6.13 shows the distribution of distance between non-showering muon tracks and associated neutron event vertices. The ratio of neutron events that are contained inside the 3 m radius cylinder is estimated to be 94.17%. Since the number of estimated background rate inside the 3 m cylinder within 2 sec since muon is 82.64 ± 14.71, the number of background events outside the 3 m cylinder is calculated to be 5.12 ± 0.91. Including the number of spallation events after 2 sec veto, the total number of spallation event background is estimated to be 5.13 ± 0.91.

The fraction of ^{9}Li events in the geo-neutrino analysis window is estimated with the theoretical energy spectrum of ^{9}Li decay. Figure 6.14 shows the ^{9}Li decay scheme, which is compiled from several tables and measurements [53–56]. As shown in the figure, ^{9}Li decays into two alpha particles and one neutron within short time, except for the branches to the ground state of ^{9}Be. There are several paths from ^{9}Li to 2α+n, and a lot of uncertainties remain in the estimation of these branching ratios, especially at 7.94 MeV excitation state of ^{9}Be; relatively wide width of the state (1.0 MeV) suggests particle decay, where alpha particle emission or neutron particle emission are the only realistic modes, though.

Both of electrons and neutrons contribute to the prompt signals of ^{9}Li decay events.

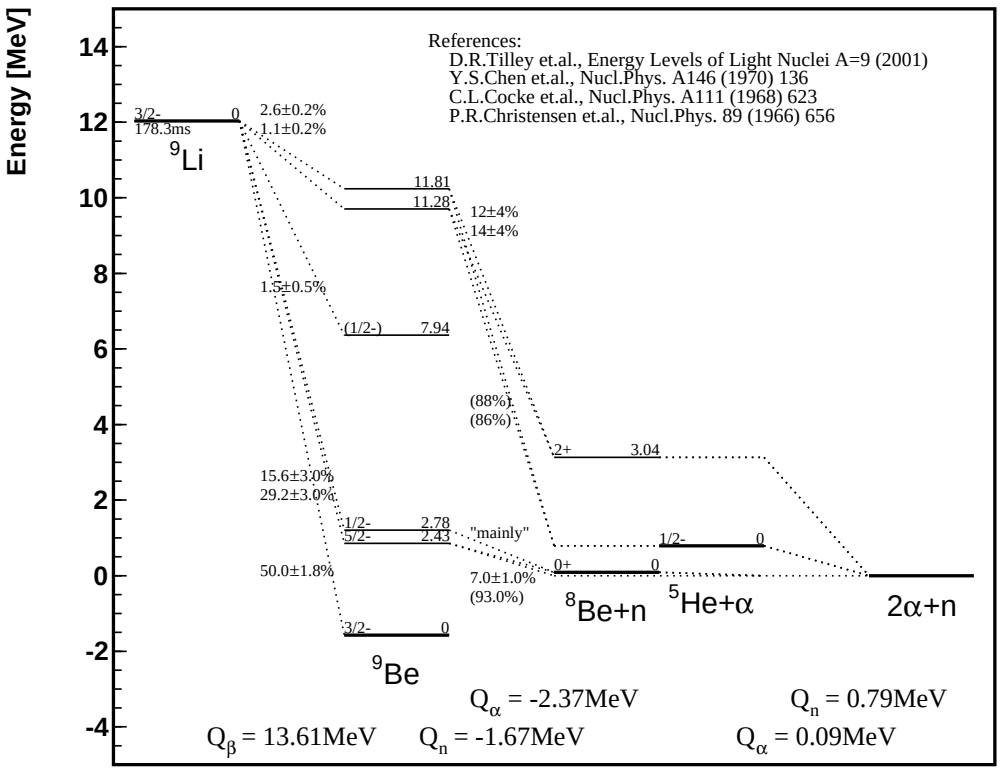

Figure 6.14: ^{9}Li Decay Scheme

Visible energy of neutrons is calculated with Monte Carlo (MC) simulation, which is constructed based on the GEANT4 simulation package with a detailed KamLAND LS geometry definition. Figure 6.15 shows simulated visible energy of mono-energetic neutrons with several initial energies that correspond to some of $^9\mathrm{Be} \rightarrow 2\alpha + n$ transition Q-values. Details of the simulation are discussed in Section 6.4.4.

Figure 6.16 shows the calculated energy spectra of ^{9}Li events. Although neutrons from an excitation state of ^{9}Be are not mono-energetic due to energy uncertainties of short-lived states of ^{9}Be, ^{8}Be and ^{5}He, mono-energetic approximation is used in this calculation because other parameters such as branching ratios and energy levels have considerable estimation uncertainties as already described, and hence making further detailed model is insignificant. As shown later, the number of ^{9}Li backgrounds is already very small compared to other backgrounds, thus these uncertainties are tolerable.

In the Figure 6.16, spectra of electron plus neutron are drawn separately for each excitation level of ^{9}Be, and the total spectrum is drawn with a black solid line. The unsure transition through the 7.94 MeV state of ^{9}Be is included in this calculation, and the spectra are normalized to the data. The total spectrum without the 7.94 MeV state of ^{9}Be is also drawn with a black dot line, after normalization to the data.

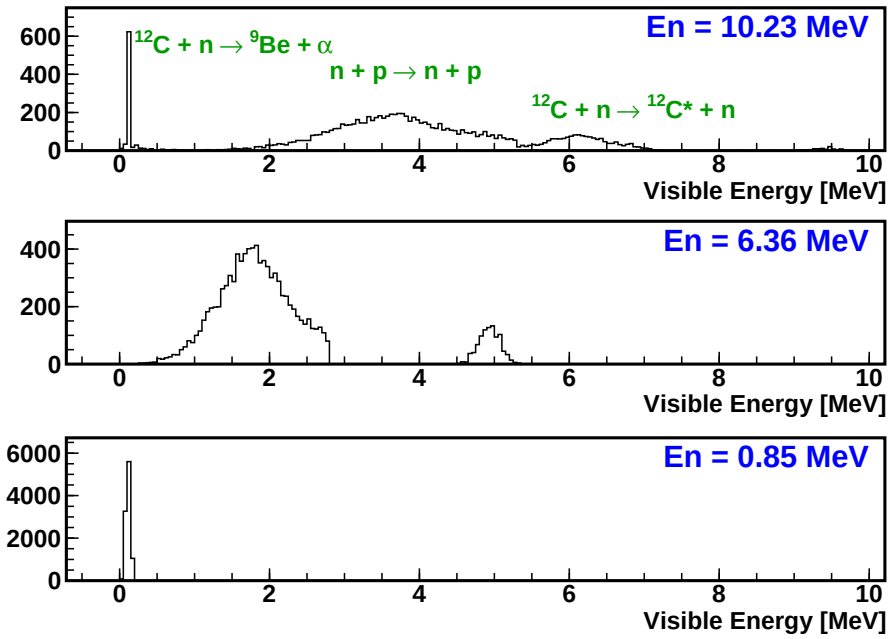

Figure 6.15: ^{9}Li Event Neutron Visible Spectrum (MC)

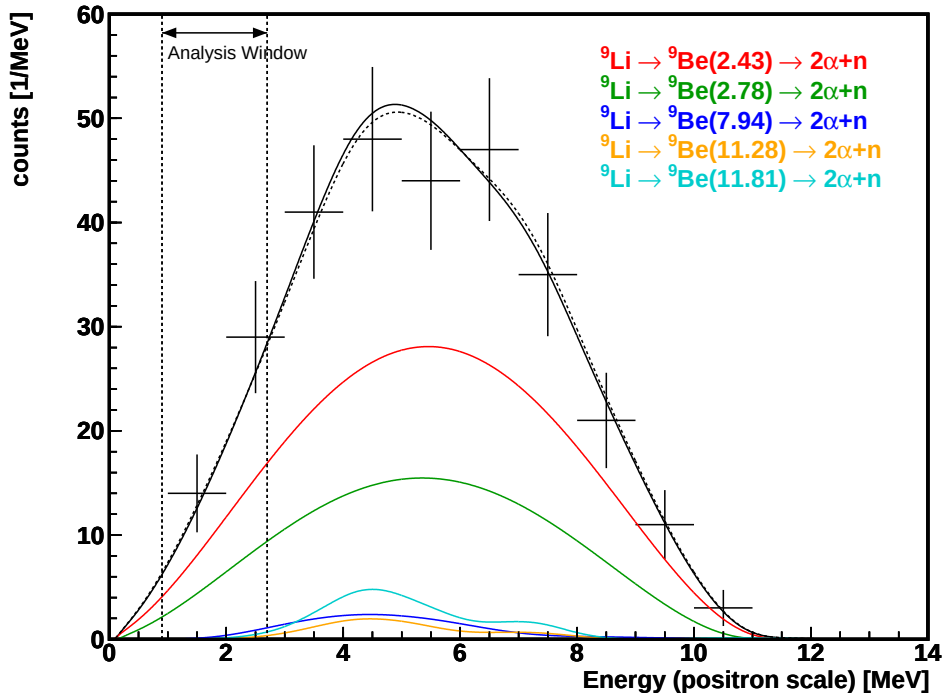

Figure 6.16: ^{9}Li Event Visible Energy Spectrum

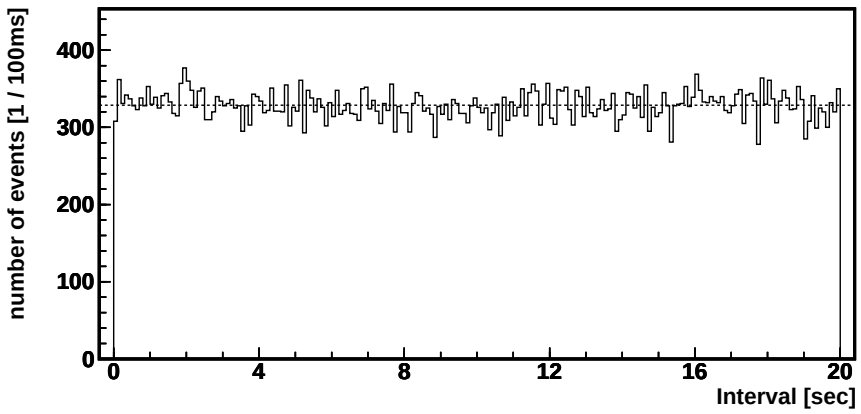

Figure 6.17: Prompt-Delayed Event Interval Distribution of Off-time Coincidence

From the spectrum, the fraction of ^{9}Li decay events in the geo-neutrino analysis window (from 0.9MeV to 2.7 MeV) is calculated to be 10.06%. If the 7.94 MeV state is excluded from the neutron emitting state, the fraction is calculated to be 10.15%, making negligible difference. The number of events in this window is then estimated to be 0.52±0.092.

6.3 Accidental Coincidence Backgrounds

The rate of accidental coincidence of non-correlated events are estimated by applying the same selection criteria as neutrino selection but different time window (off-time window). The time window for delayed signals are set to be from 10 msec to 20 sec. To reduce statistical errors, the time window is set much longer than that of neutrino selection.

Figure 6.17 shows the distribution of intervals between prompt signals and delayed signals. The distribution is flat therefore we conclude that no significant number of time correlated events are included in the samples. From this off-time coincidence, the rate of accidental coincidence backgrounds is estimated to be 1.64±0.0064 events/livetime.

Figure 6.19 shows the distribution of prompt and delayed signal vertices. High event rate around the fiducial volume boundary is due to radioactive contamination of the balloon and/or the balloon supporting structure, and gamma particles from the outside of the balloon (such as PMT, PMT supporting structure, stainless vessel etc.). High event rate along the z-axis is probably due to thermometers installed along the z-axis and cables connected to the thermometers.

Figure 6.19 shows the distribution of prompt and delayed signal energy. Unlike the neutrino event candidates, the spectrum of delayed signal energy does not have characteristic shape. The shape of prompt signal spectrum has similar structure as single event spectrum, although non-uniform distribution of sources changes the spectrum shape.

The rate of accidental coincidences is also estimated independently by random pairing

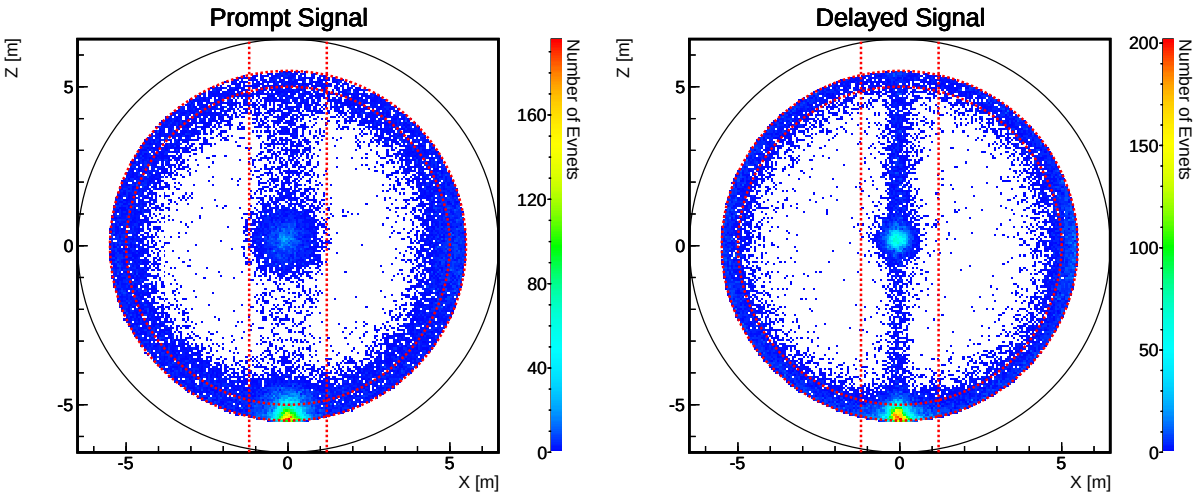

Figure 6.18: Vertex Distribution of Accidental Coincidence Events

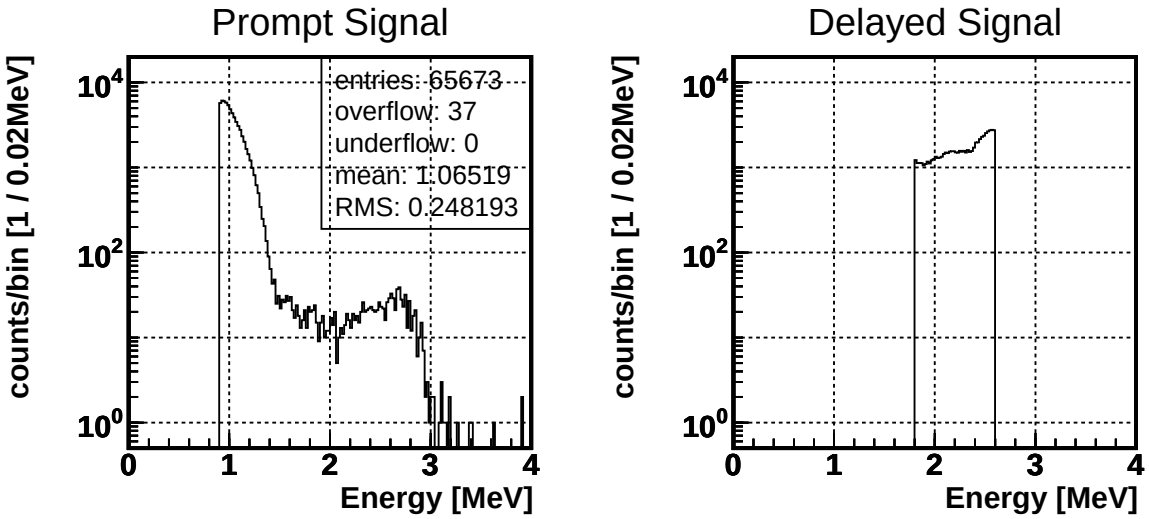

Figure 6.19: Energy Distribution of Accidental Coincidence Events

of single events and by a swapping method that swaps the selection criteria of prompt signal and delayed signal. Even though estimation precisions of these methods are not as good as the precision of the off-time method, the results are consistent with the off-time method estimation, implying that the samples of off-time method does not include time-correlated events.

6.4 Correlated Event Backgrounds by Radioactivity

6.4.1 Radioactive Contamination of LS

There are various types of radioactive sources in the KamLAND Liquid Scintillator (LS). As commonly seen in the natural environment, radioactive isotopes in the ^{238}U decay series, ^{232}Th decay series and ^{40}K are also abundant in the KamLAND LS. Among isotopes in the ^{238}U decay series, the LS contains large amount of ^{210}Pb, which is on downstream of ^{222}Rn. In the ^{232}Th decay series, ^{208}Tl emits 2.6 MeV gamma particles; this energy is high enough that gamma particles far from the fiducial volume can reach the sensitive region. The LS also includes large amount of ^{85}Kr at low energy region. Above 5 MeV, isotopes produced by muon spallation dominate the spectrum.

^{238}U and ^{232}Th Decay Rate Estimation with Bi-Po Coincidences

Under isotope equilibrium condition, the amount of ^{238}U and ^{232}Th are estimated by measuring Bi-Po cascade decay coincidences. The lifetime of ^{214}Po, which is in the U decay series, is 164 μsec, thus preceding ^{214}Bi beta decay and following ^{214}Po alpha decay make taggable coincidence events. Similarly, The lifetime of ^{212}Po, which is in the Th decay series, is 299 nsec, thus preceding ^{212}Bi beta decay and following ^{212}Po alpha decay make taggable coincidence events. The branching ratio of this decay mode is 64.06%.

$$^{214}\mathrm{Bi} \xrightarrow{Q_\beta=3.272\mathrm{MeV}} {}^{214}\mathrm{Po}\ (164.3\mu\mathrm{sec}) \xrightarrow{Q_\alpha=7.687\mathrm{MeV}} {}^{210}\mathrm{Pb}$$

$$^{212}\mathrm{Bi} \xrightarrow[64.06\%]{Q_\beta=2.254\mathrm{MeV}} {}^{212}\mathrm{Po}\ (299\mathrm{nsec}) \xrightarrow{Q_\alpha=8.784\mathrm{MeV}} {}^{208}\mathrm{Pb}$$

Table 6.5 summarizes the event selection criteria. Because of large quenching effect of the liquid scintillator, visible energy of alpha particles is considerably reduced from its energy deposit, at around 1/10. The energy window for the delayed signals are set lower accordingly.

Table 6.5: Bi-Po Coincidence Event Selection Criteria

	^{214}Bi-^{214}Po (U series)	^{212}Bi-^{212}Po (Th series)
Prompt Signal Energy	$1.5\mathrm{MeV} \leq E_p < 4.0\mathrm{MeV}$	$1.0\mathrm{MeV} \leq E_p < 3.0\mathrm{MeV}$
Delayed Signal Energy	$0.3\mathrm{MeV} \leq E_d < 0.8\mathrm{MeV}$	$0.3\mathrm{MeV} \leq E_d < 1.0\mathrm{MeV}$
Prompt-Delayed Distance	$\Delta R < 100\mathrm{cm}$	$\Delta R < 100\mathrm{cm}$
Prompt-Delayed Interval	$5\mu\mathrm{sec} \leq \Delta T < 1000\mu\mathrm{sec}$	$0.5\mu\mathrm{sec} \leq \Delta T < 1.0\mu\mathrm{sec}$

Figure 6.20 and Figure 6.21 show the energy distribution of the selected events. 10054 events and 420 events are selected for the ^{214}Bi-^{214}Po (U series) and ^{212}Bi-^{212}Po (Th series) coincidences, respectively. Since the number of ^{212}Bi-^{212}Po coincidence events is small, energy spectrum without fiducial volume cut is also shown in the figure. The spectra with

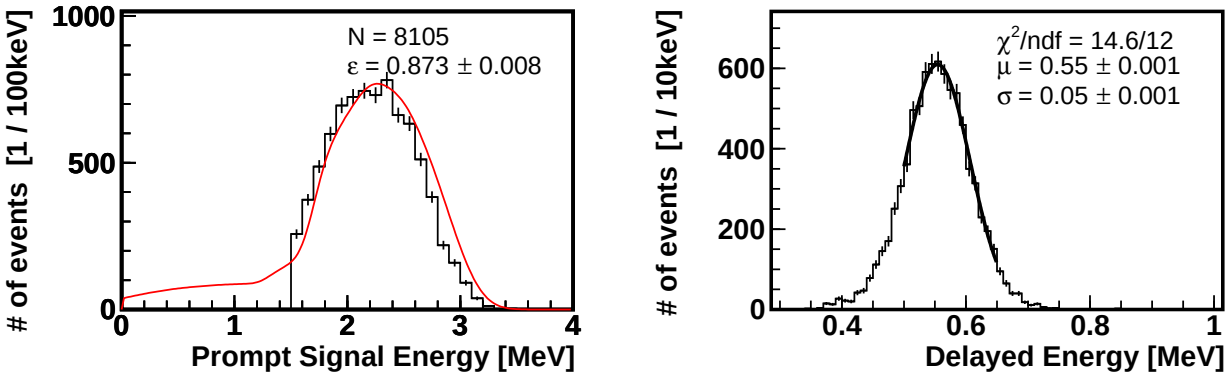

Figure 6.20: Energy Distribution of U Series Bi-Po Coincidence Events

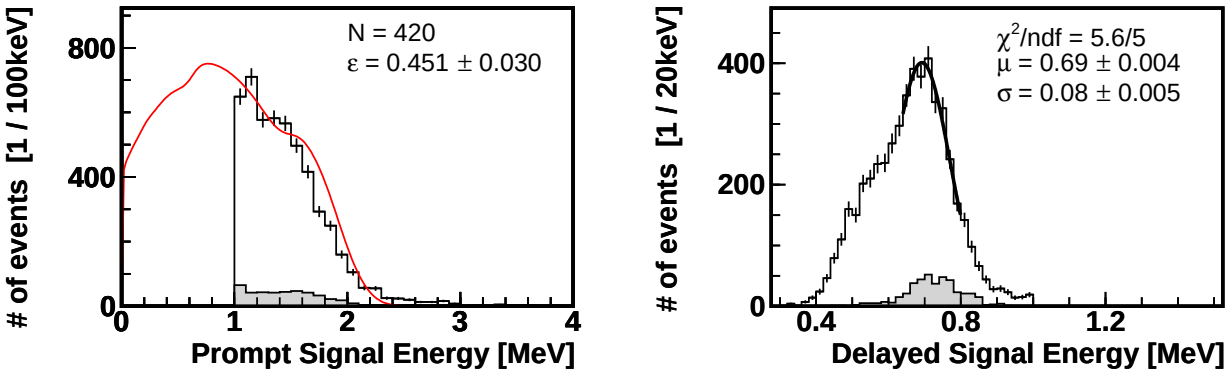

Figure 6.21: Energy Distribution of Th Series Bi-Po Coincidence Events. Black line histogram shows the energy spectrum without fiducial volume cut, and shaded histogram shows the energy spectrum of events within the fiducial volume.

fiducial volume cut is indicated with a shaded histogram. From the delayed signal energy spectra, the quenching factors of alpha particles in the KamLAND LS are estimated to be 14.0 at 7.7 MeV and 12.7 at 8.8 MeV.

Theoretically calculated spectra are also shown in those figures. Since the prompt signals generally consist of a beta particle and gamma particles, the visible energy spectra are sum of visible energies of these particles. The visible energy of beta and gamma particles are calculated with the energy scale discussed in Section 4.7.

$$E_{\rm vis} = \sum_{\rm branch} \{R_{e^-}(E_\beta) \cdot E_\beta + R_\gamma(E_\gamma) \cdot E_\gamma\} \tag{6.4}$$

where R is the conversion factor from kinetic energy to visible energy, determined by the energy scale study. In the beta decay of ^{214}Bi, there are a large number of beta decay branches with small branching-ratio, therefore 40 beta decay branches are selected and

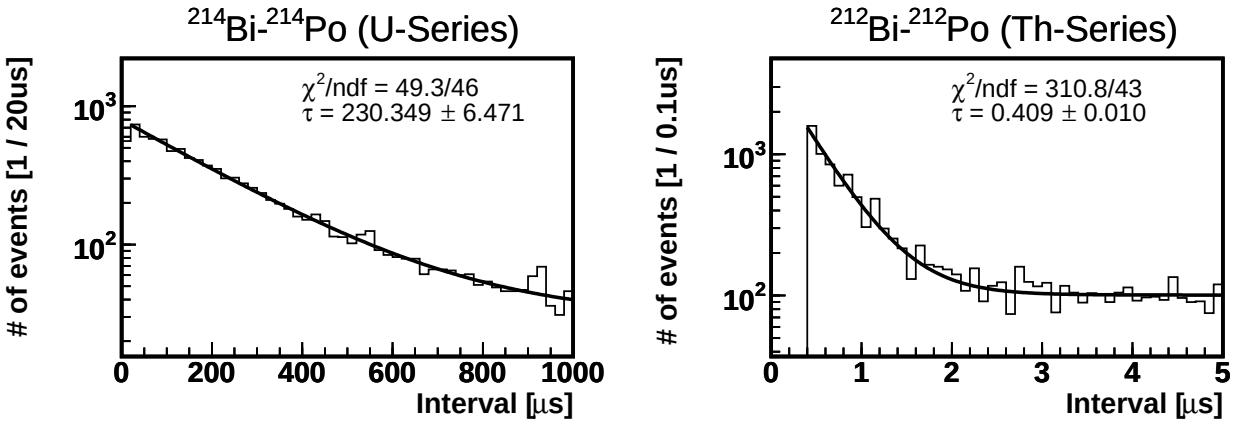

Figure 6.22: Prompt-Delayed Interval of Bi-Po Coincidence Events

included into the calculation. The selected branches' branching ratios add up to 100.46%, here the excess over 100% is due to uncertainties of estimated branching ratios.

With the calculated spectra, detection efficiencies by the energy cuts are estimated to be 0.873±0.008 and 0.451±0.030 for the ^{214}Bi-^{214}Po (U series) and ^{212}Bi-^{212}Po (Th series) coincidences respectively. The errors are estimated using the energy scale error at the lower threshold energies, to be 0.5%.

Figure 6.22 shows the distribution of prompt-delayed signal intervals. Decay time constants of ^{212}Po and ^{214}Po are estimated with the interval distribution by fitting an exponential plus constant background function, to be 230.3±6.5 μsec and 409±10 nsec, respectively. These estimated decay time constants are consistent with the lives of these isotopes, 237.0 μsec and 431.4 ns. The selection efficiencies by the time cuts are calculated from the lives, to be 0.964±0.001 and 0.297±0.002 respectively. The errors are assigned by taking the differences of the fitted decay time constants from the half-lives.

Figure 6.23 shows the distribution of prompt-delayed signal distances of the ^{214}Bi-^{214}Po coincidence events. Accidental coincidence events are estimated using events in distance 250cm $\leq \Delta R <$ 300cm, and then extrapolated to the signal region $\Delta R <$ 100cm. From the distribution, the efficiencies of the spatial correlation cuts are estimated to be 82.7 ± 1.0%. Although the detection efficiency is estimated using the ^{214}Bi-^{214}Po coincidence events, the same efficiency value is used for ^{212}Bi-^{212}Po coincidence events, because the difference in vertex correlation is considered to be small (compared to the statistical error of ^{212}Bi-^{212}Po coincidence events).

Figure 6.24 shows the distribution of prompt signal vertices. The vertices of ^{212}Bi, which is in the U decay series, are concentrated along the center Z axis. Contamination along the Z axis is considered to be caused by thermometers installed along the Z axis, wiring of the thermometers, and/or Rn injection during calibration. The vertices of ^{214}Bi, which is in the Th decay series, are rather uniformly distributed in the fiducial volume.

The number of selected events, selection efficiency, and the estimated decay rates are summarized in the Table 6.6.

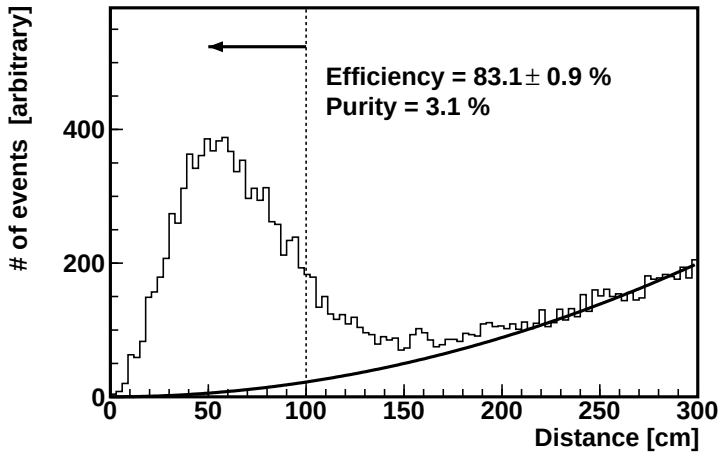

Figure 6.23: Prompt-Delayed Distance of Bi-Po Coincidence Events

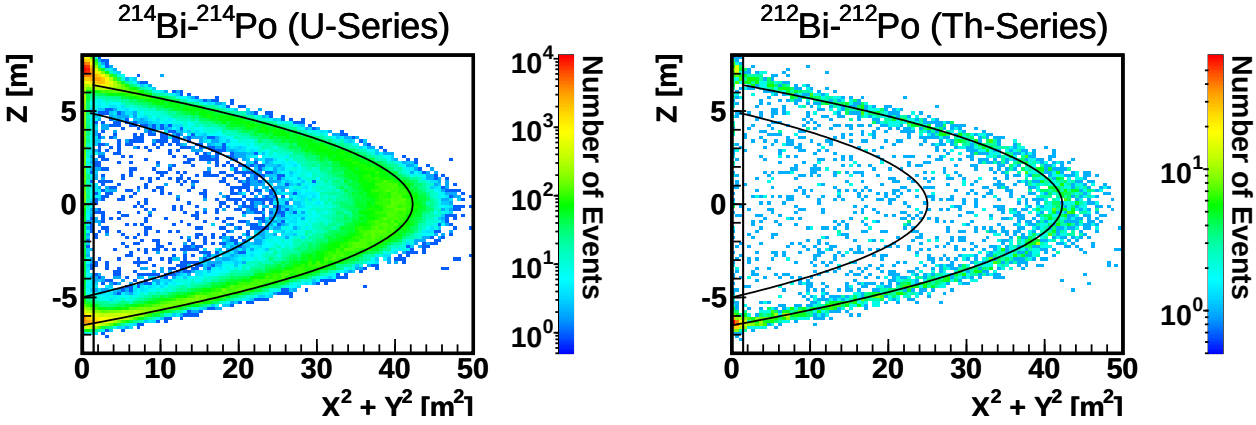

Figure 6.24: Vertex Distribution of Bi-Po Coincidence Events

Singles Spectrum Study

In the U decay series, there are two long-lived isotopes, ^{226}Ra and ^{210}Pb (see Appendix C). Due to existence of these isotopes, the assumption of isotope equilibrium might not be satisfied; thus other estimation is needed. Since there is no short-lived isotopes in the series from ^{238}U to ^{226}Ra and from ^{210}Pb to ^{206}Pb (the end of the U series) that make detectable coincidence events, singles spectrum is used to estimate the rate of these isotopes. Other radioactive sources are also studied with the singles spectrum.

Figure 6.25 shows the singles spectrum with 500 cm radius fiducial volume. Muon spallation cuts are not applied, except for the 2 msec post muon veto. Spectra of the U series isotopes, Th series isotopes, and muon spallation products, are also shown in the figure. For the U series and Th series isotopes, the rates estimated with the Bi-Po coincidence method are used. To calculate the spectra, all branches of alpha, beta and

Table 6.6: Summary of Bi-Po Coincidence Event Selection

	^{214}Bi-^{214}Po (U series)	^{212}Bi-^{212}Po (Th series)
Number of Selected Events	10054	420
Branching Ratio	1.0	0.641
Energy Cut Efficiency	0.873±0.008	0.451±0.030
Distance Cut Efficiency	0.831±0.009	0.831±0.009
Interval Cut Efficiency	0.964±0.001	0.297±0.002
Total Detection Efficiency	0.699±0.01	0.071±0.005
Estimated Number of Decays	$(1.44 \pm 0.02) \times 10^4$	$(5.92 \pm 0.42) \times 10^3$

gamma decays with branching ratio more than 0.01% are all listed and traced, and energy deposition of alpha, beta and gamma particles are accumulated with an appropreate energy conversion based on the energy scale. The level structure and branching ratio data are taken from an isotope table compiled in 1996 (Eighth Edition) [69]. For the spectra of the muon spallation products, production rate reported in T.Hagner *et al.* (2000) [52] are used, and the same method as the U/Th series isotpes are applied to calculating the visible energy spectra. Details of muon spallation products are discussed in Section 6.2.

The decay rate of ^{210}Pb is estimated by fitting the theoretical spectra at the range from 0.8MeV to 1.2MeV. As shown in Figure 6.25, ^{210}Bi dominates the spectrum at this energy range, and the fit explains the observed spectrum very well. The estimated rate is 1.34×10^9 decays/livetime. However, it should be noted that the estimated rate is very sensitive to small fluctuation of the energy scale, because the fit uses only a small tail of the ^{210}Bi spectrum.

For the series from ^{238}U to ^{226}Ra, there is no conspicuous peak that can be identified from the spectrum. Thus only an upper limit is given. By scaling the theoretical spectrum not to exceed the observed spectrum at any energy, the upper limit is set to be 2.5×10^6 decays/livetime, by the beta decay of ^{234}Pa at around 1.7 MeV.

Low Energy Region

Radioactivity of the LS below the threshold (0.9MeV) is studied with a special low threshold run conducted on April 18 2004. The data is collected with prescaled triggers to deal with very high event rate. Figure 6.26 shows the observed spectrum and fit to the spectrum with known sources. The low energy region is dominated by ^{210}Bi, ^{210}Po and ^{85}Kr. Below 0.2 MeV, the spectrum is overwhelmed by decays of ^{14}C.

From the fit to the spectrum, the number of ^{210}Pb decays is estimated to be $(0.972 \pm 0.035) \times 10^9$ decays/livetime (^{210}Bi) or $(0.968 \pm 0.027) \times 10^9$ decays/livetime (^{210}Po). This decay rate differs from the estimation made by singles spectrum of ^{210}Bi discussed above. The discrepancy might be reconciled by taking account of non-equilibrium of ^{210}Bi decay and ^{210}Po; the estimation based on the accumulated single spectrum integrates all ^{210}Bi

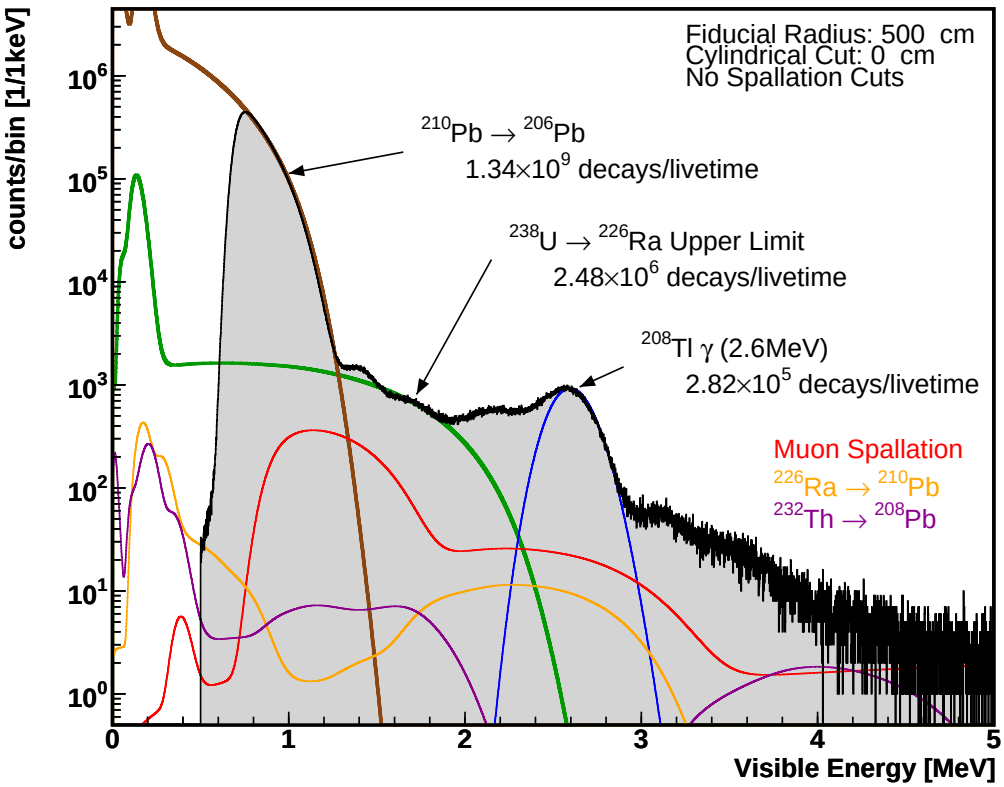

Figure 6.25: Singles Spectrum Study

decays since the KamLAND epoch, while the estimation presented here looks at only a moment on April 18 2004. The halflife of ^{210}Po is 138 days, which is comparable to this time scale. As already mentioned, the estimation of ^{210}Bi rate is not reliable due to its sensitivity to energy scale fluctuation, and as mentioned below, the estimation based on the low energy region is not reliable as well due to biases of vertex finding. These uncertainties also accounts for the discrepancy.

As described later, the alpha particles emitted by decays of ^{210}Po make serious backgrounds for geo-neutrino observation. Hence the ^{210}Po decay rate is estimated in further detail.

Firstly, possible biases of event reconstruction of such low energy events is studied. As demonstrated in Chapter 4, energy of this low energy events is proved to be well reconstructed with the ^{203}Hg (279keV γ) calibration data. However, reconstruction of vertices is found to be biased. Figure 6.27 shows the reconstructed positions of ^{203}Hg calibration source located on several positions along the Z axis, in comparison with those of the ^{68}Ge calibration data. ^{203}Hg data shows $<$ 16cm reconstructed vertex shift at Z=500 cm. This vertex bias makes 9.9% error on estimation of ^{210}Po decay rate.

The ^{210}Po decay rate is estimated by basically comparing the theoretical spectra and the observed spectrum, by means of fitting. The result is sensitive to the shapes of

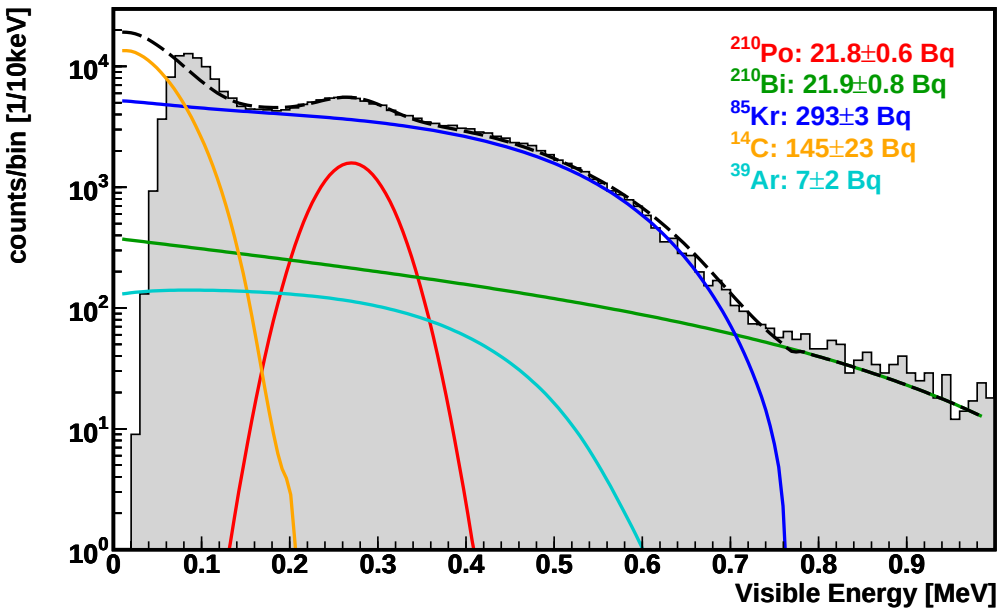

Figure 6.26: Radioactivity below Threshold

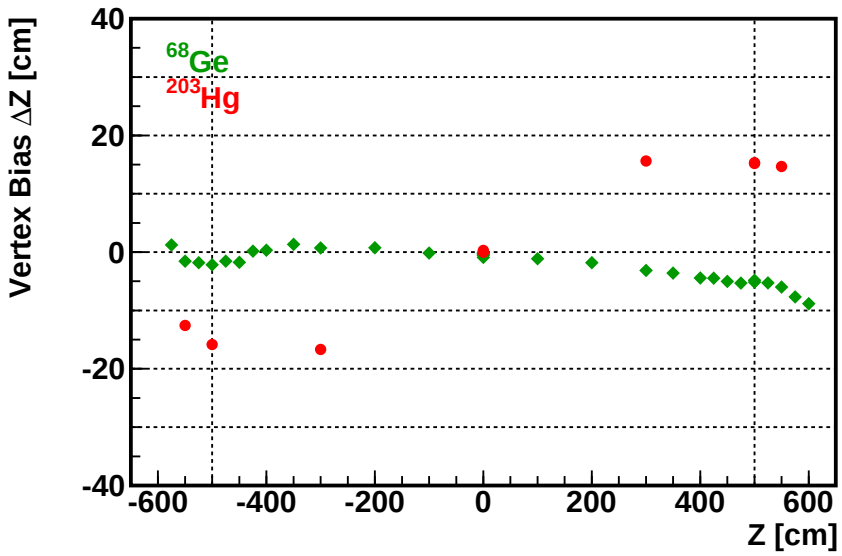

Figure 6.27: Bias in Vertex Reconstruction of Low Energy Events

the spectra, thus the estimation is unreliable due to the energy dependent vertex biases because it modify the spectrum shape. Uncertainties of other background source (^{210}Bi, ^{85}Kr, ^{39}Ar, ^{14}C) spectrum shape and rate also affect the estimation of ^{210}Po decay rate.

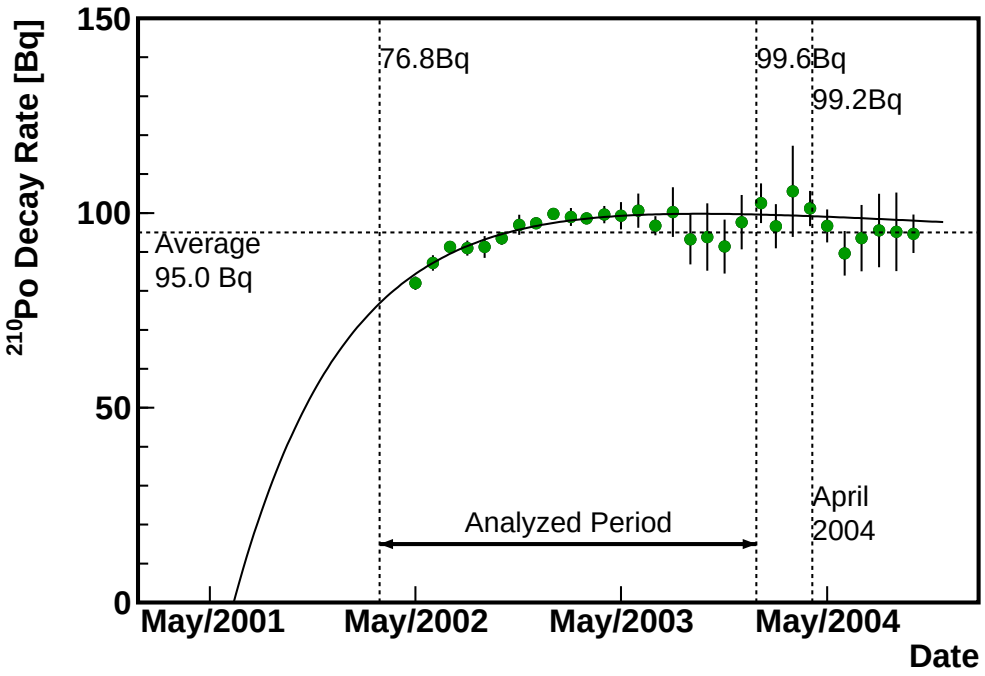

Figure 6.28: Time Variation of ^{210}Po Decay Rate

As an alternative estimation for comparison, the ^{210}Po decay rate is estimated by subtracting linear background; i.e., we fit the observed spectrum with the ^{210}Po shape plus strait background line, at the ^{210}Po energy range. The result is 25.9 ± 0.6 Bq, which is significantly different from the global fit. We include this discrepancy in the error of ^{210}Po decay rate estimation.

Finally, we estimated the effect of non-equilibrium of ^{210}Po decay. Since the ^{210}Po is below our normal trigger threshold, special runs that were conducted to monitor the detector condition before and after weekly calibration source deployment are used. In those runs, only NSum data, which represents the number of PMT hits, is recorded by the trigger circuitry, and no waveform information is available. Thus event vertices are not reconstructed, hence the fiducial volume cut is not applied.

Figure 6.28 shows the time variation of ^{210}Po decay rate. The variation is well explained with a non-equilibrium line, which is indicated with a solid line in the figure. Using the fitted non-equilibrium line, the average ^{210}Po decay rate throughout the entire KamLAND livetime is estimated to be 95.0 Bq, which is 4.2% smaller than the rate as of April 2004.

Summary

Table 6.7 summarizes the estimated radioactive contamination of the LS.

Table 6.7: Radioactive Contamination of KamLAND LS

Isotope	Method	Number of Decays / Livetime
^{238}U $\rightarrow^{226}$ Ra	^{234}Pa single spectrum	$< 2.48 \times 10^{6}$
^{226}Ra $\rightarrow^{210}$ Pb	^{214}Bi-^{214}Po coincidence	$(1.44 \pm 0.02) \times 10^{4}$
^{210}Pb $\rightarrow^{206}$ Pb	^{210}Bi single spectrum	$\sim 1.34 \times 10^{9}$
	^{210}Po single spectrum	$(1.06 \pm 0.15) \times 10^{9}$
^{232}Th $\rightarrow^{208}$ Pb	^{212}Bi-^{212}Po coincidence	$(5.92 \pm 0.42) \times 10^{3}$

6.4.2 Cascade Decay Backgrounds

Cascade decays of short-lived nuclei make delayed coincidence events that might mimic anti-neutrino events. With prompt-delayed signal interval cut ΔT, rejection efficiency $\tilde{\varepsilon}$ of the cascade decays whose time constant τ is given by

$$\tilde{\varepsilon} = 1 - \int_0^{\Delta T} \frac{1}{\tau} e^{-t/\tau} dt \;=\; e^{-\Delta T/\tau} \tag{6.5}$$

Based on the estimated decay rates listed in Table 6.7, rejection rates required to reduce the cascade decay event less than 0.1 events/livetime are calculated, as shown in Table 6.8 . For each required rejection rate, lifetime of cascade decays that meets the rejection rate only with the 1 msec timing cut is calculated with (6.5), as also shown in Table 6.8.

Table 6.8: Required Rejection Rates and Lives of Cascade Decays

Isotope	Required Rejection Rate	Lives Required Longer Than
$^{238}\mathrm{U} \rightarrow^{226}$ Ra	4.0×10^{-8}	6.9 hour
$^{226}\mathrm{Ra} \rightarrow^{210}$ Pb	6.9×10^{-6}	155 sec
$^{210}\mathrm{Pb} \rightarrow^{206}$ Pb	7.5×10^{-11}	154 day
$^{232}\mathrm{Th} \rightarrow^{208}$ Pb	1.7×10^{-5}	58.8 sec

By seeking a Table of Isotopes [69], all cascade decays whose lifetime is shorter than the required lifetime are listed as shown below;

$\underline{^{238}\mathrm{U} \rightarrow^{226} \mathrm{Ra}}$

$$\xrightarrow[100\%]{} {}^{234}\mathrm{Th} \xrightarrow{Q_\beta=0.273\mathrm{MeV}} {}^{234}\mathrm{Pa}^* \;(1.17\mathrm{min}) \xrightarrow{Q_\beta=2.197\mathrm{MeV}} {}^{234}\mathrm{U}$$

$$\xrightarrow[100\%]{} {}^{234}\mathrm{Th} \xrightarrow[0.16\%]{Q_\beta=0.273\mathrm{MeV}} {}^{234}\mathrm{Pa} \;(6.7\mathrm{hour}) \xrightarrow{Q_\beta=2.197\mathrm{MeV}} {}^{234}\mathrm{U}$$

$$\xrightarrow[0.16\%]{} {}^{234}\mathrm{Pa} \xrightarrow{Q_\beta=2.197\mathrm{MeV}} {}^{234}\mathrm{U}^*(1421) \;(33.5\mu\mathrm{sec}) \xrightarrow{E_\gamma=1.4\mathrm{MeV}} {}^{234}\mathrm{U}$$

$\underline{^{226}\mathrm{Ra} \rightarrow^{210} \mathrm{Pb}}$

$$\xrightarrow[100\%]{} {}^{218}\mathrm{Po} \xrightarrow[0.021\%]{Q_\beta=0.264\mathrm{MeV}} {}^{218}\mathrm{At}\ (1.6\mathrm{sec}) \xrightarrow[99.9\%]{Q_\alpha=6.874\mathrm{MeV}} {}^{214}\mathrm{Bi}$$

$$\xrightarrow[100\%]{} {}^{218}\mathrm{Po} \xrightarrow[0.021\%]{Q_\beta=0.264\mathrm{MeV}} {}^{218}\mathrm{At}\ (1.6\mathrm{sec}) \xrightarrow[0.1\%]{Q_\beta=2.883\mathrm{MeV}} {}^{218}\mathrm{Rn}$$

$$\xrightarrow[100\%]{} {}^{214}\mathrm{Bi} \xrightarrow{Q_\beta=3.272\mathrm{MeV}} {}^{214}\mathrm{Po}\ (164.3\mu\mathrm{sec}) \xrightarrow{Q_\alpha=7.687\mathrm{MeV}} {}^{210}\mathrm{Pb}$$

$$\xrightarrow[2.1\times10^{-6}\%]{} {}^{218}\mathrm{Rn} \xrightarrow{Q_\alpha=7.263\mathrm{MeV}} {}^{214}\mathrm{Po}\ (164.3\mu\mathrm{sec}) \xrightarrow{Q_\alpha=7.687\mathrm{MeV}} {}^{210}\mathrm{Pb}$$

$\underline{^{210}\mathrm{Pb} \rightarrow^{206} \mathrm{Pb}}$

$$\xrightarrow[100\%]{} {}^{210}\mathrm{Pb} \xrightarrow{Q_\beta=0.635\mathrm{MeV}} {}^{210}\mathrm{Bi}\ (5.0\mathrm{day}) \xrightarrow{Q_\beta=1.162\mathrm{MeV}} {}^{210}\mathrm{Po}$$

$$\xrightarrow[1.9\times10^{-6}\%]{} {}^{210}\mathrm{Pb} \xrightarrow{Q_\alpha=3.792\mathrm{MeV}} {}^{206}\mathrm{Hg}\ (8.15\mathrm{min}) \xrightarrow{Q_\beta=1.307\mathrm{MeV}} {}^{206}\mathrm{Tl}$$

$$\xrightarrow[100\%]{} {}^{210}\mathrm{Bi} \xrightarrow[1.3\times10^{-4}\%]{Q_\alpha=5.036\mathrm{MeV}} {}^{206}\mathrm{Tl}\ (4.199\mathrm{sec}) \xrightarrow{Q_\beta=1.533\mathrm{MeV}} {}^{206}\mathrm{Pb}$$

$$\xrightarrow[100\%]{} {}^{210}\mathrm{Bi} \xrightarrow{Q_\beta=1.162\mathrm{MeV}} {}^{210}\mathrm{Po}\ (138\mathrm{day}) \xrightarrow{Q_\alpha=5.047\mathrm{MeV}} {}^{206}\mathrm{Pb}$$

$\underline{^{232}\mathrm{Th} \rightarrow^{208} \mathrm{Pb}}$

$$\xrightarrow[100\%]{} {}^{224}\mathrm{Ra} \xrightarrow{Q_\alpha=5.685\mathrm{MeV}} {}^{220}\mathrm{Rn}\ (55.6\mathrm{sec}) \xrightarrow{Q_\alpha=6.288\mathrm{MeV}} {}^{216}\mathrm{Po}$$

$$\xrightarrow[100\%]{} {}^{220}\mathrm{Rn} \xrightarrow{Q_\alpha=6.288\mathrm{MeV}} {}^{216}\mathrm{Po}\ (145\mathrm{msec}) \xrightarrow{Q_\alpha=6.779\mathrm{MeV}} {}^{212}\mathrm{Pb}$$

$$\xrightarrow[100\%]{} {}^{212}\mathrm{Bi} \xrightarrow[64.06\%]{Q_\beta=2.254\mathrm{MeV}} {}^{212}\mathrm{Po}\ (299\mathrm{nsec}) \xrightarrow{Q_\alpha=8.784\mathrm{MeV}} {}^{208}\mathrm{Pb}$$

In the neutrino event selection, we require the prompt signal energy be greater than 0.9 MeV. This criterion rejects ^{234}Th $\rightarrow^{234}$ Pa* $\rightarrow^{234}$ U, ^{234}Th $\rightarrow^{234}$ Pa $\rightarrow^{234}$ U, ^{234}Pa $\rightarrow^{234}$ U* $\rightarrow^{234}$ U, ^{218}Po $\rightarrow^{218}$ At $\rightarrow^{214}$ Bi and ^{218}Po $\rightarrow^{218}$ At $\rightarrow^{218}$ Rn. Similarly, the requirement for the delayed signal energy, greater than 1.8MeV, rejects ^{210}Pb $\rightarrow^{210}$ Bi $\rightarrow^{210}$ Po. By combining branching ratios and rejection efficiencies of the time cut, ^{210}Pb $\rightarrow^{206}$ Hg $\rightarrow^{206}$ Tl and ^{210}Bi $\rightarrow^{206}$ Tl $\rightarrow^{206}$ Pb are suppressed to an ignorable level.

For the rest, we estimate rejection efficiencies of the energy cut. All of the rest cascade decays have alpha decay as their delayed signal, visible energy of which is considerably reduced from the decay Q values due to the quenching effect. In particular, alpha decays of the ^{212}Bi $\rightarrow^{212}$ Po $\rightarrow^{208}$ Pb and ^{210}Bi $\rightarrow^{210}$ Po $\rightarrow^{206}$ Pb cascades do not emit associated

gamma particles, thus all decay energy are carried by the alpha particle. The alpha energies are 8.784 MeV and 5.047 MeV respectively, which are quenched to less than 0.7 MeV in the LS as shown in a previous section. Taking account of the energy resolution 7.3 $\%/\sqrt{E_{\rm vis}}$, the alpha visible energies are 16σ away from the delayed energy window, resulting in negligible contribution to the neutrino event candidates.

If some part of decay energy is carried by gamma particles, the effective quenching factor is not as large as discussed above, because quenching factor of gamma particles is much smaller than that of alpha particle. Following is a list of gamma particles emitted in the delayed signal of the remaining cascades;

^{214}Po (164.3μsec) $\xrightarrow{Q_\alpha=7.687\text{MeV}}$ ^{210}Pb

E_γ [MeV]	BR [%]	$E_{\rm vis}$ [MeV]
0	99.9895	0.59
0.80	0.0104	1.33
1.10	6.0×10^{-5}	1.60

^{220}Rn (55.6sec) $\xrightarrow{Q_\alpha=6.288\text{MeV}}$ ^{216}Po

E_γ [MeV]	BR [%]	$E_{\rm vis}$ [MeV]
0	99.89	0.48
0.55	0.11	0.99

^{216}Po (145msec) $\xrightarrow{Q_\alpha=6.779\text{MeV}}$ ^{212}Pb

E_γ [MeV]	BR [%]	$E_{\rm vis}$ [MeV]
0	99.9981	0.52
0.80	0.0019	1.25

In this calculation, a conservative quenching factor 13.1, which is obtained from 7.7 MeV alpha particle of ^{214}Po, is used for all alpha particles. The real quenching factors are larger because of lower alpha particle energy. Except for the 1.1 MeV gamma emission from ^{214}Po, the maximum visible energy is 1.33 MeV, which is 5.6 σ away from the delayed signal energy window. Compared with the required reduction rate, contribution of these cascade decays are negligible. The ^{214}Po decay with 1.1 MeV gamma emission is also negligible because of its small branching ratio, compared with the required reduction rate.

6.4.3 Spontaneous Fissions and Neutron Emitting Decays

Spontaneous fissions, neutron emissions, and exotic decays are studied because these processes might make correlated multiple signals, some of which pass our delayed coincidence

Table 6.9: Spontaneous Fission and Uncommon Decays

Group	Isotope	Mode	Branching Ratio	Number of Events
^{238}U $\rightarrow^{226}$ Ra	^{238}U	Spontaneous Fission	5.45×10^{-5}%	< 1.36
	^{234}U	Spontaneous Fission	1.64×10^{-9}%	$< 4.1 \times 10^{-5}$
	^{234}U	$^{234}\mathrm{U} \rightarrow \mathrm{Ne} + \mathrm{X}$	9×10^{-12}%	$< 2.3 \times 10^{-7}$
	^{234}U	$^{234}\mathrm{U} \rightarrow \mathrm{Mg} + \mathrm{X}$	1.4×10^{-11}%	$< 3.5 \times 10^{-7}$
	^{230}Th	Spontaneous Fission	$< 3.8 \times 10^{-12}$%	$< 9.5 \times 10^{-8}$
^{226}Ra $\rightarrow^{210}$ Pb	^{210}Tl	$^{210}\mathrm{Tl} \rightarrow {}^{209}\mathrm{Pb} + \mathrm{n}$	7×10^{-3}%	1.7×10^{-6}
^{232}Th $\rightarrow^{208}$ Pb	^{232}Th	Spontaneous Fission	$< 1.8 \times 10^{-9}$%	$< 5.8 \times 10^{-8}$
	^{228}Th	$^{228}\mathrm{Th} \rightarrow {}^{20}\mathrm{O} + \mathrm{n} + \ldots$	1.13×10^{-11}%	3.6×10^{-10}
	^{224}Ra	$^{224}\mathrm{Ra} \rightarrow {}^{14}\mathrm{C} + \mathrm{X}$	$< 4.3 \times 10^{-9}$%	$< 1.4 \times 10^{-7}$

event selection.

By seeking an isotope table published in 1996 [69], all such processes in the U and Th decay series are listed as shown in Table 6.9. Comparing with the estimation of radioactivity summarized in Table 6.7, we find that only the ^{238}U spontaneous fission process might make detectable number of events, <1.36 events/livetime.

Spontaneous fissions are accompanied by emission of prompt neutrons and gamma particles, as well as emission of fission fragments and even more consequent particle emissions by fission fragment decay. If just one neutron is emitted by a fission, we improperly tag the event as a neutrino event candidate.

It is known that neutron multiplicity distribution is well approximated with a Gaussian distribution with width of $\sigma \sim 1.08$, regardless of fissile nuclei and regardless of neutron-induced or spontaneous [57]. According to an recent compilation of spontaneous fission data [58], the mean number of prompt neutrons from spontaneous fission of ^{238}U is reported to be 1.98±0.03 and the width is 0.89±0.08. From this estimation, probability of emitting just one neutron is calculated to be 0.25, leading to estimated number of delayed coincidence events by spontaneous fission to be <0.34 events/livetime.

The estimated number is further reduced by considering energy of prompt gamma particles. Prompt gamma particles have an role of decreasing angular momentum of excited fission fragments, and in competition with neutron emission, gamma particles carry more energy with possessing high angular momentum. Although the total gamma particle energy depends on fragment masses, it is likely as high as 7 to 9 MeV due to inhibition of neutron emission. Prompt gamma particles are emitted within $10^{-10} \sim 10^{-6}$ seconds from fission and typically about 8 gamma particles are emitted per fission with an average of 1 MeV per gamma particle [57].

Experimental data of prompt gamma particles from ^{238}U spontaneous fission is not available in hand at present. An empirical formula constructed with measurements of spontaneous fissions of some other nuclei suggests that 6.36 ± 0.47 prompt gamma particles with average energy of 0.95 ± 0.07 MeV apiece are emitted from spontaneous fission

Table 6.10: Atomic Composition of LS

Atom	Number/kton	Ratio in Number
H	8.470×10^{31}	66.30%
C	4.302×10^{31}	33.68%
N	1.593×10^{28}	0.01247%
O	7.064×10^{27}	0.005530%

of ^{238}U, resulting in 6.06 ± 0.03 MeV of total gamma particle energy [59]. Distribution of gamma particle energy is not provided; assuming a Gaussian distribution, the probability of emitting gamma particles with their total energy being in the geo-neutrino analysis window (0.9 MeV to 2.7 MeV) becomes maximum when its width σ is 4.23 MeV, giving 10.2% fraction in the geo-neutrino window. Therefore, the number of ^{238}U spontaneous fission events in the geo-neutrino event candidates is estimated to be <0.035 events/livetime.

6.4.4 Nuclear Reaction Backgrounds

Nuclear reactions that produce neutrons, such as (α,n) and (γ,n), make the same signature of events as that of neutrino events. In particular ^{13}C(α,n)^{16}O reaction makes significant contribution to the neutrino event candidates, hence this process is discussed in detail in this section.

Chemical Composition of LS

Nuclear reactions involve nuclei as a target, thus the chemical composition of the LS needs to be understood in detail. The KamLAND LS is composed of 80.2% of dodecane ($C_{12}H_{26}$), 19.8% of pseudocumene (1,2,4-trimethylbenzene, C_9H_{12}), and 1.52 g/litter of PPO (2,5-diphenyloxazole, $C_{15}H_{11}NO$). Since the LS was purified before it was filled into the KamLAND detector with water extraction and Nitrogen purging, it contains H_2O and N_2. The amount of water in the LS was measured at the time of filling to be around 20 ppm. The amount of Nitrogen is estimated to be about 250 ppm, by referencing the saturation concentration of Nitrogen in hexane. The LS also includes some Oxygen; the amount of O_2 was monitored during LS filling into the detector, giving a rough estimate of $\sim$ 20 ppm. Table 6.10 summarizes the atomic composition of the KamLAND LS, calculated from the chemical composition discussed here.

(α,n) Reaction Backgrounds

The reaction X(α,n)Y makes delayed coincidence events that almost perfectly mimic neutrino events. Neutrons produced by the reaction make prompt signals by elastic scattering on protons, and/or inelastic scattering on ^{12}C that proceeds to 4.4 MeV gamma particle emission. If the reaction X(α,n)Y results in excitation of the nucleus Y, it immediately emits gamma particles or conversion electrons which also make a prompt signal. Delayed

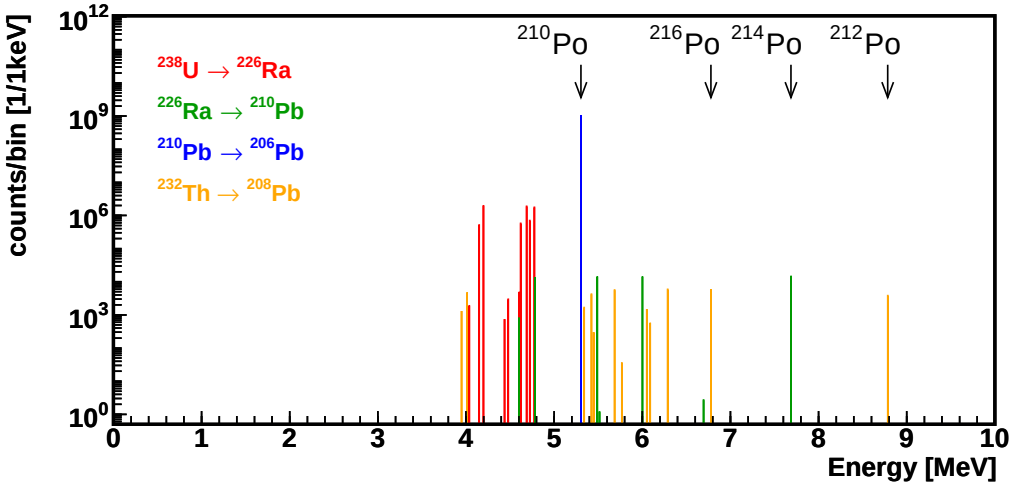

Figure 6.29: Alpha Activity in the KamLAND LS

signals are made by neutron capture on proton, which is identical to those of neutrino events.

Based on the estimated radioactivity in the LS (Table 6.7), alpha spectrum is calculated by tracing the whole U and Th decay series. Figure 6.29 shows the calculated spectrum. Although there are some uncertainties in branching ratios reported in isotope tables, two remarkable characteristics are clearly seen; firstly, the maximum alpha energy is 8.6 MeV, and secondly, ^{210}Po decay holds 99.28% of all alpha decays.

Table 6.11 lists the (α,n) reaction thresholds for isotopes which is abundant in the KamLAND LS. The threshold values are taken from a table available from National Nuclear Data Center (NNDC) at BNL [60]. As shown in Figure 6.29, the maximum alpha energy is 8.6MeV, therefore isotopes that can cause the (α,n) reaction are limited to ^{13}C, ^{14}N, ^{15}N, ^{17}O, and ^{18}O.

A database at Japanese Evaluated Nuclear Data Library (JENDL) [61] provides cross section data of the (α,n) reaction for these target isotopes. Figure 6.30 shows the (α,n) reaction cross section calculated with the JENDL data. The cross section is normalized to barn per natural carbon; the LS chemical composition shown in Table 6.10 and natural abundance of isotopes are used to weight the cross section of each isotope.

As shown in the Figure 6.30, the ^{13}C(α,n) reaction holds about 99.9% of the total (α,n) cross section below 8 MeV, and about 99% above 8 MeV. Taking into account that 5.3 MeV alpha particles from ^{210}Po dominate more than 99% of alpha emissions, the ^{13}C(α,n) reaction practically govern the total (α,n) cross section.

The JENDL estimation of ^{13}C(α,n) is based on measurement by K.K.Sekharan *et al.* (1967) [62] and J.K.Bair *et al.* (1973) [63], with modifications by resonance analysis using an appropriate R matrix. K.K.Sekharan *et al.* assign 20% error on thier cross section measurement, mainly comes from estimation of ^{13}C target enrichment and neutron detection efficiency.

Table 6.11: (α,n) reaction threshold

Target	Abundance	Threshold [MeV]
^{1}H	99.985%	115.4
^{2}H	0.015%	12.5
^{3}H	-	11.1
^{12}C	98.90%	11.3
^{13}C	1.10%	0
^{14}C	-	2.34
^{14}N	99.634%	6.09
^{15}N	0.366%	8.13
^{16}N	-	0
^{16}O	99.762%	15.2
^{17}O	0.038%	0
^{18}O	0.200%	0.85
^{19}O	-	0

Neutron yield by the (α,n) reaction is then estimated with these data. The neutron yield Y is given by

$$Y = \sum_{\alpha-\text{decays}} N_\alpha \cdot P({E_\alpha}^0) \tag{6.6}$$

where N_α is the number of emitted alpha particles and ${E_\alpha}^0$ is the emitted alpha particle energy before energy loss in LS. $P({E_\alpha}^0)$ is the neutron productivity of an alpha particle with initial energy ${E_\alpha}^0$, given by

$$P({E_\alpha}^0) = \int_{E_\alpha={E_\alpha}^0}^{0} \rho_{\text{carbon}} \cdot \frac{d\sigma}{dE_\alpha} \cdot \frac{dx}{dE_\alpha}(-dE_\alpha) \tag{6.7}$$

where ρ_{carbon} is the density of natural carbon, $\frac{d\sigma}{dE_\alpha}$ is the (α,n) reaction cross section normalized to natural carbon (shown in Figure 6.30), and $\frac{dx}{dE_\alpha}$ is reciprocal of the alpha particle energy loss $\frac{dE}{dx}$.

The energy loss of alpha particles in the KamLAND LS is obtained by Monte-Carlo (MC) simulation. The MC is constructed based on the GEANT3 package provided from CERN, with the KamLAND LS composition. Figure 6.31 shows the $\frac{dE}{dx}$ of alpha particles in the KamLAND LS, calculated with the simulation program.

By numerically integrating (6.7) with the cross section data (Figure 6.30) and the simulated $\frac{dE}{dx}$ (Figure 6.31), and then taking sum of (6.6) with the estimated alpha activity in the LS (Figure 6.29), the total neutron yield is calculated to be 64.00 neutrons/livetime. Figure 6.32 shows the neutron productivity as a function of initial alpha particle energy, and neutron yield of each alpha emission. ^{13}C(α,n) by ^{210}Po produces

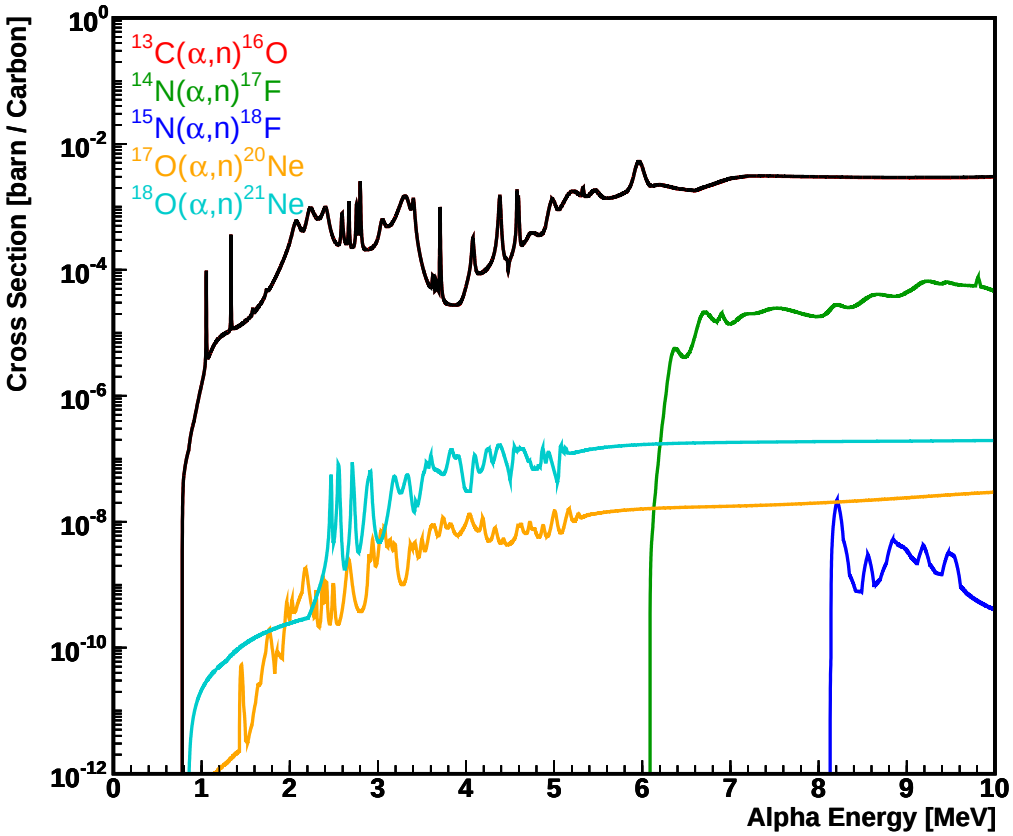

Figure 6.30: (α,n) Cross Section. The cross section is normalized to barn per natural carbon, in accordance with the LS composition shown in Table 6.10. The black line shows the total cross section and the colored lines show the cross section of each target nucleus. The cross section of ^{13}C(α,n)^{16}O (red) is hidden by the black line.

63.74 neutrons/livetime, corresponding to 99.7% of the total neutron yield. Alpha particles with energy greater than 5.3 MeV (energy of alpha from ^{210}Po decay) yield only 0.014 neutrons/livetime. Comparing these numbers with the error of the (α,n) cross section, 20%, we omit (α,n) reactions other than the ^{13}C(α,n) reaction caused by ^{210}Po from the discussion below.

The energy of neutron produced by the ^{13}C(α,n)^{16}O reaction depends on the incident alpha particle energy and the excitation energy of the final state ^{16}O nuclei. At the lab frame, the neutron energy also depends on the scattering angle of the neutrons respect to the incident alpha particle direction.

The neutron energy spectrum is given by

$$\frac{dN}{dE_n} \propto \int_{E_\alpha = E_\alpha{}^0}^{0} \int_{\cos\theta=-1}^{1} \delta(E_{\rm CM}^{\rm initial} - E_{\rm CM}^{\rm final}) \frac{d^2\sigma}{dE_\alpha d\cos\theta} \frac{dx}{dE_\alpha} d\cos\theta(-dE_\alpha) \tag{6.8}$$

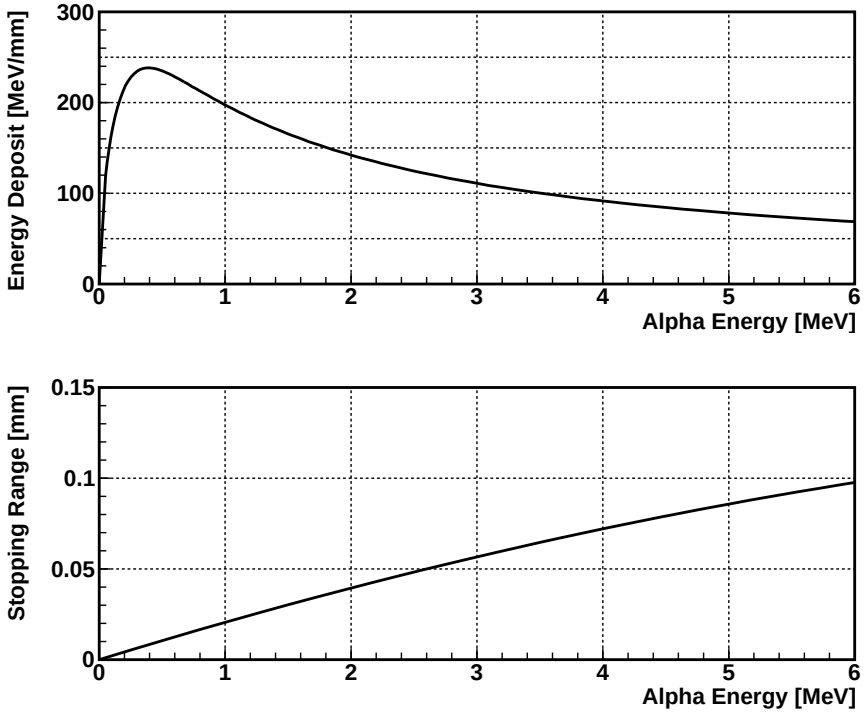

Figure 6.31: Alpha Particle Energy Loss in KamLAND LS (MC)

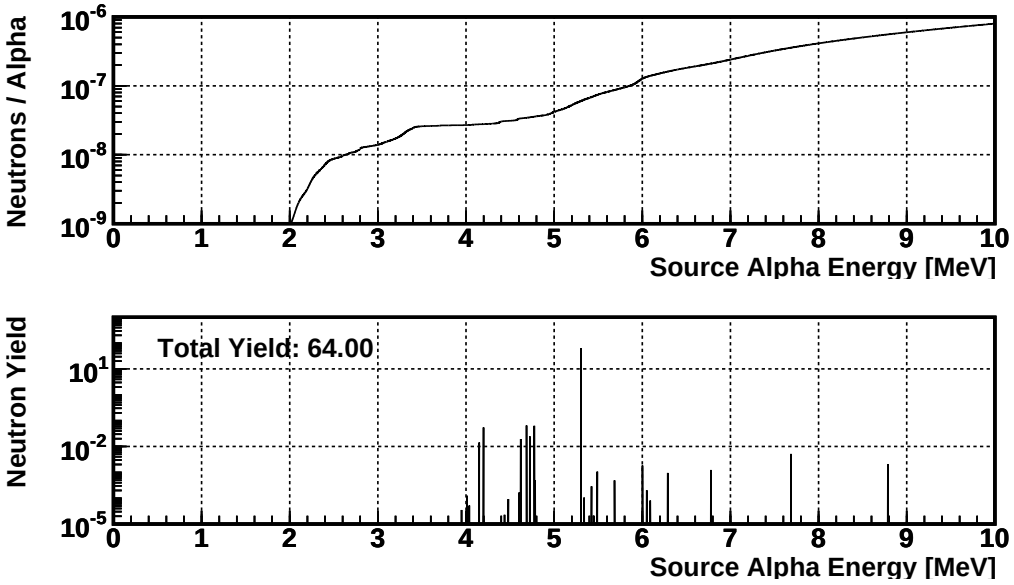

Figure 6.32: Neutron Productivity and Neutron Yield

with

$$E_{\rm CM}^{\rm initial} = \left\{(E_\alpha + M_\alpha + M_{^{13}\rm C})^2 - {P_\alpha}^2\right\}^{\frac{1}{2}} \quad (6.9)$$

$$E_{\rm CM}^{\rm final} = {E_n}^{\rm CM} + M_n + {E_{^{16}\rm O}}^{\rm CM} + M_{^{16}\rm O} + E_{\rm ex} \quad (6.10)$$

where $E_{\rm CM}$ is the Lorentz invariant center-of-mass (CM) energy, E_α and $E_{^{13}\rm C}$ are kinetic energies of the incident alpha particle and the target ^{13}C nucleus at the laboratory frame, respectively, ${E_n}^{\rm CM}$ and ${E_{^{16}\rm O}}^{\rm CM}$ are kinetic energies of the scattered neutron and the produced ^{16}O nucleus at the CM system, respectively. $E_{\rm ex}$ is the excitation energy of the product nucleus ^{16}O. $M_{\rm x}$ is the rest mass of particle x and $P_{\rm x}$ is the momentum of particle x, where $P_{\rm x} = \{(E_{\rm x} + M_{\rm x})^2 - M_{\rm x}^2\}^{1/2}$. Momentum conservation at the CM system requires ${P_n}^{\rm CM} + {P_{^{16}\rm O}}^{\rm CM} = 0$. θ is the neutron scattering angle respect to the incident alpha particle at the CM system. The delta function represents energy conservation.

The kinetic energy of the scattered neutrons at the laboratory frame E_n is calculated from the kinetic energy of the neutrons at the CM system ${E_n}^{\rm CM}$ with the velocity of the center-of-mass $\beta = p_\alpha/(E_\alpha + M_\alpha + M_{\rm C})$ and $\gamma = (1-\beta^2)^{1/2}$ by,

$$E_n + M_n = \gamma\ ({E_n}^{\rm CM} + M_n) + \beta\gamma\ {P_n}^{\rm CM}\ \cos\theta \quad (6.11)$$

With $\delta(E_{\rm CM}^{\rm initial} - E_{\rm CM}^{\rm final}) \neq 0$, these formulae give the neutron energy E_n as a function of incident alpha particle energy E_α and scattering angle θ.

The delta function in the (6.8), which represents energy conservation in terms of the center-of-mass energy $E_{\rm CM}$, is equivalent to energy conservation at the laboratory frame:

$$\delta(E_{\rm CM}^{\rm initial} - E_{\rm CM}^{\rm final}) \equiv \delta(E_\alpha - E_n - E_{^{16}\rm O} + Q - E_{\rm ex}) \quad (6.12)$$

where Q is the Q value of the ^{13}C(α,n)^{16}O reaction, given by

$$Q = (M_\alpha + M_{^{13}\rm C}) - (M_n + M_{^{16}\rm O}) = 2.216\text{MeV} \quad (6.13)$$

With the maximum alpha particle energy 5.3 MeV at the lab frame, which corresponds to 4.05 MeV at the CM system, the maximum excitation energy $E_{\rm ex}$ is 6.27 MeV. Therefore, among the excitation levels of ^{16}O, only levels whose excitation energy is less than 6.27 MeV are involved in the ^{13}C(α,n)^{16}O reaction.

Figure 6.33 shows the energy levels of the ^{16}O nucleus. There are two levels with excitation energy less than 6.27 MeV; the 0^+ state at 6.049 MeV and the 3^- state at 6.130 MeV. The JENDL data set also provides partial cross sections of ^{13}C(α,n$_{\rm x}$)^{16}O with x=0,1,2,3,4, where x denotes the levels of ^{16}O (x=0 is the ground state, x=1 is the first excitation state, etc.). The cross section of the ^{13}C(α,n$_0$)^{16}O is obtained from the inverse reaction ^{16}O(n,α)^{13}C cross section. Other partial cross sections are obtained by calculation of a statistical model (*a model of Hauser-Feshbach type* [61]). Figure 6.34 shows the partial cross section data provided by the JENDL data set.

Figure 6.35 shows the scattered neutron energy as a function of incidence alpha particle energy and scattering angle, calculated from $\delta(E_{\rm CM}^{\rm initial} - E_{\rm CM}^{\rm final}) \neq 0$ with $E_{\rm ex} = 0$. Dependence of neutron energy on the scattering angle is quite large; for 5.3 MeV alpha

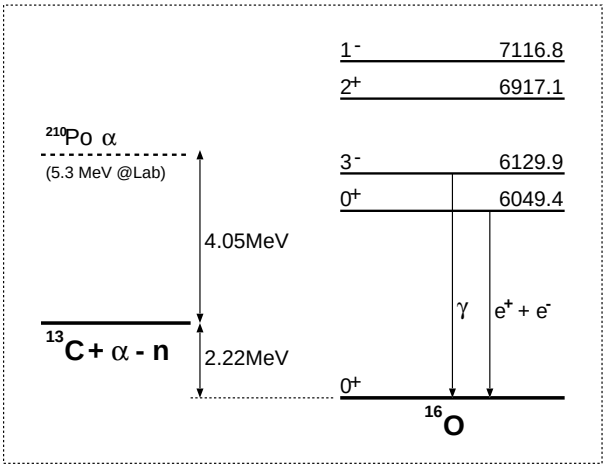

Figure 6.33: Energy Levels of ^{16}O

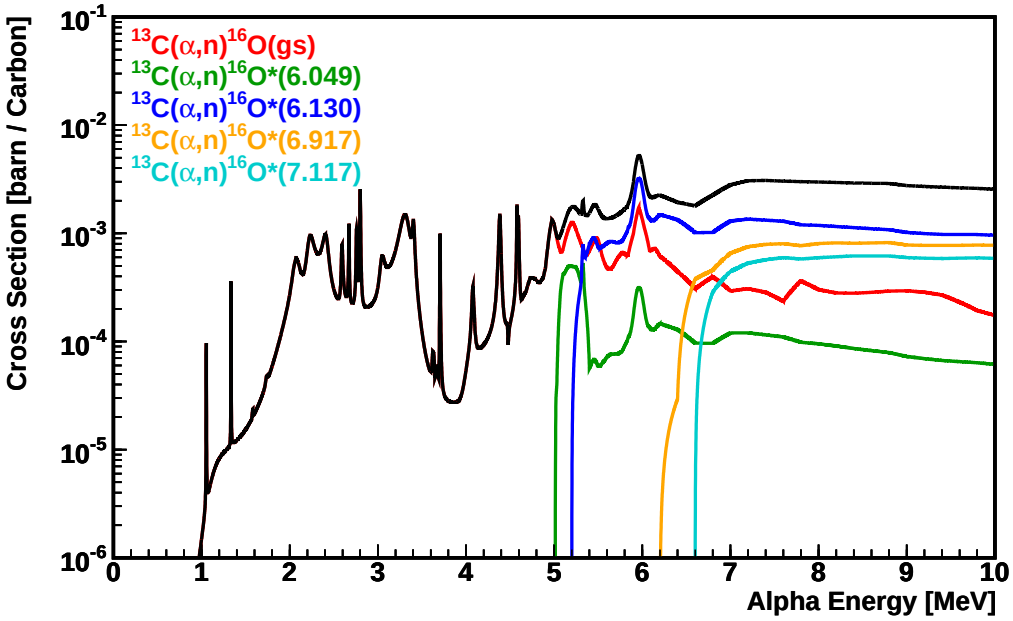

Figure 6.34: ^{13}C(α,n)^{16}O* cross section

particle, the neutron energy ranges from 4.7 MeV to 7.3 MeV, depending on the scattering angle.

The neutron angular distribution of the ^{13}C(α,n$_0$)^{16}O is measured by R.B.Walton *et al.* [64] in the energy region from 2.0 MeV to 3.4 MeV, and by G.W.Kerr *et al.* (1968) [65] from 3.64 MeV to 5.96 MeV. The measured angular distributions are parameterized with

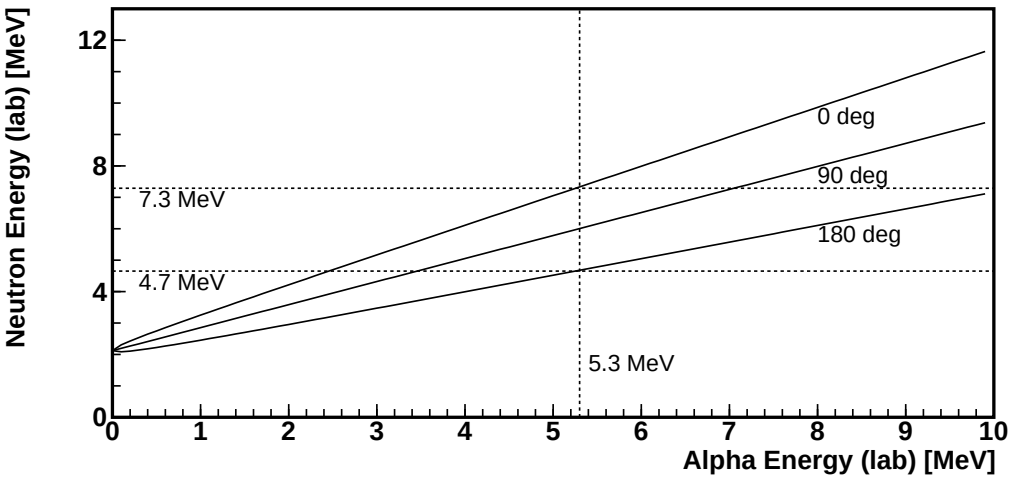

Figure 6.35: Neutron Scattering Angle and Energy

the Legendre Polynomials $P_l(x)$ as

$$\frac{d^2\sigma}{dE\, d\cos\theta} = \frac{d\sigma}{dE} \sum_l a_l P_l(\cos\theta) \tag{6.14}$$

Figure 6.36 shows the coefficients of the Legendre Polynomials as a function of energy. Although data points are sparse at around 3.5 MeV to 4 MeV, its effect to the neutron spectrum is not serious because absolute cross section in this region is also small. Neutron production is dominated by resonances, and measurements of neutron angular distribution are concentrated to the resonances. Figure 6.37 shows the angular distribution of scattered neutrons at some resonances calculated from the Legendre Polynomial coefficients.

Using the evaluated partial cross section data and the angular distribution data, the neutron spectra are calculated. Since no data on angular distribution of the n_1 and n_2 neutrons is available at present, isotropic distribution is used for these neutrons; hence the real n_1 and n_2 neutron energy spectra are slightly different from the calculation. However, the energy of these neutrons is very low, due to energy taken for the ^{16}O excitation, thus the contribution to visible energy of these neutrons is negligible in any case. Figure 6.38 shows the neutron spectra of the reaction ^{12}C(α,n_0)^{16}O, ^{12}C(α,n_1)^{16}O* and ^{12}C(α,n_2)^{16}O*. From the spectra, partial neutron yields of these reactions are calculated to be 58.07, 5.13 and 0.78, respectively.

The neutrons make prompt signals by elastic scattering on protons and/or by inelastic scattering on ^{12}C that proceeds to 4.4 MeV gamma ray emission. These processes are traced with a Monte-Carlo (MC) simulation.

Two simulation programs have been developed independently, one is constructed based on the GEANT3 package and the other is based on the GEANT4 package. Both of the simulation programs describe the chemical composition of the KamLAND LS as detail as possible, enable all electromagnetic and hadronic processes, and adopt the most precise

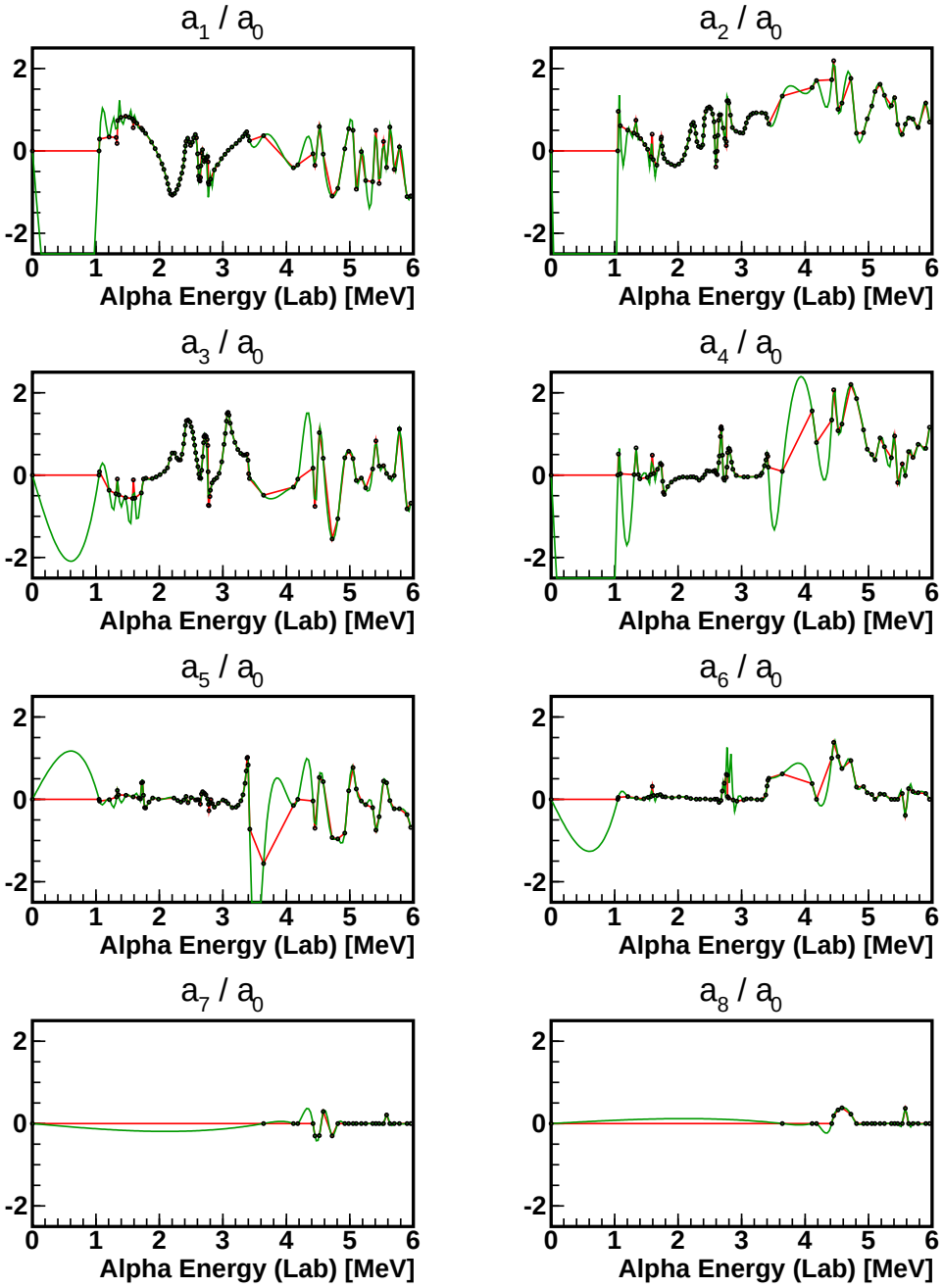

Figure 6.36: Legendre Coefficients of ^{13}C(α,n)^{16}O Neutron Angular Distribution. Black points show the Legendre coefficients given in [64] and [65]. The red lines show linear interpolation to the data, and the green lines show spline interpolation to the data. As can be seen in the figure, the spline interpolation is unstable, hence linear interpolation is used in the calculation.

neutron thermalization tracing. Modeling of effective charges of alpha particles and heavy ions are improved in GEANT4, thus the GEANT4 model of effective charge is used in the

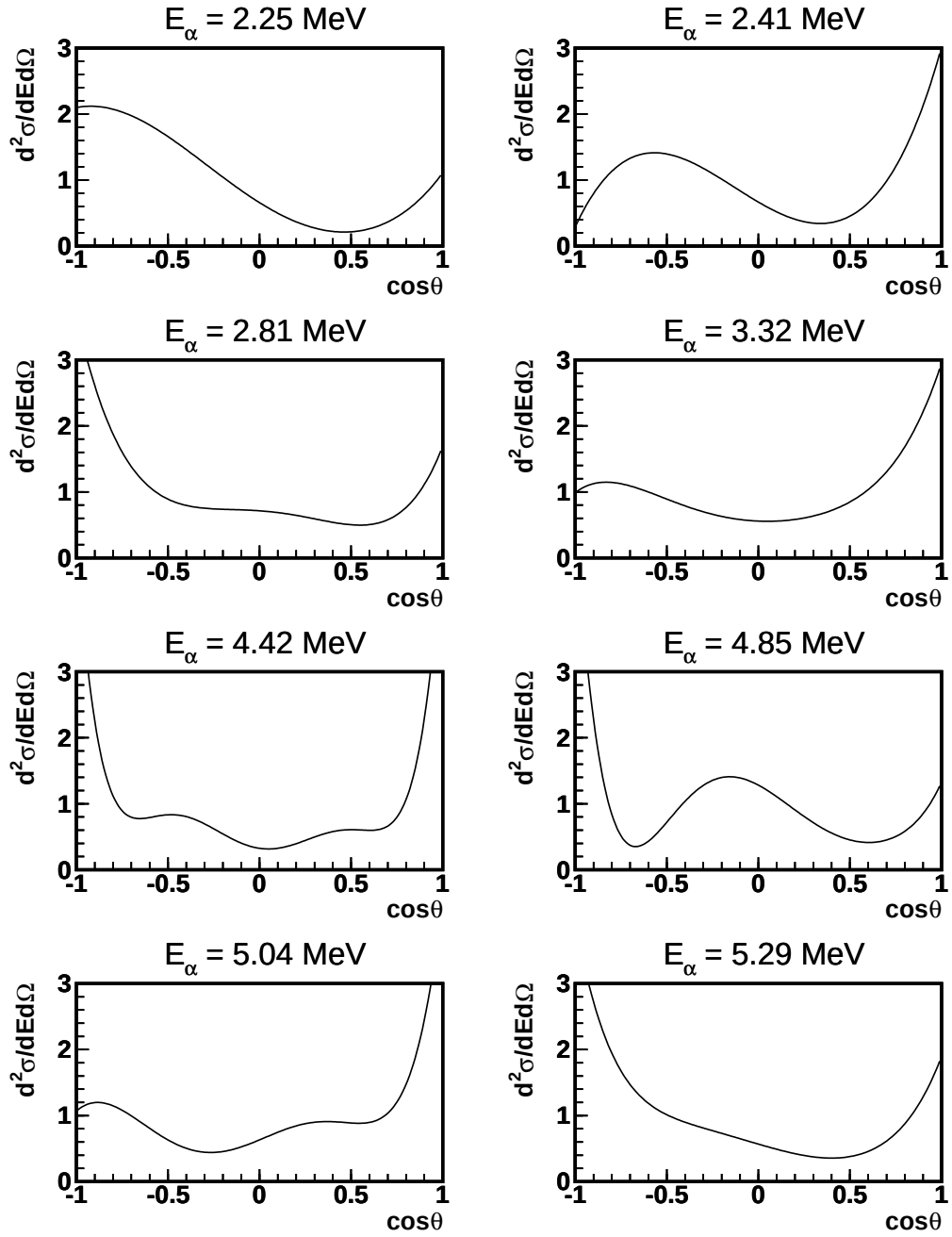

Figure 6.37: Neutron Angular Distribution at Several Resonance Energies, Calculated from the Legendre Polynomials

GEANT3 simulation. Two results are compared with each other to check consistency.

For conversion from energy deposition in the LS to photon production, the formulae established at the KamLAND energy scale study is used (Section 4.7). In the GEANT3 simulation, the tracking step size is set short enough, and energy deposition of every step

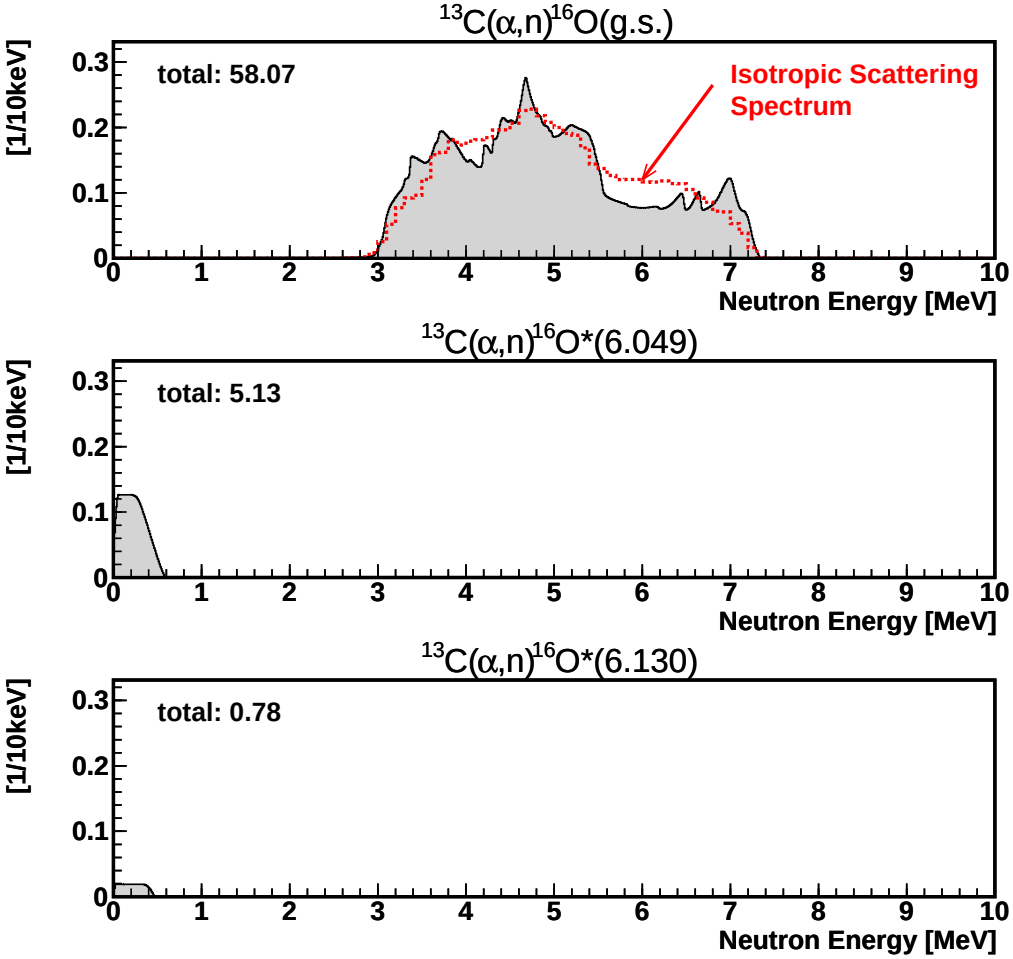

Figure 6.38: Neutron Spectra of ^{12}C(α,n$_x$)^{16}O

is used to calculate the photon production of the step. In the GEANT4 simulation, where step sizes are not explicitly set by users, energy deposition along a step is calculated by integrating $\frac{dE}{dx}$ along the step segment, then photon production of the step is calculated. The $\frac{dE}{dx}$ value is taken from a GEANT4 internal table, which is constructed for the KamLAND LS composition.

The formula to calculate photon yield from energy deposition is given by

$$dE_{\rm vis} = \left(A_{\rm sci} \cdot \frac{dN_{\rm sci}}{dE} + A_{\rm ch} \cdot \frac{dN_{\rm ch}}{dE} \right) dE \tag{6.15}$$

where $N_{\rm sci}$ and $N_{\rm ch}$ are photon yield by the scintillation process and the cherenkov light emission process, respectively, and $A_{\rm sci}$ and $A_{\rm ch}$ are the normalization factors that depend on the chemical and physical properties of the scintillator. The scintillation light yield is

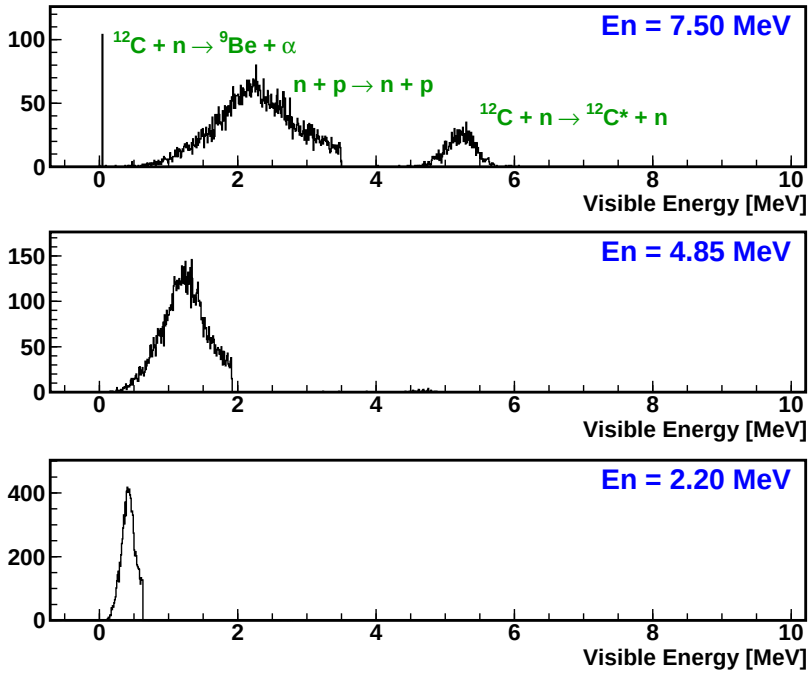

Figure 6.39: Visible Energy Spectra of Mono-Energetic Neutrons (MC)

given by the Birk's formula,

$$dN_{\rm sci} = \frac{1}{1 + k_b \frac{1}{\rho}\frac{dE}{dx} + C\left(\frac{1}{\rho}\frac{dE}{dx}\right)^2 + ...} dE \tag{6.16}$$

where k_b is the Birk's constant and C is the higher order corrections.

The parameters $A_{\rm sci}$, $A_{\rm ch}$, k_b, and C are determined with the calibration data. Two different approaches are adapted here; the first method uses the simple Birk's formula (i.e., C=0) and determines the parameters separately for alpha particles and others such as electrons, positions and gamma particles. Parameters obtained from alpha particles are used for protons; that is, $A_{\rm sci}$=1, $A_{\rm ch}$=0, and k_b=0.0115 mm/MeV. The second method utilizes the Birk's formula with the second order of $\frac{dE}{dx}$, and determines an unified set of parameters, which globally explain all energy calibration points of alpha particles, electrons, positrons, and gamma particles. The adapted set of parameters is: $A_{\rm sci}$=0.9054, $A_{\rm ch}$=0.01903, k_b=0.0078 g/cm^2/MeV, and $C = 1.88 \times 10^{-6}$ g^2/cm^4/MeV^2. The results are compared with each other, and the discrepancies are accounted for estimation errors.

Figure 6.39 shows the spectra of mono-energetic neutrons' visible energy deposited in the first 100ns time window from generation, at neutron energy of 2.2MeV, 4.85MeV and 7.5MeV. 2.2 MeV is the lowest energy of the ^{13}C(α,n$_0$)^{16}O reaction and 7.5 MeV is the highest. At low energies, elastic scattering on proton is the only process that makes visible signal, and at higher energy, inelastic scattering on ^{12}C makes significant contribution.

Validity of the simulation is confirmed by applying the simulation to the calibration Am/Be source (see Appendix D) in the KamLAND LS and comparing the result with

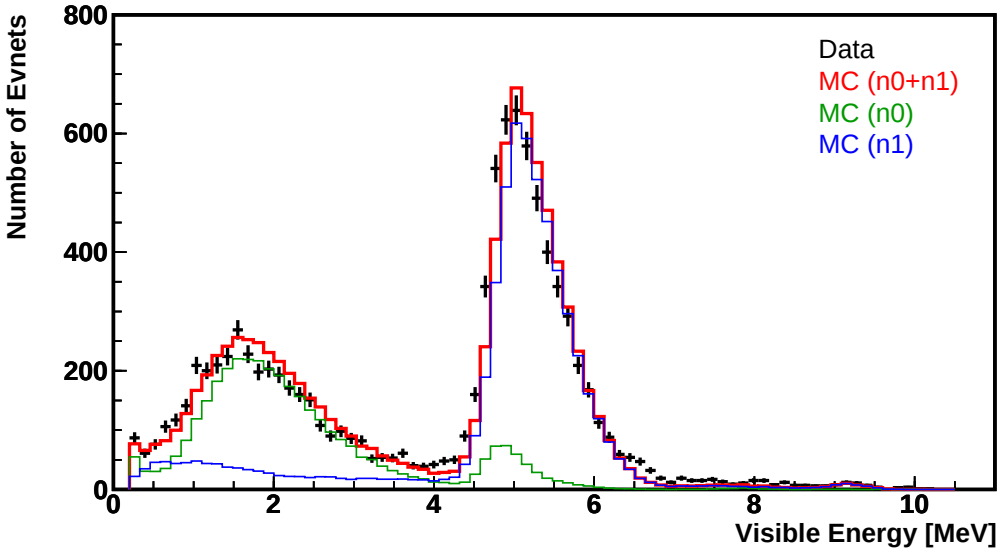

Figure 6.40: Comparison of MC and Data on Am/Be Calibration Events

the real Am/Be calibration run data. Figure 6.40 shows the simulated visible energy spectrum superposed on the real data. In the simulation, the initial neutron spectra from the Am/Be source are taken from A.D.Vijaya *et al.* (1973) [66], and effects of source container is additionally included. In the data, events are selected with the same criteria as those of the neutrino event selection.

Using the simulation and the neutron spectra of the ^{13}C(α,n)^{16}O reaction by alpha particles emitted from ^{210}Po (Figure 6.38), the visible energy spectra of the reaction are calculated as shown in Figure 6.41. Visible energies of the alpha particles, neutrons, and gamma particles or conversion electrons/positrons from de-excitation of ^{16}O* are first calculated separately, then summed up later to obtain the inclusive spectrum. Figure 6.42 shows the visible energy spectrum with $6.24\%/\sqrt{E/[\mathrm{MeV}]}$ detector energy resolution (which does not include intrinsic physics process fluctuation). From the spectrum, the number of ^{13}C(α,n)^{16}O events in the geo-neutrino analysis window is estimated to be 44.41.

Finally, errors of the spectrum are estimated. Possible error sources are the ^{210}Po decay rate, alpha particle energy deposit that depends on the alpha particle effective charge models, ^{12}C(α,n)^{16}O cross section, partial cross section of ^{12}C(α,n$_x$)^{16}O, their neutron angular distributions, ^{12}C(n,nγ)^{12}C (neutron inelastic scattering on ^{12}C) cross section, and calculation of neutron visible energy. The error on calculation of neutrino visible energy includes errors of neutron-proton scattering models of the MC, energy loss (dE/dx) of protons in the LS, treatment of ionized electrons or delta rays, and calculation of scintillator light yield. Figure 6.43 shows how these errors affect to the estimated spectrum.

As shown in the Figure 6.43, we divide the spectrum into three regions. The first

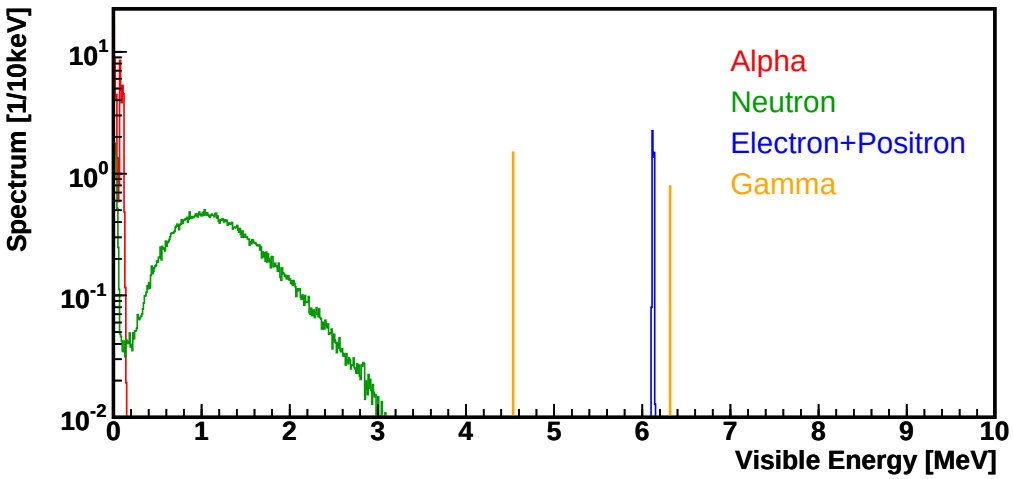

Figure 6.41: Visible Energy Spectra of ^{13}C(α,n)^{16}O by Alpha Particles from ^{210}Po

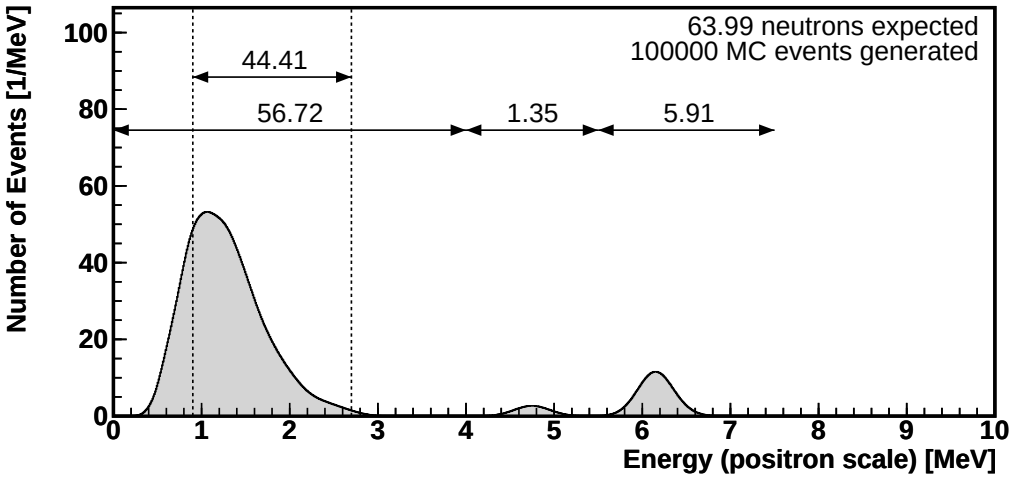

Figure 6.42: Visible Energy Spectra of ^{13}C(α,n)^{16}O by Alpha Particles from ^{210}Po, with Energy Resolution

one, Region I, extends from 0 MeV to 4 MeV. The broad peak in the region is made by protons scattered by the n_0 neutrons. The second region, Region II, contains a small peak that consists of 4.4 MeV gamma particles by the ^{12}C(n,nγ)^{12}C reaction and small contributions of scattered protons. Only the n_0 neutrons are involved in this region. The third one, Region III, is made by gamma particles or conversion electrons/positions of the ^{13}C(α,n_1)^{16}O* and ^{13}C(α,n_2)^{16}O* reactions. The energy is dominated by the gamma rays or conversion electrons/positrons and contributions of scattered protons or the initial alpha particles are negligible.

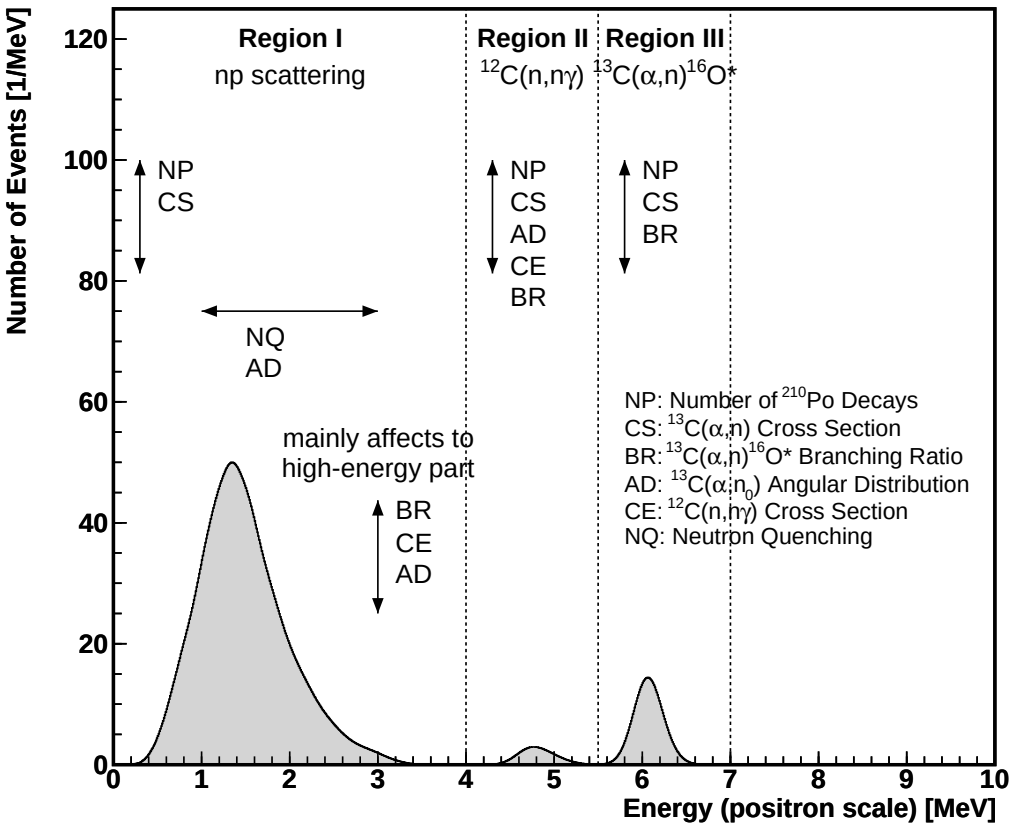

Figure 6.43: ^{13}C(α,n)^{16}O Errors

The errors of the ^{210}Po decay rate and the ^{13}C(α,n)^{16}O total cross section affect to those three regions equally; a dominant error source of the total cross section measurement is the number of ^{13}C in the target, thus it does not depend on energy. K.K.Sekharan *et al.* (1967) [62] assign 20% error in their cross section measurement. Combined with the 14% error in the ^{210}Po decay rate (Section 6.4.1), the error of spectrum vertical scaling at this point is 24%.

Our geo-neutrino analysis window is from 0.9 MeV to 2.7 MeV in the positron scale, hence only Region I is involved in our analysis. From this point, we discuss only the Region I errors.

The number of events in the Region I is also affected by the partial cross sections of ^{13}C(α,n$_x$)^{16}O and the cross sections of ^{12}C(n,nγ)^{12}C. Only high-energy alpha particles that produce high-energy neutrons are involved in the production of n_1 and n_2 neutrons, the error of the partial cross sections mainly affect to the high-energy tail of the Region I spectrum. Similarly, only hight-energy neutrons are involved in the ^{12}C(n,nγ)^{12}C reaction, the error of inelastic scattering cross section mainly affects to the high-energy tail of the Region I spectrum.

Errors of these cross sections are not explicitly given. However, since the branching

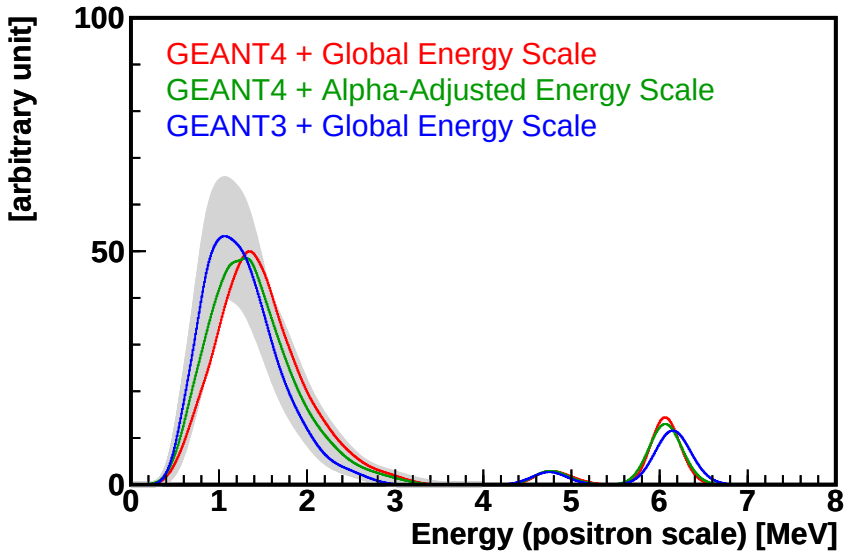

Figure 6.44: Comparison of ^{13}C(α,n)^{16}O Visible Spectra Calculated with Different Models

ratio to the Region I is such large that it contains 88% of the neutron production, errors of the cross sections are reduced by 88%. We have already assigned 24% error in the vertical scaling of the region, ~10% of errors on the cross section do not make significant difference.

Variation in the n_0 neutron angular distribution does not change the number of n_0 neutron production, however, it changes the number of events in the Region I, because it changes the energy spectrum of the n_0 neutrons and thus changes the number of neutrons above the ^{12}C(n,nγ)^{12}C reaction threshold (4.4 MeV). The errors of the angular distribution are not given as well; we compared the spectrum with that of isotropic distribution to see how angular distribution affects to the spectrum, and found that the number in the region II could be scaled by few percents. For the same reasons as the partial cross section error, effect of this error in the Region I is small enough to be absorbed into the 24% error.

Errors of neutron visible energy calculation change the spectrum shape. To see how MC modelings affect the spectrum shape, calculations based on several different models are compared. Figure 6.44 shows the comparison. Looking at the discrepancy among the spectra, we conservatively assign 10% error for horizontal scaling of the spectrum shape. For the effect of the n_0 neutron angular distribution errors to the spectrum shape, we compared the result with a calculation that uses the isotropic distribution. Although difference in the n_0 neutron spectra is significant, the difference becomes small in the visible energy spectra, because of the multiple neutron-proton scattering process. We include the errors into the 10% horizontal scaling error.

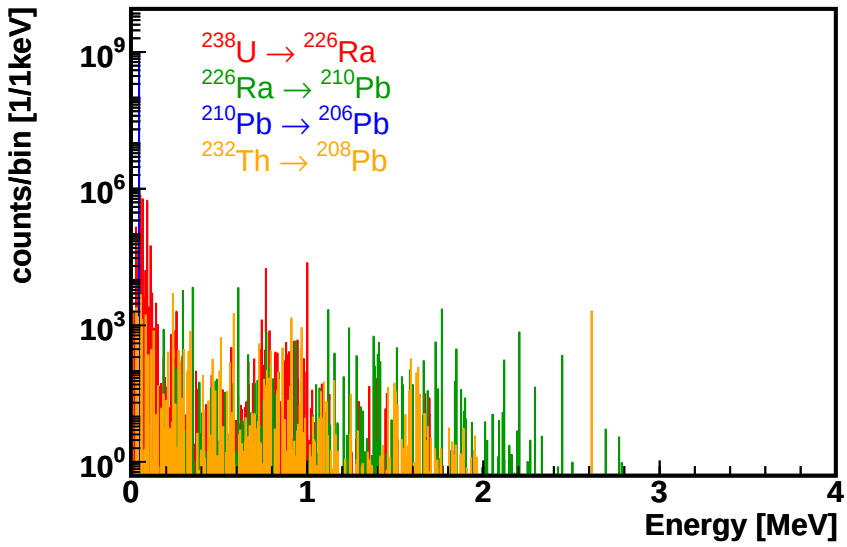

Figure 6.45: Gamma Activity in the KamLAND LS

(γ,n) Reaction Backgrounds

Similar to (α,n) reactions, (γ,n) reactions might make coincidence events that almost perfectly mimic the neutrino events. Neutron yield by (γ,n) reactions are estimated in the similar way as the (α,n) reactions. Based on the estimated radioactivity in the LS shown in Table 6.7, gamma spectrum is calculated by tracing the whole U and Th decay series. Figure 6.45 shows the calculated spectrum. Although there are some uncertainties in branching ratios listed in isotope tables, two remarkable characteristics are clearly seen; firstly, the maximum gamma particle energy is less than 3 MeV, which is much lower than alpha particle energies, and secondly, the energy region above 2 MeV is dominated by gamma particles from the isotopes in the ^{226}Ra $\rightarrow^{210}$ Pb series and the ^{232}Th $\rightarrow^{208}$ Pb series, the contaminations of which in the LS are well determined with the ^{214}Bi-^{214}Po and ^{212}Bi-^{212}Po coincidence event measurements.

Table 6.12 lists the (γ,n) reaction thresholds for isotopes which is abundant in the KamLAND LS. The threshold values are taken from National Nuclear Data Center (NNDC) at BNL [60], which is the same data source as that of the (α,n) reaction thresholds. As shown in Figure 6.45, the maximum gamma energy is less than 3 MeV, therefore only ^{2}H can cause the (γ,n) reaction.

Figure 6.46 shows the gamma ray attenuation coefficients in the KamLAND LS. The attenuation coefficients are calculated with the XCOM program [67], which is distributed from the National Institute of Standards and Technology (NIST). The chemical composition of the KamLAND LS is provided to the program to obtain the result.

The cross section of the ^{2}H(γ,n) reaction is studied by G.Rupak (2000) [68], reporting that $\sigma < 2$ mbarn at all energy range less than 3 MeV. The number of gamma particles

Table 6.12: (γ,n) reaction threshold

Target	Abundance	Threshold [MeV]
^{1}H	99.985%	-
^{2}H	0.015%	2.22
^{3}H	-	6.26
^{12}C	98.90%	18.7
^{13}C	1.10%	4.95
^{14}C	-	8.18
^{14}N	99.634%	10.6
^{15}N	0.366%	10.8
^{16}N	-	2.49
^{16}O	99.762%	15.7
^{17}O	0.038%	4.14
^{18}O	0.200%	8.04
^{19}O	-	3.96

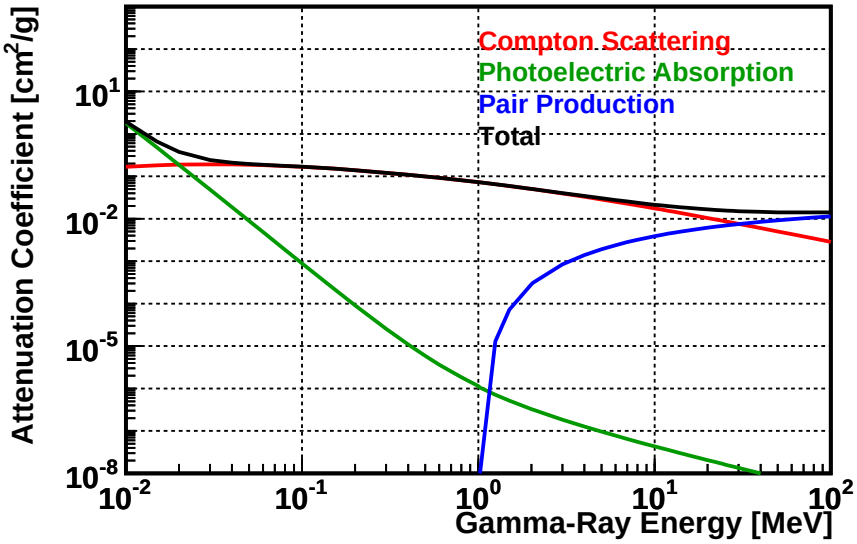

Figure 6.46: Gamma-Ray Attenuation Coefficient in the KamLAND LS

above 2.2 MeV is calculated from the spectrum to be 3.08×10^3/livetime (except for gamma particles from ^{208}Tl, which is discussed separately). The mean free path of 3 MeV gamma particles is calculated from the attenuation coefficient to be 32.5 cm. As a rough conservative estimation, we estimate the neutron yield by simply taking product of them;

$$Y < N_\gamma \cdot \rho_{^2\mathrm{H}} \cdot \sigma \cdot L = 3.08 \times 10^3 \cdot 9.91 \times 10^{18} \cdot 2 \times 10^{-27} \cdot 32.5 = 0.0020 \qquad (6.17)$$

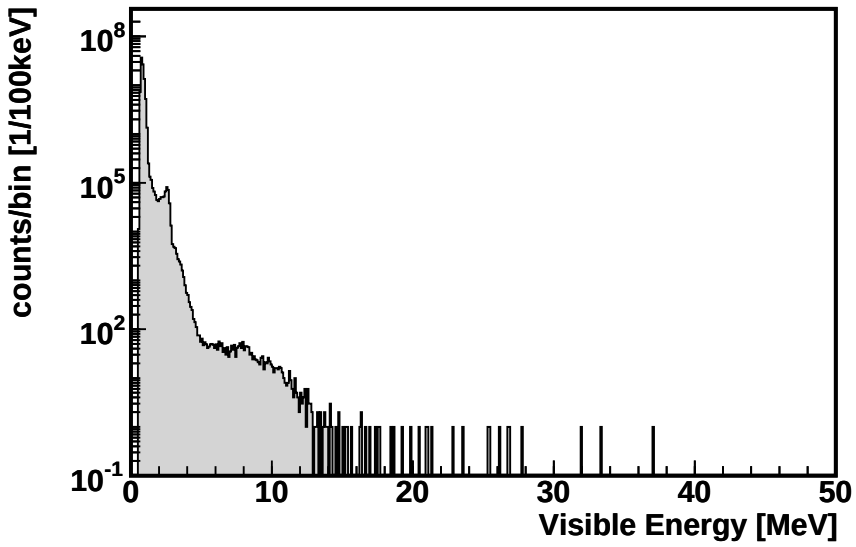

Figure 6.47: Single Event Energy Spectrum (High-Energy Region)

Unlike alpha particles, gamma particles from outside of the LS can penetrate into the fiducial volume. A typical example is the 2.6 MeV gamma particles from ^{218}Tl contained in the PMT and/or the stainless steel vessel. A peak of gamma particles from external ^{218}Tl is clearly seen in the single spectrum (Figure 6.25). Some isotopes contained in the stainless steel vessel and/or the surrounding rocks might emit very high energy gamma particles, by processes such as activities induced by muons.

Since evaluation of the composition of all such material is unpractical, a very conservative upper limit of neutron yield by external gamma sources is calculated by assuming that all observed events above 3.2 MeV are caused by gamma particles from external sources. Gamma particles below 3.2 MeV cannot make prompt signals with energy greater than 1 MeV because the (γ,n) process itself consumes at least 2.2 MeV of energy.

Figure 6.47 shows the single event energy spectrum, with energies upto 50 MeV. Events from 5 MeV to 15 MeV are mostly decays of muon spallation products, and events above 15 MeV are probably fast neutrons and/or bremsstrahlung gamma particles generated by muons outside the detector. From the single spectrum, the number of events above 3.2 MeV (and below 100 MeV) after the muon vetoes is calculated to be 1.91×10^4/livetime. The ^{2}H(γ,n) cross section is maximum at $E_\gamma \sim 4$ MeV, and at the entire energy region the cross section is less than 2.4 mbarn. The attenuation coefficient at 10 MeV is 2.10×10^{-2} [cm^2/g], corresponding to the mean free path of 61.1 cm. By taking product of these values, an upper limit of ^{2}H(γ,n) reaction backgrounds by external gamma sources is calculated to be 0.028 events/livetime.

For nuclei other than ^{2}H, the cross section data of the (γ,n) reaction is not available in hand at present. In Table 6.13, the number of events above the (γ,n) threshold is listed for each nucleus, as well as its density (the number of nuclei per unit volume) in the

KamLAND LS. By comparing the product of the target density and the number of events above threshold (ρN_γ) with that of ^{2}H, it is inferred that the X(γ,n) reaction backgrounds are negligible if the cross section is at the order of few mbarn (the same order as ^{2}H).

Table 6.13: (γ,n) Reaction Rates

Target	Density in LS ρ [1/cm^3]	Threshold $E_{\rm th}$ [MeV]	γ above $E_{\rm th}$+1MeV N_γ	$\rho \cdot N_\gamma$
^{2}H	9.91×10^{18}	2.22	19083	1.9×10^{23}
^{12}C	3.32×10^{22}	18.7	16	5.3×10^{23}
^{13}C	3.69×10^{20}	4.95	1725	6.4×10^{23}
^{14}N	1.24×10^{19}	10.6	103	1.3×10^{21}
^{15}N	4.55×10^{16}	10.8	88	4.0×10^{18}
^{16}O	5.50×10^{18}	15.7	23	1.3×10^{20}
^{17}O	2.09×10^{15}	4.14	2107	4.4×10^{18}
^{18}O	1.10×10^{16}	8.04	509	5.6×10^{18}

6.5 Summary of Backgrounds

Table 6.14 summarizes estimated number of backgrounds discussed in this chapter. For reactor neutrino backgrounds and the (α,n) reaction backgrounds, detection efficiencies that will be discussed in Chapter 7 are considered. Errors of the reactor neutrino background detection and the (α,n) reaction background detection will also be discussed in Chapter 7.

Table 6.14: Summary of Backgrounds

Background Source		Estimated Number
Reactor $\bar{\nu}_e$	Short-lived Isotopes	58.0 ± 5.3
	Long-lived Isotopes	1.37 ± 0.17
Cosmic Muon Induced	Neutrons	negligible
	Spallation Products (^{9}Li)	0.52 ± 0.092
	Fast Neutrons	< 0.1
LS Radioactivity	Accidental Coincidences	1.62 ± 0.0064
	Cascade Decays	negligible
	Spontaneous Fissions	< 0.1
	(α,n) Reactions	30.1 ± 7.9
	(γ,n) Reactions	negligible
Total		91.6 ± 9.5

Chapter 7

Analysis

7.1 Livetime

Every event acquired by the KamLAND readout electronics comes with 40 MHz clock timestamps that are synchronized to the GPS clock by the trigger circuit. Length of physics runs, as well as length of vetoed periods, is precisely determined by looking at the timestamps of the first and the last events.

For geo-neutrino data analysis, we apply muon vetoes to eliminate muon-induced backgrounds. The effect of these vetoes is studied with a simple Monte-Carlo (MC) method; for each run, a large number of MC neutrino events are generated, and vetoes are applied with using the real muon data of the run. The fraction of the vetoed events gives the ratio of vetoed period. With this method, effective time of partial-volume vetoes, which are applied to non-showering muons that pass through the LS, is automatically weighted according to the ratio of the vetoed volume. Due to the partial volume vetoes, the detector livetime slightly depends on the shape of the fiducial volume.

In this analysis, the data set taken from March 12 2002 to January 12 2004 is used. The total run time is 574.09 days, and the total livetime is estimated to be 513.92 days. The fraction of the muon-vetoed period is thus 10.5%.

7.2 Fiducial Volume

The fiducial region is defined as $R < 5$ m, where R is the radius from the balloon center to a reconstructed event vertex. Due to errors of vertex finding, the effective volume of the fiducial region might be different from the volume of 5 m radius geometrical sphere. The effective volume of the fiducial region is studied by using uniformly distributing muon spallation events.

The total amount of the liquid scintillator (LS) in the KamLAND balloon was measured to be 1171 ± 25 m^3, by flow meters during LS filling into the detector. The volume of geometrical 5 m radius sphere corresponds to 0.447 ± 0.0095 of the total LS volume.

Beta decays of ^{12}B are used to measure the ratio of the fiducial volume in the entire LS volume. ^{12}B is produced by muon spallation and decays with $\tau_{1/2}$=20.2 msec. The decay

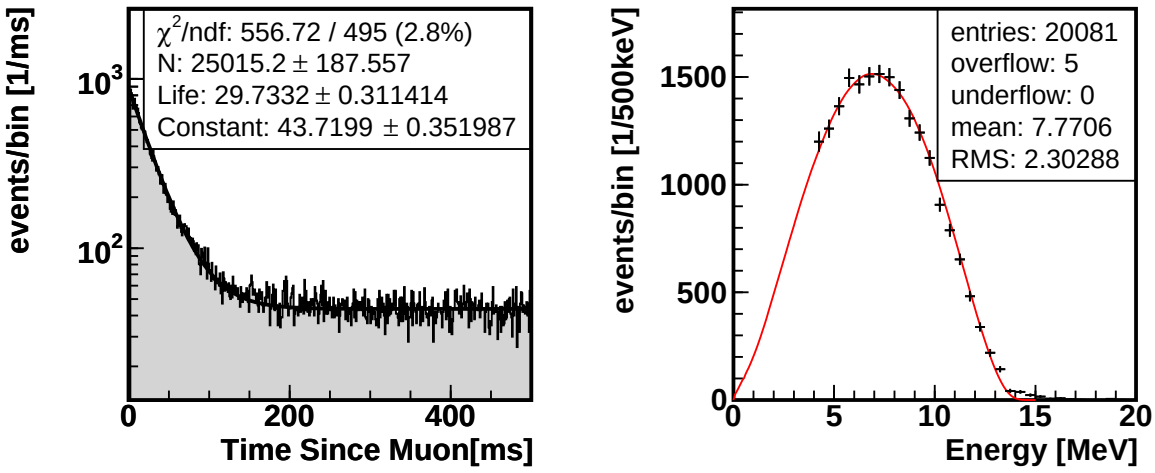

Figure 7.1: ^{12}B Event Selection

Q value is 13.4 MeV. ^{12}B beta decay evens are selected by collecting high energy events ($E_{\rm vis} > 4$MeV) after muons. Figure 7.1 shows the distribution of time since associated muon and visible energy of the selected events. In the energy spectrum, the off-time spectrum is subtracted and theoretical spectrum is superposed.

We set the time window to be from 2 msec to 60 msec, and the number of selected events in the time window is 22566. To estimate backgrounds, we set an off-time window to be from 502 msec to 560 msec. The number of events in the off-time window is 2485. Figure 7.2 shows the radial distribution of the off-time subtracted ^{12}B events, normalized to the balloon radius. The number of evens in the fiducial volume is 9154±101.24, where 101.24 is the statistical error. The ratio of the number of events in the fiducial volume is thus calculated to be 0.4558±0.0050. Considering that electrons emitted from ^{12}B travel about 5 cm, 1.5% of ^{12}B beta decays deposit a fraction of their energy outside the LS. We add 1% systematic error for ^{12}B spectrum distortion caused by this partial energy depositon,

This ^{12}B event counting ratio $R_{\rm count}$, 0.4558±0.0050(stat)±0.0046(syst), is compared with the ratio of geometrical volume ratio, or mass ratio $R_{\rm mass}$, 0.447±0.0095. The discrepancy between these ratios are: $R_{\rm mass} - R_{\rm count} = 0.0088 \pm 0.0050 \pm 0.0046 \ \pm 0.0095$. We take the whole discrepancy as fiducial volume error; i.e., $\sigma = (0.0088 + 0.0050) \oplus 0.0046 \oplus 0.0095 = 0.0174$, where $\oplus$ denotes quadrature sum. This 1.74% mass ratio (or counting ratio) error corresponds to 3.89% of the fiducial volume error.

Only ^{12}B events with energy more than 4 MeV are used for fiducial volume estimation. On the other hand, the energy of geo-neutrino events ranges from 0.9 MeV to 2.7 MeV. Hence another systematic error arises to account for possible energy dependence of fiducial volume.

This error is estimated by studying muon induced ^{9}Li events. The halflife of ^{9}Li is 178 msec, and the decay Q value is 13.6 MeV. Some of the decay branches produce

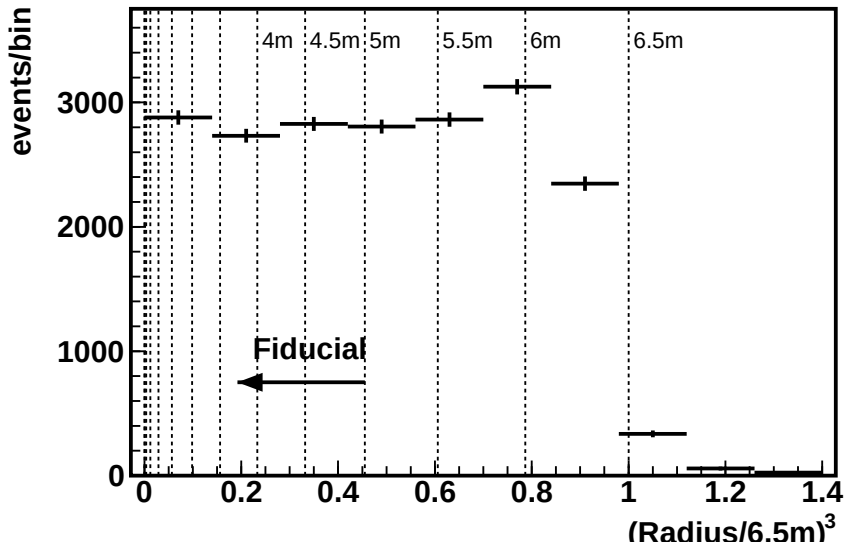

Figure 7.2: Fiducial Volume Estimation

^{9}Be, which immediately decays into two alpha particles and one neutron. The neutrons are then captured on proton, producing 2.2 MeV gamma rays. These two signals, high energy beta signals and following 2.2 MeV gamma signals, are used to estimate the energy dependence of the fiducial volume estimation.

^{9}Li events are selected by applying delayed coincidence criteria with $E_{\rm prompt} > 4$MeV after muons. The distributions of time since muon and visible energy are shown in Section 6.2.3. With the selected events, radii of prompt and delayed vertices (r_p and r_d) are compared. Figure 7.3 shows the distribution of vertex radius differences between the prompt and delayed signals ($r_d - r_p$), as a function of prompt signal vertex radius. The difference is less than 5 cm at $R < 5$m. 5 cm variation in vertex radius corresponds to 3.0% volume error for the 5 m radius fiducial region, or 1.34% error on the volume ratio $R_{\rm mass}$.

By combining the ^{12}B counting ratio, LS volume ratio, and the energy dependence estimation with ^{9}Li, the fiducial volume error is estimated to be 4.91%.

7.3 Number of Target Protons

The density of the KamLAND LS was measured during LS filling into the detector. The volume filled into the detector and the density of the LS were measured daily during the filling, and the gross volume density is estimated to be 0.77754±0.0001 g/cm^3, where the error is estimated from the precision of measurement devices. The temperature coefficient of density expansion is measured to be 7.41×10^{-4} g/cm^3/K, and the temperature of the LS in the KamLAND tank is measured to be 11.5±1.5 °C. Thus the LS density at the

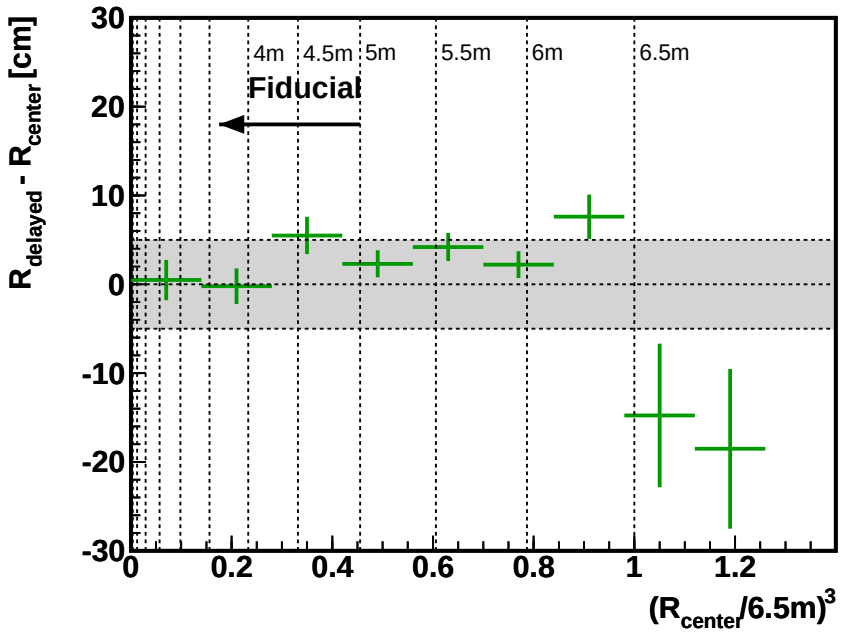

Figure 7.3: Fiducial Volume Energy Dependence

KamLAND tank temperature is estimated to be 0.78013 g/cm^3. The 1.5 °C temperature variation makes 0.1% error.

As discussed in Section 3.2.1, the KamLAND LS consists of 80.2% of dodecane ($C_{12}H_{26}$), 19.8% of pseudocumene (1,2,4-trimethylbenzene, C_9H_{12}), and 1.52 g/litter of PPO (2,5-diphenyloxazole, $C_{15}H_{11}NO$). The number of free protons is calculated from the chemical composition and the natural abundance of ^{1}H (99.985%), to be 8.469×10^{31}/kton.

The volume of the 5 m radius fiducial region is 523.599 m^3, that contains 408.48 tons of LS. The number of free protons contained in the geometrical fiducial region is calculated to be 3.459×10^{31}.

7.4 Cross Section

Geo-neutrinos are detected by the inverse beta-decay reaction, $\bar{\nu}_e p \rightarrow e^+ n$. Without radiative corrections and recoil of neutrons, the cross section σ as a function of neutrino energy $E_{\bar{\nu}_e}$ is given by

$$\frac{d\sigma(E_{\bar{\nu}_e})}{d\cos\theta} = \frac{{G_F}^2 \cos^2\theta_c}{2\pi} \left\{ (f^2 + 3g^2) + (f^2 - g^2)\beta_e \cos\theta) \right\} E_e\, p_e \tag{7.1}$$

where G_F is the Fermi constant, $f = 1.0$ is the vector coupling constant, $g = 1.267$ is the axial vector coupling constant, and θ_c is the Cabibbo angle. E_e, p_e and β_e are positron

energy, momentum and velocity respectively, given by

$$E_e = E_{\bar{\nu_e}} - \Delta \tag{7.2}$$
$$p_e = \sqrt{{E_{\bar{\nu_e}}}^2 - {m_e}^2} \tag{7.3}$$
$$\beta_e = p_e/E_e \tag{7.4}$$

where $\Delta = M_n - M_p = 1.29$MeV. By integrating the cross section over $\cos\theta$, we have the total cross section as

$$\sigma(E_{\bar{\nu_e}}) = \frac{{G_F}^2 \cos^2\theta_c}{\pi}(f^2 + 3g^2)\, E_e\, p_e \tag{7.5}$$
$$= 9.30 \times 10^{-44} \frac{E_e}{[\mathrm{MeV}]} \frac{p_e}{[\mathrm{MeV}]} \ [\mathrm{cm}^2] \tag{7.6}$$

Detailed calculations of the $\bar{\nu_e}p \to e^+n$ reaction cross section with nucleon recoil and radiative corrections were made by P.Vogel *et al.* (1999) [70] and A.Kurylov *et al.* (2003) [71], as summarized below.

With the matrix element

$$\mathcal{M} = \frac{G_F \cos\theta_c}{\sqrt{2}} \cdot \bar{v}_{\bar{\nu}} \gamma^\mu (1-\gamma_5) v_e \cdot \bar{u_n} \left(\gamma_\mu (f - g\gamma_5) - i f_2 \sigma_{\mu\nu} \frac{q^\nu}{2M} \right) u_p \tag{7.7}$$

where $f_2 = \mu_p - \mu_n = 3.706$ and $M = (M_p + M_n)/2 = 938.9$ MeV, the differential cross section at the zero-th order of 1/M (i.e., neglect recoil) is given by

$$\left(\frac{d\sigma}{d\cos\theta}\right)^{(0)} = \frac{\sigma_0}{2} \left\{ (f^2 + 3g^2) + (f^2 - g^2)\beta_e^{(0)} \cos\theta) \right\} E_e^{(0)} p_e^{(0)} \tag{7.8}$$

with

$$\sigma_0 = \frac{G_F^2 \cos^2\theta_c}{\pi}(1+\delta) \tag{7.9}$$

where δ is the radiative correction (energy independent part of which is about 0.024), which is presented later. At the first order of O(1/M), the positron energy depends on the scattering angle, and is given by

$$E_e^{(1)} = E_e^{(0)} \left[1 - \frac{E_\nu}{M}(1 - \beta_e^{(0)} \cos\theta) \right] - \frac{\Delta^2 - m_e^2}{2M} \tag{7.10}$$

The differential cross section at this order is

$$\left(\frac{d\sigma}{d\cos\theta}\right)^{(1)} = \frac{\sigma_0}{2} \left\{ (f^2 + 3g^2) + (f^2 - g^2)\beta_e^{(1)} \cos\theta) \right\} E_e^{(1)} p_e^{(1)} - \frac{\sigma_0}{2} \left[\frac{\Gamma}{M} \right] E_e^{(0)} p_e^{(0)} \tag{7.11}$$

where

$$\begin{aligned}\Gamma &= 2(f+f_2)g\left[(2E_e^{(0)}+\Delta)(1-\beta_e^{(0)}\cos\theta)-\frac{m_e^2}{E_e^{(0)}}\right]\\ &+ (f^2+g^2)\left[\Delta(1-\beta_e^{(0)}\cos\theta)+\frac{m_e^2}{E_e^{(0)}}\right]\\ &+ (f^2+3g^2)\left[(E_e^{(0)}+\Delta)\left(1-\frac{1}{\beta_e^{(0)}}\cos\theta\right)-\Delta\right]\\ &+ (f^2-g^2)\left[(E_e^{(0)}+\Delta)\left(1-\frac{1}{\beta_e^{(0)}}\cos\theta\right)-\Delta\right]\beta_e^{(0)}\cos\theta \end{aligned} \tag{7.12}$$

The radiative correction δ is expressed as a sum of virtual part g_v and bremsstrahlung part g_b,

$$\delta(E)=\frac{\alpha}{\pi}(g_v(E)+g_b(E)) \tag{7.13}$$

where α is the fine-structure constant. $g_v(E)$ is given by

$$\begin{aligned} g_v(E) &= \frac{3}{2}\log\left(\frac{M_p}{m_e}\right)\\ &+ 2\log\left(\frac{E_e-m_e}{m_e}\right)\left[\frac{1}{2\beta_e}\log\left(\frac{1+\beta_e}{1-\beta_e}\right)-1\right]\\ &+ \frac{3}{4}+\mathcal{A}(\beta_e)-1.12 \end{aligned} \tag{7.14}$$

with

$$\mathcal{A}(\beta_e)=\frac{1}{2}\beta_e\log\left(\frac{1+\beta_e}{1-\beta_e}\right)-1-\frac{1}{\beta_e}\left[\frac{1}{2}\log\left(\frac{1+\beta_e}{1-\beta_e}\right)\right]^2+\frac{1}{\beta_e}L\left(\frac{2\beta_e}{1+\beta_e}\right) \tag{7.15}$$

where

$$L(\beta_e)=\int_0^{\beta_e}\frac{\log(|1-x|)}{x}dx \overset{|\beta_e|\le 1}{=} -\sum_{k=1}^{\infty}\frac{{\beta_e}^k}{k^2} \tag{7.16}$$

and $g_b(E)$ is given by

$$\begin{aligned} g_b(E) &= \mathcal{C}(\beta_e)\\ &+ \frac{1}{2{E_e}^2\beta_e}\int_{m_e}^{E_e}(E_e-x)\log\left(\frac{1+\beta(x)}{1-\beta(x)}\right)dx\\ &+ \frac{2}{E_e\beta_e}\int_{m_e}^{E_e}\frac{x\beta(x)F(x)-E_e\beta_eF(E_e)}{E_e-x}dx \end{aligned} \tag{7.17}$$

with

$$F(E_e)=\frac{1}{2\beta_e}\log\left(\frac{1+\beta_e}{1-\beta_e}\right)-1 \tag{7.18}$$

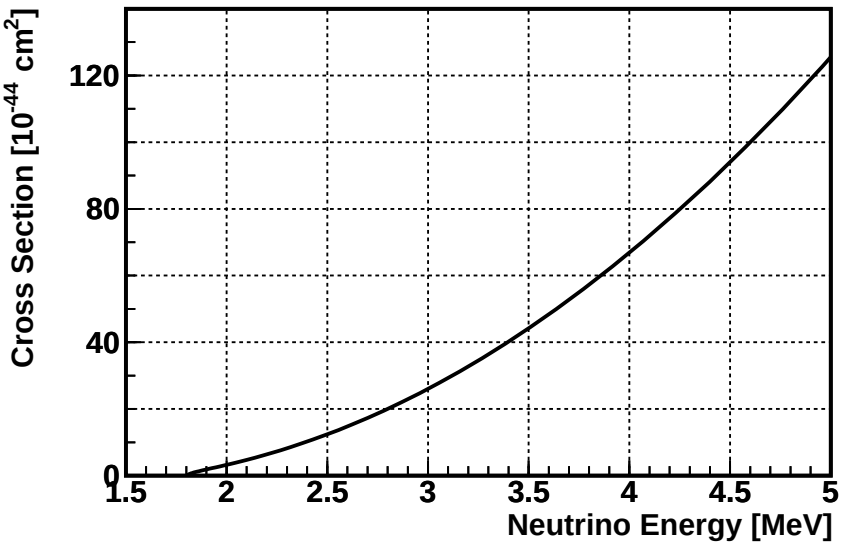

Figure 7.4: $\bar{\nu}_e p \rightarrow e^+ n$ Cross Section

and

$$\begin{aligned}
\mathcal{C}(\beta_e) &= (2\log 2) \times \left[\frac{1}{2\beta_e}\log\left(\frac{1+\beta_e}{1-\beta_e}\right) - 1\right] + 1 \\
&+ \frac{1}{4\beta_e}\log\left(\frac{1+\beta_e}{1-\beta_e}\right) \times \left[2 + \log\left(\frac{1-{\beta_e}^2}{4}\right)\right] \\
&+ \frac{1}{\beta_e}[L(\beta_e) - L(-\beta_e)] \\
&+ \frac{1}{2\beta_e}\left[L\left(\frac{1-\beta_e}{2}\right) - L\left(\frac{1+\beta_e}{2}\right)\right] \qquad (7.19)
\end{aligned}$$

Figure 7.4 shows the total cross section $\sigma(E_\nu)$ calculated with these formulae.

7.5 Detection Efficiencies

Not all $\bar{\nu}_e p \rightarrow e^+ n$ events in the fiducial volume are selected because of untagged coincidence modes, limited trigger efficiency, and various cuts applied to select neutrino events. In particular, cuts on the spatial correlation ΔR and the time correlation ΔT applied tightly to reduce the accidental coincidence backgrounds introduce large inefficiencies in the neutrino event selection. These efficiencies/inefficiencies are discussed in this section.

7.5.1 Delayed Coincidence Efficiency (Neutron Capture)

We tag the $\bar{\nu}_e p \rightarrow e^+ n$ events by coincidence of two sequential signals, the prompt signal from a positron and annihilation gamma particles, and the delayed signal from a 2.2

Table 7.1: Neutron Absorption Cross Section

Isotope	Natural Abundance [%]	Fraction in KamLAND LS [%]	Absorption Cross Section [barn]	Ratio of Neutron Capture [%]	Subsequent γ Energy [MeV]
^{1}H	99.985	66.29	0.332	99.48	2.22
^{2}H	0.015	0.00995	0.0005	2.25×10^{-5}	6.26
^{12}C	98.900	33.31	0.0034	0.512	4.95
^{13}C	1.100	0.370	0.0009	1.50×10^{-3}	8.18
^{14}N	99.634	0.0124	0.0750	4.21×10^{-3}	10.83
^{16}O	99.762	0.00552	0.0002	4.98×10^{-6}	4.14

MeV gamma particle following neutron capture on proton. However, not all neutrons are captured on proton, but some of them are captured on other nucleus such as ^{12}C.

The composition of the KamLAND LS is presented in Section 6.4.4. Table 7.5.1 lists the neutron absorption cross sections of those isotopes, as well as compositional fraction in the KamLAND LS and ratio of neutron captures. The efficiency of neutron capture on ^{1}H is calculated from these values to be 99.48%.

7.5.2 Trigger Efficiency

Trigger decisions are made by number of PMT hits (NSum), while our analysis window is defined with energy that is calculated from charges of PMT hits and reconstructed vertices. Since number of PMT hits depends on position of event vertex, and is affected by statistical fluctuations, inefficiency induced by trigger threshold remains up to higher energy.

The effect of the trigger threshold is studied by comparing two energy spectra taken with two different threshold settings. In the geo-neutrino analysis, we use data taken with the NSum threshold 200 (the prompt trigger). Another trigger, the delayed trigger, is introduced to increase detection efficiency of correlated events with lower threshold, 120. The delayed trigger is enabled only for 1msec after prompt triggers. We collected all events triggered by the delayed trigger, and from the event set we selected events that are also triggered by the prompt trigger. Figure 7.5 shows these two spectra and estimated trigger efficiency. The left panel in the figure shows the energy spectra of two different trigger conditions; one is acquired only by delayed triggers (NSum$\geq$120), and the other is acquired by both of the prompt and delayed triggers (NSum$\geq$200). The right panel shows the ratio of these two spectra, which represents the prompt trigger efficiencies as a function of energy.

The effect of the trigger efficiency to neutrino event detection is calculated by applying

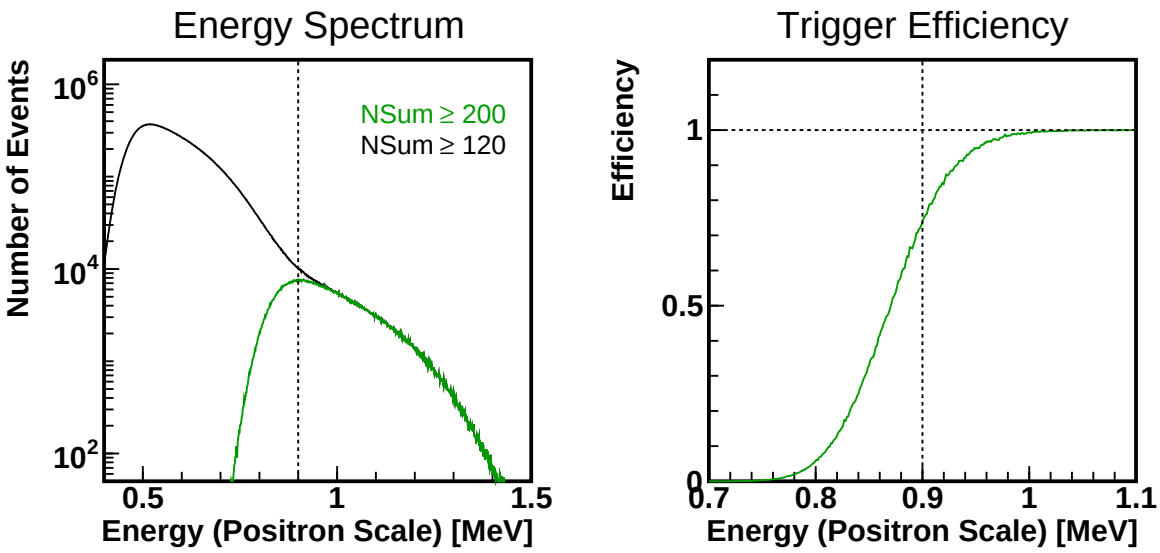

Figure 7.5: Trigger Efficiency Estimation

Table 7.2: Trigger Efficiency

	Efficiency [%]	Error [%]
U-Series Geo-neutrino	99.96	0.04
Th-Series Geo-neutrino	99.90	0.09
Reactor Neutrino	99.99	0.007

the obtained trigger efficiency to the expected neutrino spectra,

$$\varepsilon^{\text{trigger}} = \int_{E=0.9\text{MeV}}^{2.7MeV} \varepsilon(E) \cdot \frac{dN}{dE} dE \tag{7.20}$$

where $\varepsilon(E)$ is the trigger efficiency as a function of energy, $\frac{dN}{dE}$ is the expected neutrino spectrum. The error of this is estimated by shifting the energy scale by 2%. Table 7.2 summarizes the result.

7.5.3 Spatial Correlation Cut Efficiency

The detection efficiency of the spatial correlation cut is studied with a Monte-Carlo (MC) method. Neutrino event vertices (the points where $\bar{\nu}_e p \rightarrow e^+ n$ reactions occur) are generated uniformly in the fiducial volume and around the fiducial volume, and vertices of the prompt signals and delayed signals are generated accordingly. The spatial cut efficiency is defined as the number of events that pass both of the fiducial volume cuts and the spatial cuts divided by the number of event generated in the fiducial volume. Effects of the fiducial volume boundary, inroads of external events and leakage of internal events, are thus included in the spatial cut efficiency.

Vertices of prompt and delayed signals differ from the position of neutrino interaction by two effects; one is charge deposition disperse by physics processes such as neutron thermalization and gamma ray scatterings. The other is finite resolution of vertex reconstruction.

Charge dispersion by physics processes is simulated with a MC method. The MC program is developed based on the GEANT3 package, and precise models of physics processes in the KamLAND LS are constructed on it. Parameters are adjusted to explain all KamLAND calibration data consistently.

By combining the charge disperse simulation and the reconstructed data of source calibrations, vertex reconstruction resolution is obtained. If vertices are reconstructed with using 20 inch PMT data, the reconstruction resolution is given by:

$$\sigma = \frac{(20.6 \pm 0.3) - (0.125 \pm 0.015) \times (R/[\mathrm{m}])^2}{\sqrt{E_{\mathrm{vis}}/[\mathrm{MeV}]}}\ [\mathrm{cm}] \tag{7.21}$$

where R is the distance of vertices from the balloon center. If vertices are reconstructed without 20 inch PMT data, the resolution becomes:

$$\sigma = \frac{(24.0 \pm 0.3) - (0.15 \pm 0.01) \times (R/[\mathrm{m}])^2}{\sqrt{E_{\mathrm{vis}}/[\mathrm{MeV}]}}\ [\mathrm{cm}] \tag{7.22}$$

Figure 7.6 shows a result of vertex fluctuation simulation. In this simulation, the lowest energy neutrino events ($E_{\bar{\nu_e}}$=1.8MeV) are generated. The charge dispersion of prompt events is mainly due to gamma ray scatterings, and that of delayed events is mainly due to neutron thermalization processes. The charge dispersion of prompt events becomes smaller as neutrino energy increases, because more charges are deposited by positrons which travel only a few centi meters, resulting in centralized charge deposition around the neutrino interaction points.

Validity of the simulation is examined by comparing the simulation result with source calibration data. For the prompt signals, ^{68}Ge source that emits positrons is used (see Appendix D). Positrons from ^{68}Ge are absorbed in the container, and two 0.511 MeV annihilation gamma rays are emitted. This process makes similar signals as prompt signals of the lowest-energy neutrino events. For the Delayed signals, the Am/Be source that emits neutrons is used (see Appendix D). ^{241}Am emits 5.5 MeV alpha particles, that are then converted into neutrons via the $^{9}\mathrm{Be}(\alpha, n)^{12}\mathrm{C}$ reaction. This process makes similar signals as delayed signals of neutrino events. On the MC side, the geometry is modified to include Am/Be source container, because the container makes significant effect to the neutron thermalization process. The container geometry is described just as it is, without any parameter adjustments. Figure 7.7 shows the MC results superposed on calibration data. The same coincidence event selection criteria as those of the neutrino event selection are applied to select delayed signals of Am/Be source events.

Using the vertex fluctuation simulation and the estimated vertex reconstruction resolution, the selection efficiency of the spatial correlation cuts is estimated with a simple MC method. As described above, neutrino interaction points are generated uniformly, and prompt and delayed signal vertices are then generated from the neutrino interaction points

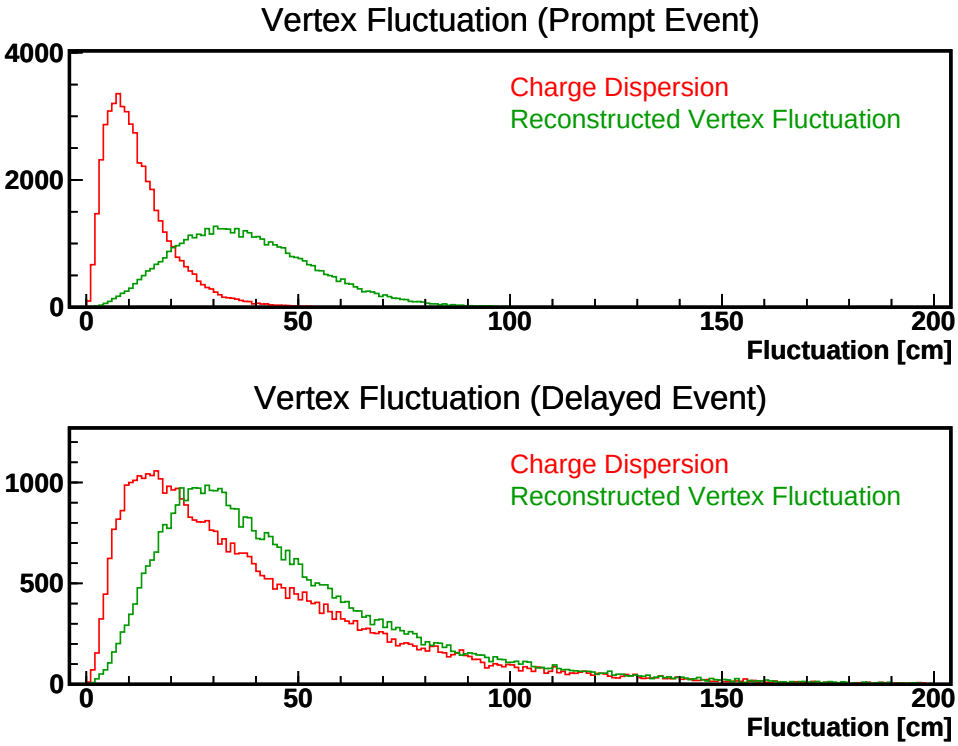

Figure 7.6: Vertex Fluctuation Simulation

with the charge dispersion simulation and the reconstruction resolution. Since the charge dispersion depends on physics processes, and the resolution depends on visible energy, selection efficiency depends on particles and energy spectra. Hence selection efficiencies are estimated separately for each of the U-series geo-neutrinos, Th-series geo-neutrinos, the reactor neutrino backgrounds, and the (α,n) reaction backgrounds. To see the energy dependence of selection efficiency, estimations are also made for mono-energetic 0 MeV and 1.5 MeV positron plus neutron events. 0 MeV positron events correspond to the lowest energy neutrino events and mono-energetic 1.5 MeV positrons correspond to the highest energy geo-neutrino events. Commissioning of the 20 inch PMT's is reflected in the vertex reconstruction resolution accordingly, based on the actual run conditions.

Figure 7.8 shows the distribution of the prompt and delayed signal distance, and the selection efficiency as a function of the ΔR cut value. From this MC calculation, selection efficiencies are estimated as summarized in Table 7.3.

Error of the spatial cut efficiency is estimated by comparing the result with an estimation based on source calibration data. Since the pair of Ge as prompt signals and Am/Be as delayed signals is the only available source calibration data for this purpose, comparison is made at the 0 MeV positron point (the lowest energy neutrino event). The MC is modified to include the Am/Be source container into the geometry definition, since it makes significant effects to the neutron thermalization process.

Using the Ge+Am/Be data, and using the modified MC data, spatial cut efficiencies are calculated respectively with the same method used above. For the vertex reconstruc-

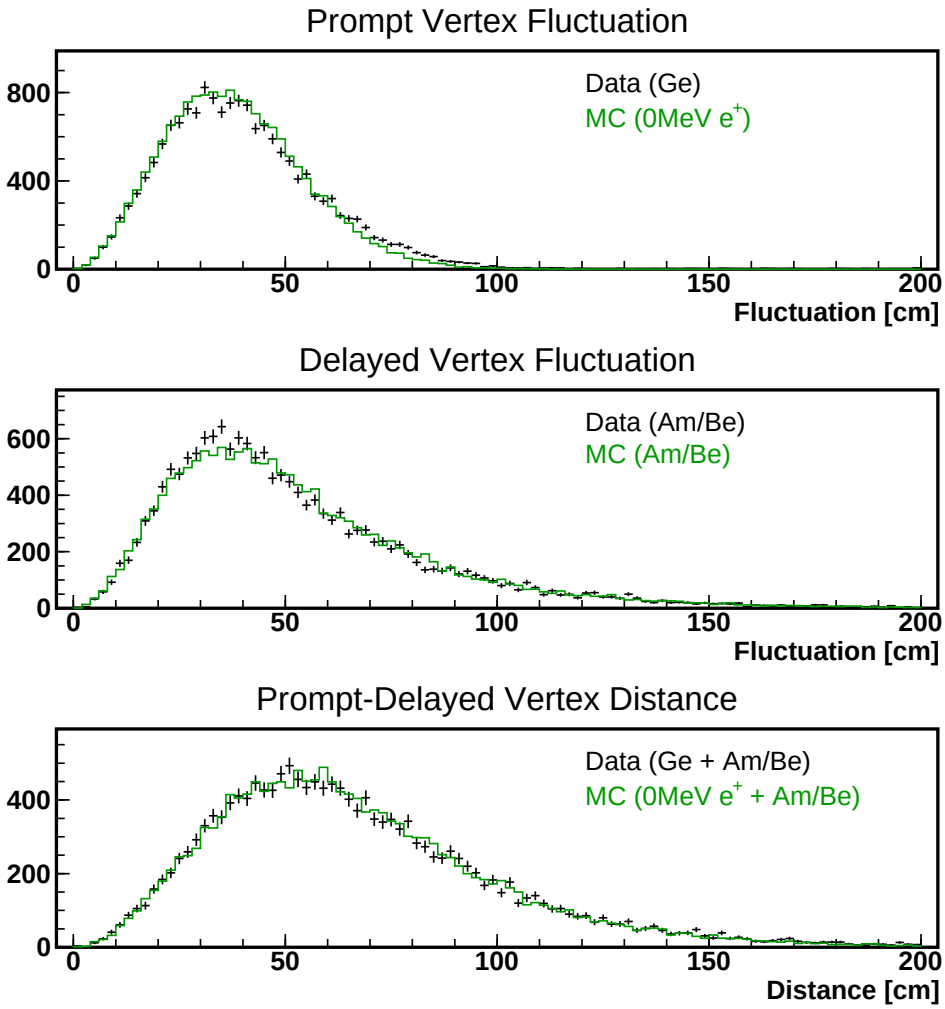

Figure 7.7: Comparison of MC and data on Vertex Fluctuation

Table 7.3: Spatial Cut Efficiency

Signal	Efficiency [%]
U-series Geo-neutrino	77.0
Th-series Geo-neutrino	75.7
Reactor Neutrino (1.8∼3.3 MeV)	77.3
(α,n) Reaction	76.1
0 MeV Positron + Neutron	74.2
1.5 MeV Positron + Neutron	78.1

tion resolution in the MC side, the resolution at the balloon center (z=0) is used because the source calibration data used here is taken with locating the source at the center. All source calibration data used here are reconstructed with using 20 inch PMT data, thus

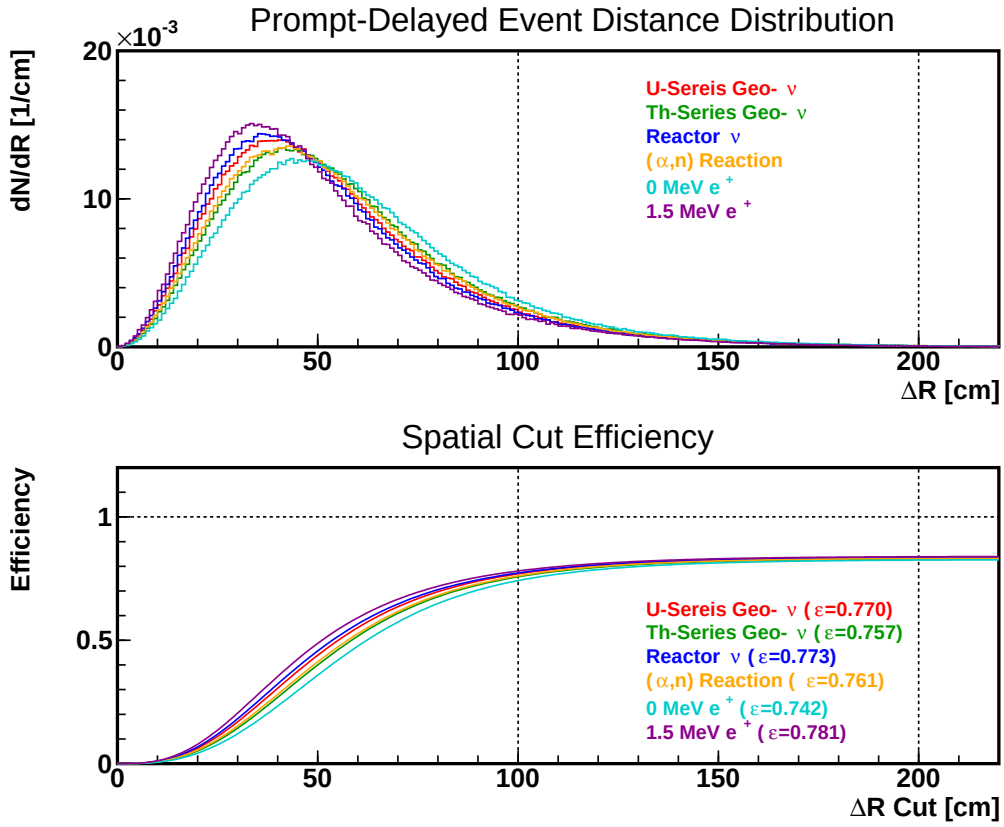

Figure 7.8: Spatial Cut Efficiency Estimation

narrower vertex reconstruction resolution is used in the MC side accordingly. Figure 7.9 shows the result. The upper panel and the middle panel are the same ones as those of efficiency estimation (Figure 7.8), and the lower panel shows the discrepancy between the two estimations. The difference around $\Delta R = 100$ cm is less than 1%.

7.5.4 Timing Correlation Cut Efficiency

The interval of the prompt signals and the delayed signals is essentially determined by the neutron thermalization and capture process. The time of neutron thermalization and capture is estimated with three different methods; measurement of muon-induced neutron capture time, Am/Be source calibration, and the Monte-Carlo (MC) method.

Muon induced neutron events are selected by collecting 2.2 MeV events following muons passing through the LS. Figure 7.10 shows the distribution of neutron capture event time since an associated muon event. By fitting an exponential curve plus constant background to the time distribution, the neutron capture time is estimated to be 211.2±2.6 μsec.

Figure 7.11 shows the distribution of the prompt signal energy and prompt-delayed signal intervals of Am/Be source calibration. Events are selected with essentially same criteria as those of neutrino event selection. To avoid accidental coincidences of two

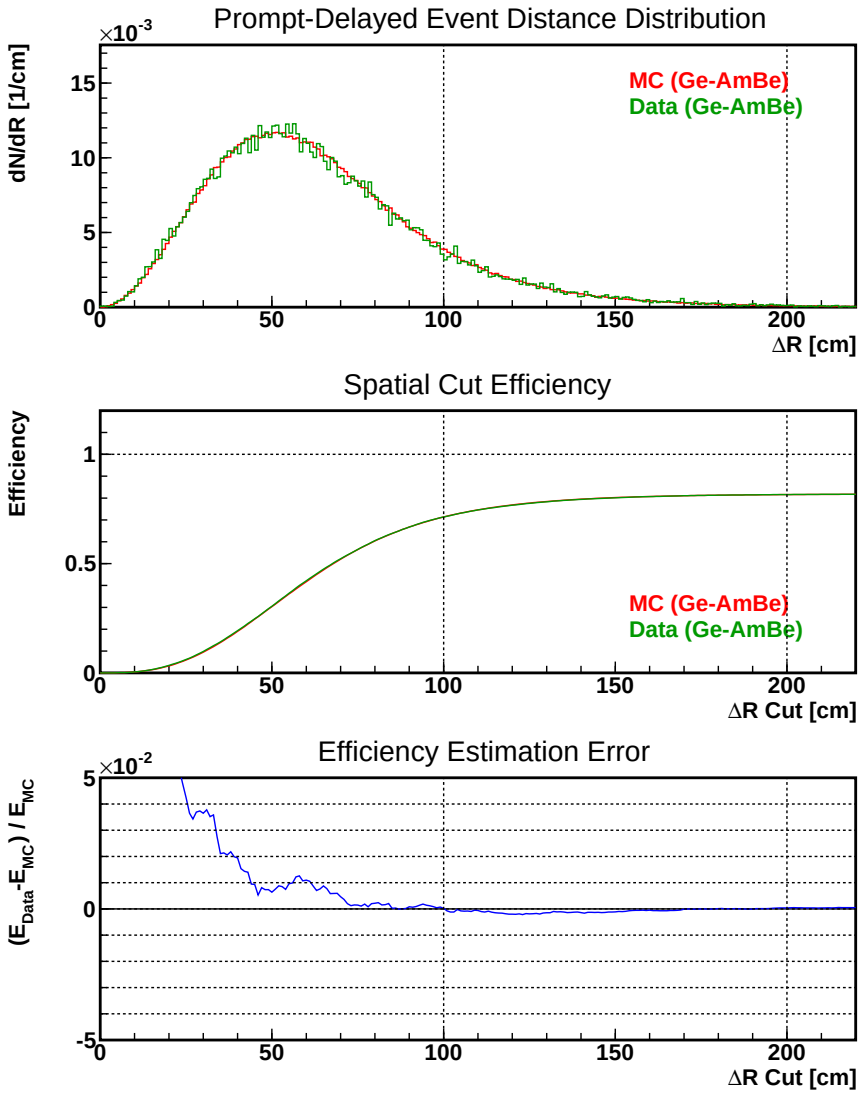

Figure 7.9: MC/Data Comparison in Spatial Cut Efficiency Estimation

neutrons, events with prompt signal energy greater than 2.6 MeV are used to estimate the capture time. By fitting an exponential curve plus constant background to the time distribution, the neutron capture time is estimated to be 212.3±5.1 μsec. Although this estimated time is consistent with estimation made with the muon-induced neutrons, this result is used to check the consistency, because the capture time might be slightly affected by the source container.

The neutron capture time is also estimated with a MC simulation. 400keV neutrons, which is in the same energy range as neutrino events, are generated in the KamLAND LS geometry, and time to capture on protons is calculated. Figure 7.12 shows the distribution of the simulated capture time. By fitting an exponential curve to the time distribution, the neutron capture time is estimated to be 210.0±2.7 μsec. This is consistent with the capture time estimated with muon induced neutrons.

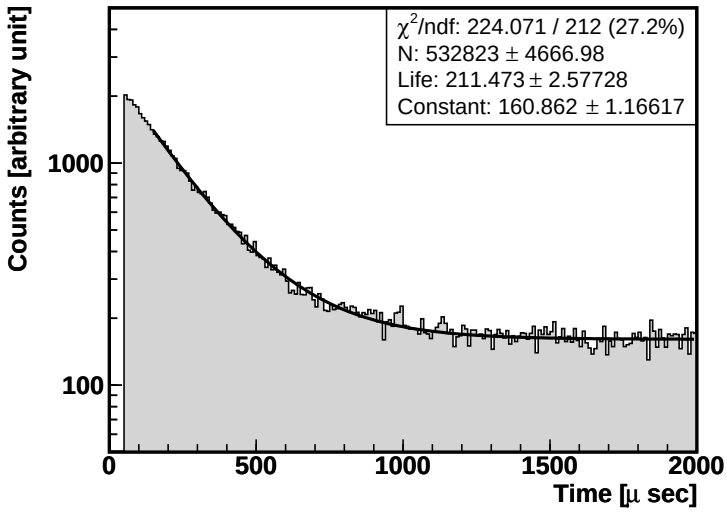

Figure 7.10: Muon-Induced Neutron Capture Time

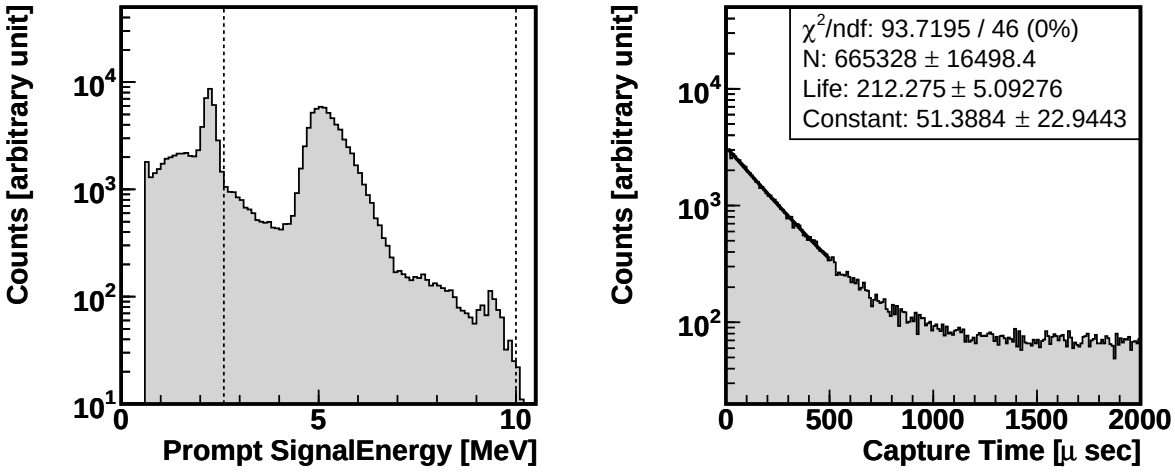

Figure 7.11: Am/Be Source Neutron Capture Time

Using the measured neutron capture time τ, efficiency of the timing correlation cut ε is estimated. In the timing correlation cut, we require the interval between the prompt and delayed signals ΔT be more than 0.5 μsec and less than 500 μsec. The efficiency is calculated by:

$$\varepsilon = \int_{\Delta T=0.5\mu\mathrm{sec}}^{500\mu\mathrm{sec}} \frac{1}{\tau} e^{-t/\tau} dt \tag{7.23}$$

with τ=211.2±2.6 μsec, ε=0.9039±0.0027.

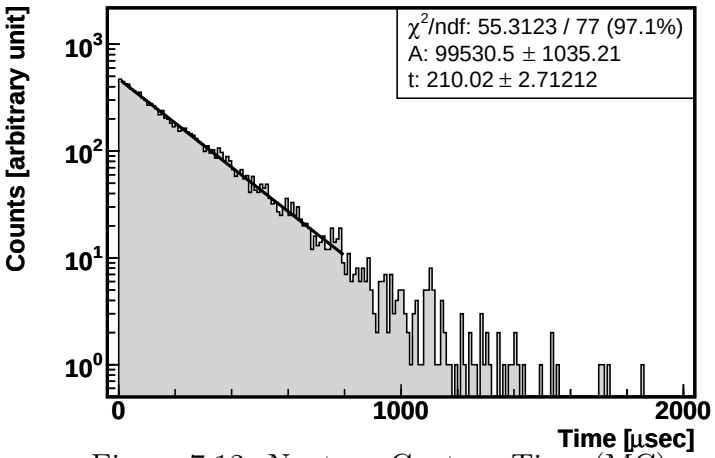

Figure 7.12: Neutron Capture Time (MC)

7.5.5 Delayed Signal Energy Cut Efficiency

The delayed signal of the neutrino delayed coincidence event is the 2.225 MeV gamma particles emitted by neutron capture on proton. In the neutrino event selection, we require the delayed signal energy be more than 1.8 MeV and less than 2.6 MeV in the visible energy scale. With $7.25\%/\sqrt{E_{\rm vis}/[\rm MeV]}$ energy resolution, the efficiency of this cut is calculated to be 99.97%.

7.5.6 Summary of Detection Efficiencies

Table 7.4 summarizes the estimated detection efficiencies.

Table 7.4: Summary of Detection Efficiencies

	Efficiency [%]			
	U-series $\bar{\nu}_e$	Th-series $\bar{\nu}_e$	Reactor $\bar{\nu}_e$	(α,n) Reaction
Neutron Capture on ^{1}H	99.48			
Trigger	99.96	99.90	99.99	-
Spatial Correlation	77.0	75.7	77.3	76.1
Timing Correlation	90.39			
Delayed Signal Energy	99.97			
Total	69.2	68.0	69.5	(68.4)

7.6 Systematic Errors

7.6.1 Neutrino Detection Errors

Systematic errors on neutrino detection, such as errors of cross section, livetime, fiducial volume and detection efficiencies, are already discussed in previous sections. Table 7.5 summarizes the estimated systematic errors.

Table 7.5: Neutrino Detection Systematic Errors

Source	Error [%]
$\bar{\nu_e}p \rightarrow e^+n$ Cross Section	0.2
Livetime	0.06
Fiducial Volume	4.91
Trigger Efficiency	0.04 / 0.09 / 0.007
Spatial Cut Efficiency	1.0
Timing Cut Efficiency	0.3
Total	5.0

7.6.2 Reactor Neutrino Background

Fission Rate Errors Errors of Japanese commercial nuclear reactor powers and fuel compositions are presented in Section 6.1, to be 2.1% and 1.0%, respectively.

Korean Reactors Neutrinos from Korean nuclear reactors are estimated based on published operational data, however, their fuel composition data is currently not available. The contribution of the Korean reactors to the total reactor neutrino flux at KamLAND is calculated to be 3.41±0.34%, where the error is assigned by varying the fuel compositions in some possible ranges.

Other Reactors For the other reactors, such as reactors in the other countries and non-commercial research reactors, no operational data are available in hand. Neutrinos from these reactors are estimated based on their design capacity. The maximum contribution of these reactors to the total KamLAND reactor neutrino flux is calculated to be 1.04%. We assign 100% error for this value.

Fission Spectrum Uncertainties The effect of fission spectrum uncertainties is studied by calculating the neutrino spectra expected at KamLAND, with the real reactor operation conditions and the real fuel composition. Figure 7.13 shows the calculated spectra. In the upper panel of the figure, the solid line indicates the center value, and the dotted lines indicate the range of 1 σ error, which is converted from the fission spectrum uncertainties. Integration of the spectra over the geo-neutrino analysis window is

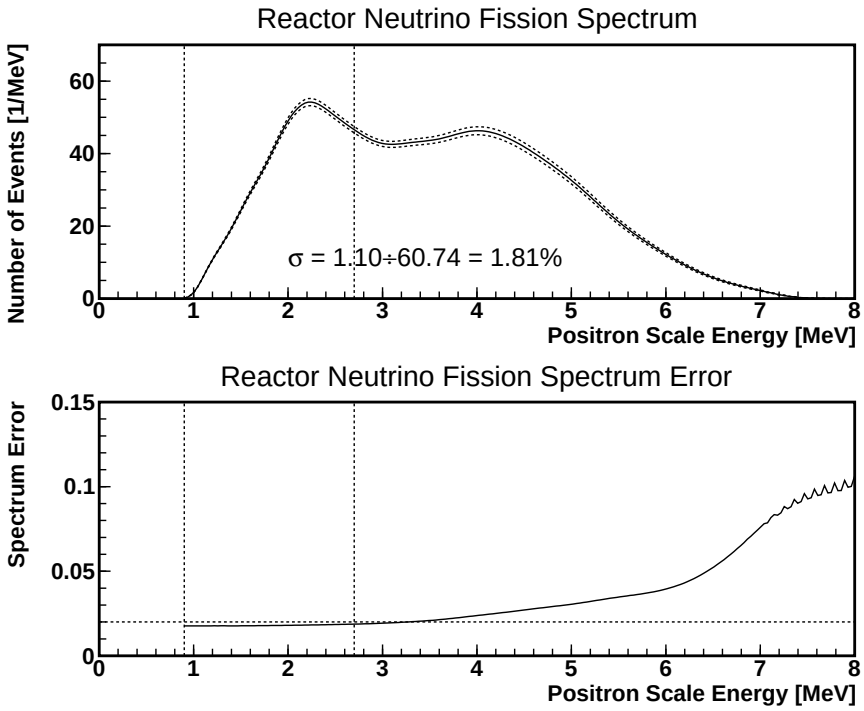

Figure 7.13: Reactor Neutrino Fission Spectrum Error

60.74±1.10, corresponding to 1.81% error. The spectrum error as a function of energy is shown in the lower panel. The error is almost constant throught the geo-neutrino analysis window.

Threshold Effects The geo-neutrino analysis window ends at 2.7 MeV, where the energy scale error is 2%. The reactor neutrino spectrum density at the 2.7 MeV threshold is 46.58/MeV, hence the 2% energy scale error makes ±2.52 event error, corresponding to 4.14% error of the reactor neutrinos in the geo-neutrino analysis window.

Oscillation Parameter Uncertainties The reactor neutrino backgrounds are also affected by uncertainties of the neutrino oscillation parameters. A recent study [2] estimated the parameters to be $\Delta m^2 = 7.9^{+0.6}_{-0.5} \times 10^{-5}\mathrm{eV}^2$ and $\tan^2\theta = 0.40^{+0.10}_{-0.07}$. Figure 7.14 shows the oscillation parameter estimation errors (χ^2 table) and number of reactor neutrino events in the geo-neutrino analysis window as a function of oscillation parameter value. The oscillation parameter is determined in [2] by a global analysis of the KamLAND measurement and solar neutrino observations.

As shown in the Figure 7.14, the number of reactor neutrino events depends on both of the $\sin^2 2\theta$ and Δm^2 values. To estimate the errors of the number of events, the χ^2 values are scanned respect to $(\Delta m^2, \sin^2 2\theta)$ to find the minimum χ^2 value (χ^2_{min}) for each given number of events;

$$\chi^2_{\mathrm{min}}(N) = \min_{N(\Delta m^2, \sin^2 2\theta)=N} \chi^2(\Delta m^2, \sin^2 2\theta) \tag{7.24}$$

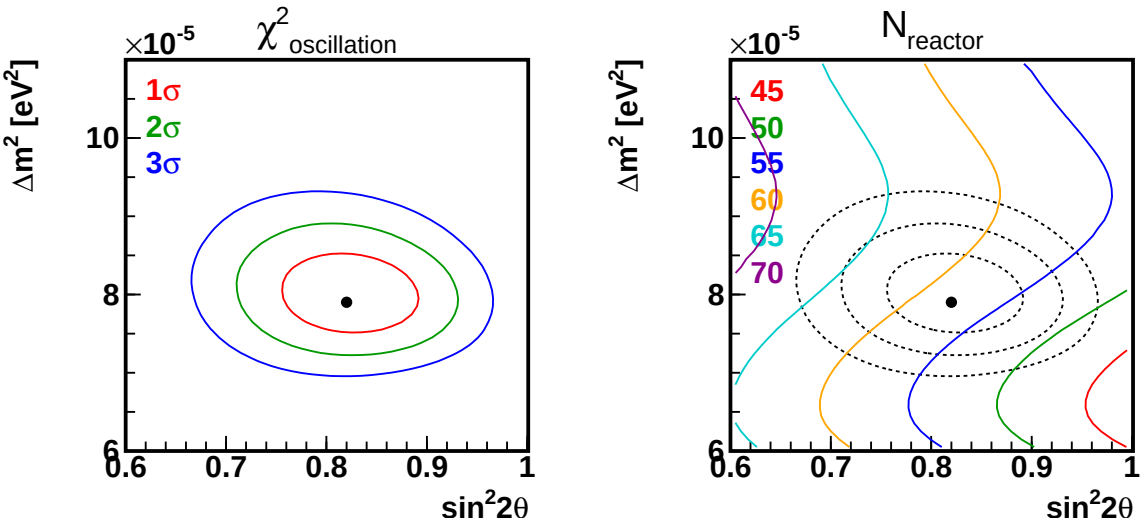

Figure 7.14: Neutrino Oscillation Parameters and Number of Reactor Neutrinos at KamLAND

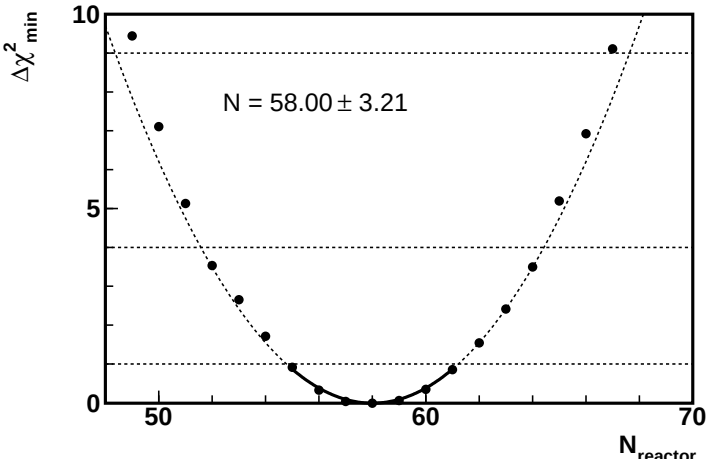

Figure 7.15: Reactor Neutrino Background Error by Oscillation Parameter Uncertainties

Figure 7.15 shows the minimized χ^2 values ($\chi^2_{\rm min}(N)$) for each number of events. $\chi^2_{\rm min}$ is minimum at the best estimation point (N=58.00). A fit of a parabola curve around the best estimation point gives an error estimation to be ±3.21 events.

7.6.3 (α,n) Reaction Background

As discussed in Section 6.4.4, there are a number of error sources in estimation of the (α,n) reaction backgrounds. As a conservative measure, we assign inclusive large errors to both of vertical scaling and horizontal scaling independently in the Region I of the spectrum. Taking account of the 14% Po decay rate error and the 20% (α,n) cross section error, we assign 24% error on the vertical scaling. Based on comparison of several neutron

Table 7.6: Reactor Neutrino Detection Errors

Source	Error [%]
Reactor Power	2.1
Fuel Composition	1.0
Korean Reactors	0.34
Other Reactors	0.52
Fission Spectrum	1.8
Oscillation Parameters	5.5
Energy Threshold	4.1
Neutrino Detection	5.0
Total	9.0

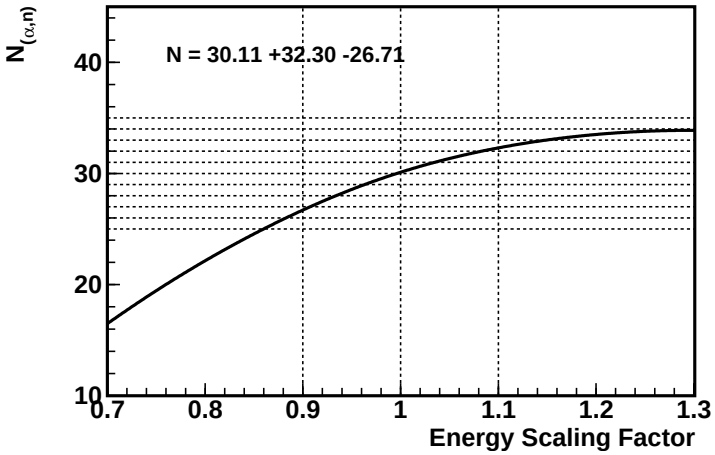

Figure 7.16: (α,n) Background Error by Spectrum Shape Uncertainties

quenching calculations, we assign 10% error on the horizontal scaling. The Region II and Region III of the spectrum do not directly affect to the geo-neutrino analysis window.

Figure 7.16 shows the number of the (α,n) reaction backgrounds as a function of the horizontal scaling (energy scaling). As shown in the figure, 10% horizontal scaling error corresponds to 9.3% error on the number of events.

In addition to the spectrum shape errors, the background estimation suffers from other systematic errors as the same way as the neutrino detection. The errors of livetime and fiducial volume are same as those of neutrino detection. The errors of detection efficiency is discussed in Section 7.5. The spectrum densities at the 0.9 MeV threshold and at the 2.7 MeV threshold are 24.8/MeV and 1.07/MeV, respectively. The energy scale error is about 2% at both of the two threshold energies, resulting in $\pm$0.45 and $\pm$0.06 event errors, which corresopnds to 1.5% and 0.20% errors, respectively.

Table 7.7 summarizes the errors on the (α,n) reaction background counting.

Table 7.7: (α,n) Reaction Background Errors

Source	Error [%]
Spectrum Vertical Scaling	24
Spectrum Horizontal Scaling	9.3
Livetime	0.06
Fiducial Volume	4.9
Spatial Cut Efficiency	1.0
Timing Cut Efficiency	0.3
2.7MeV Threshold	0.20
0.9MeV Threshold / Trigger Threshold	1.5
Total	26.3

7.7 Expected Event Rate and Spectrum

Using the estimated detector livetime, number of target protons and detection efficiencies, expected spectra of geo-neutrinos are calculated by:

$$\frac{dN}{dE_p} = \varepsilon(E_p) \cdot N_{\text{proton}} \cdot \tau \cdot \int_{E'_p=0}^{\infty} \left\{ \sigma(E'_p) \left(\frac{dn}{dE'_p} \right) \cdot \frac{1}{\sqrt{2\pi s^2}} e^{-\frac{(E_p - E'_p)^2}{2s^2}} \right\} dE'_p \tag{7.25}$$

where E_p is the prompt signal energy in positron energy scale, ε is the detection efficiency, N_{proton} is the number of target protons, τ is the detector livetime, $\sigma(E_p)$ is the $\bar{\nu}_e + p$ cross section, s is the energy resolution, and $\frac{dn}{dE_p}$ is the geo-neutrino spectrum. The total number of expected geo-neutrino events is obtained by integrating the spectrum over the analysis window;

$$N = \int_{E_p=0.9\text{MeV}}^{2.7\text{MeV}} \frac{dN}{dE_p} dE_p \tag{7.26}$$

With my best Earth reference model presented in Chapter 2, 10.27±0.51(syst) of the U-series geo-neutrinos and 2.71±0.14(syst) of the Th-series geo-neutrinos are expected, where the errors include only systematic errors of neutrino detection at KamLAND, and do not include the model uncertainties and statistical errors. The total number of the geo-neutrino events is thus expected to be 12.98±0.65(syst).

Figure 7.17 shows the expected geo-neutrino spectra and the estimated background spectra, superposed on observed data spectrum.

7.8 Rate Analysis

As shown in Chapter 5, we observed 113 events as candidates of geo-neutrino events. As discussed in Chapter 6, we estimated the number of background events in our candidate

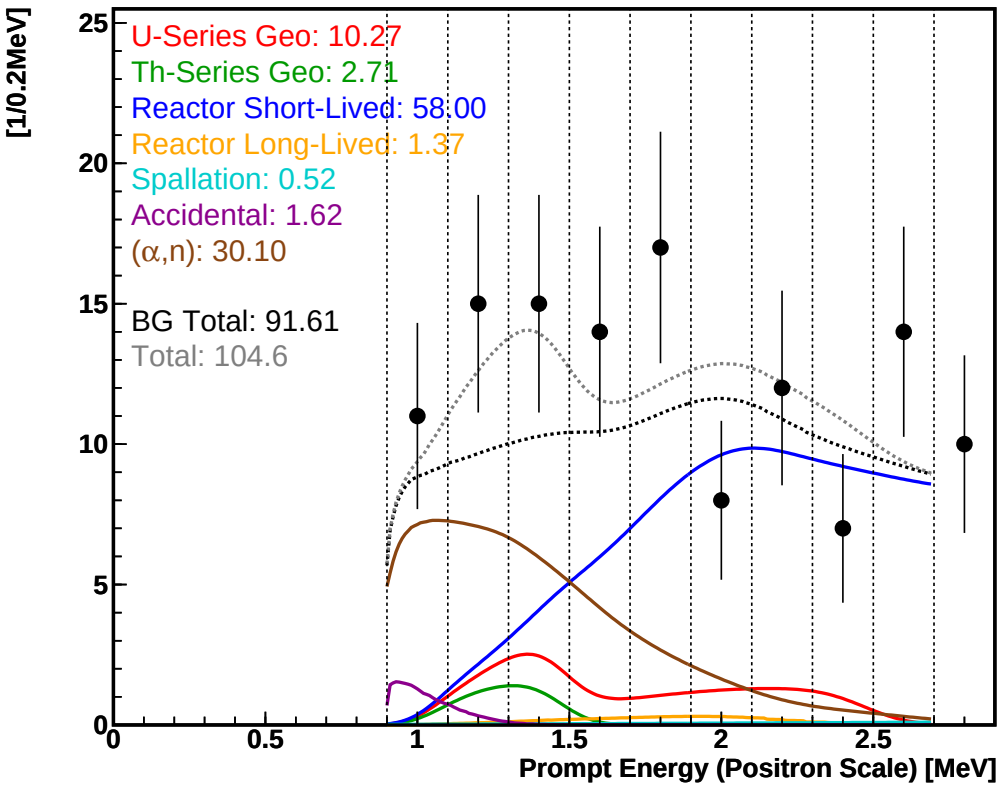

Figure 7.17: Expected Spectrum

set to be 91.61±9.52(syst)±9.57(stat). By simply subtracting the number of estimated background events from the number of observed events, we obtain the estimated number of geo-neutrino events to be 21.4±13.5.

The significance of geo-neutrino signal positivity is examined by testing a null hypothesis that we do not observe any geo-neutrinos. Under this null hypothesis, the probability that we could observe greater number of events than we actually observed is calculated, with considering both of the Gaussian systematic errors of the background estimation and the Poisson statistical errors, given by

$$P(N \geq N^{\rm obs}) = \int_{\nu=0}^{\infty} \left(\frac{1}{\sqrt{2\pi\sigma^2}} e^{-\frac{(\nu - N^{\rm hyp})^2}{2\sigma^2}} \times \sum_{N=N^{\rm obs}}^{\infty} \frac{\nu^N}{N!} e^{-\nu} \right) d\nu \tag{7.27}$$

$$= \sum_{N=N^{\rm obs}}^{\infty} \left\{ \int_{\nu=0}^{\infty} \left(\frac{1}{\sqrt{2\pi\sigma^2}} e^{-\frac{(\nu - N^{\rm hyp})^2}{2\sigma^2}} \times \frac{\nu^N}{N!} e^{-\nu} \right) d\nu \right\} \tag{7.28}$$

where $N^{\rm obs}$ is the number of actually observed events, $N^{\rm hyp}$ is the number of expected events under the null hypothesis (i.e., the number of backgrounds), and σ is the systematic error of $N^{\rm hyp}$ estimation.

Figure 7.18 shows the probability density function of observing N events, under the

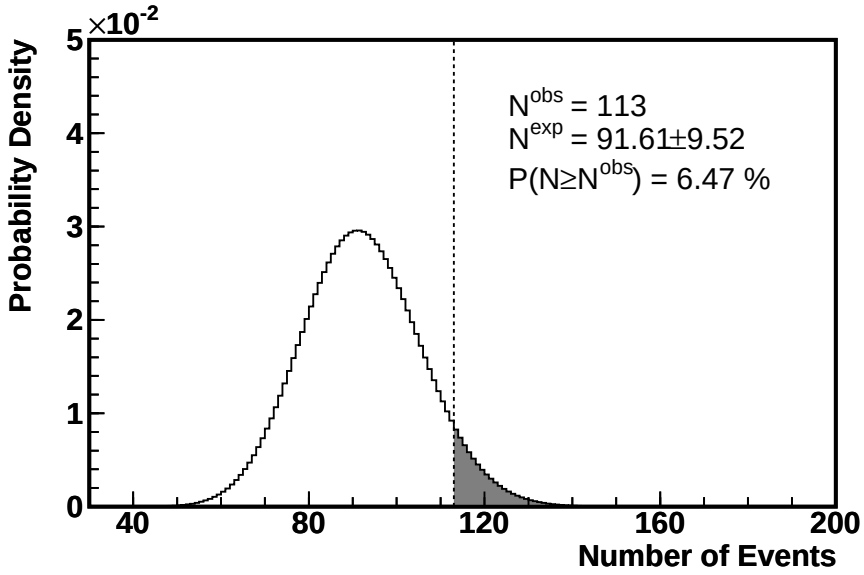

Figure 7.18: Zero Geo-Neutrino Hypothesis Test

null hypothesis. The probability of observing more than or equal to $N^{\rm obs}$ events is calculated to be 6.47%. The significance of positive number of geo-neutrino observation is then 93.5%.

If the geo-neutrino flux is $F_{\rm geo}$ in the TNU unit (the number of events with 10^{32} targets, 1 year observation, 100% efficiency), the number of expected geo-neutrino events $N_{\rm geo}^{\rm exp}$ in our data set without statistical error is

$$N_{\rm geo}^{\rm exp} = \frac{68\%}{100\%} \cdot \frac{3.459 \times 10^{31}}{10^{32}} \cdot \frac{513.92\ [\rm day]}{1\ [\rm year]} \cdot \frac{F_{\rm geo}}{[\rm TNU]} \tag{7.29}$$

$$= 0.33 \cdot \frac{F_{\rm geo}}{[\rm TNU]} \tag{7.30}$$

The total number of events is then:

$$N^{\rm exp} = \left[\left\{(N_{\rm geo}^{\rm exp} + (N_{\rm reactor} \pm \sigma_{\rm reactor})\right\} \pm \sigma_{\rm syst}\right] + (N_{\rm BG} \pm \sigma_{\rm BG}) \tag{7.31}$$

where $N_{\rm reactor}$ and $\sigma_{\rm reactor}$ are the number of estimated reactor neutrino events and its error of flux calculation, $N_{\rm BG}$ and $\sigma_{\rm BG}$ are the number of estimated non-neutrino background events and its error. The geo-neutrino events and the reactor neutrino events share most of systematic errors ($\sigma_{\rm syst}$) such as errors on fiducial volume and detection efficiencies. Although the (α,n) reaction background shares some of these errors, contribution of which are negligible compared with the other errors such as errors on spectrum shape, hence we treat the errors of the (α,n) reaction backgrounds as independent from errors of neutrino events. With the estimated values, (7.31) is calculated to be

$$N^{\rm exp} = \left[\left\{(0.33\frac{F_{\rm geo}}{[\rm TNU]} + (58.00 \pm 7.5\%)\right\} \pm 5.0\%\right] + (33.61 \pm 7.13) \quad (7.32)$$

$$= \left\{0.33\frac{F_{\rm geo}}{[\rm TNU]} + 91.61\right\} \pm \left\{(0.017\frac{F_{\rm geo}}{[\rm TNU]} + 2.9) \oplus 8.36\right\} \quad (7.33)$$

$$:= \mu^{\rm exp} \pm \sigma^{\rm exp} \quad (7.34)$$

For each given $F_{\rm geo}$, the probability of observing N events is calculated with including statistical error by

$$P(N; F_{\rm geo}) = \int_{\nu=0}^{\infty} \left(\frac{1}{\sqrt{2\pi(\sigma^{\rm exp})^2}} e^{-\frac{(\nu-\mu^{\rm exp})^2}{2(\sigma^{\rm exp})^2}} \times \frac{\nu^N}{N!} e^{-\nu} \right) d\nu \quad (7.35)$$

Under an hypothesis that the geo-neutrino flux is $F_{\rm geo}$, an interval $[\beta_{\rm lower}, \beta_{\rm upper}]$ of N where fraction α of observations are included in the interval is expressed by

$$\int_{\beta_{\rm lower}}^{\beta_{\rm upper}} P(N; F_{\rm geo}) dN = \alpha \quad (7.36)$$

In this analysis, we construct two types of intervals; one is 1 σ two side interval, and the other is 99% one side interval. In the former case, we set α=68.3% and set β in a manner that $N^{\rm exp}$ becomes the center of the region. In the latter case, we set α=99%, and set the upper boudary to be ∞.

$$1\sigma \text{ two side} : \int_{N^{\rm exp}-\beta}^{N^{\rm exp}+\beta} P(N; F_{\rm geo}) dN = 0.683 \quad (7.37)$$

$$99\% \text{ one side} : \int_{\beta}^{\infty} P(N; F_{\rm geo}) dN = 0.99 \quad (7.38)$$

Figure 7.19 shows the intervals of N as defined above, for each given $F_{\rm geo}$. Each horizontal line segment corresponds to one hypothetical $F_{\rm geo}$ value, and the segment indicates the interval of N under the hypothesis. The confidence interval (C.I.) of flux, which is defined by a set of $F_{\rm geo}$ whose N interval includes the actually observed number of events $N^{\rm obs}$, are found from the figure to be $23.5 < F_{\rm geo} < 106.7$ [TNU] (two side 68.3% C.L.) and $F_{\rm geo} < 172.2$ [TNU] (one side 99% C.L.), respectively.

Table 7.8 summarizes the results of the rate analysis.

7.9 Spectrum Shape Analysis

The maximum likelihood method is utilized to analyze the spectrum shape. The principle of the method is to find out the set of parameters that gives the maximum probability density of observing data that was actually observed.

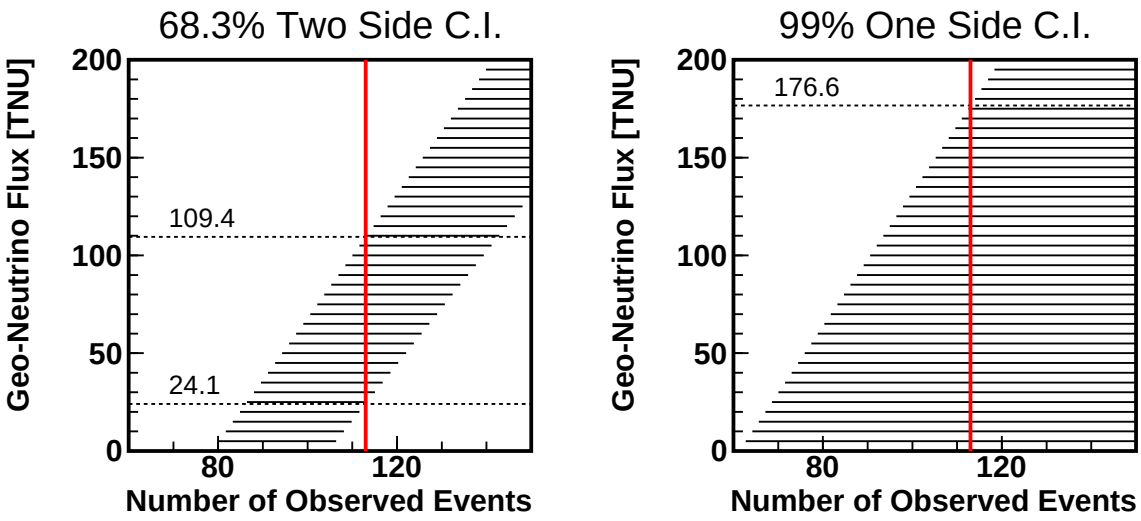

Figure 7.19: Confidence Interval of Geo-Neutrino Flux

Table 7.8: Summary of Rate Analysis

Number of Observed Events	113
Number of Estimated Backgrounds	91.61±9.52(syst)
Number of Estimated Geo-neutrino Events	21.4±13.5
Significance of Positive Geo-neutrino Signal	93.5%
Estimated Geo-neutrino Flux	$64.8^{+44.6}_{-40.7}$ [TNU]
Geo-neutrino Flux Upper Limit (99% C.L.)	176.6 [TNU]

With a given set of hypothetical parameters α_k and observed data set x_i, the likelihood statistic $\mathcal{L}(x_i;\alpha_k)$ is defined by the joint probability density of observing x_i under the assumption of α_k,

$$\mathcal{L}(x_i;\ \alpha_k) = \prod_i \frac{dP}{dx}(x_i;\ \alpha_k) \tag{7.39}$$

where $\frac{dP}{dx}(x;\alpha_k)$ is the theoretical probability density function. The maximum likelihood estimator $\hat{\alpha}_i$ is defined by the set of values that maximizes the likelihood statistic $\mathcal{L}$, for a given set of x_i.

For a large set of x_i, the central limit theorem usually assures that $\mathcal{L}$ will be well approximated by a multivariate Gaussian (with some exceptions, such as a case that estimator is biased). In this case, errors of the likelihood estimators $\hat{\alpha}_i$ can be conveniently estimated with χ^2 distributing statistic $\chi^2 = -2\log\mathcal{L}$.

In this analysis, we parameterize the U-series geo-neutrino flux F_{U} and the Th-series geo-neutrino flux F_{Th}. For convenience, we express the parameters in terms of number of

observed events; $N_{\rm U} \equiv 0.33 F_{\rm U}/[\rm TNU]$ and $N_{\rm Th} \equiv 0.33 F_{\rm Th}/[\rm TNU]$. It should be emphasized that N is not the number of observed events itself. To convert to the number of events, we need to include the systematic and statistical errors.

We also parametrize the contribution of some major backgrounds. As discussed in Chapter 6, the reactor neutrino backgrounds and the (α,n) reaction backgrounds account for 95% of the total backgrounds. Hence the neutrino oscillation parameters, Δm^2 and $\sin^2 2\theta$, and the (α,n) spectrum error parameters, $\alpha_{\rm vertical}$ for vertical scaling and $\alpha_{\rm horizontal}$ for horizontal scaling, are included into the likelihood definition.

$$\mathcal{L}(\text{data};\ N_{\rm U}, N_{\rm Th}, \text{parameters}) = \prod_i \frac{dP}{dE}(E_i;\ N_{\rm U}, N_{\rm Th}, \text{parameters}) \tag{7.40}$$

where "parameters" denotes the background parameters, Δm^2, $\sin^2 2\theta$, $\alpha_{\rm vertical}$ and $\alpha_{\rm horizontal}$. dP/dE is the energy probability density function, given by the normalized expected-spectra,

$$\frac{dP}{dE} = \frac{\sum_k \frac{dN_k}{dE}}{\int_{E=0.9\rm MeV}^{2.7\rm MeV} \left(\sum_k \frac{dN_k}{dE}\right) dE} \tag{7.41}$$

where dN_k/dE is the spectrum of each signal or background source labeled by k; U-series geo-neutrinos, Th-series geo-neutrinos, reactor neutrinos, reactor long-lived fission product neutrinos, muon spallation products, accidental coincidences, and the (α,n) reactions. These spectra are given in Section 7.7.

We express the spectrum shape likelihood statistic by a χ^2 statistic for convenience;

$$\chi^2{}_{\text{uc-shape}} = -2 \log \mathcal{L}(\text{data};\ N_{\rm U}, N_{\rm Th}, \text{parameters}) \tag{7.42}$$

where "uc-shape" denotes "unconstrained shape"; since the background parameters are constrained by other independent estimations, the constraints should be incorporated for a better estimation of the geo-neutrino flux. The reproductivity nature of the χ^2 statistic (i.e., $\chi^2{}_{\rm a+b} = \chi^2{}_{\rm a} + \chi^2{}_{\rm b}$) eases this operation;

$$\chi^2{}_{\text{shape}} = \chi^2{}_{\text{uc-shape}} + \chi^2{}_{\text{parameters}} \tag{7.43}$$

with

$$\chi^2{}_{\text{parameters}} = \chi^2(\Delta m^2, \sin^2 2\theta) + \frac{(\alpha_{\rm vertical} - 1)^2}{\sigma^2{}_{\rm vertical}} + \frac{(\alpha_{\rm horizontal} - 1)^2}{\sigma^2{}_{\rm horizontal}} \tag{7.44}$$

The χ^2 values of the neutrino oscillation parameters, $\chi^2(\Delta m^2, \sin^2 2\theta)$, are taken from a recent estimation based on a global analysis of the KamLAND reactor neutrino measurement and the solar neutrino observations [2].

Constraints from the rate analysis are also incorporated into the shape analysis.

$$\chi^2{}_{\text{rate+shape}} = \chi^2{}_{\text{uc-rate}} + \chi^2{}_{\text{uc-shape}} + \chi^2{}_{\text{parameters}} \tag{7.45}$$

where $\chi^2{}_{\text{uc-rate}}$ is the χ^2 representation of the rate statistic. $\chi^2{}_{\text{uc-rate}}$ is constructed basically in the same way as the rate analysis, except for errors of the oscillation parameters and

the (α,n) background spectrum shape are separated to ${\chi^2}_{\rm parameters}$. Without these errors, the reactor neutrino flux error is calculated from Table 7.6 to be 5.1%, and the (α,n) background error is calculated from Table 7.7 to be 5.2%. From Table 6.14 in Chapter 6, the number of all other backgrounds is calculated to be 3.51±0.24. The expected total number of events given in (7.31) is calculated to be:

$$\begin{aligned} N^{\rm exp} &= [\{N_{\rm geo} + (N_{\rm reactor} \pm 5.1\%)\} \pm 5.0\%] + (N_{(\alpha,{\rm n})} \pm 5.2\%) + (3.51 \pm 0.24) \\ &:= \mu^{\rm exp} \pm \sigma^{\rm exp} \end{aligned} \tag{7.46}$$

with

$$\begin{aligned} N_{\rm geo} &\equiv 0.33 \cdot \frac{F_{\rm U} + F_{\rm Th}}{[{\rm TNU}]} \\ \mu^{\rm exp} &= N_{\rm geo} + N_{\rm reactor} + N_{(\alpha,{\rm n})} + 3.51 \\ \sigma^{\rm exp} &= \{(N_{\rm geo} + N_{\rm reactor}) \times 5.0\%\} \oplus (N_{\rm reactor} \times 5.1\%) \oplus (N_{(\alpha,{\rm n})} \times 5.2\%) \oplus 0.24 \end{aligned}$$

With taking account of statistical errors, the unconstrained rate χ^2 is defined as

$${\chi^2}_{\rm uc\text{-}rate} = \frac{(N^{\rm obs} - \mu^{\rm exp})^2}{\mu^{\rm exp} + (\sigma^{\rm exp})^2} \tag{7.47}$$

Combined with the parameter constraint χ^2, the unconstrained rate χ^2 becomes the rate χ^2, which represents the rate statistic in the χ^2 representation.

$${\chi^2}_{\rm rate}(N_{\rm geo}, \sin^2 2\theta, \Delta m^2, \alpha_{\rm vertical}, \alpha_{\rm horizontal}) = {\chi^2}_{\rm uc\text{-}rate} + {\chi^2}_{\rm parameters} \tag{7.48}$$

If the ${\chi^2}_{\rm rate}$ is minimized respect to the oscillation parameters and the (α,n) spectrum shape parameters, it gives the one-parameter χ^2 value for each given $N_{\rm geo}$. The C.I. constructed from the ${\chi^2}_{\rm rate}(N_{\rm geo})$ distribution should give the identical result as provided in the rate analysis shown in the previous section.

Figure 7.20 shows the distribution of ${\chi^2}_{\rm rate}(N_{\rm geo})$ constructed in this way. The two-side C.I. of 68.3% C.L. is given by the interval of $N_{\rm geo}$ that corresponds to $\chi^2 < 1.0$. It is found to be $21.4^{+15.0}_{-14.1}$ events, or $62.9^{+44.1}_{-41.5}$ TNU. This result is consistent with the estimation presented in the previous section, although both of the estimations involve some Gaussian approximations in different ways.

Using the procedure presented above, distribution of $\chi^2(N_{\rm U}, N_{\rm Th})$ is calculated with the observed data set. For each pair of $N_{\rm U}$ and $N_{\rm Th}$, $\chi^2(N_{\rm U}, N_{\rm Th}, {\rm parameters})$ is minimized respect to the "parameters" (i.e., Δm^2, $\sin^2 2\theta$, $\alpha_{\rm vertical}$, and $\alpha_{\rm horizontal}$). Figure 7.21 shows the contour plots of the $\chi^2(N_{\rm U}, N_{\rm Th})$ distributions, one for the shape only χ^2 and one for the rate+shape χ^2.

These two contours are quite similar, and consistent with each other. They are also consistent with the rate analysis. The best fit point is found at $N_{\rm U} = 0.0$ and $N_{\rm Th} = 10.1$ with the spectrum shape only analysis, and $N_{\rm U} = 1.4$ and $N_{\rm Th} = 11.9$ with the rate plus spectrum shape analysis. However, the 1 σ region, which is indicated with blue lines in the figure, includes most of the region with $N_{\rm U} + N_{\rm Th} < 25$. The 1 σ region includes the best-expected geo-neutrino flux, $N_{\rm U} = 10.27$ and $N_{\rm Th} = 2.71$. At the best fit points, the

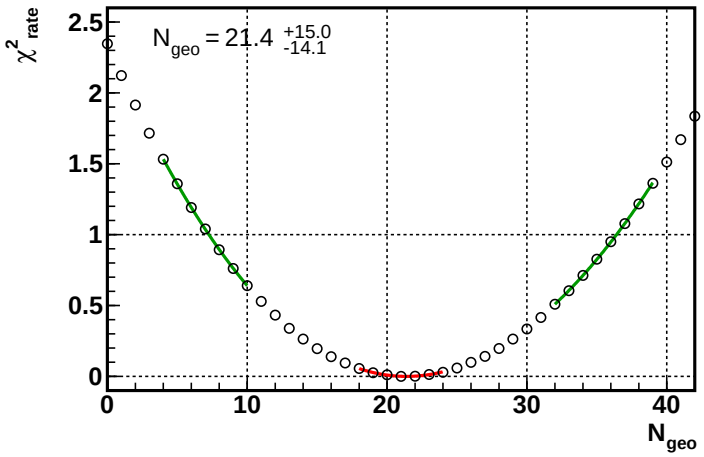

Figure 7.20: Geo-Neutrino Rate Analysis in χ^2 Representation

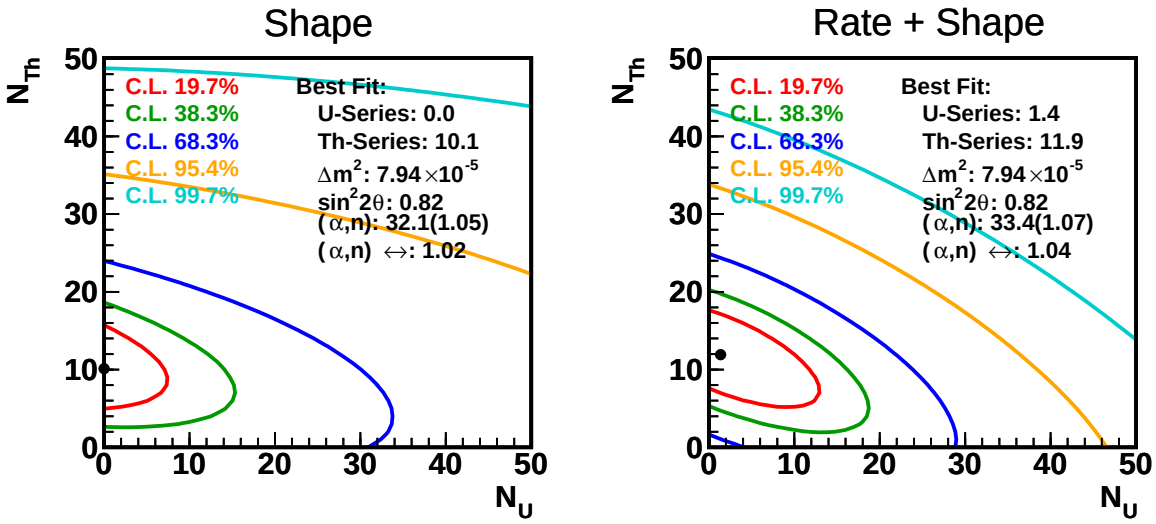

Figure 7.21: Geo-Neutrino Spectrum Shape Analysis

neutrino oscillation parameters are scaled by less than 1% in both analyses, and (α,n) background parameters are scaled vertically by 5% (0.2σ) in the shape analysys and 7% (0.3σ) in the rate+shape analysis, and horizontally by 2% (0.2σ) in the shape analysis and 4% (0.4σ) in the rate+shape analysis. These small scalings indicate that the shape analysis is consistent with the background estimations (as far as the backgrounds are relevant to the shape analysis). Validity of the fit is discussed further in the next section.

Figure 7.22 shows the distribution of 1-parameter χ^2 for $N_{\rm U}$ or $N_{\rm Th}$ in the spectrum shape analysis. To obtain the 1-parameter χ^2, the 2-parameter χ^2 is minimized respect to $N_{\rm Th}$ for a given $N_{\rm U}$, and vice versa. The geo-neutrino fluxes are estimated to be $N_{\rm U} = 0.0^{+15.9}_{-0.0}$ and $N_{\rm Th} = 10.1^{+8.7}_{-7.8}$. Figure 7.23 shows the distribution of 1-parameter χ^2 in the rate+shape analysis. The fluxes are estimated to be $N_{\rm U} = 1.4^{+17.7}_{-1.4}$ and $N_{\rm Th} = 11.9^{+8.5}_{-10.2}$.

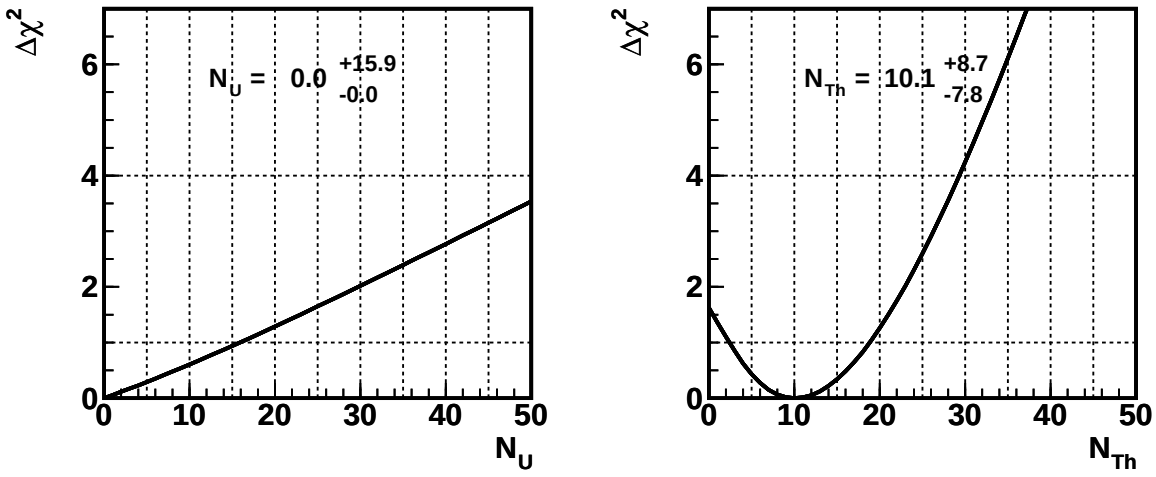

Figure 7.22: Geo-Neutrino Spectrum Shape Analysis (1-parameter estimation)

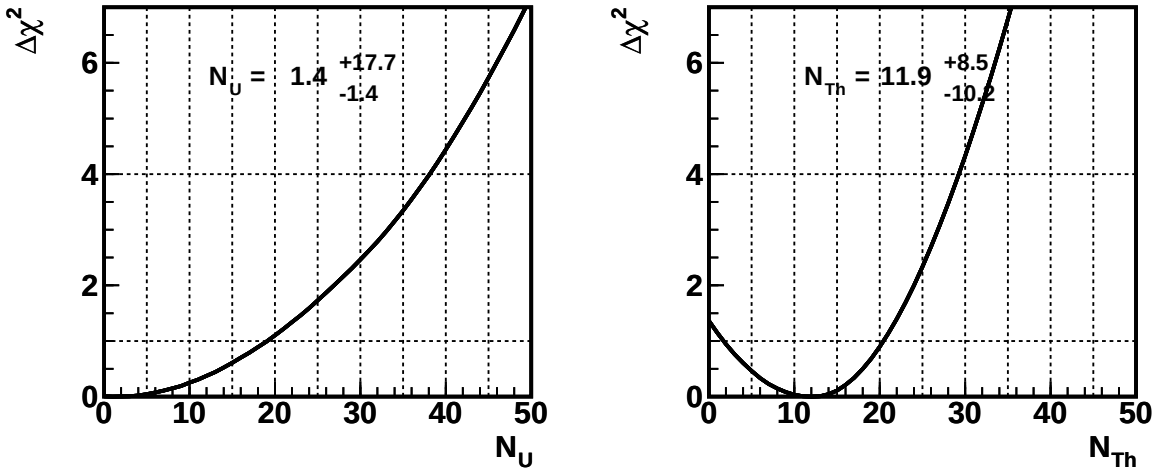

Figure 7.23: Geo-Neutrino Spectrum Rate+Shape Analysis (1-parameter estimation)

As can be seen in the Figure 7.21, the spectrum shape analysis is less sensitive to the $N_{\rm U}/N_{\rm Th}$ ratio than the total geo-neutrino flux ($N_{\rm U}+N_{\rm Th}$). From geophysical/geochemical point of view, the total flux is of particular interest, while the U/Th ratio is well determined from cosmo-chemical arguments. Behaviors of Uranium and Thorium in the Earth are quite similar to each other, and their ratio in various Earth components is fairly stable. Hence it is interesting to display the 2-parameter χ^2 contour in a way that the total flux and the U/Th ratio are separated.

Figure 7.24 shows the distribution of χ^2, which is identical to that of Figure 7.21, but displayed in a $(N_{\rm U}+N_{\rm Th})$ v.s. $(N_{\rm U}-N_{\rm Th})/(N_{\rm U}+N_{\rm Th})$ plane. The vertical axis shows the total flux and the horizontal axis corresponds to the U/Th flux ratio. Figure 7.25 shows

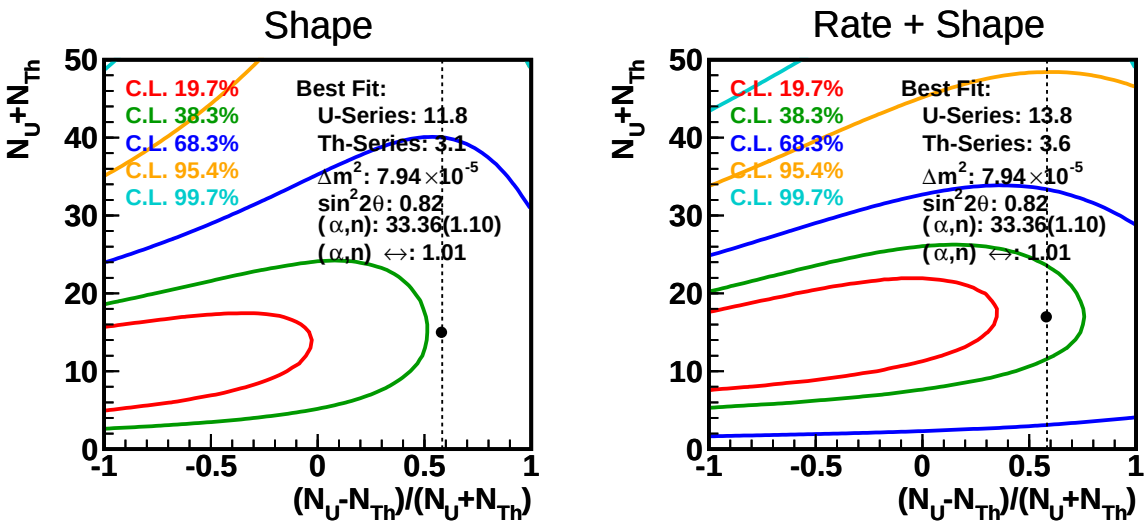

Figure 7.24: Geo-Neutrino Spectrum Shape Analysis

1-parameter χ^2 for $N_{\rm U} + N_{\rm Th}$, where χ^2 is minimized respect to $(N_{\rm U} - N_{\rm Th})/(N_{\rm U} + N_{\rm Th})$. 1-$\sigma$ range of the total geo-neutrino flux is estimated to be $10.1^{+14.6}_{-7.6}$ from the shape only analysis and $13.4^{+13.2}_{-8.2}$ from the rate+shape analysis.

Geochemistry predicts that the ratio of geo-neutrino flux ($N_{\rm U}/N_{\rm Th}$) is ∼3.8. This constraint is indicated in the Figure 7.24 with a vertical dot line. Figure 7.26 shows the distribution of 1-parameter χ^2 along the geochemical constraint line. The best fit value along the constraint line is found to be $N_{\rm U}+N_{\rm Th} = 14.9^{+21.9}_{-14.9}$ with the spectrum shape only analysis and $N_{\rm U} + N_{\rm Th} = 17.5^{+12.5}_{-11.5}$ with the rate+shape analysis. These best-fit points are within the 1 σ region of the unconstrained contour, and scaling of the background parameters at the best-fit points is in similar magnitude as that at the unconstrained best-fit points.

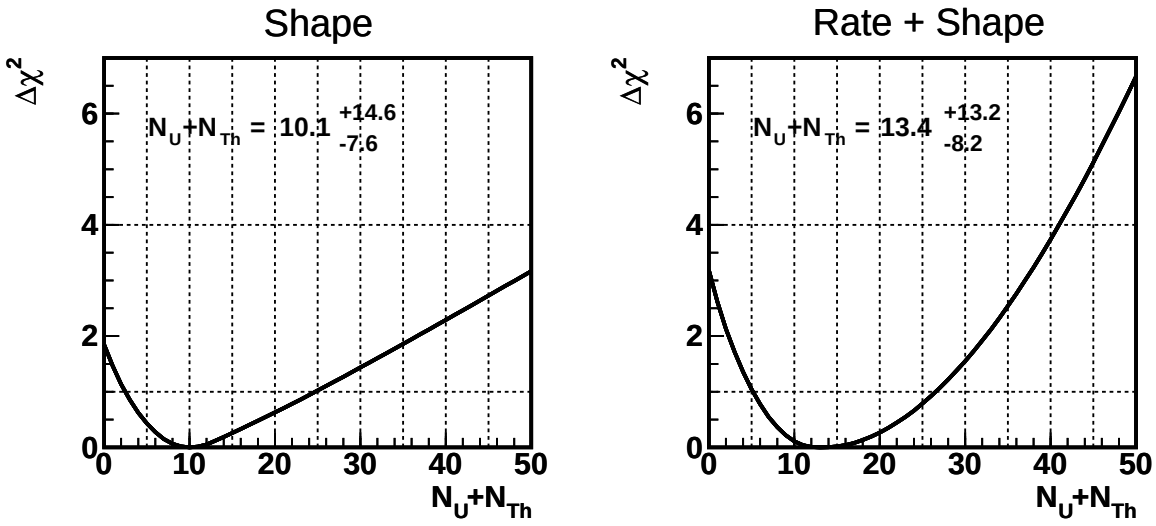

Figure 7.25: Geo-Neutrino Spectrum Shape Analysis (U/Th Ratio Floated)

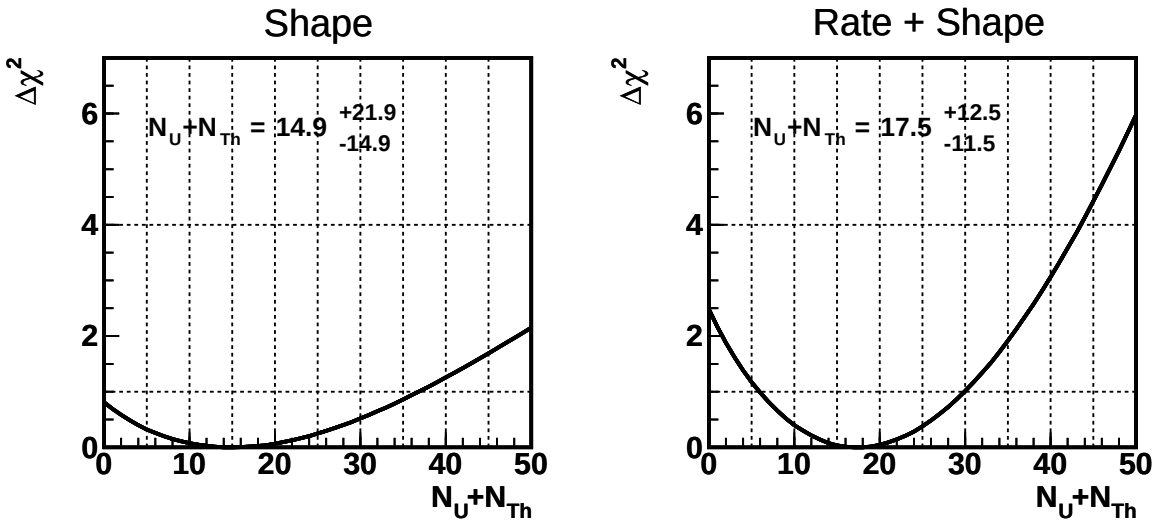

Figure 7.26: Geo-Neutrino Spectrum Shape Analysis (U/Th Ratio Fixed)

Table 7.9 and Figure 7.27 summarizes the results of the spectrum shape analysis.

Table 7.9: Spectrum Shape Analysis Summary

	$0.33 \cdot F_{\mathrm{U}}$ [TNU]	$0.33 \cdot F_{\mathrm{Th}}$ [TNU]	$0.33 \cdot (F_{\mathrm{U}} + F_{\mathrm{Th}})$ [TNU]
Rate Only (χ^2 method)	-	-	$21.4^{+15.0}_{-14.1}$
Shape Only	$0.0^{+15.9}_{-0.0}$	$10.1^{+8.7}_{-7.8}$	$10.1^{+14.6}_{-7.6}$
Rate+Shape	$1.4^{+17.7}_{-1.4}$	$11.9^{+8.5}_{-10.2}$	$13.4^{+13.2}_{-8.2}$
Shape Only (U/Th Fixed)	$11.8^{+17.3}_{-11.8}$	$3.2^{+4.6}_{-3.1}$	$14.9^{+21.9}_{-14.9}$
Rate+Shape (U/Th Fixed)	$13.8^{+9.9}_{-9.1}$	$3.7^{+2.6}_{-2.4}$	$17.5^{+12.5}_{-11.5}$

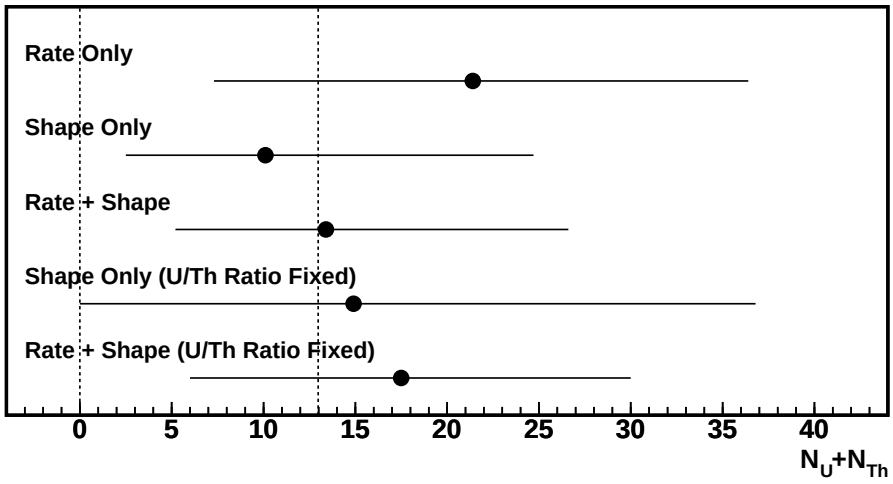

Figure 7.27: Summary of Spectrum Shape Analysis

7.10 Best-fit Spectrum and Goodness-of-fit Test

Figure 7.28 shows the energy spectra calculated with the rate+shape best-fit parameters, one for the fit with U/Th ratio floated and one for the fit with U/Th ratio fixed to 3.8 based on geochemical constraints. Observed spectrum is also shown by a histogram with 0.2 MeV bins from 0.9 MeV to 2.7 MeV.

Goodness-of-fit (GOF) is tested with binned histogram χ^2; the best-fit spectra are represented with histograms with the same bins as the observed data, and χ^2 of the best fit is calculated by:

$$\chi^2{}_{\mathrm{GOF}} = \sum_{\mathrm{bin}} \frac{(n_i - f_i)^2}{f_i} \tag{7.49}$$

where n_i is the number of observed events in the i-*th* bin, and f_i is the number of estimated events in the i-*th* bin calculated from the best-fit spectrum. The ${\chi^2}_{\rm GOF}$ values are calculated to be 7.72 for the fit with floated U/Th ratio, and 7.62 for the fit with fixed U/Th ratio.

In the rate+shape fitting with floated U/Th ratio, there are 6 parameters. However, the number of degree of freedom (ndf) is not obvious in this case because 4 of the 6 parameters are constrained by the parameter χ^2. The ndf value is less than 7, which is the number of bins minus the number of free parameters ($N_{\rm U}$ and $N_{\rm Th}$), and more than 3, which is the number of bins minus the number of all parameters. The significance of the fit, which is the probability that another imaginary KamLAND observes data that is less consistent than our real data, is calculated from the GOF χ^2 and ndf of the GOF χ^2 to be between 5.2% (ndf=3) and 35.8% (ndf=7). Similary, the probability is caclulated for the fit with fixed U/Th ratio to be between 10.7% (ndf=4) and 47.1% (ndf=8), where the ndf is increased by 1 due to the constraint of the fixed U/Th ratio. Although the ndf values are not given exactly, the significace of fit is not too large, and not too small, implying that the fitting is appropriate within the statistical errors.

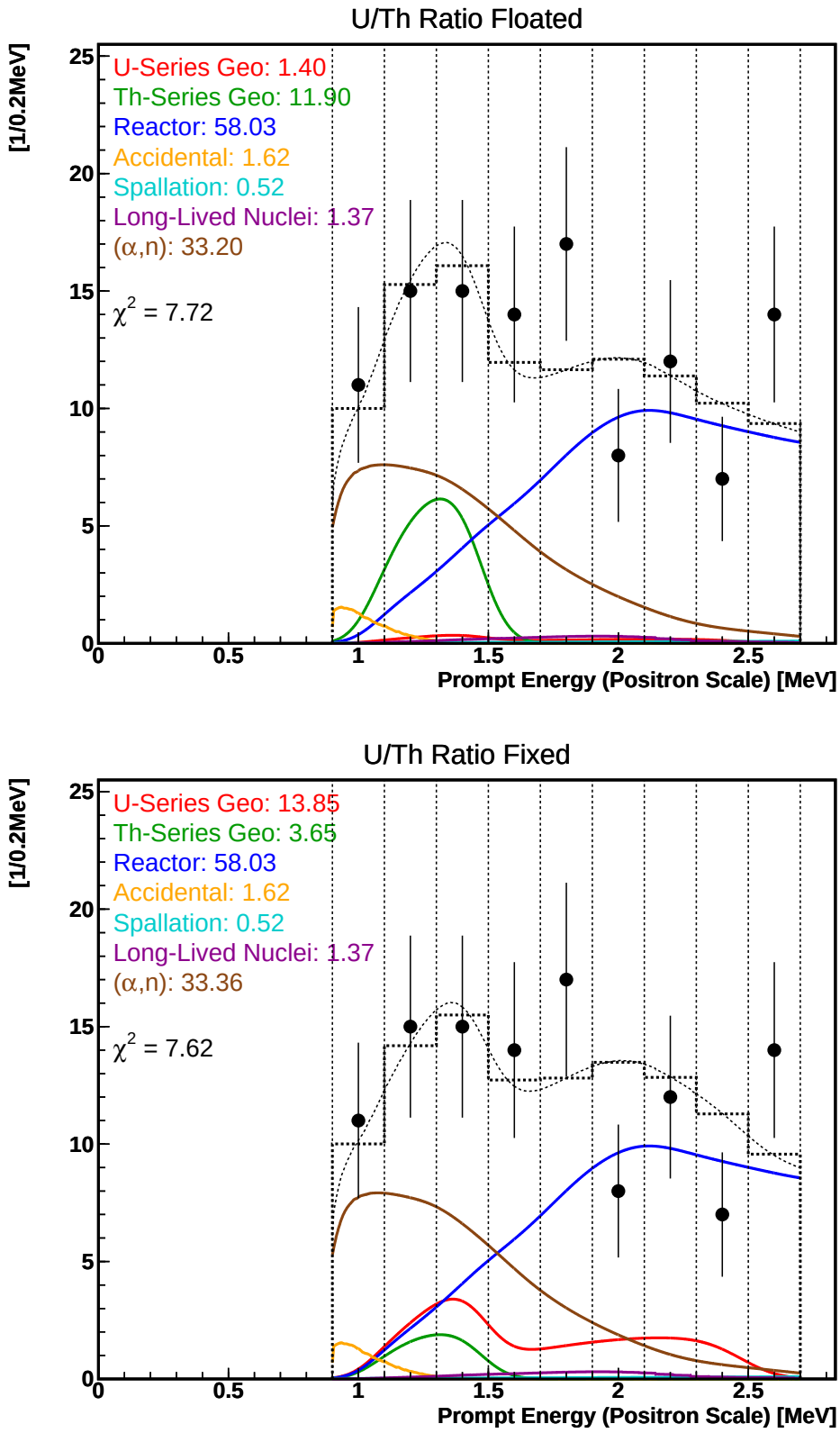

Figure 7.28: Best-Fit Spectrum. Black dot lines show the total best-fit spectrum and the colored lines show the best-fit spectrum of each signal/background source. The black circles with error bars are observed data histogrammed with 0.2 MeV width bins from 0.9 MeV to 2.7 MeV, and the black dot histogram is the best-fit spectrum with the same bin.

Chapter 8

Discussion

8.1 KamLAND Observation

As shown in Chapter 7, we observed 21.0 ± 13.1 events excess from the estimated backgrounds in the geo-neutrino energy region. The excess is significant at 93.5% confidence level. All backgrounds are carefully discussed in Chapter 6. KamLAND data above the geo-neutrino energy window was also analyzed independently for neutrino oscillation study [2], and the background estimation was found to be consistent as well in that energy region.

If the excess is attributed to geo-neutrinos, the geo-neutrino flux is estimated to be $64.8^{+44.6}_{-40.7}$ TNU. The upper limit of geo-neutrino flux is set from the observation to be 176.6 TNU at 99% Confidence Level. The spectrum shape is consistent with the theoretical geo-neutrino spectrum, and the shape-only analysis gives consistent flux estimation, $30.6^{+44.2}_{-23.0}$ TNU. By combining the counting rate analysis and the spectrum shape analysis, the geo-neutrino flux is estimated to be $40.6^{+40.0}_{-24.8}$ TNU.

KamLAND observation is rather less sensitive to the ratio of the U-series and Th-series geo-neutrinos, compared to sensitivity to the absolute geo-neutrino flux. Geochemistry, on the other hand, predicts the U/Th ratio quite reliably compared to absolute amount estimation. If the KamLAND observation is constrained by the geochemical argument, the total geo-neutrino flux is estimated to be $45.2^{+66.4}_{-45.2}$ TNU (shape only) or $53.0^{+37.9}_{-34.8}$ TNU (rate+shape).

Based on the reference Earth model presented in Chapter 2, 38.6 TNU of geo-neutrino flux is predicted at KamLAND, with $\sim$20% of geological/geochemical uncertainties. Our observation is consistent with the prediction; in the rate+shape analysis, $\Delta\chi^2$ of the predicted flux is 0.0014 (0.04σ away), and in the rate+shape analysis with geochemical constraints, $\Delta\chi^2$ is 0.14 (0.4σ away). Relatively large errors in the obvervation may account for the good agreement.

Figure 8.1 is the geo-neutrino flux response chart with the KamLAND observation. Again our observation agrees well with the model constructed on the BSE model. Our 99% C.L. upper limit of the geo-neutrino flux constrains the total U+Th amount looser than the limit set by the fully radiogenic model of 44TW surface heat flow (the model is outside of the 1-σ region though).

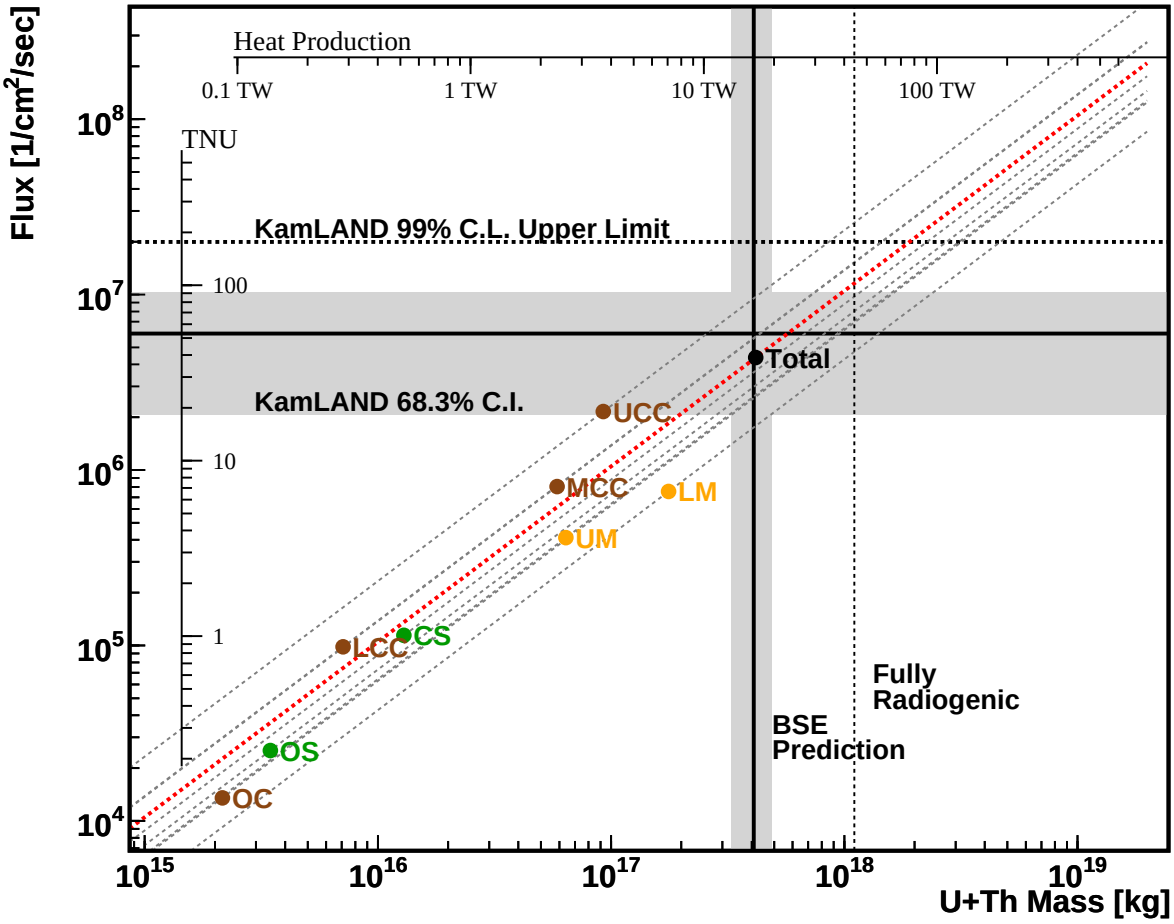

Figure 8.1: KamLAND Geo-Neutrino Observation

8.2 Future Prospects

8.2.1 Tomorrow KamLAND Plans

The KamLAND collaboration is now working on upgrading the detector toward ^{7}Be solar neutrino detection. The main feature of the upgrade is further purification of the Liquid Scintillator. Several techniques, such as distillation, adsorption, and water extraction, are now being studied. The goal of the purification is set to be $1/10^{6}$ reduction of ^{210}Pb, and present studies with small scale apparatus have achieved $1/10^{4}$ reduction. Under such ultra-low radioactivity environment, radioactive backgrounds such as the (α,n) reactions are sufficiently suppressed to an ignorable level.

Figure 8.2 shows the expected spectrum after the purification. The same livetime, fiducial volume and selection efficiencies as those of this analysis are used to calculate the spectrum. As clearly seen, the reactor neutrinos are essentially the only backgrounds.

By simply referring the numbers estimated in this analysis, the number of observed

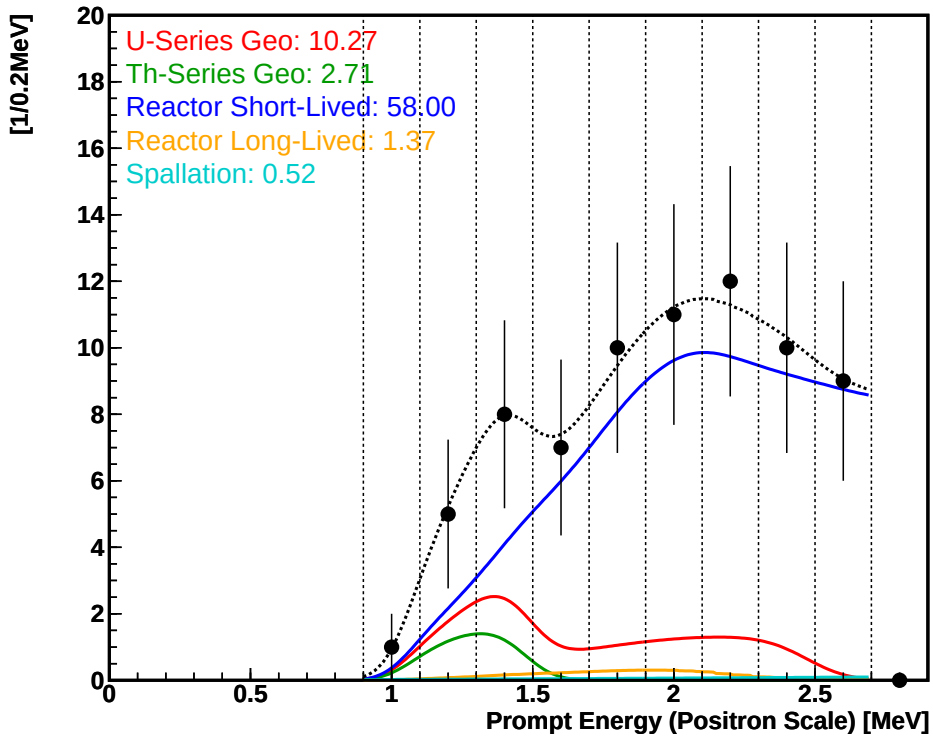

Figure 8.2: Expected Spectrum after Purification

events after the purification is expected to be 81.3 ± 7.91, with expected background estimation 59.89 ± 5.30. The geo-neutrino flux will be then estimated to be $64.9^{+33.6}_{-31.6}$ TNU, where the error is reduced by 23% from this analysis. The significace of the positive number of geo-neutrino detection will be 98.6%.

Figure 8.3 shows the expected result of spectrum shape analysis. Contours are tighter than this analysis, reflecting the reduction of backgrounds. However, separation of the U-series geo-neutrinos and the Th-series geo-neutrinos are still poor. This can be understood by looking at the expected spectrum shown in Figure 8.2; the spectra of these two are quite similar below 1.6 MeV, and differences appear above 1.6 MeV, where the spectrum is overwhelmed by the huge reactor neutrino backgrounds. Incorporating time variation data of reactor neutrino flux into the likelihood definition might improve the situation.

8.2.2 Next Geo-Neutrino Detectors

There are several neutrino experiments that have feasibility to observe geo-neutrinos in the near future. The Borexino experiment, which uses 300 ton liquid scintillator to detect neutrinos, is expected to start operation within few years. The detector is located at the Gran Sasso National Laboratory in Italy. The primary goal of the Borexino experiment is to detect the ^{7}Be solar neutrinos, however, it is also sensitive to geo-neutrinos. The location is apart from nuclear power reactors, resulting in better signal-to-noise ratio ($\sim$1).

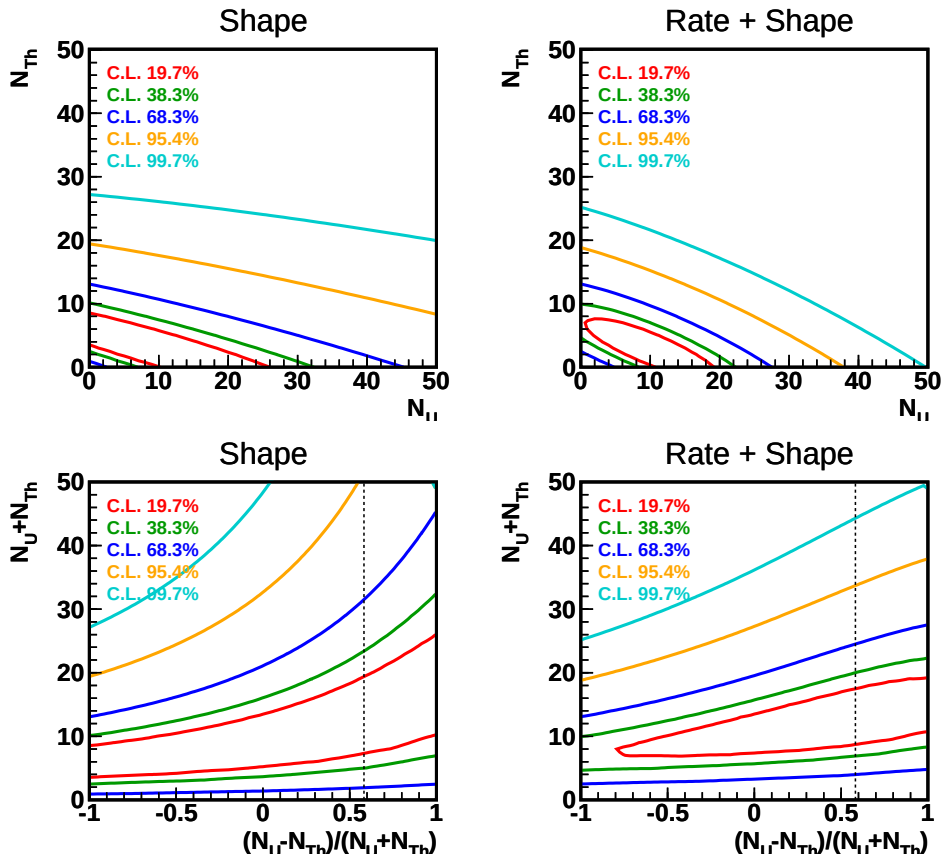

Figure 8.3: KamLAND Geo-Neutrino Observation Future Prospects

The SNO experiment, which is now in operation of solar neutrino observation with heavy water target, is studying an option of replacing the target with liquid scintillator. The SNO detector is located in a famous nickel mine at Sudbury in Canada.

Figure 8.4 and Figure 8.5 show neutrino flux response charts for observation at Gran Sasso and Sudbury, calculated with the model presented in Chapter 2. The figures also show the relative contribution of the crust and mantle by a map of MC generated geo-neutrino production points.

Since both of Gran Sasso and Sudbury are located in mid of continents, contribution of the continental crust to the total geo-neutrino flux is large, about 75% to 80%. An interesting characteristics of geo-neutrino observation in such continental regions is the fact that geo-neutrinos are sensitive to area-weighted bulk composition. Geochemical studies based on rock sampling tend to suffer from small scale variations, such as rock-by-rock heterogeneity or vertical biases; representativeness of the samples is frequently a matter of controversy. Geo-neutrinos, on the other hand, averages the area at about 100 km scale, which means that microscopic heterogeneity and/or small scale geological effects are all averaged out.

Observation at Sudbury is sensitive to the bulk composition of the Archean/Proterozoic continent, which is a key knowledge to understand the history of crustal formation. Ob-

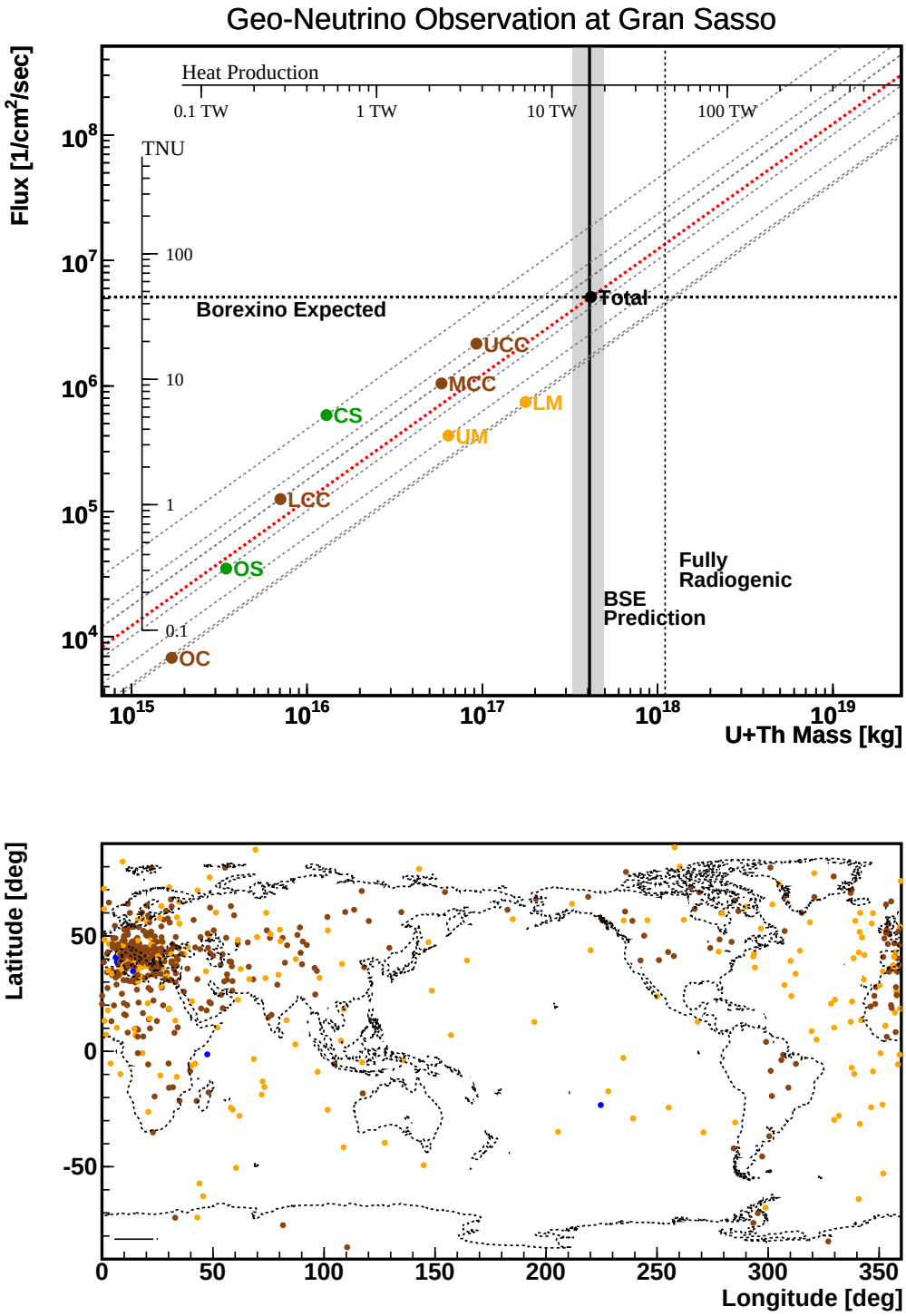

Figure 8.4: Geo-Neutrino Observation at Gran Sasso

servation at Gran Sasso is sensitive to the regional average composition of the Alpine Orogenic zone. At KamLAND, we are essentially looking at the bulk composition of the Japan Island Arcs, where new continental crust is being formed.

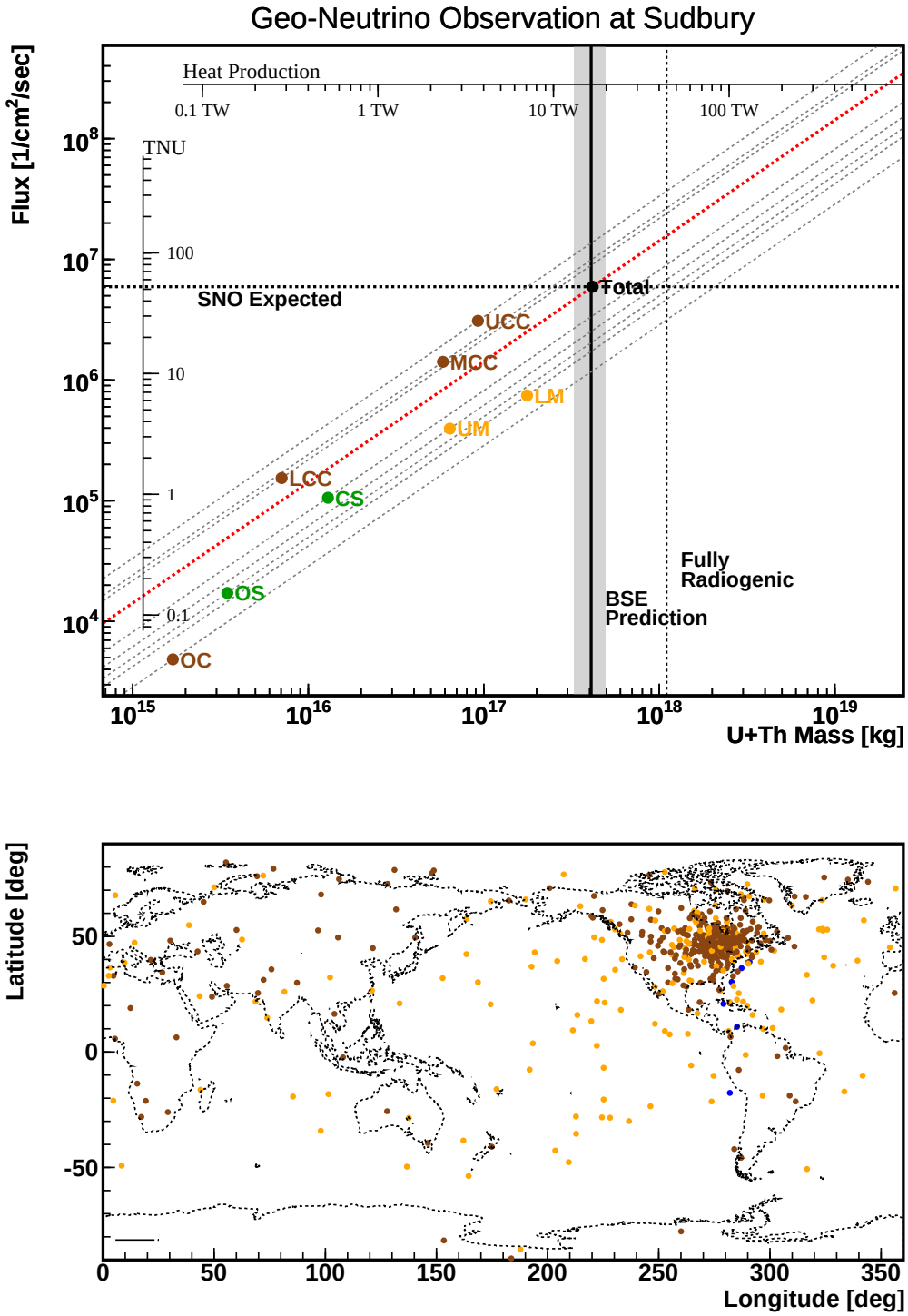

Figure 8.5: Geo-Neutrino Observation at Sudbury

8.2.3 Future Geo-Neutrino Detectors

From the geophysical/geochemical point of view, one of the most interesting place for geo-neutrino observation is Hawaii. Since Hawaii is isolated islands in the vast Pacific Ocean, contribution of the continental crust is tiny, therefore the neutrino flux is sensitive to the other part, such as the mantle.

Figure 8.6 is the geo-neutrino flux chart for observation at Hawaii. The lower mantle makes the largest contribution, 46.8%. The flux from the bulk mantle totals 73.0% of the total geo-neutrino flux. Owning to the large contribution from the mantle, the difference in flux between the homogeneous mantle model and the heterogeneous mantle model becomes ∼10%. From this point of view, one may say that Hawaii is an ideal place to study the mantle strucure with geo-neutrinos.

Local geology of the Hawaii Islands is rather simple. The islands essentially consist of only Oceanic Island Basalt (OIB), which originates relatively deep part of the Earth. The oceanic crust is formed at mid ocean ridges, by partial melting of surface-mantle-origin rocks. Although OIB tends to contain more LIL elements than Mid-Ocean-Ridge Basalt (MORB), the difference is fairly small compared to the difference from the continental crust. Moreover, the small Uranium/Thorium concentration in OIB further reduces the uncertainties caused by the local geologies since contribution of OIB to the total flux is tiny.

Similar to Hawaii, geo-neutrino observation at Tahiti is sensitive to the chemical composition of the lower mantle. However, since the Tahiti islands are located above the South Pacific Super Plume (see Figure A.5 in Appendix A), it is particularly sensitive to the chemical composition of the Mantle Super Plume. In connection to the seismological analysis, geo-neutrino observation at Tahiti in comparison with that at Hawaii is of great interest, because it hints us the global structure of material circulation.

Another interesting place for geo-neutrino observation is islands on mid ocean ridges, where new oceanic crust is being formed. Knowing the chemical composition of the mantle beneath mid-ocean ridges, which is the source of the new crust, help understanding the crustal formation processes. Since formation of the oceanic crust extracts incompatible elements from the mantle, comparison of chemical compositions between the mantle beneath mid-ocean ridges and the mantle beneath normal oceanic crust gives a clue to understand the long term mantle evolution process and the mantle circulation process.

Figure 8.7 shows a map of oceanic crustal age, provided by R.D.Müller *et al.* [32]. Mid-ocean ridges surrounded by young oceanic crust are clearly seen. There are several islands on active mid-ocean ridges, such as the Easter Islands in South Pacific Ocean, Azores Islands in North Atlantic Ocean, and Kerguelen Islands in the South Indian Ocean. Measuring geo-neutrino flux on several points might be of interest, because comparison of the mantle composition beneath different ages and different activities of mid-ocean ridges enables us to extract knowledge in chemical evolution of the mantle, crust, and the entire Earth.

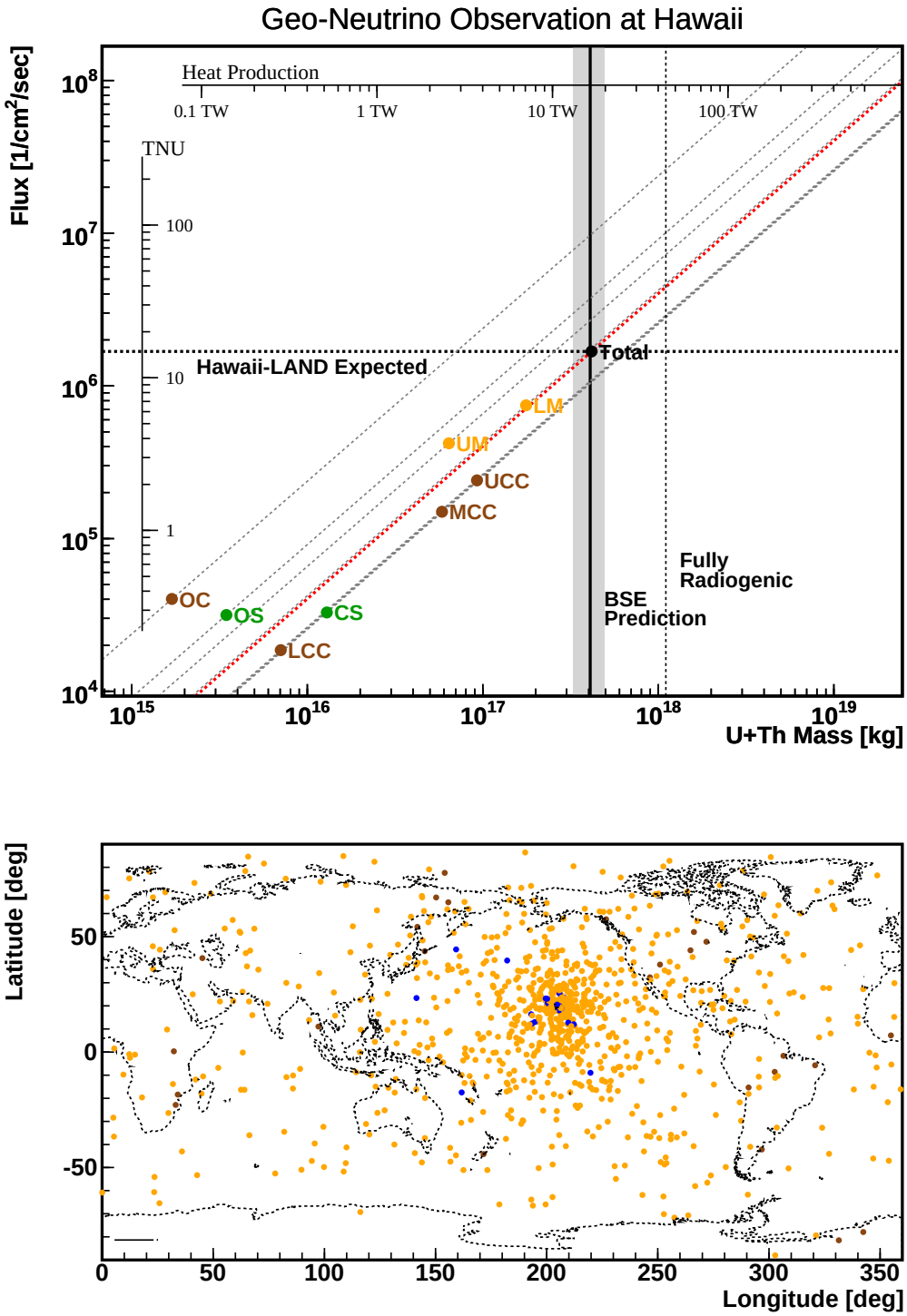

Figure 8.6: Geo-Neutrino Observation at Hawaii

Portable Geo-Neutrino Detector

As demonstrated above, measuring geo-neutrino flux at several points on the Earth provides us vast knowledge in various aspects of geophysics and geochemistry. Locating the

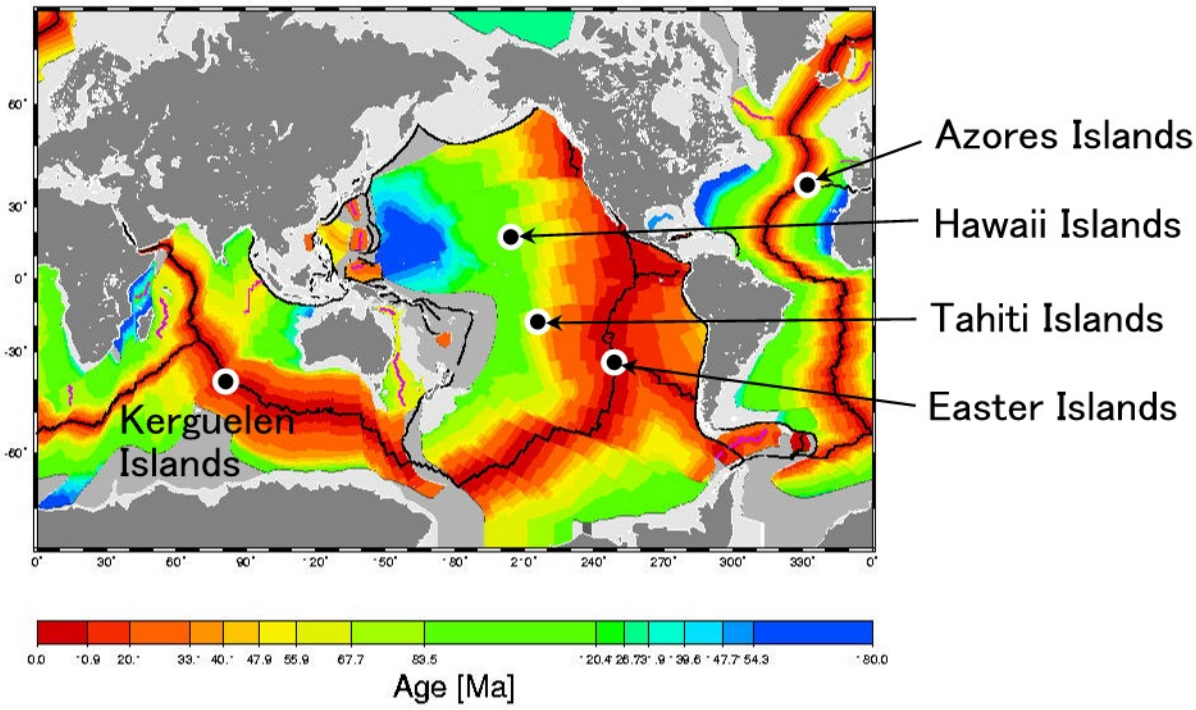

Figure 8.7: Crustal Age Map

detector on arbitrary place results in not only enabling us to pinpoint the geophysical processes of interest, but also reduction of geological uncertainties, because comparison of flux at several points cancels common geological effects. This fact naturally leads us into dreaming a portable geo-neutrino detector.

Few year measurement with a sub-KamLAND class detector under deep sea water will produce fruitful observation. If the detector is located at around 4000 m depth in water, the cosmic muon rate is suppressed to about 1/10 of the rate at KamLAND, which is low enough not to be a major background source. We can use ultra-purified liquid scintillator developed for the next phase of KamLAND, which does not contain sizable amount of ^{210}Pb. Most of places on the Earth are apart from nuclear power reactors. Under such environment, geo-neutrinos are the only source of the delayed coincidence events.

Use of other nuclei for the geo-neutrino target might be an option. ^{3}He, for example, has as low energy threshold as 1.041 MeV, and its reaction rate is nearly 500 times as high as that of ^{1}H target [7] (the rate depends on geo-neutrino spectra). It means that the detector is sensitive to the ^{40}K geo-neutrinos, and $\sim$0.4 ton of ^{3}He target observes approximately the same number of geo-neutrinos as the current KamLAND does. The reaction is $^{3}\mathrm{He}+\bar{\nu}_e \rightarrow {}^{3}\mathrm{H}+e^{+}$, thus the delayed coincidence technique cannot be employed in this case. However, it still remains the feature of realtime event-by-event detection with sensitivity to the incident neutrino energy. Future realization of D-D fusion reactors may provide sufficient amount of ^{3}He, or realization of D-^{3}He fusion reactors may establish transportation of lunar ^{3}He to the Earth.

Chapter 9

Conclusion

Neutrinos from radioactive isotopes in the Earth, geo-neutrinos, provide an unique method to explore the Earth. Observation of geo-neutrinos reveals the chemical constitution of the deep portion of the Earth, and of particular interest, it brings direct information in the Earth energy generation mechanism, which also connects to understanding of the planetary formation and evolution. Even at an early stage of geo-neutrino observation with rather small statistics, it provides a test to an essential geochemical paradigm, the Bulk Silicate Earth (BSE) model. With large statistics of global multiple detectors, observation of geo-neutrinos are expected to bring knowledge in the lower mantle composition, upper mantle heterogeneity, and regional bulk crustal composition.

The KamLAND detector, which consists of $\sim$1000 tons of ultra-pure Liquid Scintillator surrounded by 1879 photomultiplier tubes, is the first detector that equips enough number of target nuclei to make a meaningful observation of geo-neutrinos. 513.92 days exposure of the detector observed 21.4$\pm$13.5 geo-neutrino candidate events, which correspond to $64.8^{+44.6}_{-40.7}$ TNU of geo-neutrino flux. The observation is positive at 93.5% significance. Both of the event rate analysis and the spectrum shape analysis, with and without geochemical constraints, resulted in consistent estimations.

Due to large backgrounds from surrounding nuclear power reactors and radioactivity of the liquid scintillator, the error of geo-neutrino flux estimation is not sufficiently suppressed as yet, compared to uncertainties of geophysical/geochemical prediction. The observation shows slight tendency of disfavoring the model of 44TW fully-radiogenic case, which is an upper limit set by the surface heat flow measurement, however, the 99% CL upper limit set by this geo-neutrino observation is much looser than this geophysical limit. The estimated flux agrees with the geochemical expectation based on the BSE model, and the best-estimated flux is fairly close to the best-predicted flux (less than 0.4σ away).

Further accumulation of statistics and planed reduction of the radioactive backgrounds at KamLAND will soon enable us to discuss geophysical topics based on the observation. In this study, we observed a clear tendency of positive geo-neutrino signals, and we also have demonstrated that geo-neutrinos are now a new practical probe to explore the Earth. Subsequent observations and further development in relevant topics will establish a new field, neutrino geophysics.

Appendix A

Earth Structural Data Set

Figure A.1: Crustal Thickness Map (CRUST 2.0)

This figure illustrates the crustal thickness data provided by C.Bassin *et al.* (2000) [16], which is also known as the CRUST 2.0 data set. The data set consists of thickness, density, Vp and Vs data of the ice, water, soft sediment, hard sediment, upper crust, middle crust, and lower crust layers, at $2^\circ \times 2^\circ$ resolution. In this analysis, only crustal thickness data is used, and the sedimentary thickness data is taken from G.Laske *et al.* (1997) [17], which is shown below.

Figure A.2 Crustal Thickness Map (CRUST 2.0), Japan Area

This figure shows the same data as Figure A.1, with focus on the Japan Island area. At the $2^\circ \times 2^\circ$ resolution, the Japan Island consists of only few points, therefore the resolution might not be good enough for precise flux estimation.

Figure A.3: Sedimentary Thickness Map

This figure illustrates the sedimentary thickness data provided by G.Laske *et al.* (1997) [17]. This data set is related to the CRUST 2.0 compilation activity, but it gives the sedimentary thickness at $1^\circ \times 1^\circ$ resolution. It is remarkable that sediment is much thicker around continents, such as the Sea of Japan and the East China Sea, than vast ocean such as the Pacific Ocean.

Figure A.4: Crustal Thickness Map beneath Japan

This figure shows the crustal thickness data beneath Japan provided by D.Zhao *et al.* (1992) [18]. The map is constructed with natural earthquake data, and the resolution is much better than that of CRUST 2.0 dataset.

Figure A.5: Seismic Speed Anomaly in Mantle

This figure illustrates the data of seismic wave speed anomaly in the mantle, provided by C.Mégnin *et al.* (2000) [19]. The color indicates the difference of seismic wave speed from the PREM model [15], the red part is slower and the blue part is faster. The scale is the same as shown in Figure 2.6 in Chapter 2. Two hot plumes beneath South Pacific Ocean and Africa, and one cold plume beneath Asia are clearly seen.

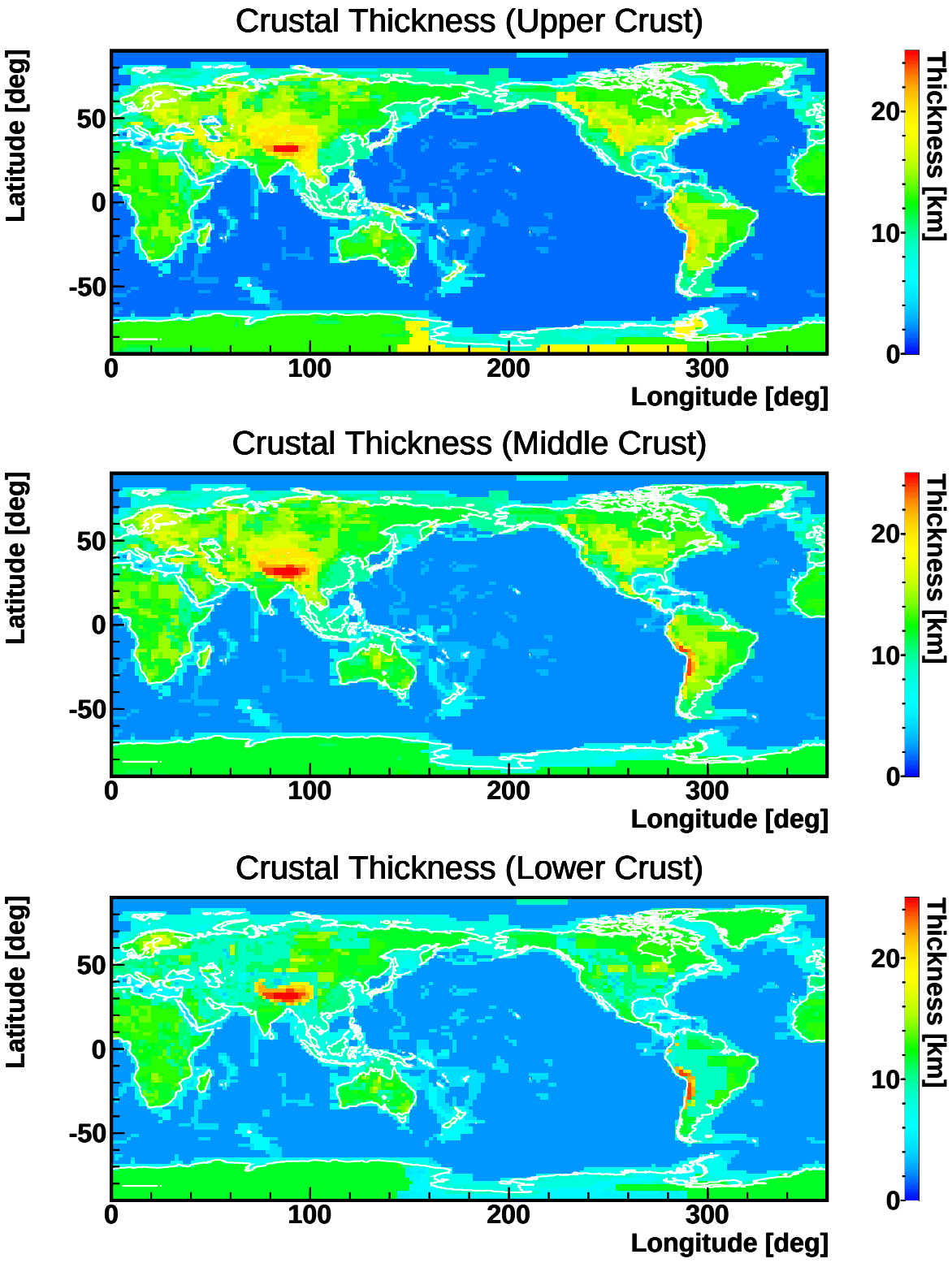

Figure A.1: Crustal Thickness Map given by C.Bassin *et al.* (CRUST 2.0)

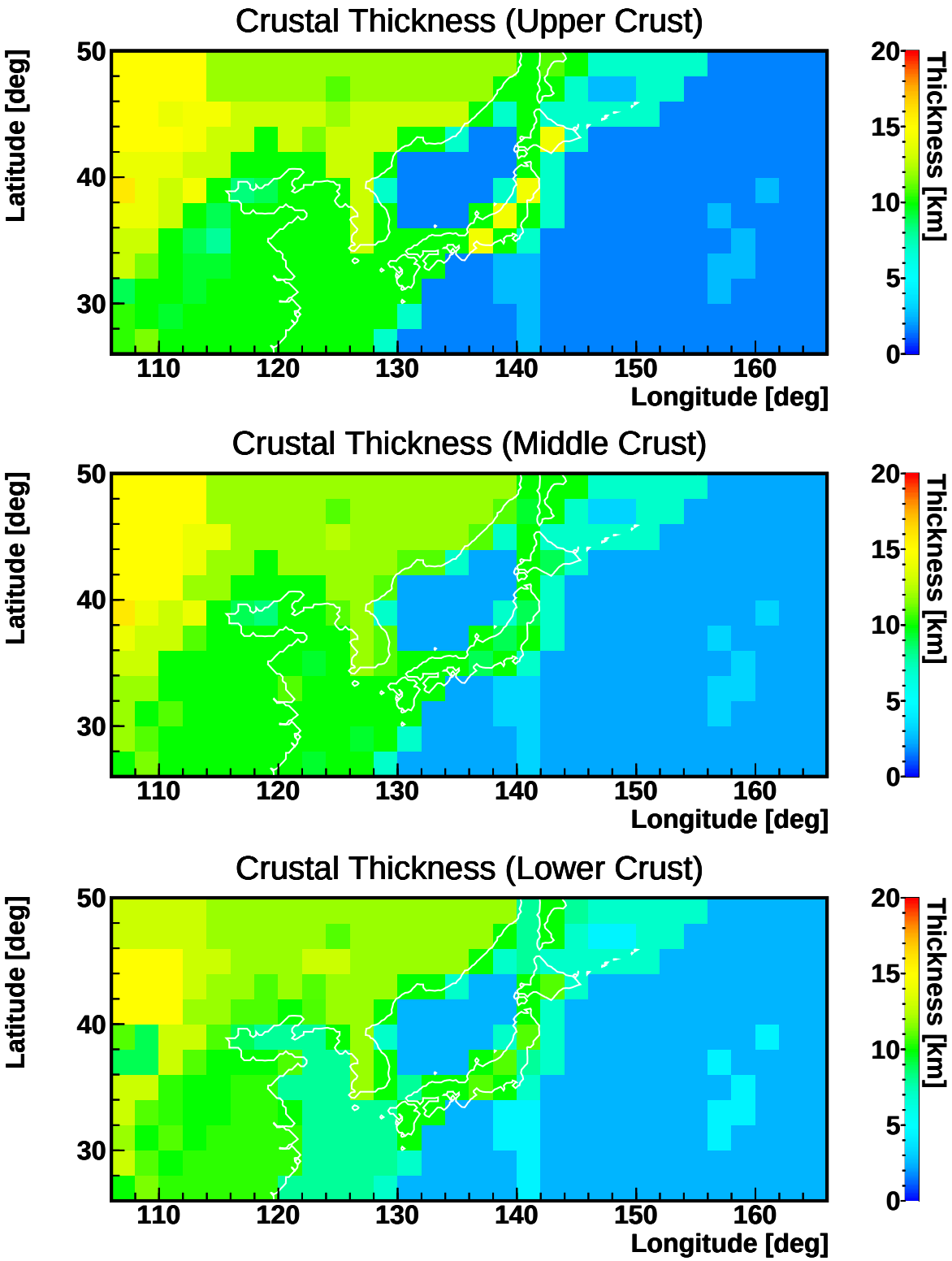

Figure A.2: Crustal Thickness Map given by C.Bassin *et al.* (CRUST 2.0)

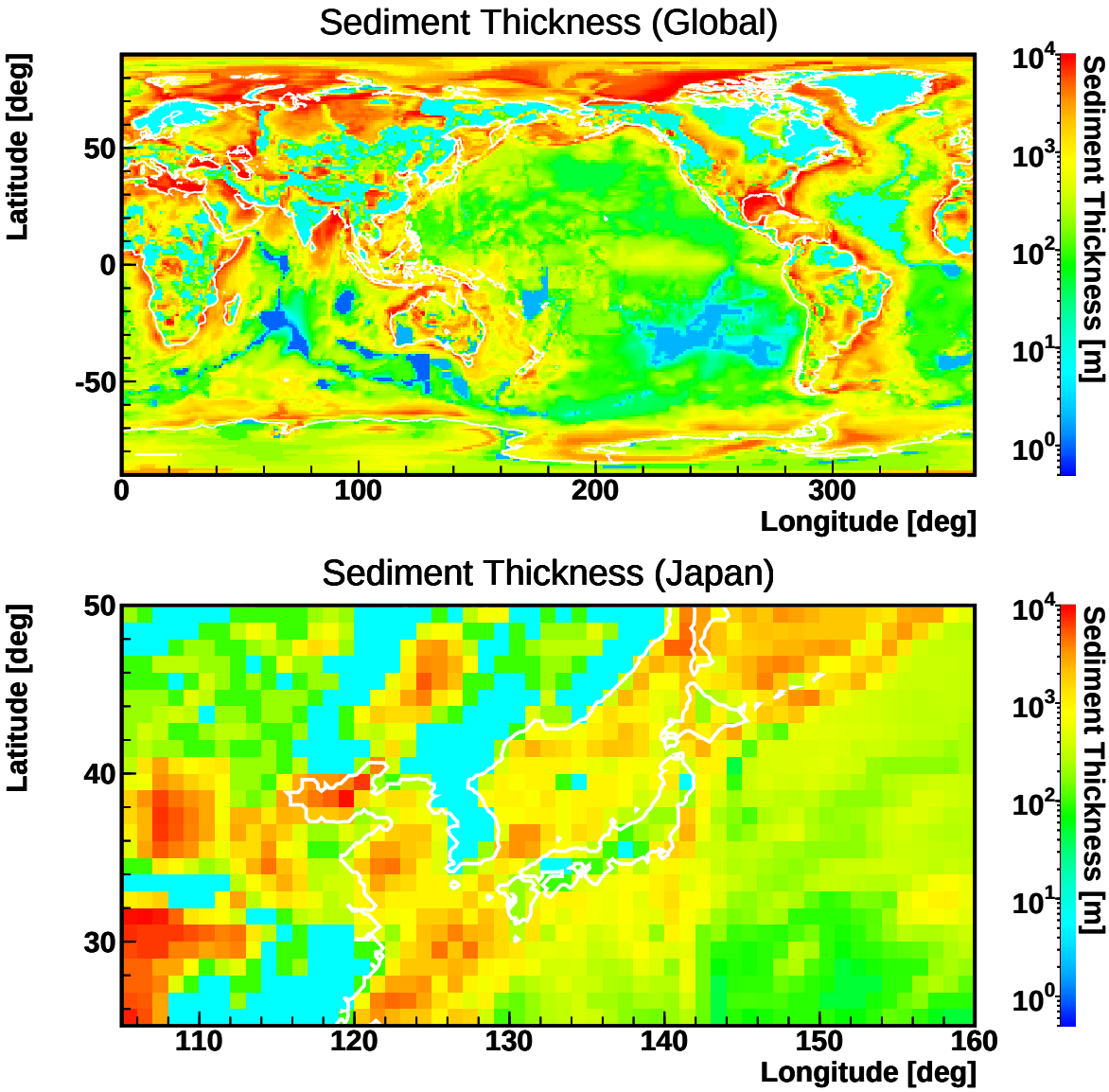

Figure A.3: Sedimentary Thickness Map given by G.Laske *et al.*

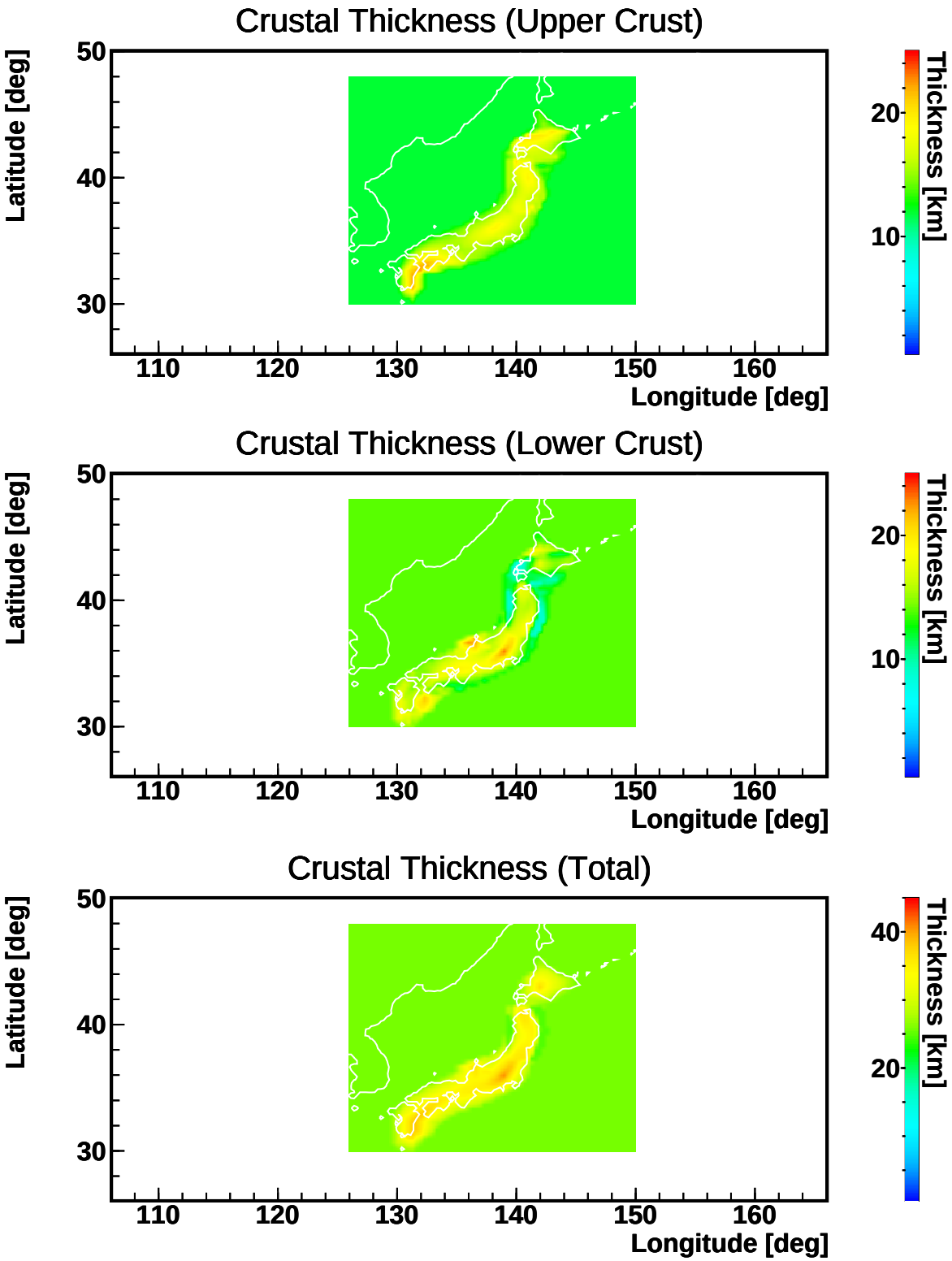

Figure A.4: Crustal Thickness Map beneath Japan given by D.Zhao *et al.*

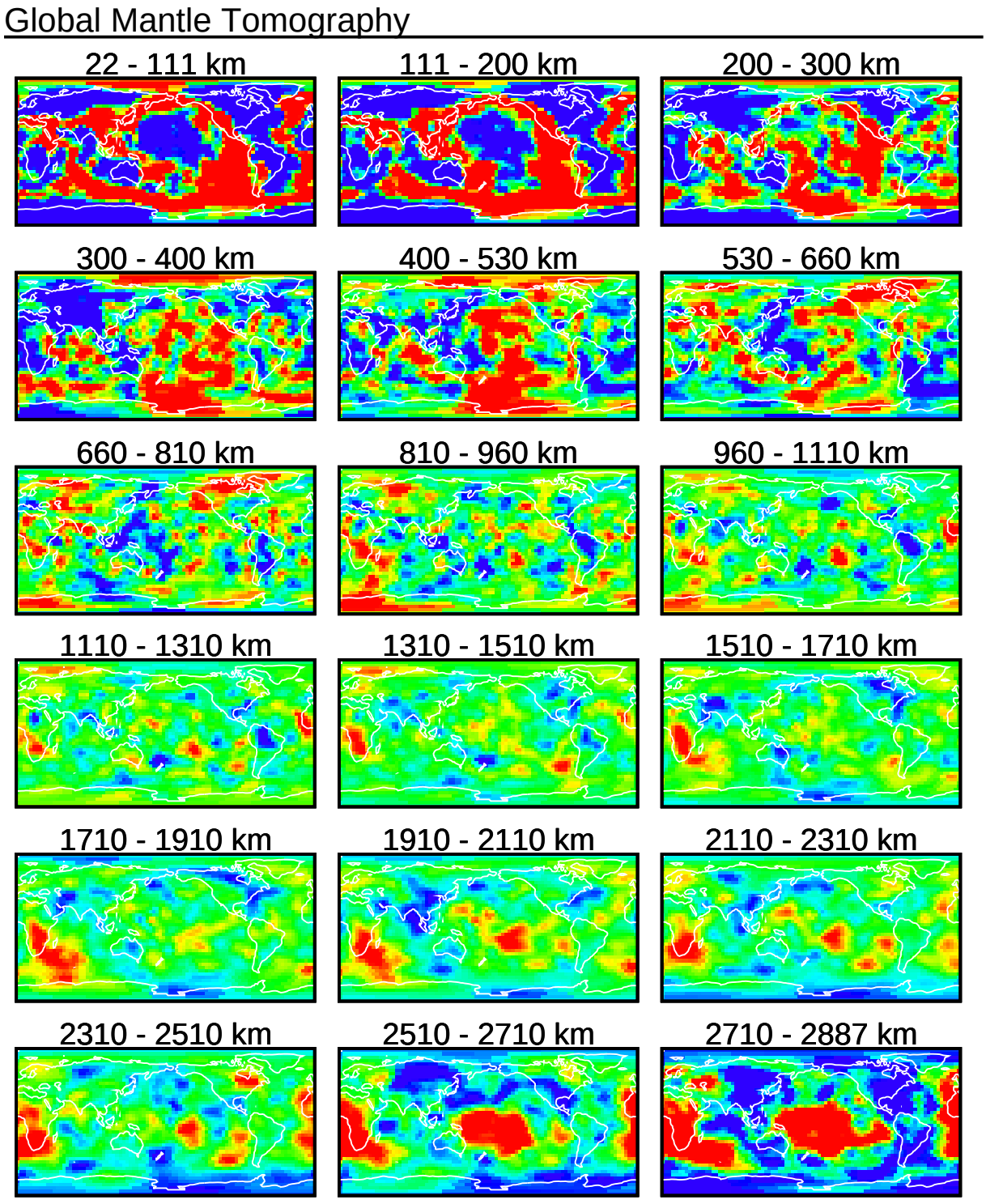

Figure A.5: Seismic Wave Speed Anomaly in Mantle

Appendix B

Japan Local Geology Data Set

Figure B.1: GSJ Japan Geological Map

This figure illustrates the geological map published from Geological Survey of Japan [33]. The original map is associated with 165 geological groups, classified by rock formation age and rock types (sedimentary, volcanic, plutonic, etc). In this figure, the geological groups are simplified into 5 rock types to display. The 5 rock types (Sedimentary, Accretionary, Volcanic, Plutonic, and Metamorphic) are indicated with colors shown in the figure.

Figure B.2: GSJ Japan Geological Map (Hida/Kamioka Area)

This figure shows the same data as shown Figure B.1 with focusing on the Kamioka area. Meanings of the colors are same as those in Figure B.1. The metamorphic rocks surrounding the KamLAND site are known as Hida Metamorphic Rocks, which are one of the oldest rock group in Japan. The composition of the Hida Metamorphic rocks has similarity to that of rocks found in North-East China (Sino-Korean block) [36], and the rocks seem to have experienced metamorphism several times. The sedimentary rocks covering the Hida Metamorphic Rocks are the Tetori Group, formed during the Cretaceous era, the time when the Hida area was under water. The plutonic rocks surrounding the Hida Metamorphic Rocks and the Tetori Group are mainly Funatsu Granite, which are intrusive rocks being in active during the Jurassic era. Funatsu Granite is the only granite formed during the Jurassic era in Japan. The accretionary rocks seen around the Hida area is a part of the Mino belt.

Figure B.3: Japan Geochemical Data, Uranium (Togashi *et al.* (2000))

This figure visualizes the Uranium concentration data of Japanese rock samples given by Togashi *et al.* (2000) [34]. The colors correspond to the geological groups shown in Figure B.1. It can be seen that variation of Uranium concentration among sedimentary rocks is rather small, implying that they are well homogenized during the processes of erosion, transportation and sedimentation. In contrast, igneous rocks show more variety in Uranium concentration.

Figure B.4: Japan Geochemical Data, Thorium (Togashi *et al.* (2000))

This figure visualizes the Thorium concentration data of Japanese rock samples

given by Togashi *et al.* (2000) [34], in the same way as Figure B.3. Similarly to the Uranium concentration, sedimentary rocks show well homogenized composition while igneous rocks have more variety. Over the all rock types, the concentration of Thorium shows similar tendency as that of Uranium concentration, resulting in a stable Uranium/Thorium ratio in most of rock types.

Figure B.5: GSJ Japan Geochemical Map, Uranium

This figure shows the Uranium concentration distribution provided by a Geochemical Map which was recently published from GSJ [35]. The geochemical map essentially shows chemical composition of very surface, where processes of erosion and sedimentation play an important role. At this point, the geochemical map is different from the elemental distribution map based on a geological map which emphasizes basement composition. However, both of the maps should show the same tendency of elemental distribution in a certain scale (the scale of elemental mobility), thus the geochemical map is useful for seeing consistency of distribution maps.

Figure B.6: GSJ Japan Geochemical Map, Thorium

This figure shows the Thorium concentration distribution provided by the Geochemical Map published from GSJ [35], in the same way as Figure B.5. It is particularly of interest to see whether the Thorium distribution has the same structure as that of Uranium distribution. The similarity in the distribution implies that the Uranium/Thorium ratio is well preserved even after the processes of erosion, transportation and sedimentation.

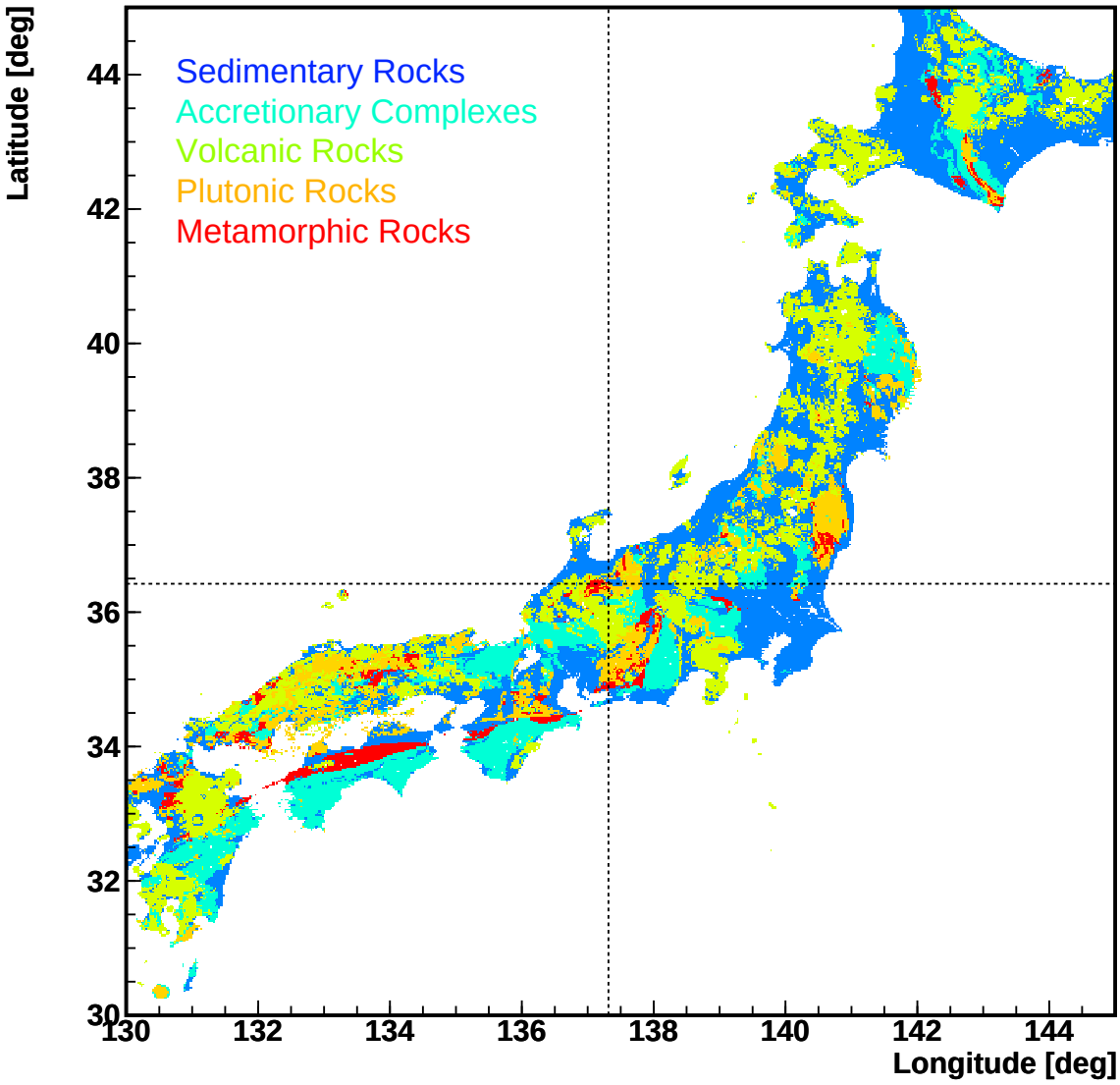

Figure B.1: GSJ Japan Geological Map

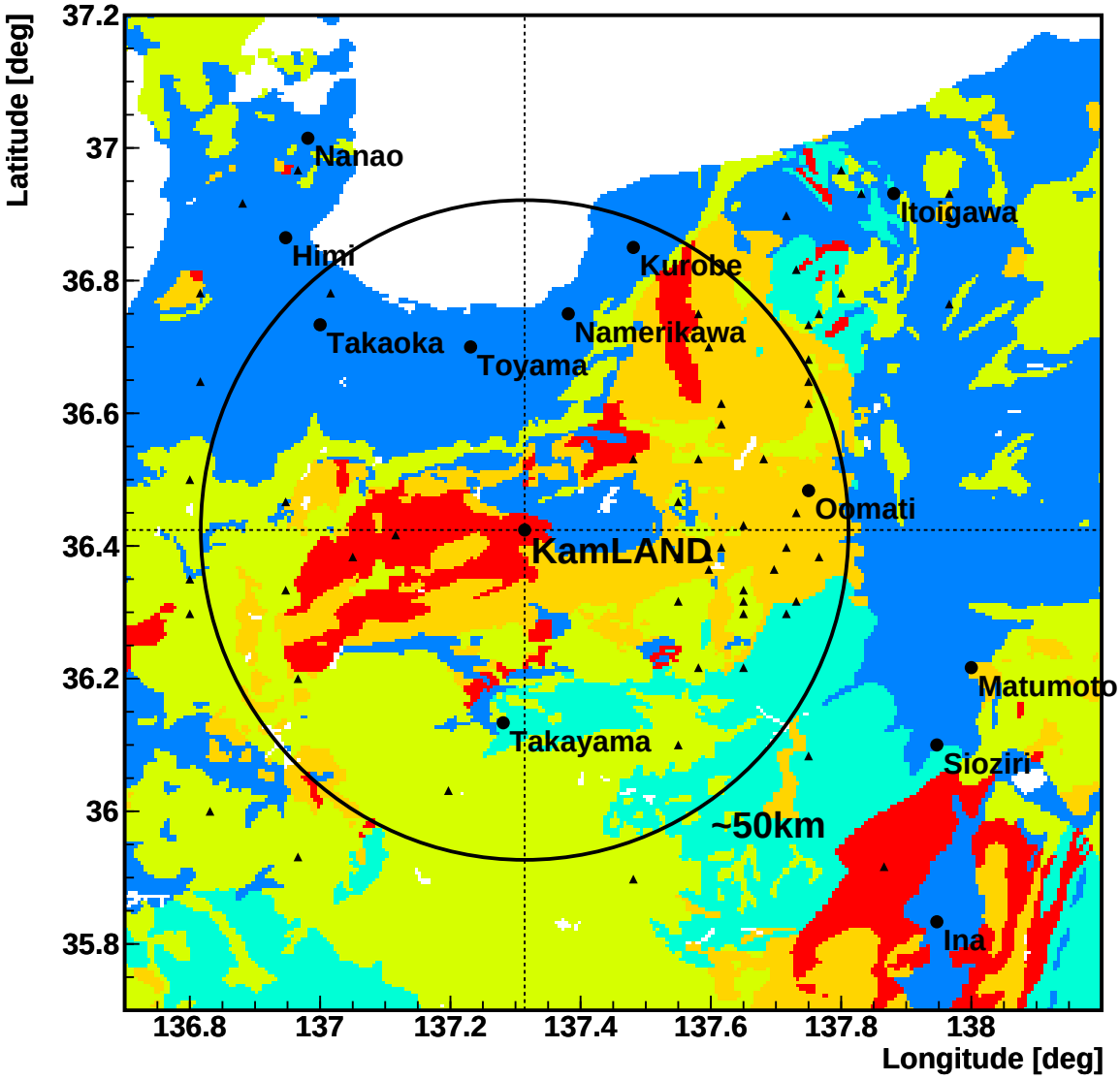

Figure B.2: GSJ Japan Geological Map (Kamioka Area)

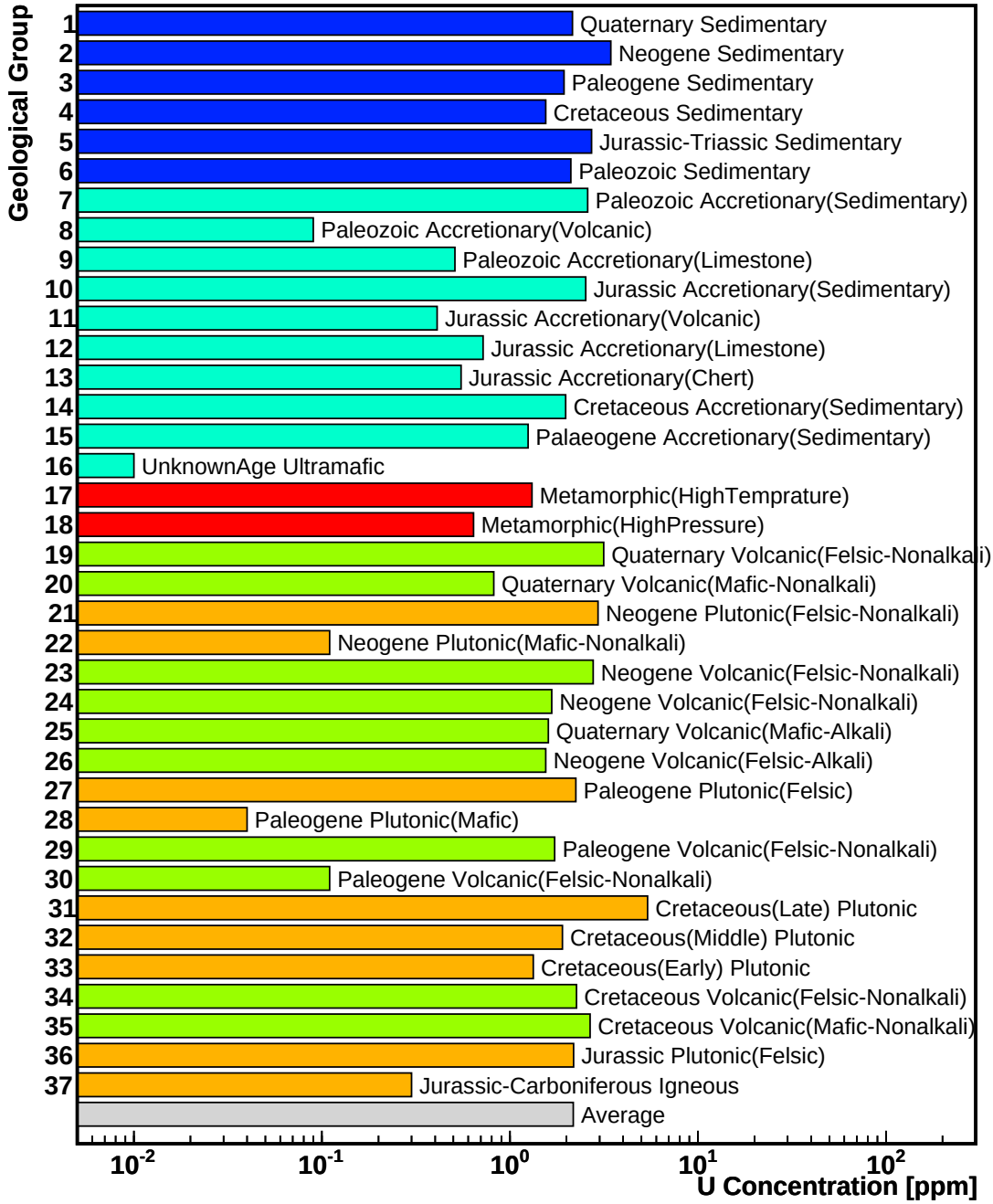

Figure B.3: Japan Geochemical Data, Uranium (Togashi *et al.* (2000))

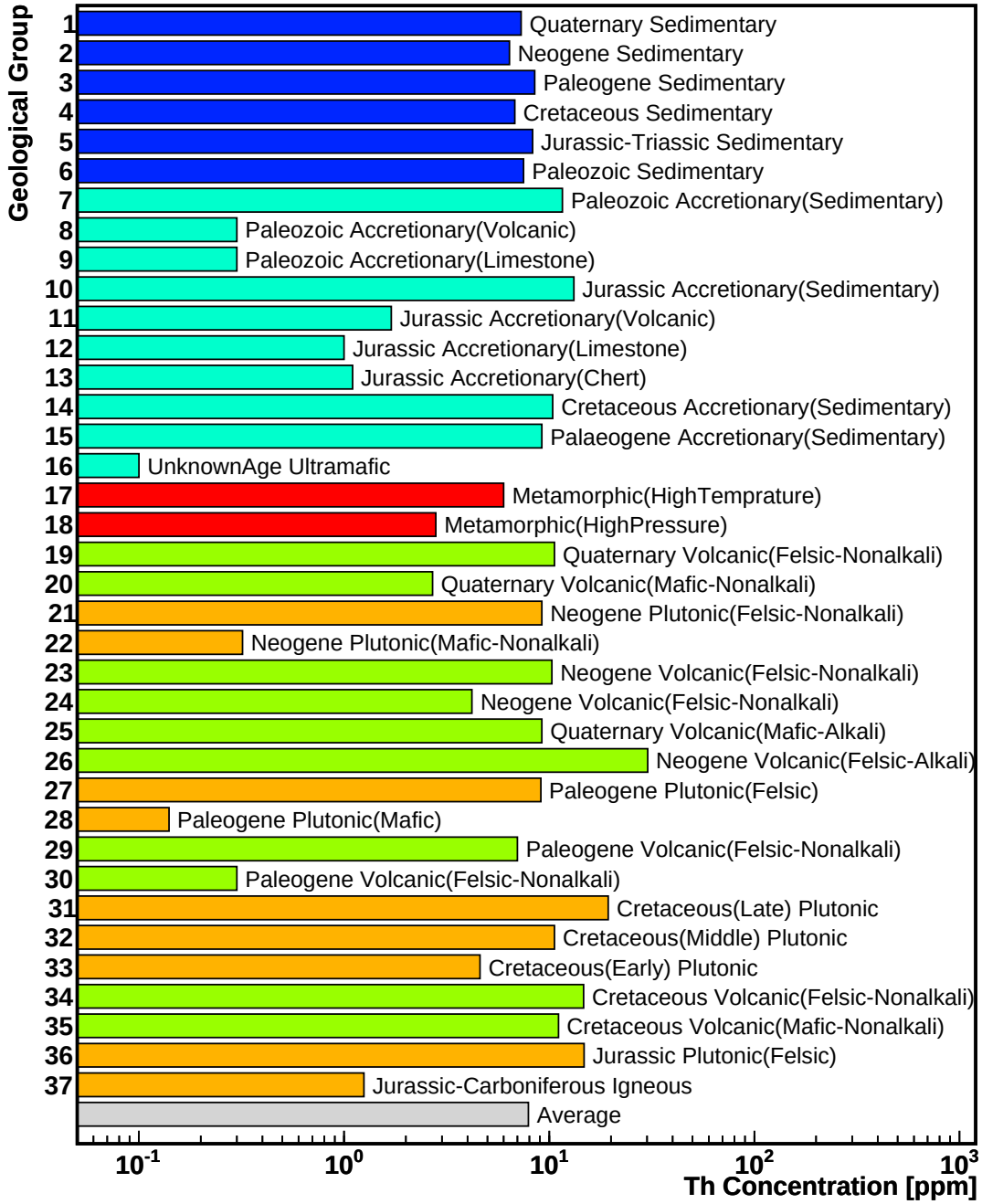

Figure B.4: Japan Geochemical Data, Thorium (Togashi *et al.* (2000))

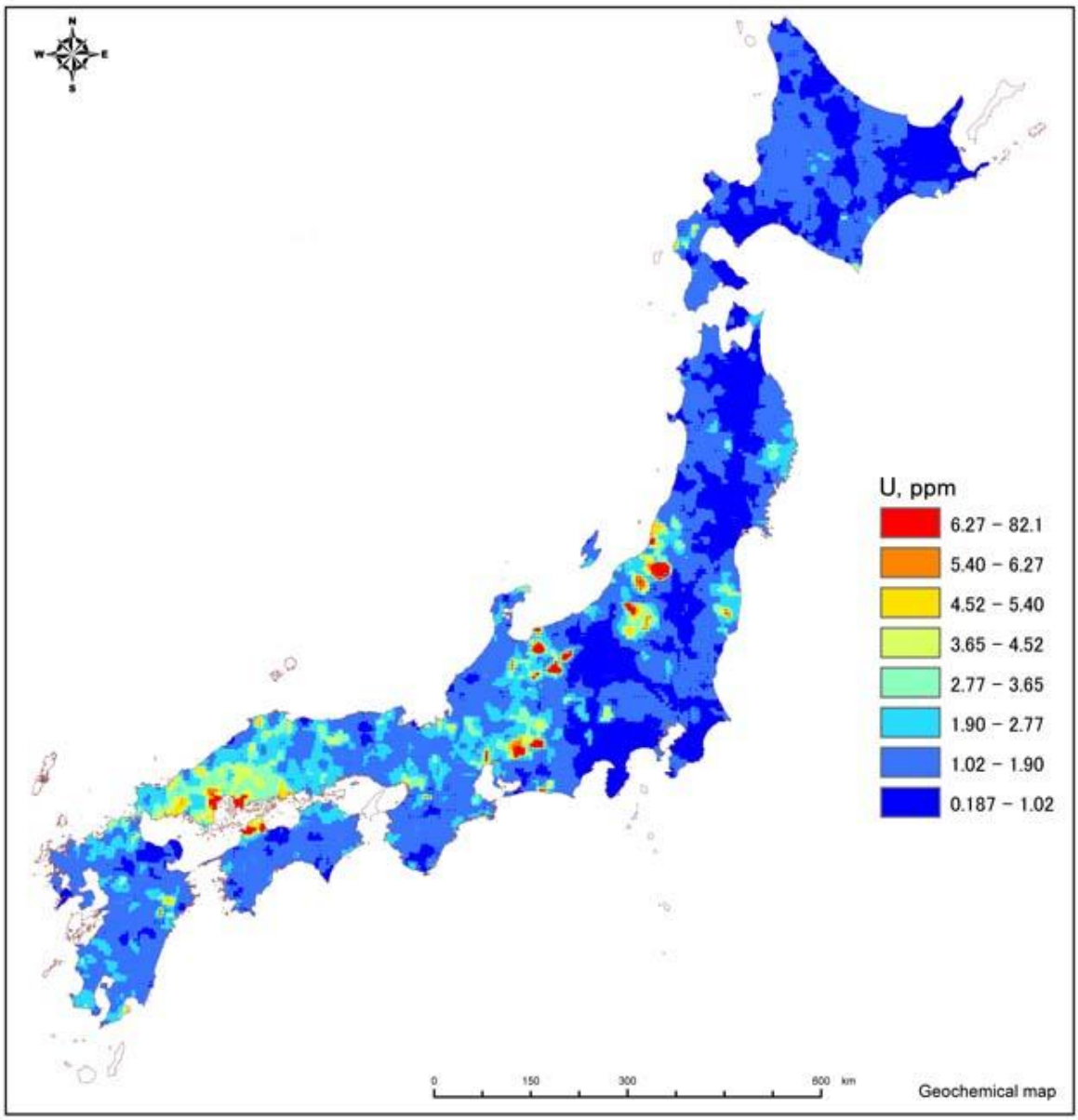

Figure B.5: GSJ Japan Geochemical Map, Uranium

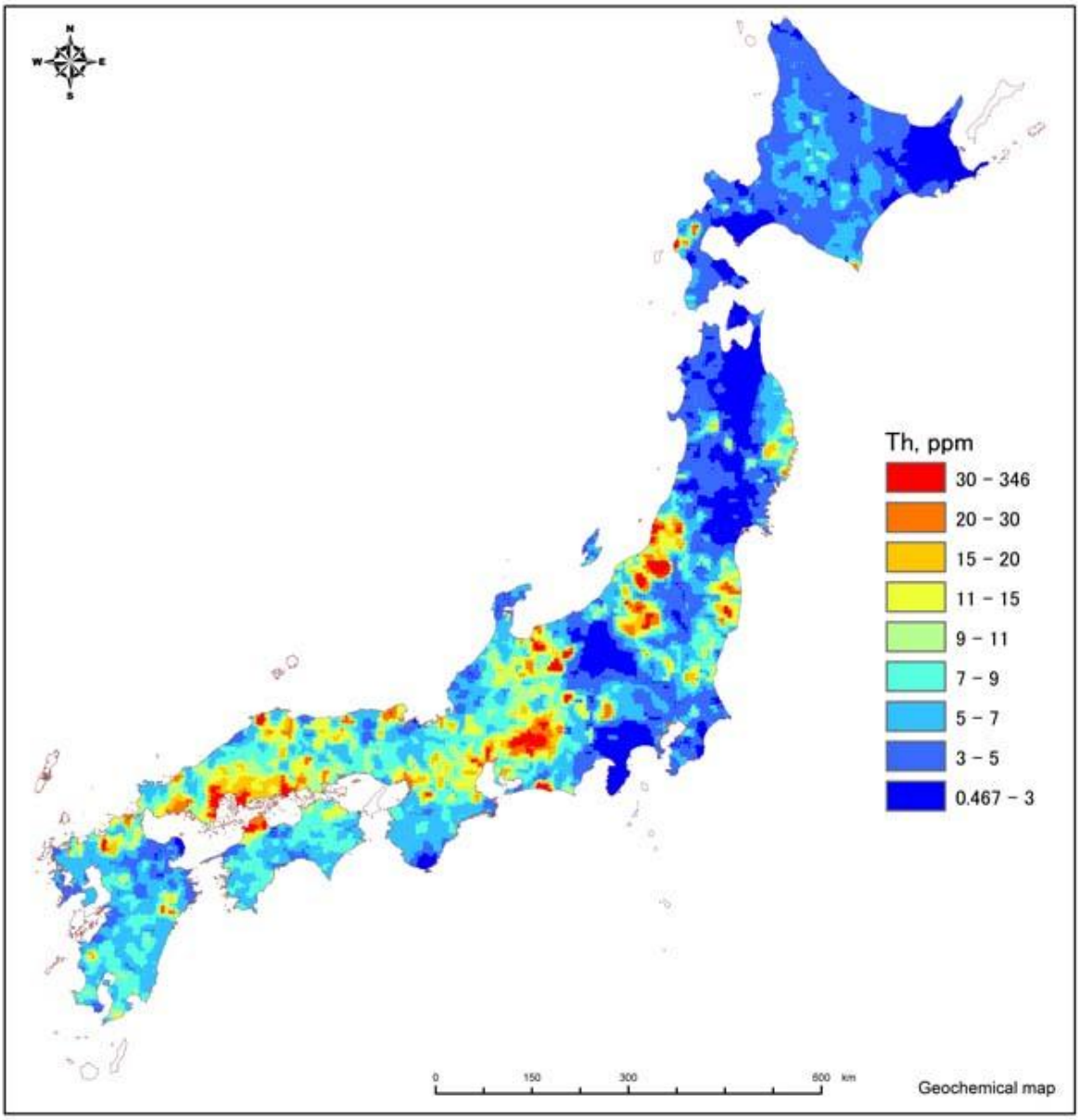

Figure B.6: GSJ Japan Geochemical Map, Thorium

Appendix C

Isotope Decay Series

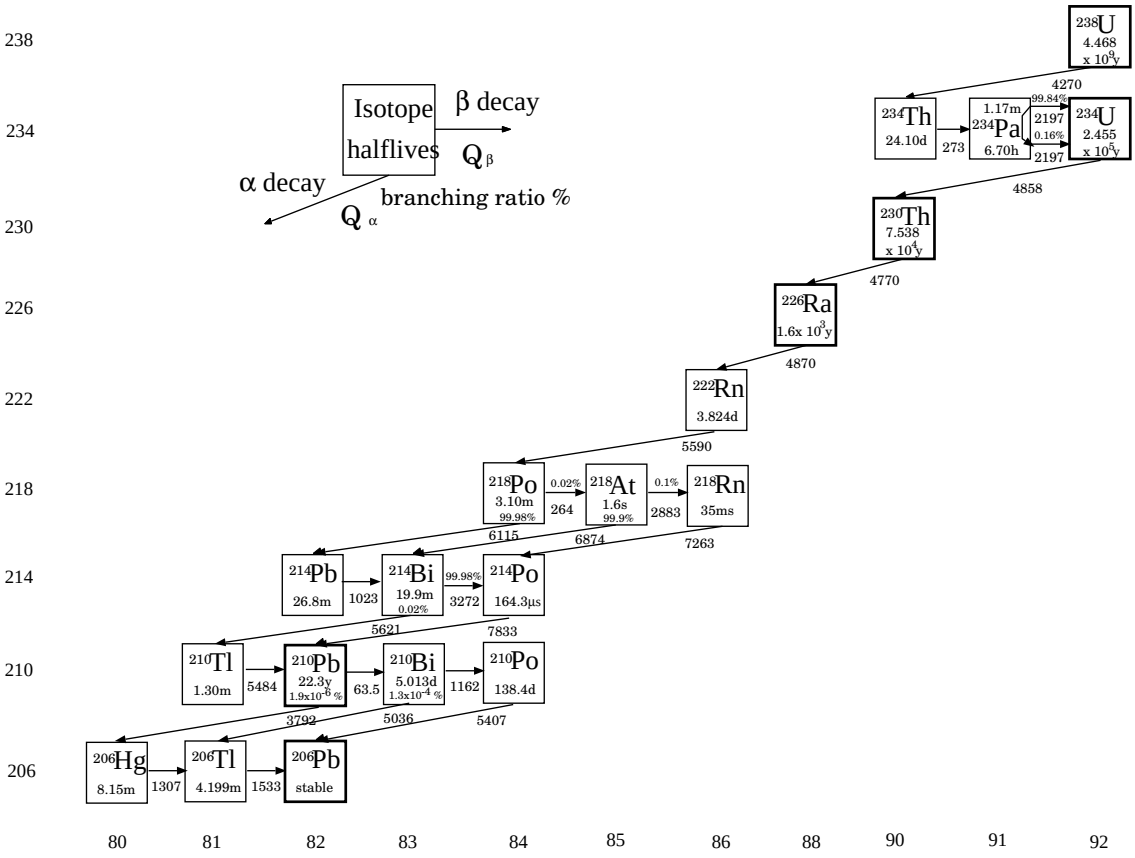

Figure C.1: U-Series Decay Chain

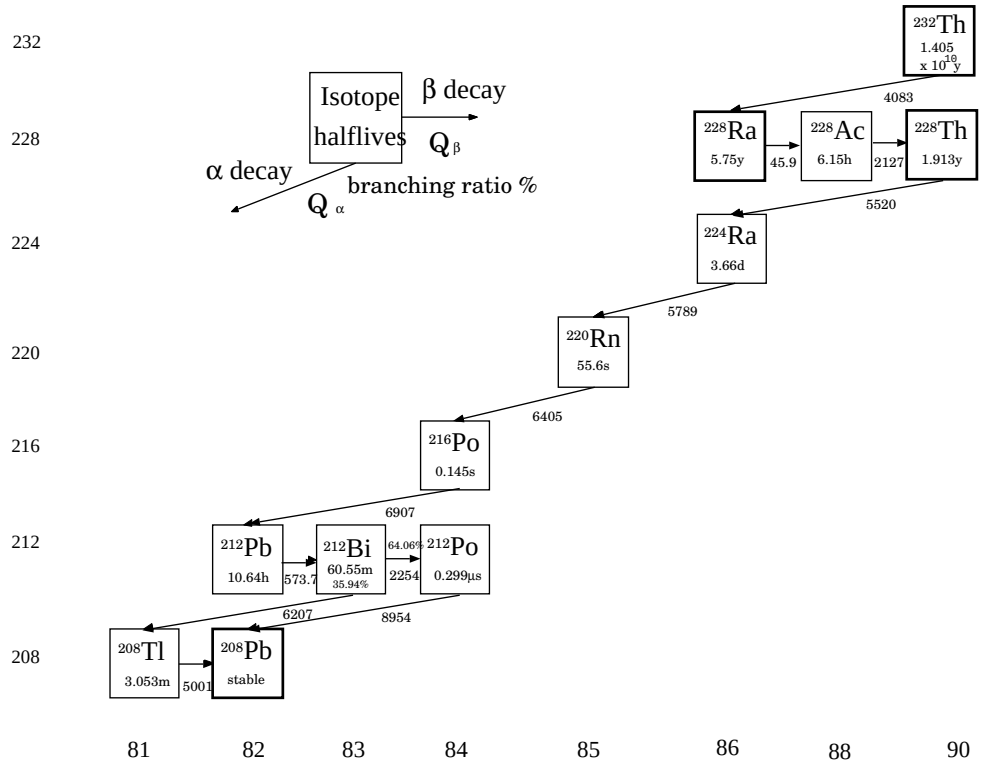

Figure C.2: Th-Series Decay Chain

Appendix D

Level Diagrams of Calibration Sources

^{60}**Co**

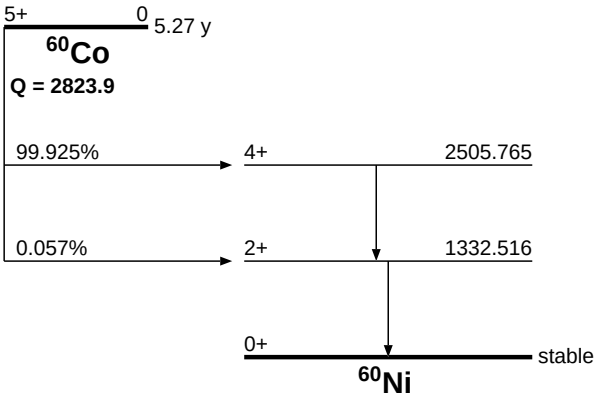

^{65}**Zn**

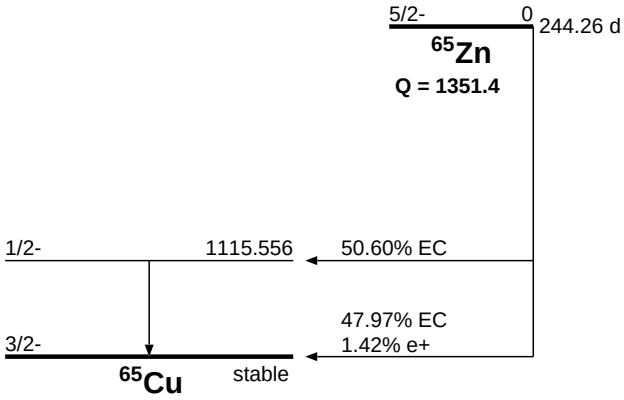

^{68}Ge

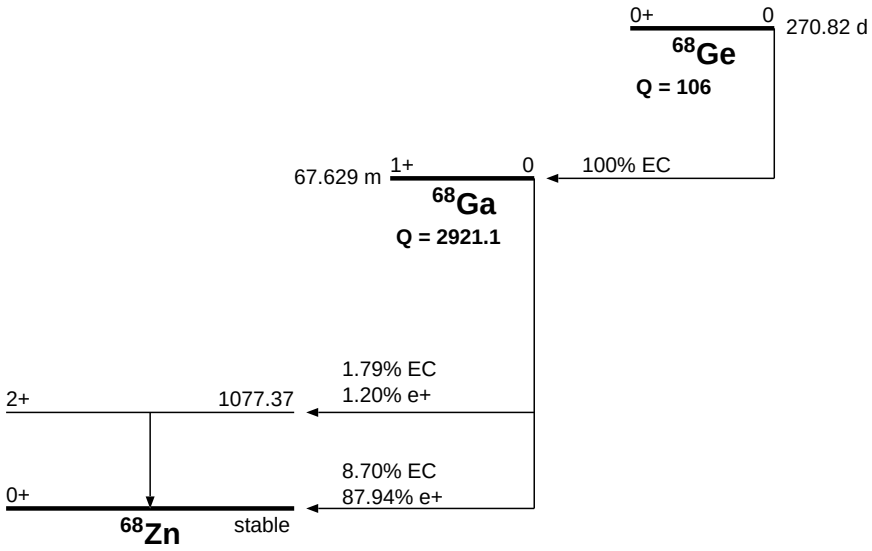

^{203}Hg

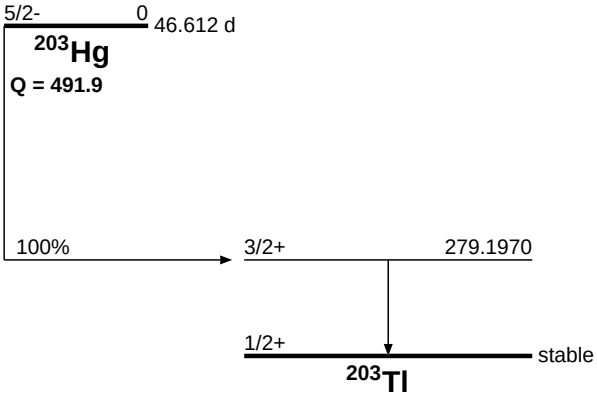

^{241}Am/^{9}Be

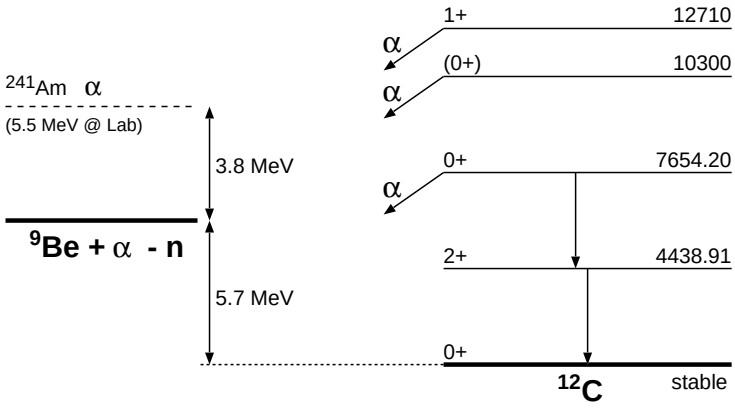

Bibliography

[1] K.Eguchi *et al.*, First Results from KamLAND: Evidence for Reactor Anti-Neutrino Disappearance, *Physical Review Letters* **90**, 021802 (2003)

[2] T.Araki *et al.*, Measurement of Neutrino Oscillation with KamLAND: Evidence of Spectral Distortion, *to appear in Physical Review Letters* (2005) [hep-ex/0406035]

[3] G.Eder, TERRESTRIAL NEUTRINOS, *Nuclear Physics* **78**, 657 (1966)

[4] G.Marx, GEOPHYSICS BY NEUTRINOS, *Czechoslovak Journal of Physics* **B19**, 1471 (1969)

[5] L.M.Krauss *et al.*, Antineutrino astronomy and geophysics, *NATURE* **310**, 191 (1984)

[6] C.Avilez *et al.*, Earth as a source of antineutrinos, *Physical Review* **D23**, 1116 (1981)

[7] M.Kobayashi *et al.*, THE EARTH AS AN ANTINEUTRINO STAR, *Geophysical Research Letters* **18**, 633 (1991)

[8] R.S.Raghavan *et al.*, Measuring the Global Radioactivity in the Earth by Multidetector Antineutrino Spectroscopy, *Physical Review Letters* **80**, 635 (1998)

[9] C.G.Rothschild *et al.*, Antineutrino geophysics with liquid scintillator detectors, *Geophysical Research Letters* **80**, 1083 (1998)

[10] G.Fiorentini *et al.*, Neutrinos and Energetics of the Earth, *Physics Letters* **B557**, 139 (2003)

[11] G.Fiorentini *et al.*, KamLAND, terrestrial heat sources and neutrino oscillations, *Physics Letters* **B558**, 15 (2003)

[12] F.Mantovani *et al.*, Antineutrinos from Earth: A reference model and its uncertainties, *Physical Review* **D69**, 013001 (2004)

[13] H.N.Pollack *et al.* HEAT FLOW FROM THE EARTH'S INTERIOR: ANALYSIS OF THE GLOBAL DATA SET, *Reviews of Geophysics* **31**, 267-280 (1993)

[14] A.M.Hofmeister *et al.* Earth's heat flux revised and linked to chemistry, *Tectonophysics* **395**, 159-177 (2005)

[15] A.M.Dziewonski *et al.* Preliminary reference Earth model, *Physics of the Earth and Planetary Interiors* **25**, 297-356 (1981)

[16] C.Bassin *et al.*, The Current Limits of Resolution for Surface Wave Tomography in North America, *EOS Trans. AGU* **81**, 897 (2000) [http://mahi.ucsd.edu/Gabi/rem.html]

[17] G.Laske *et al.*, A Global Digital Map of Sediment Thickness, *EOS Trans. AGU* **78**, 483 (1997)

[18] D.Zhao *et al.*, Seismic velocity structure of the crust beneath the Japan Islands, *Tectonophysics* **212**, 289-301 (1992)

[19] C.Mégnin *et al.*, The 3D shear velocity structure of the mantle from the inversion of body, surface, and higher mode waveforms, *Geophysical Journal International* **143**, 709-728 (2000)

[20] W.F.McDonough *et al.*, The composition of the Earth, *Chemical Geology* **120**, 223 (1995)

[21] W.F.McDonough, EARTH'S CORE, ENCYCLOPEDIA of GEOCHEMISTRY 151-156, Kluwer Academic Publishers (1999)

[22] S.M.McLennan *et al.*, EARTH'S CONTINENTAL CRUST, ENCYCLOPEDIA of GEOCHEMISTRY 145-150, Kluwer Academic Publishers (1999)

[23] S.R.Taylor *et al.*, THE GEOCHEMICAL EVOLUTION OF THE CONTINENTAL CRUST, *Reviews of Geophysics* **33**, 241-265 (1995)

[24] K.H.Wedepohl, The composition of the continental crust, *Geochimica et Cosmochimica Acta* **59** 1217-1232 (1995)

[25] R.L.Rudnick *et al.*, NATURE AND COMPOSITION OF THE CONTINENTAL CRUST: A LOWER CRUSTAL PERSPECTIVE, *Reviews of Geophysics* **33**, 267-309 (1995)

[26] K.C.Condie, Chemical composition and evolution of the upper continental crust: Contrasting results from surface samples and shales, *Chemical Geology* **104**, 1-37 (1993)

[27] S.R.Taylor *et al.*, The Continental Crust: Its Composition and Evolution, Blackwell Oxford (1985)

[28] T.Plank *et al.*, The chemical composition of subducting sediment and its consequences for the crust and mantle, *Chemical Geology* **145**, 325-394 (1998)

[29] U.Christensen, Effects of phase transitions on mantle convection, *Annual Review of Earth and Planetary Sciences* **23**, 65-87 (1995)

[30] A.W.Hofmann, Chemical differentiation of the Earth: the relationship between mantle, continental crust, and oceanic crust, *Earth and Planetary Science Letters* **90**, 297-314 (1988)

[31] C.Hawkesworth *et al.*, Elemental U and Th variations in island arc rocks: implications for U-series isotopes, *Chemical Geology* **139**, 207-221 (1997)

[32] R.D.Müller *et al.*, Digital Isochrons of the World's Ocean Floor, *Journal of Geophysical Research* **102**, 3211-3214 (1997)

[33] Geological Survey of Japan, Geological Map of Japan 1:1,000,000 CD-ROM 3rd Edition, Geological Survey of Japan (1995)

[34] S.Togashi *et al.*, Young upper crustal chemical composition of the orogenic Japan Arc, *Geochemistry Geophysics Geosystems* **1** 2000GC000083 (2000)

[35] Geological Survey of Japan, Geochemical Map of Japan, Geological Survey of Japan (2005)

[36] F.Jin *et al.* Petrological and geochemical study on Hida gneisses in the upper reach area of Tetori river: Comparative study on the pelitic metamorphic rocks with the other areas of Hida belt, Sino-Korean block and Yangtze block, *Journal of Mineralogy, Petrology and Economic Geology* **92**, 213-230 (1997)

[37] Mitsui Mining and Smelting Co.,Ltd., Kamioka-Kouzan ni okeru tansa, "Nihon no Koushou Tansa" vol.1, The Society of Resource Geology, 11-69 (1981)

[38] S.Akiyama, Geological structure of the Hida metamorphic belt and mineralization of the Kamioka-type ore deposits - Studies on regional geology and mineralization in the Kamioka district No.1, *Mining Geology* **30**, 345-362 (1980)

[39] S.Akiyama, Recent information about the mineralization in the Kamioka mining area - Studies on regional geology and mineralization in the Kamioka district No.2, *Mining Geology* **31**, 157-168 (1981)

[40] Agency for Natural Resources and Energy, Kouiki Chishitsu Chousa Houkokusho, Hida Chiiki

[41] Geological Map of the Kamiola/Mozumi Mine, Kamioka Mining & Smelting Co.,Ltd. (2003) [not published]

[42] M.Yamamoto *et al.*, Background Level of Natural Radioactivities in a Giant Water Cherenkov Detector and Its Surrounding Environment - KAMIOKANDE-II -, *Hoken Butsuri* **24**, 321-329 (1989)

[43] Power Reactor and Nuclear Fuel Development Corporation, Nihon no Uran Shigen, PNCTN7420 94-006 (1994)

[44] Y.Daclais *et al.*, Study of reactor antineutrino interaction with proton at BUGEY nuclear power plant,*Physics Letters* **B338**, 383-389 (1994)

[45] K.Schreckenbach *et al.*, DETERMINATION OF THE ANTINEUTRINO SPECTRUM FROM ^{235}U THERMAL NEUTRON FISSION PRODUCTS UP TO 9.5 MeV, *Physics Letters* **B160**, 325-330 (1985)

[46] F.Feilitzsch *et al.*, EXPERIMENTAL BETA-SPECTRA FROM ^{239}Pu AND ^{235}U THERMAL NEUTRON FISSION PRODUCTS AND THEIR CORRELATED ANTINEUTRINO SPECTRA, *Physics Letters* **B118**, 162-166 (1982)

[47] A.A.Hahn *et al.*, ANTINEUTRINO SPECTRA FROM ^{241}Pu AND ^{239}Pu THERMAL NEUTRON PRODUCTS, *Physics Letters* **B218**, 365-368 (1989)

[48] P.Vogel *et al.*, Reactor antineutrino spectra and their application to antineutrino-induced reactions. II, *Physical Review* **C24**, 1543-1553 (1981)

[49] P.Vogel *et al.*, Neutrino electromagnetic form factors, *Physical Review* **D39**, 3378-3383 (1989)

[50] V.I.Kopeikin *et al.*, Inverse Beta Decay in a Nonequilibrium Antineutrino Flux from a Nuclear Reactor, *Physics of Atomic Nuclei* **64**, 849-854 (2001)

[51] Ministry of Economy, Trade and Industry, Genshiryoku Shisetsu Unten Kanri Nenpou

[52] T.Hagner *et al.*, Muon-induced production of radioactive isotopes in scintillation detectors, *Astroparticle Physics* **14**, 33-47 (2000)

[53] D.R.Tilley *et al.*, Energy Levels of Light Nuclei A=9 (2001)

[54] Y.S.Chen *et al.*, DECAY MODES OF ^{9}Li AND STATES OF ^{9}Be, *Nuclear Physics* **A146**, 136-148 (1970)

[55] C.L.Cocke *et al.*, NEUTRON WIDTH IN ^{9}Be, *Nuclear Physics* **A111**, 623-651 (1968)

[56] P.R.Christensen *et al.*, NEUTRON DECAY OF THE 2.43 MeV AND 3.03 MeV STATES IN ^{9}Be TO ^{8}Be(g.s.), *Nuclear Physics* **89**, 656 (1966)

[57] R.Vandenbosch *et al.*, Nuclear Fission, ACADEMIC PRESS INC. (1973)

[58] D.C.Hoffman *et al.*, Spontaneous Fission, Lawrence Berkeley Laboratory, LBL-33001/UC-413 (1992)

[59] T.E.Valentine, EVALUATION OF PROMPT FISSION GAMMA RAYS FOR USE IN SIMULATING NUCLEAR SAFEGUARD MEASUREMENTS, Oak Ridge National Laboratory, ORNL/TM-1999/300 (1999)

[60] QCALC - Q-value calculator with Database version of Nov 18 2003, a program available at National Nuclear Data Center (NNDC)

[61] JENDL (α,n) Reaction Data File 2003, JAERI

[62] K.K.Sekharan *et al.*, ^{13}C(α,n)^{16}O Reaction Cross Section between 1.95 and 5.57 MeV, *Physical Review* **156**, 1187-1190 (1967)

[63] J.K.Bair *et al.*, Total Neutron Yield from the Reactions ^{13}C(α,n)^{16}O and ^{17,18}O(α,n)^{20,21}Ne, *Physical Review* **C7**, 1356-1364 (1973)

[64] R.B.Walton *et al.*, Interaction of Neutrons with Oxygen and a Study of the C^{13}(α,n)O^{16} Reaction, *Physical Review* **107**, 1065-1075 (1957)

[65] G.W.Kerr *et al.*, ENERGY LEVELS OF ^{17}O FROM ^{13}C(α,α_0)^{13}C AND ^{13}C(α,n)^{16}O, *Nuclear Physics* **A110**, 637-656 (1968)

[66] A.D.Vijaya *et al.*, THE NEUTRON SPECTRUM OF Am-Be NEUTRON SOURCES, *Nuclear Instruments and Methods* **111**, 435-440 (1973)

[67] M.J. Berger *et al.*, XCOM: Photon Cross Sections Database, a program available at National Institute of Standards and Technology (NIST)

[68] G.Rupak, Precision calculation of np→d cross section for big-bang nucleosynthesis, *Nuclear Physics* **A678**, 405-423 (2000)

[69] R.B.Firestone *et al.*, Table of Isotopes Eighth Edition, A Wiley-Interscience publication (1996)

[70] P.Vogel *et al.*, Angular distribution of neutron inverse beta decay $\bar{\nu_e} + p \rightarrow e^+ + n$, *Physical Review* **D60**, 053003 (1999)

[71] A.Kurylov *et al.*, Radiative corrections to low energy neutrino reactions, hep-ph/0211306 (2002)